DIRECTIONAL THERMAL EMISSION

AND ABSORPTION FROM SURFACE

MICROSTRUCTURES IN METALIZED PLASTICS

DISSERTATION

Michael D. Seal, Major, USAF

AFIT-ENP-DS-13-S-03

DEPARTMENT OF THE AIR FORCE
AIR UNIVERSITY

AIR FORCE INSTITUTE OF TECHNOLOGY

Wright-Patterson Air Force Base, Ohio

DIRECTIONAL THERMAL EMISSION

AND ABSORPTION FROM SURFACE

MICROSTRUCTURES IN METALIZED PLASTICS

DISSERTATION

Presented to the Faculty

Graduate School of Engineering and Management

Air Force Institute of Technology

Air University

Air Education and Training Command

in Partial Fulfillment of the Requirements for the

Degree of Master of Science in Electrical Engineering

Michael D. Seal, M.S.E.E.

Major, USAF

September 2013

DIRECTIONAL THERMAL EMISSION

AND ABSORPTION FROM SURFACE

MICROSTRUCTURES IN METALIZED PLASTICS

Michael D. Seal, M.S.E.E.
Major, USAF

Approved:

_____

Michael A. Marciniak, Ph.D. (Chairman)

23 Aug 13
_____
Date

Michael Havrilla
_____

Michael J. Havrilla, Ph.D. (Member))
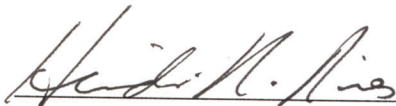
21 Aug 2013
_____
Date

_____

Milo W. Hyde IV, Ph.D. (Member)

23 Aug 2013
_____
Date

Accepted:

_____

HEIDI R. RIES, Ph.D.
Interim Dean, Graduate School of Engineering
and Management

29 Aug 2013
_____
Date

Abstract

Thermal emission, exhibiting antenna-like directivity, has been generated by a wide variety of both simple and complex micro-structures. The basic demonstrations of directional emission, and specific device performance evaluations, have been conducted at elevated temperatures, typically several hundred degrees Celsius. The most common applications for these high-temperature designs are thermal photo-voltaic and spectroscopic sources. A wide range of lower temperature applications, such as spacecraft thermal management and mid- to far-infrared optical train stray light management, are precluded by the cost and complexity of the fabrication processes employed.

In this work, a novel fabrication and physical surface optimization of a seminal directionally emitting structure is conducted in metalized plastic. The fabrication method is derived from the high-throughput compact disc manufacturing process and exploits the advantageous surface electromagnetic properties of aluminium, at the expense of forgoing high-temperature operation. Then, a novel directionally emitting structure, exhibiting a broader angular response, is design and fabricated by the same methods. The performance of both structures is evaluated through reflectance and self-emission measurements, and compared to rigorous modeling results. The necessity of conducting low-temperature emission and reflectance measurements, on instruments designed for radiometry rather than scatterometry, requires consideration of the longitudinal spatial coherence of field incidence on the surface. To this end, a well-developed modeling method was extended to include finite longitudinal spatial coherence excitation.

To my wife and children

Acknowledgments

First, I would like to thank the members of my committee for their expertise, patience, and time spent reviewing and commenting on this document. Particular thanks are due to my advisor, Dr. Michael Marciniak, who helped me negotiate the convoluted path this research has followed. I am also very grateful to Dr. Michael Havrilla for both his instruction and challenge to understand the material of my work in different ways. I am equally indebted to Maj. Milo Hyde IV, who helped me actually see what I was looking at more often than he suspects. I cannot possibly list everyone who assisted me in executing this work, but I would particularly like to thank Jack Lombardi, Neil Murphy, and Greg Smith for their persistent assistance with the fabrication efforts. Additional thanks are due to Derrick Langley, Nate Glauvitz, Robert Fitch, Andrew Browning, and Mike Grimm for their expertise in the cleanroom.

Michael D. Seal

Table of Contents

List of Figures

xi

Figure   Page

xiii

List of Acronyms

Acronym	Definition
AFIT	Air Force Institute of Technology
AFRL	Air Force Research Laboratory
AFRL/RYD	AFRL, Sensors Directorate, Aerospace Components and Sub-systems Technology Division
AFRL/RX	AFRL, Materials and Manufacturing Directorate
BRDF	Bi-directional Reflectance Distribution Function
CRC	Coupled Resonant Cavity
DC	Direct Current
DFS	Discrete Fourier Series
DFT	Discrete Fourier Transform
DRIE	Deep Reactive Ion Etching
EC	Energy Conservation
FDT	Fluctuation Dissipation Theorem
FDTD	Finite Difference Time Domain
FTIR	Fourier Transform Infrared
GM	Gold Mirror
HDR	Hemispheric Directional Reflectance
HDT	Hemispherical Directional Transmittance
ICP	Inductively Coupled Plasma
IR-VASE	Infrared Variable Angle Spectroscopic Ellipsometer
LHS	Left-Hand-Side
MIM	Metal-Insulator-Metal
MSE	Mean Squared Error

Acronym	Definition
OAP	Off-Axis Parabolic
PEC	Perfect Electrical Conductor
PMMA	polymethyl methacrylate
PWM	Pulse-Width Modulated
RCWA	Rigorous Coupled Wave Analysis
RF	Radio Frequency
RHS	Right Hand Side
RIE	Reactive Ion Etching
RX	Receiver
SEM	Scanning Electron Microscope
SG	Shallow Grating
SI	International System
SPP	Surface Plasmon Polariton
TE	Transverse Electric
TM	Transverse Magnetic
TPV	Thermal Photo-Voltaic
TX	Transmitter

DIRECTIONAL THERMAL EMISSION

AND ABSORPTION FROM SURFACE

MICROSTRUCTURES IN METALIZED PLASTICS

I. Introduction

1.1   Directional Thermal Emission Introduction

The study of the spectrally and directionally dependent reflection, transmission, absorption, and emission of infrared radiation from surfaces is well established. For most planar surfaces, the directional distribution of the reflected scatter is well modeled by the Bi-directional Reflectance Distribution Function (BRDF). These functions typically divide the scatter into specular, directional scatter, and diffuse, isotropic scatter components [1]. For periodically patterned surfaces, such as diffraction gratings, multiple distinct scatter lobes are present, with an angular width depending upon the coherence properties of both the surface and the incident field [2]. However, the directional distribution of the emissivity of a thermally excited surface is generally isotropic in nature, even for a grating [3]. A small degree of directional emissivity may be observed, largely dependent upon the surface structure of the material [4].

Macroscopic-scale thermal management applications generally employ nearly specular reflecting or nearly isotropic absorbing materials to manage the radiative component of heat transfer. For thermal reflectors and thermal barrier coatings, it is spectral selectivity that is generally emphasized, rather than directional selectivity, at the material level. Any directional aspects of the heat transfer problem are generally treated separately on a macroscopic scale with device geometries [5].

1

However, steady progress has been made in generating highly directional thermal emission from microstructured surfaces [6]. These structures exploit surface currents which exhibit spatial coherence over distances well beyond a single free-space wavelength to generate directivity [7, 8]. These surface currents arise at certain material interfaces, where they may be described in terms of Surface Plasmon Polariton (SPP) oscillations [9] or induced currents from random emitters within the material [10].

1.2   Research Motivation

The current driving application of directional emission is Thermal Photo-Voltaic (TPV) power generation. For TPVs, a heated element should preferentially emit at the photonic bandgap energy of a generating photo-voltaic junction, and not emit at other wavelengths which tend to heat the junction, reducing its efficiency. Directional confinement of the emitted field may further enhance the power generation efficiency [6]. Other directional thermal emission applications include spectroscopy sources [11].

In general, the fabrication of directional thermal emitters involves complex and expensive microfabrication processes. The following examples are typical of the microfabrication processes employed to produce the necessary periodic surface structures. To produce directional thermal emitters in silicon carbide, a process achieving an etch rate of $60nm/min$ was employed to reach a depth of $4.6\mu m$. This requires a 76 minute etch-step and the employment of a nickel chrome mask on each sample produced [11]. In the fabrication of a tungsten selective emitter, the deposition of chromium, a proprietary anti-reflection coating, and photoresist over a tungsten substrate was required. A series of dry- and wet-etching steps was required to transfer the surface patterned into the tungsten substrate, requiring extensive chemical expenditure and processing time [12].

More complex, or fabrication error intolerant, directional thermal emitter designs require even more complex processes. The production of periodic arrays of high-aspect-ratio plasmonic nanocavities required that etched silicon sacrificial molds be coated with

2

gold, then chromium, before bonding to a bulk substrate with a high temperature epoxy. It was then necessary to dissolve the silicon mold used by each sample, which requires a high through-put silicon fabrication technique to feed the emitter fabrication process [13]. The fabrication of three-dimensionally periodic tungsten photonic crystals required that silicon dioxide be deposited, patterned and etched to create a mold. The mold was then filled with a $500nm$ thick tungsten film and polished by a chemical mechanical process. The silicon dioxide mold-forming and tungsten mold-filling processes were repeated to form layers, resulting in a three-dimensional structure. Finally, the silicon dioxide structure was dissolved to release the photonic-crystal structure [14].

These are only a few examples of the complex microfabrication processes employed. Structures requiring electron beam lithography for patterning, or focused ion beam milling of surfaces, require even longer individual sample fabrication times. A wide array of designs, including split-ring resonators and arrayed antenna elements, employing these process are presented review articles [15, 16].

A clear shortfall exists in the engineering of directional thermal emitters and fabrication processes suitable for mass production. The most direct, published contribution towards this objective was a process to produce a binary periodic structure in polished steel [17]. This effort emphasized lower temperature applications, where surface oxidization is not substantially accelerated. While cost effective, the fabricated profiles suffered from both granular roughness from the base material and the isotropic etch profile produced by wet-etching. Substantial contributions in this area remain to be made, to enable the efficient fielding of directional thermal emitters.

The primary low temperature application of military interest relates to far-infrared imaging, where the observed wavelengths coincide with the self-emission wavelengths of the optical train structures. In a cooled long-wave system, stray light from the scene and

optical body is terminated on a cold stop. This is a cooled absorbing surface situated as the aperture stop of the system. Larger sections of the optical body may also be cooled [3].

However, the advancement and fielding of uncooled microbolometer array detectors have stimulated a design trade. If the cooling mechanism is removed from the detection system, then the cold stop must also be removed from the optical system. One method of mitigating the negative effects of this design trade is to develop detectors with narrow acceptance angles to alleviate the need for a stop to block stray light. This type of infrared antenna is being substantially explored, and involve complex and expensive microfabrication processes [18–20]. These processes are readily justifiable for detectors, with areas on the order of $1 cm^2$, but not for applications requiring large surface areas.

Infrared antenna elements alone cannot solve the stray light problem in all cases. The minimum achievable acceptance angle is limited by the finite span of each detector element, in particular for large dense arrays [21]. The inclusion of directional thermal emitters and absorbers into the optical designs of far-infrared imaging systems' optical trains introduces a previously unavailable degree of freedom into the stray light management problem.

The incorporation of directional thermal emitters and absorbers into optical design methodologies requires the establishment of BRDFs for these periodic surfaces. To produce BRDFs from rigorously computed diffracted order weights, it is necessary to assign some angular lobe width to the scattered orders. Fundamentally, this is because the BRDF of a periodic structure is sensitive to the number of periodic elements which contributed coherently to form the scattered lobes. The lobe width is a function of both the length over which the structure's features are periodically consistent enough to produce scattered fields with a fixed phase relationship and the longitudinal spatial coherence length of the incident field [22].

The current method of assigning lobe widths is to simply convolve the computed order weights with an angular Gaussian spreading function, indicative of the assumed

total longitudinal spatial coherence length, and normalize the results to conserve energy [23]. However, this method fails to produce accurate results when angularly dependent absorption losses are present. Since a directional thermal emitter must also exhibit the directional absorption of thermal radiation, partial spatial coherence must be introduced into the computational method to produce accurate data for BRDFs. Therefore, a second engineering shortfall clearly exists in the computation of BRDFs which accurately predict the spectrally and directionally dependent behavior of light scattered from periodically patterned surfaces.

Finally, any directional thermal emitter which is to be employed in optical design must also be accurately assessed as-fabricated. It has been shown that the assessment of low-temperature directional thermal emitter performance requires spectrally broadband measurements to fully resolve the emission features [11]. This requires that a balance be struck between measurement instrument angular resolution and signal level, resulting in substantially larger apertures being employed than are typically fielded in scatterometry instruments [24]. The reflected background signal may also be non-negligible at low temperatures, contributing substantially to the measured radiance from the directional thermal emitter. Therefore, to fully address the modeled-to-measured performance of low-temperature directional thermal emitters, both reflection- and emission-based measurements are necessary. The comparison of these measurements further requires that the modeled data, including instrument effects for each instrument, be computed from a common data set.

1.3 Dissertation Contributions

To address the three identified shortfalls, a series of research contributions are outlined. The first addresses scatter from directional emitters and absorbers for modeling in optical design. The second describes a pair of contributions in which structures are designed,

fabricated and measured. Finally, an instrumentation modeling contribution is made, specific to the evaluation of directional thermal emitters.

1.3.1   Finite Longitudinal Spatial Coherence Modeling.

The Rigorous Coupled Wave Analysis (RCWA) method for predicting the scatter from periodic surfaces is extended to include the excitation of a surface by an incident field with finite longitudinal spatial coherence. This extension overcomes the failure of the current method to accurately represent the effects of directional absorption on the reflected scatter from a periodic surface. The extension allows for the accurate generation of data for BRDFs for directional emitters, which can then be incorporated into ray-tracing-based optical design methods.

1.3.2   Novel Fabrication of Coupled Resonant Cavity Structures.

A cost-effective and high-throughput method of fabricating microstructures for low-temperature mid- to far-infrared applications is proposed, based on the compact disc manufacturing process. In compact disc manufacturing, a polycarbonate, typically Lexan, is injection molded into a stamp which carries data, encoded as a pattern of lands and pits. A reflective aluminium coating is then deposited, usually by Direct Current (DC) magnetron sputtering, onto the surface [25]. The process proposed here extends this concept to deeper structures and allows orders-of-magnitude increases in fabrication throughput, for directional thermal emitter designs which are compatible with the process, over those fabricated by the current methods.

This process is applied in the novel fabrication of a Coupled Resonant Cavity (CRC) directional thermal emitter design, optimized for low-temperature operation. The CRC structure is stamped into a polymethyl methacrylate (PMMA) substrate, and then aluminium is DC magnetron sputtered onto the patterned substrate. The novel incorporation of a DC magnetron sputter deposition model into the design process, rather than solely in the evaluation process, allows the prediction of the structure's evolving

6

response to increasing metal deposition thickness. Increasing the metal deposition depth is desirable to improve the mechanical, thermal and electrical properties of the structure. The unique result of this design and fabrication process is a mass-producible, low-temperature directional thermal emitter with enhanced surface durability due to its extended metal deposition thickness.

1.3.3 Dual-Cavity-Width Structure Design.

With the novel fabrication process established, a new directional thermal emitter design, well-suited this process, was developed towards the objective of generating an angularly broadened directional thermal emission response from a periodic surface microstructure. By exploiting the advantageous surface wave properties of aluminium in the mid- to far-infrared, the design shifts the primary mechanism of spectral tuning from material properties to surface feature dimensions.

1.3.4 Novel Infrared Instrumentation Modeling.

Finally, a process of instrument characterization is developed to correlate the results of specular reflectance, hemispherical directional reflectance, and low temperature emissivity measurements, including reflected components, of directional thermal emitters with a common set of modeled data. The novelty of the approach lies in the use of a common modeled data set across the different instruments. The comparison of measured data from multiple instruments to a common modeled data set improves the assessment of fabrication quality for directional thermal emitters, which are otherwise difficult to assess as-fabricated.

1.4 Dissertation Organization

A broad-ranging theoretical background section is presented in Chapter II to develop spectrally and directionally selective reflection and emission. Next, a review of published literature, Chapter III, traces the development of directionally selective emitters and reports on the state-of-the-art for a variety of designs.

Chapter IV describes measurement and modeling tasks, which were necessary to enable the design work in Chapter VI. First, the measurement of the complex index of refraction values for aluminium and its native oxide is presented. Then, a well-established model for predicting the physical profile changes in a DC magnetron sputtered surface structure is presented. The complex index of refraction values and surface profile model are employed in the design work. In Chapter V, the RCWA method is necessarily extended as described previously to allow for finite longitudinal spatial coherence in the incident field.

A design trade space analysis is presented in Chapter VI, justifying the design concepts. The CRC design is then developed, along with the physical optimization method. This is followed by the design of a novel dual-cavity-width structure. In Chapter VII, the fabrication process is described and intermediate fabrication results are presented for both test articles and the final products. An instrument characterization and model development process is presented in Chapter VIII, leading to the designed structure measurement results. The results for each structure are presented and analyzed in turn. Finally, the work is summarized, specific contributions are highlighted, and suggestions for future research are presented in Chapter IX.

II. Theoretical Background

2.1 Introduction

The objective of this section is to establish the theoretical underpinning for spectrally and angularly selective emission from a thermally excited surface. The dependence of the scatter from an interface on material properties is established by Maxwell's equations, and the classic Fresnel's reflection formulation is presented to predict the angular and spectral scatter from an interface between materials. Then, a more versatile numerical solution to Maxwell's equations is presented to predict the angular and spectral scatter from a periodically patterned surface. The law of conservation of energy is then invoked to predict absorption from reflection and transmission computations, under certain conditions. This predicted absorption is shown to carry an angularly selective behavior. The development then moves into the conventions of radiometry to predict the spectral content of the isotropic radiation from an ideal thermally excited surface. This ideal surface is modified, by material properties, to predict the thermal emission from real surfaces. The introduction of material properties implies directional selectivity in emission, through Kirchhoff's Law, and requires that the spatial coherence of the emitting surface currents be addressed.

The far-field spatial coherence of blackbody radiation follows Van Cittert-Zernike theory at a distance from the surface, but is not applicable in the near-field [2]. Generating a greater degree of directivity requires that the spatial coherence of the field near the surface be known. This may be done by computing the cross-spectral correlation of the field a short distance above an interface [26]. The necessary Green's function to predict the fields above a material interface is presented in a manner which explicitly maintains the visibility of the Fresnel transmission coefficients [10]. The relationship between the Fresnel transmission coefficients and near-field spatial coherence is examined under thermal excitation. Then, several means of radiating the coherent field to generate directional emission are described.

2.2 Spectrally and Directionally Selective Reflection

2.2.1 *Maxwell's Equations.*

The behavior of electromagnetic fields is predicted by Maxwell's equations, shown below in their differential forms [27]. Equation (2.1) is Faraday's Law, in which $\bar{E}$ is the electric field intensity, $\bar{M}$ is the magnetic current density, and $\bar{B}$ is the magnetic flux density taken in a time derivative [27].

$$\nabla \times \bar{E} = -\bar{M} - \frac{\partial \bar{B}}{\partial t} \tag{2.1}$$

Equation (2.2) is Ampere's law with Maxwell's correction, in which $\bar{H}$ is the magnetic field intensity, $\bar{J}$ is the current density, and $\bar{D}$ is the electric flux density taken in a time derivative [27].

$$\nabla \times \bar{H} = \bar{J} + \frac{\partial \bar{D}}{\partial t} \tag{2.2}$$

Equation (2.3) is Gauss's law where q_{ev} is the charge density and equation (2.4) is Gauss's law for magnetism where q_{mv} is the equivalent magnetic charge density. Equation (2.5) is the continuity equation, where $\bar{J}$ is the current density. Finally Equation (2.6) is the continuity equation where $\bar{M}$ is the magnetic current density [27].

$$\nabla \cdot \bar{D} = q_{ev} \tag{2.3}$$

$$\nabla \cdot \bar{B} = q_{mv} \tag{2.4}$$

$$\nabla \cdot \bar{J} = -\frac{\partial q_{ev}}{\partial t} \tag{2.5}$$

$$\nabla \cdot \bar{M} = -\frac{\partial q_{mv}}{\partial t} \tag{2.6}$$

Taken together, this set of equations describes how electric and magnetic fields are emitted from, or may excite, current distributions. For linear, homogeneous, isotropic materials, the complex permittivity, ϵ, which may be frequency dependent, relates the electric flux density $\bar{D}$ to the electric field intensity $\bar{E}$. For a non-magnetic material, this

relationship carries all of the information necessary to represent the electrical behavior of the material due to the bound charges associated with its electron structure.

$$\bar{D} = \epsilon \bar{E} \tag{2.7}$$

In optics, bulk material parameters are commonly presented in terms of the complex index of refraction, rather than complex permittivity [28]. The complex index of refraction is readily derived from the complex permittivity by equation (2.8). The complex relative permeability, μ_r, of natural materials is virtually unity at optical frequencies, and by convention, the index of refraction is relative to free-space, so the relative permeability term and both free space values in the expressions are often dropped. This leaves the relation expressed solely in terms of the relative permittivity, ϵ_r. Since ϵ_r is generally frequency dependent, the complex index of refraction, n, also carries a frequency dependency.

$$n = \sqrt{\epsilon_r \mu_r} \tag{2.8}$$

2.2.2   Scatter from Smooth Surfaces.

At a planar interface between two infinite material halfspaces, the distribution of energy from an incident field into the halfspaces may be predicted by Maxwell's equations, in closed form. In this solution the Transverse Electric (TE) (s-polarization) subscript denotes that the electric field lies normal to a plane of incidence defined to be perpendicular to the plane of the halfspace interface. The Transverse Magnetic (TM) (p-polarization) subscript denotes that the magnetic field lies normal to the plane of incidence. The rotation of the plane of incidence about its central axis is not explicitly specified, but is usually aligned to peak features of anisotropic materials or in line with some surface feature, if it exists [28].

For convenience, the interface is taken to lie parallel to the y-direction and the field of interest is transverse electric to the y-axis (TE^y) in this development. A propagating field may then may be expressed entirely by a propagation constant, $\bar{k}$, with only x- and z-direct

11

components.

$$\bar{k} = k_x\hat{x} + k_z\hat{z} = k\hat{k} \tag{2.9}$$

The Fresnel reflection coefficients, r_{TM} and r_{TE}, are then developed by satisfying the continuity of tangential fields at the infinite interface, for propagating and evanescent waves in each region, in terms of the complex value γ_L for each region, $L = 1, 2$.

$$\gamma_L = \sqrt{\epsilon_L\left(\frac{\omega}{c}\right)^2 - k^2} \tag{2.10}$$

When complex index of refraction of region 1, n_1, is fully real for all wavelengths and k_1 is restricted to real values, r_{TM} and r_{TE} may be simplified to the forms on the Right Hand Side (RHS) of equations (2.11) and (2.12), assuming that the field is incident from region 1 in terms of the angle of incident, θ_i, and transmitted angle, θ_t.

$$r_{TM} = \frac{\epsilon_2\gamma_1 - \epsilon_1\gamma_2}{\epsilon_2\gamma_1 + \epsilon_1\gamma_2} = \frac{n_2 \cos(\theta_i) - n_1 cos(\theta_t)}{n_2 \cos(\theta_i) + n_1 \cos(\theta_t)} \tag{2.11}$$

$$r_{TE} = \frac{\gamma_1 - \gamma_2}{\gamma_1 + \gamma_2} = \frac{n_1 \cos(\theta_i) - n_2 \cos(\theta_t)}{n_1 \cos(\theta_i) + n_2 \cos(\theta_t)} \tag{2.12}$$

Snell's law may then be applied to write the θ_t values in terms of θ_i, to produce an expression dependent only upon the physical parameters of the interface and the angle of incidence, θ_i.

$$\frac{\sin(\theta_i)}{\sin(\theta_t)} = \frac{n_2}{n_1} \tag{2.13}$$

With a further simplification, assuming the incident field arrives from free space, $n_1 = 1+i0$, and that the complex index of refraction in region 2 is wavelength, λ, dependent, the polarization-dependent solutions to the scatter of an incident plane wave may be expressed in a common geometric optics form of Fresnel's Equations (2.14) and (2.15)[29].

$$r_{TM}(\lambda, \theta_i) = \frac{n_2(\lambda) \cos(\theta_i) - n_1 \sqrt{1 - \left(\frac{n_1}{n_2(\lambda)} \sin(\theta_i)\right)^2}}{n_2(\lambda) \cos(\theta_i) + n_1 \sqrt{1 - \left(\frac{n_1}{n_2(\lambda)} \sin(\theta_i)\right)^2}} \tag{2.14}$$

$$r_{TE}(\lambda, \theta_i) = \frac{n_1 \sqrt{1 - \left(\frac{n_1}{n_2(\lambda)} \sin(\theta_i)\right)^2} - n_2(\lambda) \cos(\theta_t)}{n_1 \sqrt{1 - \left(\frac{n_1}{n_2(\lambda)} \sin(\theta_i)\right)^2} + n_2(\lambda) \cos(\theta_t)} \tag{2.15}$$

12

The polarized reflectance values, R_{TM} and R_{TE}, express the normalized scatter into region 1 in terms of intensity or power rather than complex field.

$$R_{TM}(\lambda, \theta_i) = |r_{TM}(\lambda, \theta_i)|^2 \tag{2.16}$$

$$R_{TE}(\lambda, \theta_i) = |r_{TE}(\lambda, \theta_i)|^2 \tag{2.17}$$

The reflectance from a lossless dielectric, fused silica glass, is shown in Figure 2.1 (a) and for a metal, aluminium, in Figure 2.1 (b). The reflectance value is clearly directionally dependent in both cases.
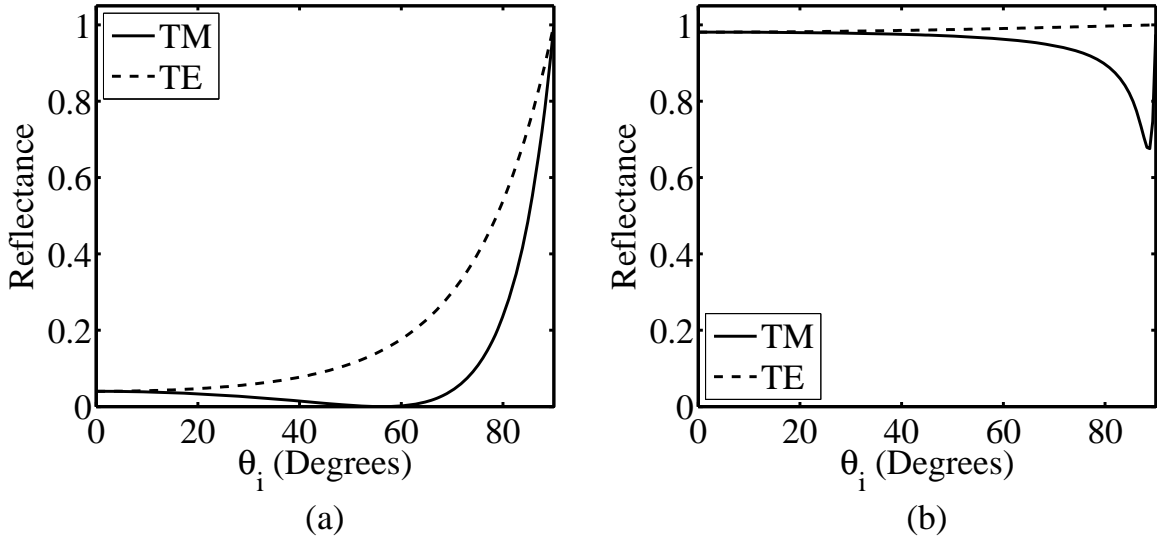
Figure 2.1: Directionally and spectrally dependent Fresnel reflectance from (a) glass, n=1.5+i0, and (b) aluminium n=8+i40, at the modeled wavelengths.

2.2.3 Rigorous Coupled Wave Analysis.

When a plane wave is incident on a periodically patterned surface, the phase of induced surface current oscillations are related by the surface profile. If discrete points on the profile are then taken as discrete emitters, or Huygens Fresnel emitters, then a pattern of constructive and destructive interference is observed in the far-field pattern. Each peak is identified by an order, m, and is located at diffracted angle, $\theta_{d,m}$, determined by the classic

13

grating equation for a fixed grating period, Λ.

$$\theta_d, m = \sin^{-1}\left(\frac{m\lambda}{\Lambda} - \sin(\theta_i)\right) \tag{2.18}$$

Equation (2.18) gives the angular distribution of the orders, but not the distribution of power, or diffraction efficiencies of the orders. Closed-form solutions are only available for the simplest profiles and material assumptions. However, a large family of rigorous numerical computation methods has been developed to predict the angular and spectral scatter from periodic structures under a wide range of conditions. One method, particularly suited to the proposed application, is the RCWA method developed by Moharam and Gaylord in 1981 [30].

RCWA has proven to be the computational tool of choice for surface relief gratings due to its performance in calculating the diffraction efficiencies. This analysis technique, although confined to lamellar or rectangular structures, is computationally performant because numerical integration is replaced by the computation of the eigenvectors and eigenvalues of matrixes [31]. An enhanced computational implementation which improved numerical stability was published in 1995 [32], followed almost immediately by a method of extending the technique to multi-layered structures [33].

Difficulties with the convergence of the RCWA technique for conductive materials and deep structures, which plagued the method for over 20 years, were overcome systematically, beginning with publications by Lifeng Li in 1993 [34]. In 1996, Li published a correction to the Fourier factorization scheme used in the RCWA method. In the original development, Laurent's Rule was misapplied, which resulted in the continuity of fields not being uniformly preserved across discontinuities in the periodic structure. However, when sufficient Fourier terms were used, the results approximated their correct values. When the correction was applied, the convergence rate of the method improved by more than an order of magnitude. Reducing the number of Fourier terms required produced a commensurate reduction in computation time [35]. When corrected in this manner, the

14

RCWA method is sometimes referred to as the Fourier Modal Method, in particular when applied to gratings which are periodic in two dimensions [36].

In RCWA, an incident field is expanded as a series of plane waves above the periodic region of the structure, per the Rayleigh expansion, so Bloch-Floquet boundary conditions are appropriate. It is similarly expanded below the last periodic layer of the structure. Within the periodic region, the complex permittivity of a unit cell of the structure is expanded into Fourier coefficients matching the Rayleigh expansion orders. The continuity of tangential fields is incrementally applied to produce a unique solution. Therefore, it is a particular implementation of mode matching, which is applicable to the continuum of modes found within conductive lamellar features. This method produces a field solution which is rigorous, and the accuracy of the solution depends solely upon the number of Fourier terms retained in the expansions. The solution is physical to the extent that perfect coherence is assumed in the incident field impinging on an infinite array [7].

An RCWA method code was implemented from Moharam's work formulation for a one-dimensional binary grating illuminated and examined in the TM (p)-polarized orientation [32, 33] including the Fourier factorization correction developed by Lifeng Li [35]. This development provided a rigorous and extremely computationally efficient solution for single- and multiple-depth grating structures periodic in one dimension. Both TE, (s)-polarized, and conical diffraction implementations have also been published [32].

By the convention of the cited works, the TM polarization implies that the periodic variation of the grating, periodic in only one dimension, lies in the plane of incident. The geometry of the TM polarization problem is shown in Figure 2.2. The z-direction is normal to the surface and x-direction is along the surface, in the plane of incidence. Material parameter data is primarily derived from optical resources in this work, and the complex component of the index of refraction of a lossy dielectric or metal is commonly published as a positive value [29]. However, in the convention of the RCWA development, which

uses the $+j\omega t$ convention, the complex conjugate values of the complex index of refraction must be used.
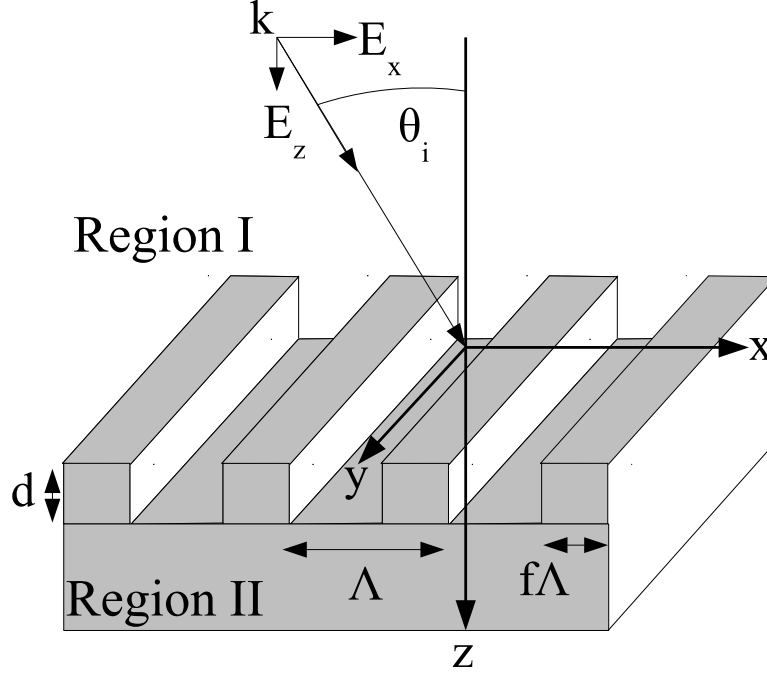
Figure 2.2: TM (p-polarization) planar diffraction RCWA geometry is shown for a binary structure periodic along the x-axis and invariant along the y-axis. A field, described by its electrical components, E_x and E_z, in the x-z plane is incident at an angle θ_i upon the structure, which has a period, Λ. The structure defines the interface between two material regions in terms of a groove depth, d, and a fill factor, f, which is a fraction of the period.

$$H_{i,y} = \exp\left[-jk_0 n_I \left(x \sin(\theta_i) + z \cos(\theta_i)\right)\right] \tag{2.19}$$

The incident normalized magnetic field is given by equation (2.19) where λ_0 is the free space wavelength of the incident field and $k_0 = 2\pi/\lambda_0$. The total incident, reflected diffracted, and transmitted diffracted fields are given by equation (2.20). The normalized magnetic field amplitude for the m-th backward diffracted wave is R_m and the normalized magnetic field amplitude for the m-th forward diffracted wave is T_m. D_L is the final layer

16

depth of the grating.

$$H_{I,y} = \exp\left[-jk_0 n_I \left(x \sin(\theta_i) + z \cos(\theta_i)\right)\right] + \sum_m R_m \exp\left[-j\left(k_{xm}x - k_{I,zm}z\right)\right]$$

$$H_{II,y} = \sum_m T_m \exp\left[-j\left(k_{xm}x - k_{II,zm}\left(D_L - z\right)\right)\right]$$

(2.20)

The x-directed component of the backward diffracted propagation constant, k_{xm}, is determined by the Floquet condition in equation (2.21), which depends upon the angle of incidence, θ_i, the grating period, Λ, and diffraction order, m. The z-directed propagation constant, $k_{L,zm}$, in region, L=I or L=II, varies according to equation (2.22). By the convention of the development, the propagation constants must be either positive real or negative imaginary, since the final diffraction efficiency results are for the far field. A growing exponential field, under this condition, is non-physical.

$$k_{xm} = k_0 \left[n_I \sin\left(\theta_i\right) - m\left(\lambda_0/\Lambda\right)\right]$$

(2.21)

$$k_{L,zm} = k_0 \left[k_0^2 n_L^2 - k_{xm}^2\right]^{1/2}$$

(2.22)

However, enforcing this condition requires some care when dealing with the square roots and squares of complex numbers. The square root of a real or complex number has both a positive and negative form, both of which are mathematically correct. By default, MATLAB® selects the primary or positive form of the square root of a negative real number. When the RCWA algorithm is implemented for fully real materials in all regions, the sign convention may be efficiently enforced by applying the complex conjugate operation to equation (2.22), which has no effect on the positive real solution.

When the index of refraction is complex in a region, this computationally efficient method is no longer correct. In order to retain the convention of negative imaginary components of the index of refraction corresponding to a lossy material, equation (2.22) must be implemented as shown. If for consistency sake, it is desirable to retain the conjugate operation, then a negative imaginary component such as *eps*, the smallest

17

number representable by the computer system, may be added to any fully real material's index of refraction with minimal impact.

The complex permittivity in the periodic region is expressed as a sum of its Fourier components as shown in equation (2.23) with the number of factorization terms selected to match the number of diffraction orders. Per Li, another form of this factorization, shown in equation (2.24), is required to correct the Fourier factorization error in the original development [35]. Without this factorization change, the originally published RCWA formulations [32, 33] do not converge with a manageable number of Fourier orders for the materials and structures considered in this work.

$$\epsilon_p = \sum_m \epsilon_{p,m} \exp\left(j2\pi m/\Lambda\right) \tag{2.23}$$

$$\frac{1}{\epsilon_p} = \sum_m \zeta_{p,m} \exp\left(j2\pi m/\Lambda\right) \tag{2.24}$$

In the modulated region, the tangential magnetic and electric fields are expressed as Fourier expansions in terms of the spatial harmonic fields as shown in equations (2.25) and (2.26), respectively. $U_{ym}(x)$ and $S_{xm}(x)$ are the normalized amplitudes of the m-th spatial harmonic field components.

$$H_{p,gy} = \sum_m U_{p,ym}(z) \exp\left(-jk_{xm}x\right) \tag{2.25}$$

$$E_{p,gx} = \left(\frac{\mu_0}{\epsilon_0}\right)^{1/2} \sum_m S_{p,xm}(z) \exp\left(-jk_{xm}x\right) \tag{2.26}$$

The fields in equations (2.25) and (2.26) satisfy Maxwell's equations in the grating region through

$$\frac{\partial H_{p,gy}}{\partial z} = -j\omega\epsilon_0\epsilon_p(x) E_{p,gx} \tag{2.27}$$

$$\frac{\partial E_{p,gx}}{\partial z} = -j\omega\mu_0 H_{p,gy} + \frac{\partial E_{p,gz}}{\partial x} \tag{2.28}$$

A set of coupled equations is then formed by substituting equations (2.25) and (2.26) into equations (2.27) and (2.28) and eliminating $H_{p,gy}$. The coupled wave equation is shown

18

in matrix form after reduction in equation (2.29), where E_p is defined in equation (2.30) and B_p is defined in equation (2.31).

$$\left[\frac{\partial^2 U_{p,y}}{\partial (k_0 z)^2}\right] = \left[E_p\right]\left[B_p\right]\left[U_{p,y}\right] \tag{2.29}$$

$$\left[E_p\right] = toeplitz(\epsilon_{p,m}) \tag{2.30}$$

In equation (2.31), K_x is a diagonal matrix of elements k_{xm}/k_0 and I is the identity matrix.

$$\left[B_p\right] = [K_x]\left[E_p^{-1}\right][K_x] - [I] \tag{2.31}$$

The matrix F_p is defined similarly to E_p, but incorporates the Fourier factorization from equation (2.24).

$$\left[F_p\right] = toeplitz\left(\zeta_{p,m}\right) \tag{2.32}$$

The eigenvectors of the product of the B_p matrix from equation (2.31) and F_p matrix from equation (2.32) are efficiently numerically computed to form the matrix of eigenvectors, W_p. The square roots of the vector of eigenvalues, v_p, are taken to form the diagonal matrix Q_p.

$$\left[W_p\right], \left[v_p\right] = eig\left(\left[F_p^{-1}\right]\left[B_p\right]\right) \tag{2.33}$$

A final matrix product is taken to form the V_p matrix.

$$\left[V_p\right] = \left[F_p\right]\left[W_p\right]\left[Q_p\right] \tag{2.34}$$

These per-layer components are then used in the enhanced transmission matrix approach to solve for the reflection and transmission coefficients [11]. At z=0, the interface between free space and the first grating layer, the tangential electromagnetic fields are found through

$$\begin{bmatrix} \delta_{m0} \\ j\delta_{m0}\cos(\theta_i)/n_I \end{bmatrix} + \begin{bmatrix} I \\ -jZ_I \end{bmatrix} R = \begin{bmatrix} W_1 & W_1 X_1 \\ V_1 & -V_1 X_1 \end{bmatrix}\begin{bmatrix} c_1^+ \\ c_1^- \end{bmatrix} \tag{2.35}$$

At the boundary between the p-1 layer and the p-th layer, where $z = D_{p-1}$, the tangential fields are matched by

$$\begin{bmatrix} W_{p-1}X_{p-1} & W_{p-1} \\ V_{p-1}X_{p-1} & -V_{p-1} \end{bmatrix} \begin{bmatrix} c_{p-1}^+ \\ c_{p-1}^- \end{bmatrix} = \begin{bmatrix} W_p & W_pX_p \\ V_p & -V_pX_p \end{bmatrix} \begin{bmatrix} c_p^+ \\ c_p^- \end{bmatrix} \quad (2.36)$$

Finally, at the boundary between the final grating layer L and the output region $z = D_L$, tangential fields are matched by

$$\begin{bmatrix} W_LX_L & W_L \\ V_LX_L & -V_L \end{bmatrix} \begin{bmatrix} c_L^+ \\ c_L^- \end{bmatrix} = \begin{bmatrix} I \\ jZ_{II} \end{bmatrix} T \quad (2.37)$$

This may be expressed as the product,

$$\begin{bmatrix} \delta_{m0} \\ j\delta_{m0}\cos(\theta_i)/n_I \end{bmatrix} + \begin{bmatrix} I \\ -jZ_I \end{bmatrix} R =$$
$$\prod_{p=1}^{L} \begin{bmatrix} W_p & W_pX_p \\ V_p & -V_pX_p \end{bmatrix} \begin{bmatrix} W_pX_p & W_p \\ V_pX_p & -V_p \end{bmatrix}^{-1} \begin{bmatrix} I \\ jZ_{II} \end{bmatrix} T \quad (2.38)$$

At this point, it is possible, although numerically unstable, to seek a direct solution through a brute-force solution of simultaneous equations. To preempt the numerical instability, the matrix inversions of equation (2.38) may be expanded as a product of two matrices, where $f_{L+1} = I$ and $g_{L+1} = jZ_{II}$ when p=L.

$$\begin{bmatrix} W_L & W_LX_L \\ V_L & -V_LX_L \end{bmatrix} \begin{bmatrix} W_LX_L & W_L \\ V_LX_L & -V_L \end{bmatrix}^{-1} \begin{bmatrix} f_{L+1} \\ g_{L+1} \end{bmatrix} T =$$
$$\begin{bmatrix} W_L & W_LX_L \\ V_L & -V_LX_L \end{bmatrix} \begin{bmatrix} X_L & 0 \\ 0 & I \end{bmatrix}^{-1} \begin{bmatrix} W_L & W_L \\ V_L & -V_L \end{bmatrix} \begin{bmatrix} f_{L+1} \\ g_{L+1} \end{bmatrix} \quad (2.39)$$

The RHS of equation (2.39) reduces to equation (2.40), where the a_L and b_L are related to the final f_{L+1} and g_L values by equation (2.41).

$$\begin{bmatrix} W_L & W_LX_L \\ V_L & -V_LX_L \end{bmatrix} \begin{bmatrix} X_L & 0 \\ 0 & I \end{bmatrix} \begin{bmatrix} a_{L+1} \\ b_{L+1} \end{bmatrix} \quad (2.40)$$

20

$$\begin{bmatrix} a_L \\ b_L \end{bmatrix} = \begin{bmatrix} W_L & W_L \\ V_L & -V_L \end{bmatrix}^{-1} \begin{bmatrix} f_{L+1} \\ g_{L+1} \end{bmatrix} \tag{2.41}$$

A substitution of $T = a_L^{-1} X_L T_L$ in the final layer into equation (2.38) produces

$$\begin{bmatrix} f_L \\ g_L \end{bmatrix} T_L = \begin{bmatrix} W_L \left(I + X_L b_L a_L^{-1} X_L \right) \\ V_L \left(I - X_L b_L a_L^{-1} X_L \right) \end{bmatrix} T_L \tag{2.42}$$

This process is repeated for all layers to obtain equation (2.43), where the final T value is defined by equation (2.44).

$$\begin{bmatrix} \delta_{m0} \\ j\delta_{m0} \cos\theta/n_I \end{bmatrix} + \begin{bmatrix} I \\ -jZ_I \end{bmatrix} R = \begin{bmatrix} f_1 \\ g_1 \end{bmatrix} T_1 \tag{2.43}$$

$$T = a_L^{-1} X_L \ldots a_p^{-1} X_p \ldots a_1^{-1} X_1 T_1 \tag{2.44}$$

The R_m and T_m values, equivalent to the Fresnel reflection and transmission coefficients for an unmodulated surface, are then readily extracted algebraically and the diffraction efficiencies may be calculated. The reflected and transmitted diffraction efficiencies rigorously predict the direction in which power is reflected from, or transmitted through, the surface on a spectral basis. The Fresnel reflectance term, R, from the Fresnel equations (2.16) is precisely equivalent to the reflected diffraction efficiency, DE_R, in RCWA. Likewise, the transmittance term, T, is precisely equivalent to the transmitted diffraction efficiency, DE_T.

$$DE_R = RR^* \mathrm{Re}\left[\frac{k_{I,zm}/n_I^2}{k_0 n_I \cos\theta_i} \right] \tag{2.45}$$

$$DE_T = TT^* \mathrm{Re}\left[\frac{k_{II,zm}/n_{II}^2}{k_0 n_I \cos\theta_i} \right] \tag{2.46}$$

Since multilayered structures may be represented by this algorithm, it was naturally proposed that a smooth profile could be approximated by a series of stair steps to produce nearly arbitrary profiles for dielectric [37] and metallic [31] structures. Indeed, this is precisely the type of discretization observed in basic Finite Difference Time Domain

(FDTD) computations. Initial results showed excellent agreement with other methods and measured values. It was not until the Fourier factorization rules were corrected and rapid convergence for deep metal structures was possible that this assumption was seriously questioned [38]. This study shows that the two components of the electric field vector are discontinuous across different segments of the grating profile, causing localized field maxima which do not homogenize with increasing numbers of layers of Fourier terms for the TM polarization. These high-field points contaminate the solution, precluding the convergence of an approximated smooth profile solution with the solution to a rigorously represented profile [38].

Although the investigation into the source and degree of the error concluded that RCWA should only be used for approximating coarse structures with stair steps, this uncaveated conclusion is overstated. Studying deep metallic structures, which was not considered in the accuracy study, in the mid- to far-infrared imposes several negative convergence criteria on the solution, regardless of the method employed. Besides the extended depth, the real and imaginary components of the complex index of refraction values for metals are quite large. This increases the number of Fourier terms required for solution in all of the differential methods, and requires finer meshing in FDTD computations due to the substantial numerical dispersion [39]. Therefore, this source of error must be considered as part of the trade off between computation time and solution accuracy in all cases.

2.3 Conservation of Energy and Absorption

Two means of predicting the reflection and transmission of a plane-wave incident on a halfspace have been presented. For the closed system assumed, in which an incident field illuminating a material surface carries all of the significant energy, conservation of energy may be expressed by the sum of the absorbed, A, reflected, R, and transmitted, T, fractions of the total energy [5]. This allows the absorptance to be computed as the energy

unaccounted for by transmission or reflection (2.47).

$$1 = A\left(\lambda, \theta_i\right) + R\left(\lambda, \theta_i\right) + T\left(\lambda, \theta_i\right) \tag{2.47}$$

Referring back to Figure 2.1, it can be seen that a directional reflectance was observed both for a lossless (a) and very lossy (b) dielectric halfspace. In the lossy halfspace, after a sufficient propagation distance within the lossy medium, the power from the incident field is asymptotically dissipated or absorbed, so the transmittance term goes to zero. In this case, a directional absorptance is predicted by the directional reflectance, when an incident coherent field is assumed.

$$1 = A\left(\lambda, \theta_i\right) + R\left(\lambda, \theta_i\right) \tag{2.48}$$

Directional absorptance may be considered in terms of classic antenna theory, whereby a plane wave is preferentially absorbed over a range of incident angles, and rejected over other ranges. This defines the antenna pattern [21]. This effect is shown in Figure 2.3, for an isotropic, half-wave dipole, and short array of isotropic elements. In each case, the absorptance is normalized to the peak value for the given configuration. The angular region in which the absorptance approaches unity becomes narrower, implying that the reflectance increases outside the pattern region. The directional absorptance, computed by RCWA for a periodic structure, can readily be shown to exhibit array-like absorptance behaviors, under plane-wave illumination. The implications of this absorptance behavior in terms of emission are developed in the next section, after the classical thermal radiation process is established.

2.4   Spectrally and Directionally Selective Emission

2.4.1   Basic Heat Transfer.

To define thermal emission from a surface, it is necessary to review certain heat transfer terms. The first is temperature, defined as the total of the vibrational energy of the atoms or molecules, and sometimes electrons, of a material [40]. The temperature

23
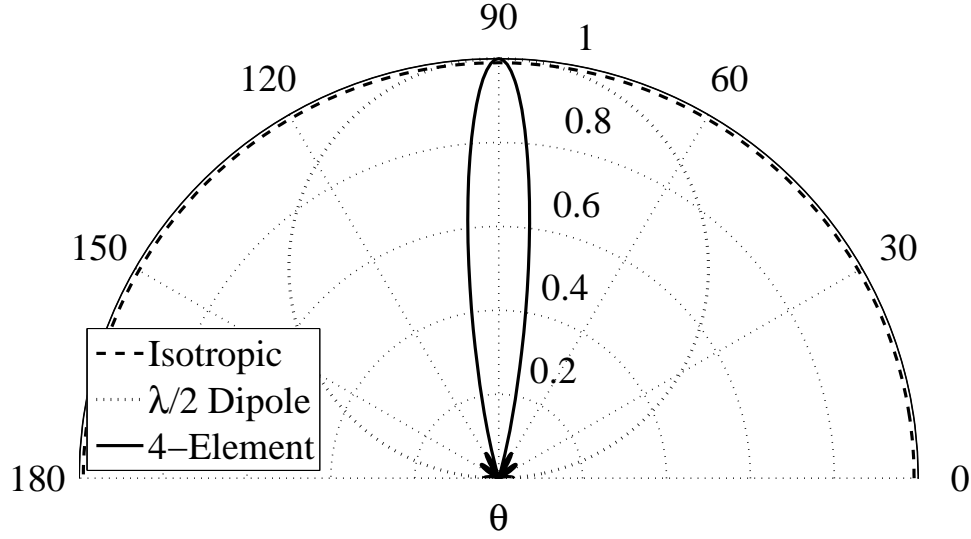
Figure 2.3: Normalized angular absorptance patterns for isotropic, half-wave dipole and an array of four isotropic elements with zero phase deviation and one wavelength separation between elements.

of a material may be changed by the three modes of heat transfer conduction, radiation and convection. Conduction is the transfer of kinetic energy within or through a medium as vibrational energy. Convection is a special case of conduction in which particles at a material interface with elevated kinetic energy may flow away from the interface and be replaced by particles with lower kinetic energy. Finally, radiation is the transfer of energy as electromagnetic waves and is the only mechanism by which thermal energy is transferred across free-space [40].

The energy transfer via electromagnetic waves is best modeled by Maxwell's Equations, but the fields of interest in this work are those which are thermally excited. So, the connection between the temperature of a material and its thermal emission is developed from quantum mechanics. An axiomatic method is taken to describe the emission from an ideal surface leading to the blackbody formalism common to radiometry.

2.4.2 Blackbody Emission.

An ideal solid material can be described as a lattice or network of molecules, held in place by interatomic forces. The molecules can only vibrate around their equilibrium positions, and the allowed oscillations define a vibrational mode structure. Since vibrational modes dominate molecular behavior at the temperatures of interest, only these modes will be considered, although rotational modes and electron transitions are also present. These vibrational modes then define the energy states which the molecule can occupy. Some of these states are degenerate, or indistinguishable by their frequencies, and the density of states, $p(\omega)$, for a three dimensional cavity or lattice goes as the frequency, ω, squared, where c is the speed of light in free space [41].

$$p(\omega) = \frac{8\pi}{c^3}\omega^2 \tag{2.49}$$

The time-average energy at any given frequency then depends upon the energy of the, possibly degenerate, state and the probability that the state is occupied. The energy, E_P, of each non-degenerate state is defined by the Planck Relation, depending upon Planck's constant, $\hbar$, and the oscillation frequency, ω.

$$E_P = \hbar\omega \tag{2.50}$$

The probability that the state is occupied is given by the Bose-Einstein distribution, where the probability that a state, $f_{BE}(\omega)$, with an oscillation frequency, ω, is occupied is a function of the lattice temperature, T, Planck's Constant, $\hbar$, and Boltzmann's Constant, k_B.

$$f_{BE}(\omega) = \frac{1}{e^{\hbar\omega/k_BT} - 1} \tag{2.51}$$

A molecule oscillating at an elevated energy state surrounded by an environment at zero absolute temperature would lower its energy state by emitting photons in all directions, until the molecule's temperature reached absolute zero. The energy of the emitted photons necessarily corresponds to the discrete energy of the states. The same distribution of

emitted photons is observed, even if the material gains energy through a heat transfer mechanism to maintain thermodynamic equilibrium. The emitted energy per unit volume, per unit frequency is then simply the product of the equations (2.49), (2.50), and (2.51) [41].

$$S(\omega) = \frac{\hbar\omega}{1} \frac{8\pi}{c^3} \omega^2 \frac{1}{e^{\hbar\omega/k_B T} - 1} \tag{2.52}$$

The ideal material described thus far, is termed a blackbody, but the expression is in terms of oscillation frequencies and a material volume element. Since radiation is primarily a surface phenomenon, it is desirable to express the emission in terms of surface areas, and by radiometric convention, in wavelength rather than frequency. If the wavelength form of the density of states expression, $p(\omega) = 8\pi/\lambda^4$ is substituted, and multiplied by $c/4$ to reflect the energy density on a bounding surface, further scaled by $1/2$ assuming thermodynamic equilibrium, then Plank's relation for frequency and wavelength, may be applied to produce Planck's Law in its most common form for radiometry, once the derivative substitution, $d\omega = -cd\lambda/\lambda^2$ is included.

$$E_{b\lambda}(T, \lambda) = \frac{2\pi hc^2}{\lambda^5 \left(e^{hc/\lambda k_B T} - 1\right)} \tag{2.53}$$

In this common form of Planck's Law, equation (2.53), the spectrally varying emissive power distribution is expressed as the power leaving a unit area of a halfspace at a fixed temperature[5]. In the International System (SI) units, the Boltzmann's constant, $k_B = 1.3806 \times 10^{-23} J/K$, Planck's Constant, $h = 6.626 \times 10^{-34} Js$, and the speed of light in a vacuum, $c = 2.99792458 \times 10^8 m/s$, take on the listed values and units[3]. The body's temperature, T, is expressed in Kelvin and the wavelength, λ, is expressed in micrometers (μm) to produce a spectral emissive power per unit area in $\frac{W}{m^2 - \mu m}$. The spectral emissive power derived in equation (2.53) assumes integration over a complete half-sphere surrounding the isotropically emitting blackbody surface. It is related to the

spectral radiance, $L(T, \lambda)$, in $\frac{W}{m^2-sr-\mu m}$ by the Lambertian assumption, $E = \pi L$ [3].

$$L(T, \lambda) = \frac{2hc^2}{\lambda^5 \left(e^{hc/\lambda kT} - 1\right)} \tag{2.54}$$

The spectral radiance may be integrated over wavelength, surface area, and solid angle subtended to determine the total power leaving the surface in a given wavelength range and solid angle. The blackbody radiance follows the Planckian form shown in Figure 2.4. When these terms are integrated over all wavelengths and emission angles, this quantity is denoted as the total exitance. Radiance is necessary for prediction the emission from real materials which exhibit both spectral and angular deviations from the perfect blackbody case [3].
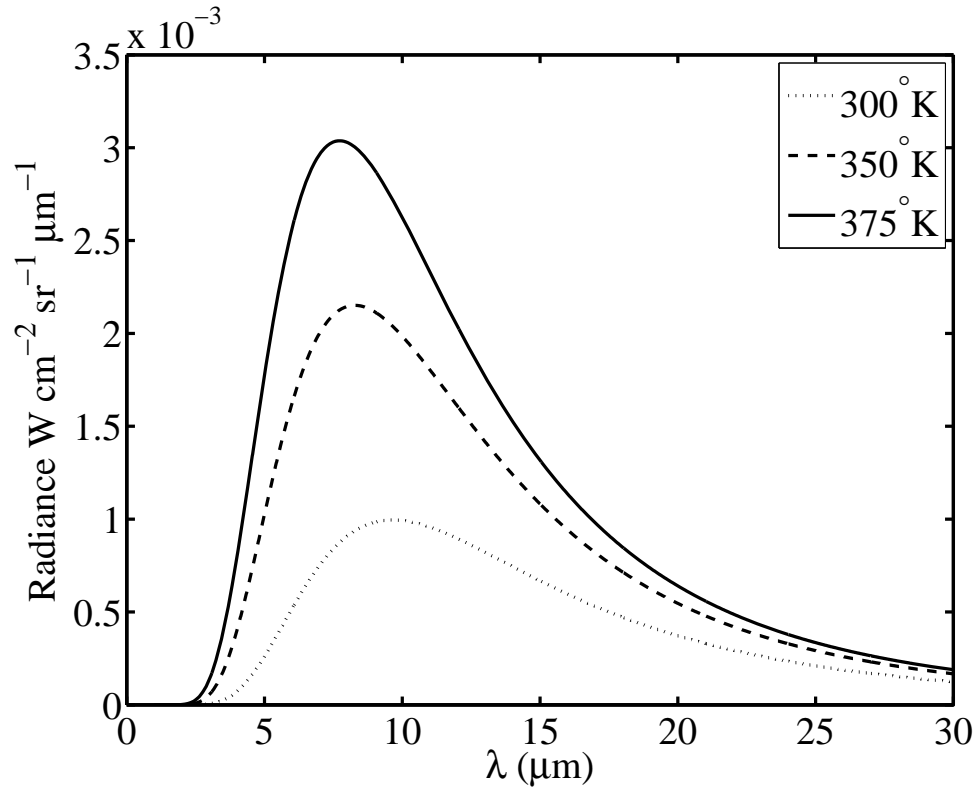
Figure 2.4: Blackbody spectral radiance for three temperatures.

2.4.3 Non-ideal Emission.

Most materials generate, at best, an approximation the blackbody spectral radiance. A linearly scaled approximation is termed a graybody, while the spectral radiance of real materials may be arbitrarily complicated. The spectral scaling factor is called the emissivity, and it represents the fraction of the power emitted by the sample compared to a blackbody source. An example is shown in Figure 2.5. The radiance, from thermal self-emission, is always less than or equal to the ideal blackbody value in both the graybody and any properly measured real material case [3].
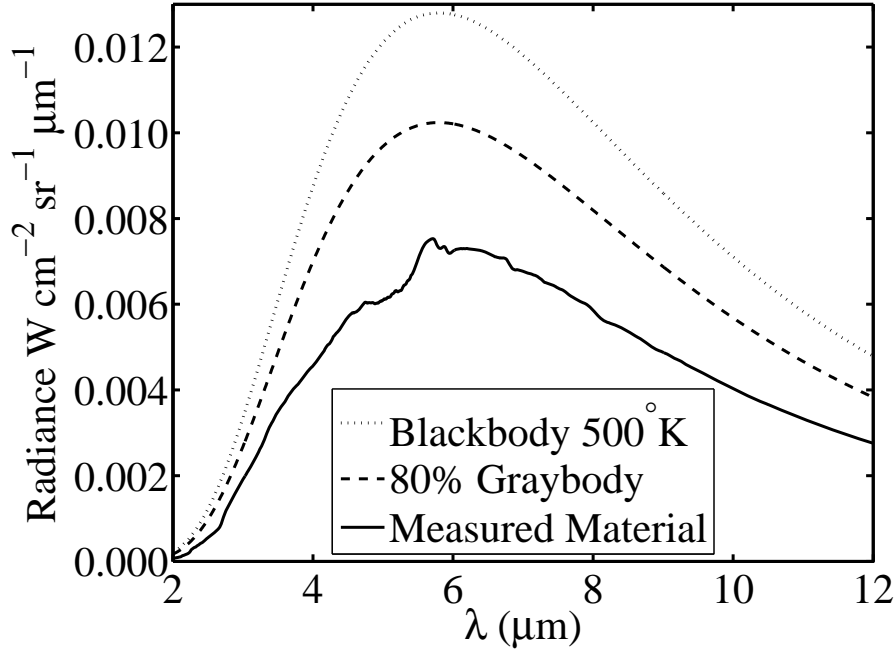
Figure 2.5: Blackbody spectral radiance, 80% graybody, and a measured sample radiance at $500°K$.

When a lossless material is presumed, no absorptance profile is developed, and the emittance is isotropic, as a blackbody. When the material does exhibit losses, the results can be quite different. By Kirchhoff's Law for a body at thermodynamic equilibrium, the emittance, $E(\lambda, \theta_o)$, and absorptance, $A(\lambda, \theta_i)$, are equal and may be substituted in equation

28

(2.47). In the particular case of an opaque surface, where the transmittance term goes to zero, reflectance and emittance are directly related by equation (2.55), and the angle of incidence is equal to an angle of observation, θ_o, for the emittance term [5].

$$E\left(\lambda, \theta_o\right) = 1 - R\left(\lambda, \theta_i\right) \tag{2.55}$$

So, the Fresnel equations may be used to predict the directional and spectral emittance of a lossy material directly. For the remainder of this work, the microstructure of the surface will be considered an intrinsic property of the material half-space, and the term emissivity will be used in lieu of the more general emittance. Tungsten is chosen as an example in Figure 2.6. The angular dependence is clearly observable near grazing, in particular for shorter wavelengths. The spectral radiance values of an ideal blackbody may be scaled by the spectral emissivity values of a surface to predict the angular and spectrally dependent emission from a surface at a fixed temperature.

The predicted directional, spectral emissivity is the far-field distribution of the value, by virtue of the use of plane-wave excited reflectance calculations. For thermally induced emission to be directional, the incident field plane-wave must not be the source of coherence for the surface currents. It is shown in the next section why the observed far-field coherence longitudinal spatial coherence does not provide any insight into the coherence of the field at the surface. Then, a method of predicting the near-field coherence is presented.

2.4.4 Spatial Coherence.

Mutual coherence represents the ability of electromagnetic waves emitted from two points to produce fringes on an observation plane. The Van Cittert-Zernike theorem relates the mutual intensity, J , of two points on an observation plane, Q, far away from a source plane, P, for a given wavelength, λ, by integrating the intensity contributions of many points P over a source surface area, S. The distance between the points P and Q_1, defined as r_1,
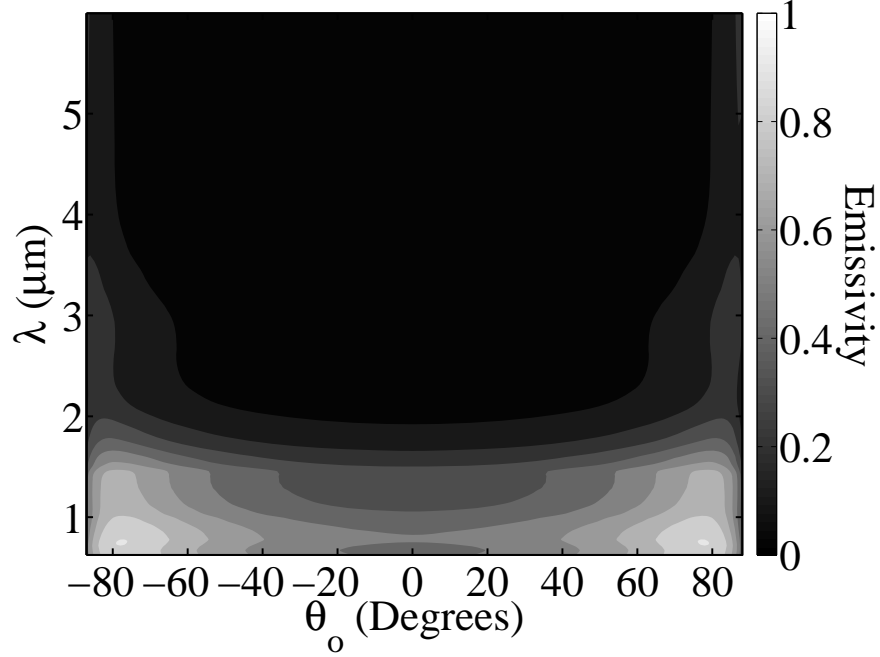
Figure 2.6: Tungsten directional, spectral emissivity, derived from the Fresnel reflectance. Tungsten was selected to demonstrate the change in its surface emissivity below approximately 1.5μm. Below this wavelength, the emissivity observably increases due to the spectrally dependent complex permittivity.

and the between the points P and Q_2, r_2, are assumed to be much longer than the distances between points Q_1 and Q_2 and the distance between any points, P, in area S [2].

A blackbody source area is assumed to be composed of point current emitters with a random distribution of intensity and random phases, so the surface exhibits a delta correlation function. Any given pair of points, however, will exhibit a complex degree of coherence between zero and unity, and the expected value of the mutual coherence between all pairs of points at a single observation point is the mean of the phase distribution [2].

$$\bar{J}(Q_1, Q_2) = \frac{k}{(\lambda z)^2} \int_\Sigma \int I(P_1) \exp\left[-i\frac{2\pi}{\lambda}(r_2 - r_1)\right] dS \qquad (2.56)$$

The general result is that propagation acts as a low-pass spatial frequency filter, and spatial coherence increases slowly with propagation distance. However, the Van Cittert-Zernike Theorem assumes the form of the source current self-coherence and could not be

used to compute coherence in the near field even if a non-singular self-coherence function was assumed for the source currents, since most of the simplifying assumptions do not apply [2]. So, the observation of longitudinal spatial coherence in the far-field is not sufficient to imply coherence in the near field.

In the near field, the electric or magnetic field must be directly computed and the cross-spectral correlation determined. In this case, a Dyadic Green's function, $\overset{\leftrightarrow}{G}$, explicitly developed to show the Fresnel's transmission coefficients, t_{21}^{TE} and t_{21}^{TM}, is used to predict the field above a medium at an interface to free-space from a distribution of point current sources below the interface. Fluctuation Dissipation Theorem (FDT) provides the spatial correlation function of this statistical collection of point current sources in the medium. The cross-spectral correlation of the field may then be determined to predict the longitudinal spatial coherence [26].

Following the same definitions as equation (2.9) and (2.10), the Fresnel transmittance terms through a complex material ϵ_2 to a real material ϵ_1 are determined, when $\text{Re}\left(\sqrt{\epsilon_m}\right) \geq 0$ for real values of ω or λ. The values of the square root, $k = \sqrt{k_x^2 + k_y^2}$, are chosen such that $\text{Im}(k) \geq 0$ or $\text{Im}(k) = 0$ and $\text{Re}(k) > 0$, for a real valued ω and complex k. Due to requirement for real imaginary values of k and the presence of the complex permittivity terms, the TM Fresnel transmission coefficient may have complex poles, while the TE transmission coefficient cannot [10].

$$t_{21}^{TE} = \frac{2\gamma_2}{\gamma_2 + \gamma_1} \tag{2.57}$$

$$t_{21}^{TM} = \frac{2\sqrt{\epsilon_1}\sqrt{\epsilon_2}\gamma_2}{\epsilon_1\gamma_2 + \epsilon_2\gamma_1} \tag{2.58}$$

Sipe derived a Dyadic Green's function, which explicitly preserves observability of the Fresnel transmission coefficients. In the function, $\overset{\leftrightarrow}{G}$, $\bar{R} - \bar{R}'$ is the vector between the source and observation points, $k_{1,2} = \sqrt{\epsilon_{1,2}}k$, and the $\gamma_{1,2}$ values are as defined in equation (2.10), $\bar{r} = \left(\bar{R}, z\right)$, $\hat{s} = \hat{K} \times \hat{z}$, and $p_{1,2} = \left(\left|\bar{K}\right|\hat{z} + \gamma_{1,2}\hat{K}\right)/k_{1,2}$. A source current at $\bar{r}'$ in the

region, $z < 0$, is related to an electric field value in region, $z > 0$, at $\bar{r}$ by an integral over the $\bar{K}$ space [10].

$$\overleftrightarrow{G}(\bar{r}, \bar{r}', \omega) = \frac{i}{8\pi^2} \int \frac{1}{\gamma_2} \left(\hat{s} t_{21}^{TE} \hat{s} + \hat{p}_1 t_{21}^{TE} \hat{p}_1 \right) \exp\left[i\bar{K} \cdot \left(\bar{R} - \bar{R}' \right) \right]$$
$$\times \exp\left(i\gamma_1 z - i\gamma_2 z' \right) d^2 \bar{K} \tag{2.59}$$

The electric field, $\bar{E}(\bar{r}, \omega)$, at an observation point $\bar{r}$ may be computed, once a spectral current source distribution, $\bar{j}(\bar{r}', \omega)$, is defined.

$$\bar{E}(\bar{r}, \omega) = i\omega \int_V \overleftrightarrow{G}(\bar{r}, \bar{r}', \omega) \cdot \bar{j}(\bar{r}', \omega) d^3 \bar{r}' \tag{2.60}$$

The mean energy of a harmonic oscillator, at thermal equilibrium, at a temperature, T, follows Bose-Einstein statistics.

$$\Theta(\omega, T) = 2\pi\hbar\omega + \frac{2\pi\hbar\omega}{\exp\left(\frac{2\pi\hbar\omega}{kT} - 1 \right)} \tag{2.61}$$

The distribution of the individually singularly correlated source current oscillations may be determined by FDT and employed to find the spatial correlation function of thermal current fluctuations in the frequency domain.

$$\left\langle j_m(\bar{r}, \omega) j_n^*(\bar{r}', \omega') \right\rangle = \frac{\omega}{\pi} \epsilon_0 \text{Im}(\epsilon_2) \Theta(\omega, T) \delta(\bar{r} - \bar{r}') \delta_{mn} \tag{2.62}$$

The second-order coherence of a vector field, in the space-frequency domain, is defined by the cross-spectral density tensor, W_{uv}.

$$\left\langle \bar{E}_u(\bar{r}, \omega) \bar{E}_v^*(\bar{r}, \omega) \right\rangle = W_{uv}(\bar{r}_1, \bar{r}_2, \omega) \tag{2.63}$$

So, inserting equation (2.60) into equation (2.63), and simplifying the expression, with equation (2.62), leaves an expression for the cross spectral density tensor, W_{uv}, in a volume integral [26].

$$W_{uv}(\bar{r}_1, \bar{r}_2, \omega) = \frac{\omega^3}{\pi} \epsilon_0 \text{Im}(\epsilon_2) \Theta(\omega, T) \int_V \bar{G}_{mn}(\bar{r}_1, \bar{r}', \omega) \bar{G}_{uv}^*(\bar{r}_2, \bar{r}', \omega) d^3 \bar{r}' \tag{2.64}$$

32

This expression may be further simplified into a single integral in $\bar{K}$ using equation (2.59). The resulting integral only depends on the magnitude of $\bar{K}$, on the trace, and it has been shown that the normalized diagonal cross-spectral density tensor elements are well approximated by the expression in equation (2.65), where the separation between the observation points is defined by $s = |\bar{r}_2 - \bar{r}_1|$, and H_q is a Hankel function of order, q. The propagation constant of a wave traveling along the material interface, k_{sw}, must meet the surface wave condition requirements for the coherence to be enhanced [42].

$$w_{uu}(s, z) \approx \frac{3\pi}{2} \frac{|\epsilon_2|^2}{|\epsilon_2 + 1|^{7/2}} \exp(-2k_{sw}z) \left(\frac{1}{2} \text{Re} \left[H_0(k_{sw}s) - H_2(k_{sw}s) + \frac{4i}{\pi(k_{sw}s)^2} \right] \right) \quad (2.65)$$

In a lossy dielectric, the coherence in the TM polarization is enhanced by the pole in the Fresnel transmission coefficient and the scaling term expressed as the imaginary component of the complex permittivity, when it is greater than unity. The implication of the field distribution is that the randomly phased point emitters below the surface induce currents at the interface which are coherent over long distances, due to the presence of the pole in the transmission coefficient [42].

For a lossless material, such as fused silica, the correlation falls to 0.01 within 0.5λ, as generally considered for a blackbody radiator. Therefore, a correlation metric of 0.01 is employed to indicate when the surface is exhibiting a degree of coherence measurably above the correlation shown by an effectively incoherent radiator. Figure 2.7 shows the correlation, computed by the approximation in equation (2.65) for a gold and silver interface at $620nm$, evaluated at $z = 0.1\lambda$ above the interface. By the stated metric, gold exhibits a correlation length of 16λ and silver a correlation length of 65λ, as previously published [42].

With the conditions for partial near-field spatial coherence established, a convenient means of predicting the longitudinal spatial coherence length is desirable. Fortunately, all of the necessary information is contained in the complex permittivity values of the media [9], and it has been further shown that the enhanced partial spatial coherence goes as the
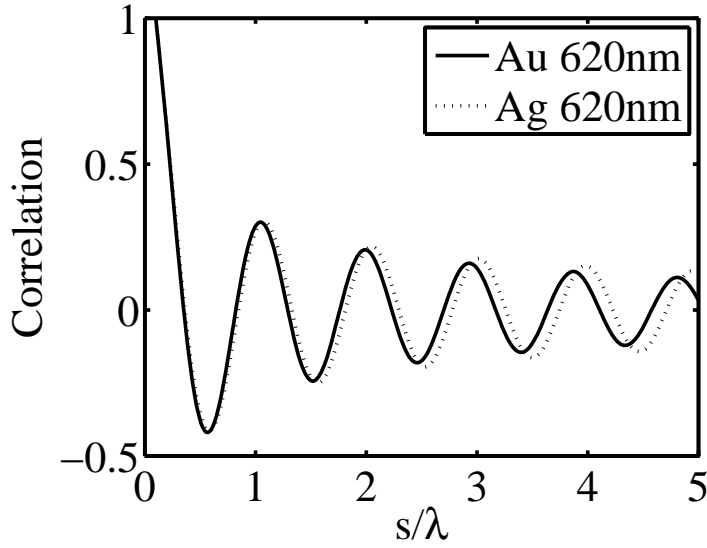
Figure 2.7: The correlation of the electric field above a gold and silver interface to free space at $\lambda = 620nm$ is shown, as a function of the observation point separation distance in wavelengths, at a point $z = 0.1\lambda$ above the interface. For silver (Ag), the correlation falls below the 0.01 metric at 65λ, while for gold (Au) it falls below the metric at 16λ.

surface wave propagation distance for a flat interface [43]. When present, these partially coherent surface waves play an important role in determining the value and form of the emissivity from a structured surface.

2.4.5   *Thermal Emission from Smooth, Rough, and Periodic Surfaces.*

The field above an interface between a thermally excited material and free-space is rigorously modeled as the summed complex field contributions from random current density fluctuations within the skin depth of the surface [43]. The field produced by each individual current fluctuation propagates to, and interacts with, the surface interface. This interaction at the surface determines the angular distribution of thermally excited field which propagates to free-space, and the surface emissivity at a particular wavelength is highly dependent upon the physical structure of the surface [44].

To demonstrate this dependence, two materials with complex permittivities at a wavelength of $\lambda_0 = 4\mu m$, aluminium (Al) and aluminium oxide (Al_2O_3) are considered. At

34

$4\mu m$, a measured Al sample exhibited a complex permittivity of $\epsilon = -9.066 + i406.7$, while the complex permittivity of its native oxide, Al_2O_3, was measured at $\epsilon = 2.444 + i2.073$. For Al, the skin depth is $10.3nm$, and for Al_2O_3, it is $516nm$. So, both materials are opaque at $4\mu m$ within one wavelength.

The emissivities to free-space for both smooth and randomly roughened infinite surfaces of these materials were calculated by conservation of energy and Kirchhoff's Law from the total scatter of an incident plane-wave at the indicated angle of observation, θ_o, shown in Figure 2.8 [45]. The polarization of the incident field in these cases is perpendicular (s-polarized) to the plane of incidence. The emissivity of the smooth Al interface is nearly constant and low, as expected for this highly reflective mirror-like interface. The gross directional dependence of the Al_2O_3 emissivity is driven by the real-valued dielectric response [28].

The total scatter was also computed for both surfaces roughened by a random distribution of 1/4 wavelength deep rectangular pillars. The pillar-widths and gap-widths were uniformly distributed between 0 and 2 wavelengths. In both cases, the emissivity increased and induced some changes in the directionality of the emission. The approximately isotropic emissivities of both flat interfaces increased, and in the case of Al_2O_3, the angular distribution became more isotropic.

When the emitted field polarization is parallel to the plane of observation (p-polarization), the effect of surface waves must be considered. In particular, surface plasmons or coherent electron oscillations, may arise at an interface between two materials in this polarization [9]. Surface plasmons are associated with evanescent surface waves which travel parallel to the interface between material half-spaces, regions I and II, with complex permittivities, ϵ_I and ϵ_{II}. For an interface which lies in the x-y plane and a plane of observation which lies in the x-z plane, continuity of fields requires that the wavevector

35

Figure 2.8: The directional emissivities of smooth and randomly roughened surfaces of aluminium (Al) and aluminium oxide (Al_2O_3) are shown in the s-polarization state at $4\mu m$. The emissivity of both surfaces is increased by the random roughness, and the directional distribution from the Al_2O_3 surface became more isotropic.

components in the z-direction in region I, k_{zI}, and in region II, k_{zII} meet the following condition [9].

$$\frac{k_{zI}}{\epsilon_I} + \frac{k_{zII}}{\epsilon_{II}} = 0 \tag{2.66}$$

The complete wavevector is expressed by (2.67) for the y-invariant geometry considered. In this case, it is convenient to define the speed of light, c, in *cm* since the equations are expressed in wavenumber units for comparison with other published sources.

$$\varepsilon_{I,II}\left(\frac{\omega}{c}\right)^2 = k_x(\omega)^2 + k_{zI,II}^2 \tag{2.67}$$

A dispersion relation for the wavevector component parallel to the interface, $k_x(\omega)$, as a function of frequency in wavenumber, ω, is arrived at algebraically by substituting Equation (2.66) into Equation (2.67), and solving for $k_x(\omega)$.

$$k_x(\omega) = \frac{2\pi}{\omega} \sqrt{\frac{\epsilon_{II}(\omega)\,\epsilon_I(\omega)}{\epsilon_I(\omega) + \epsilon_{II}(\omega)}} \tag{2.68}$$

For a surface wave condition to hold, the field components directed normal to the interface must exponentially decay. This requires that $Re[\epsilon_I] \leq -Re[\epsilon_{II}]$ in Equation (2.66).

The surface wave condition is expressed by the dispersion relation, Equation (2.68) for real values of ω and ϵ_I, when the real valued component of $k_x(\omega)$ is larger than the free-space wavevector, $k_0 = \sqrt{\epsilon_I}\omega/c$ of the same frequency. The resulting wavevectors lie to the right of k_0, the light line, and are non-radiative [9].

The real valued components of this dispersion relation are shown for Al_2O_3 in Figure 2.9 (a) and for Al in Figure 2.9 (b), over a larger frequency range. The wavevector, $k_x(\omega)$, for Al_2O_3 is to the left of the free-space wavevector, k_0, or light line, for all frequencies shown. This indicates that a smooth interface between Al_2O_3 and free-space does not support surface waves. Conversely, the wavevector, $k_x(\omega)$, for Al is to the right of the light line, indicating that aluminium does support surface waves for the extended frequency range shown. The frequency range is extended to make the separation of the wavevector from the light line visible. The wavevector stays very close to, but to the right of, the light line over the smaller frequency range shown for Al_2O_3.
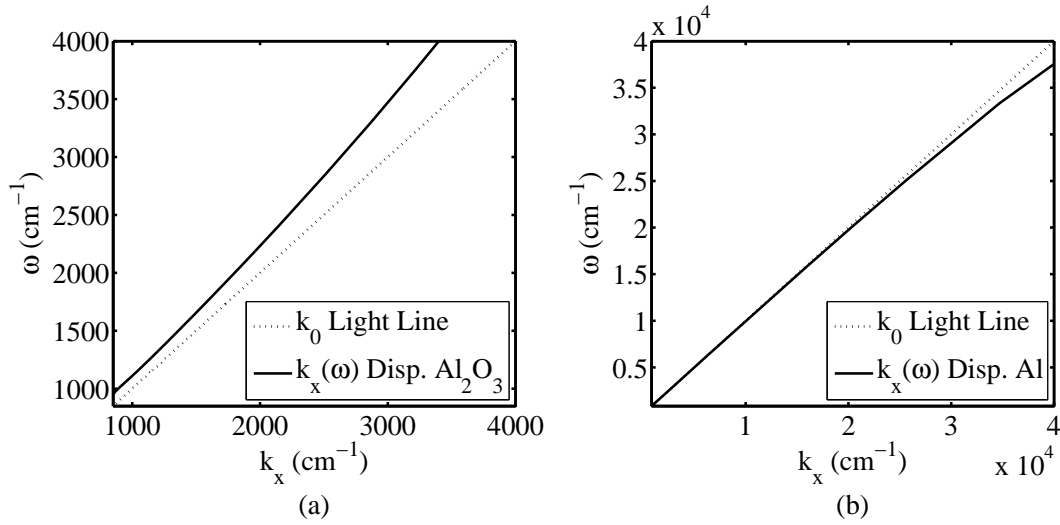
Figure 2.9: (a) The dispersion relation for the wavevector parallel to an interface, $k_x(\omega)$, for an aluminium oxide (Al_2O_3) surface and free-space is shown for real values of ω and the real component of $k_x(\omega)$. In the region to the left and above the light-line, k_0, fields can propagate to free space. In the region to the right of and below the k_0 line, a surface wave condition holds. In the region shown, Al_2O_3, does not support surface waves. (b) The same relation is shown for Al.

Polar dielectrics may also support similar surface waves. The phonon resonances, associated with coherent crystal lattice oscillations do not exhibit the extremely broadband behavior which surface plasmons [46]. The dispersion relation for Silicon Carbide (SiC) and aluminium are compared in Figure 2.10. The phonon resonance for silicon carbide occurs near $950cm^{-1}$, defining a distinctive frequency region over which a silicon carbide interface may support surface waves. As shown in Figure 2.9, the aluminium dispersion relation lies very near to, but to the right of, the line in this frequency range.
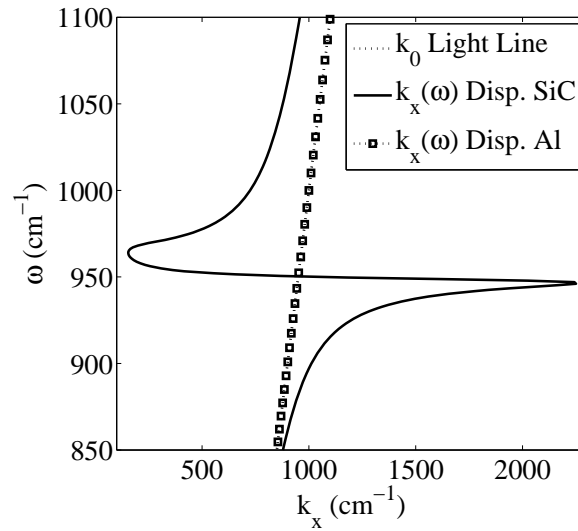
Figure 2.10: (a) The dispersion relations for the wavevector parallel to an interface to free-space, $k_x(\omega)$, for both Silicon Carbide (SiC) and Aluminium (Al) are shown for real values of ω and the real component of $k_x(\omega)$. SiC shows a highly variable behavior around its phonon resonance frequency at $950cm^{-1}$. The SiC interface supports surface waves below the resonance frequency down to $850cm^{-1}$, but does not support surface waves at frequencies above the resonance. Aluminium supports surface waves over the entire frequency range shown.

With the presence, or absence, of surface waves established for the materials in the p-polarization state, the smooth and rough surface emissivities may be considered. The emissivities were calculated in the same manner as those for the s-polarization state, and are shown for aluminium and aluminium oxide in Figure 2.11. The smooth Al_2O_3 surface

exhibits a nearly isotropic response, which is only nominally modified by the surface roughness. The Al surface also exhibits low and nearly isotropic emissivity, showing the normal increase near grazing for a metal in this polarization [28]. The same roughness distribution was applied to both materials as was used the s-polarized case.
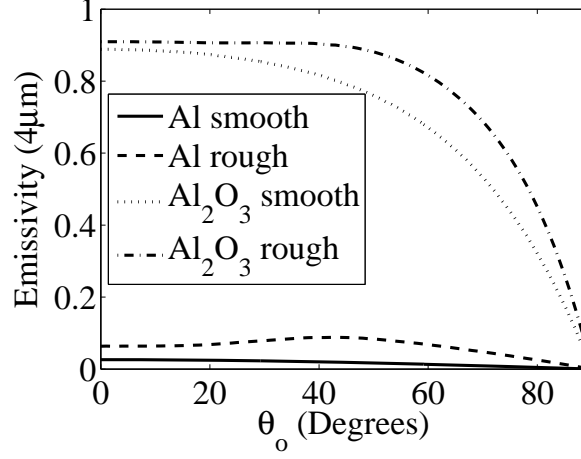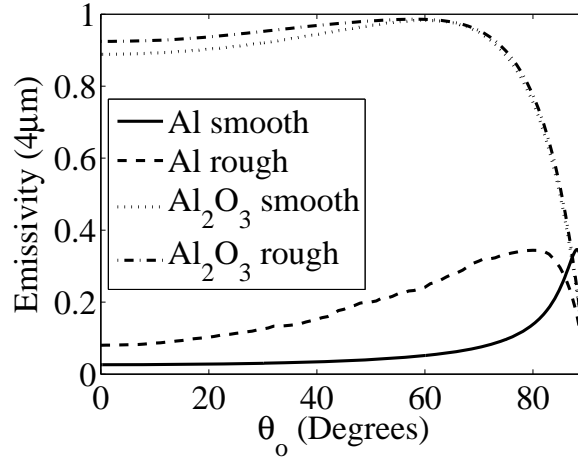

Figure 2.11: The directional emissivities of smooth and randomly roughened surfaces of aluminium (Al) and aluminium oxide (Al_2O_3) are shown in the p-polarization at $4\mu m$. The emissivity of the surface was increased by the random roughness in both cases.

When the s-polarization and p-polarization results for aluminium are directly compared in Figure 2.12, it becomes evident that the p-polarization state exhibits a substantially larger increase in emissivity than the s-polarization state for the same surface modification. The reason for this is that the roughening allows surface waves, associated with surface plasmons, to randomly scatter to the far field. Although surface plasmons may exhibit a high degree of longitudinal spatial coherence, the random scatterers decorrelate the field [9].

A strikingly different angular distribution of emissivity is observed if the surface is perturbed by a periodic perturbation, in this case a Shallow Grating (SG). The change in emissivity is shown in Figure 2.13 for Al and Al_2O_3 for the p-polarization when a $3\mu m$
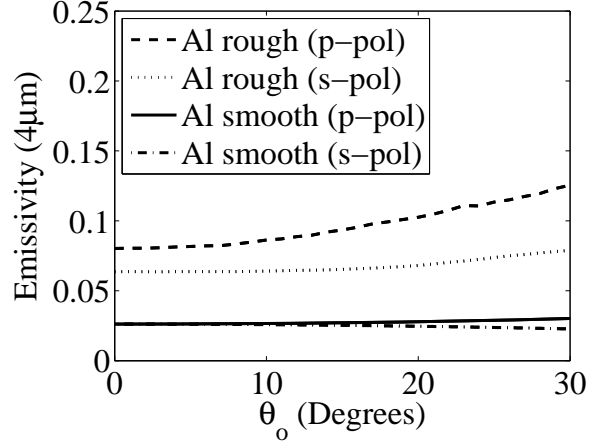
Figure 2.12: The directional emissivities for smooth and roughened Al in p-polarization and s-polarization are shown. Although the same roughness distribution was used in both cases, the increase in emissivity is substantially higher for the p-polarized case.

period shallow grating is ruled on the surface. The emissivities of smooth surfaces are shown for reference. The Al_2O_3 surface does not support surface waves at $4\mu m$ and only a very small and non-directional emissivity enhancement over the smooth surface is observed due to the surface perturbation. The Al surface, however, shows a highly directional peak at 19.3 degrees, greatly enhanced above the smooth surface emissivity.
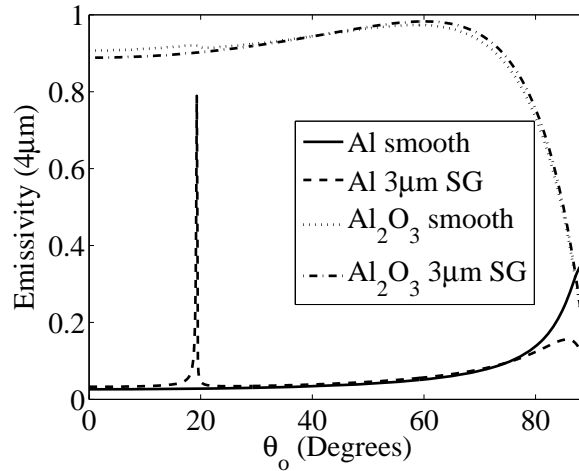
Figure 2.13: The emissivities of smooth and periodically patterned surfaces of aluminium (Al) and aluminium oxide (Al_2O_3) are shown in the p-polarization state for $4\mu m$. The shallow grating (SG) is ruled with a $3\mu m$ period and is shallow at $250nm$ of depth.

The angular distribution of this highly directional emission peak is best understood from the dispersion relation for the wavevector parallel to the material interface of a one-dimensionally periodic ideal grating. The parallel wavevector, $k_{x,M}(\omega)$, associated with a grating order, M, is readily determined from the grating equation, for a fixed frequency, ω, angle, θ_o, and grating period, Λ.

$$k_{x,M}(\omega) = \frac{\omega}{c} \sin\theta_o - M\frac{2\pi}{\Lambda} \tag{2.69}$$

If the grating is shallow compared to the wavelength of interest, the surface plasmon wavevector, $k_x(\omega)$, is not substantially perturbed and the conditions under which the grating wavevector and surface plasmon wavevector are equal may be established for a fixed θ_o and M, as shown in equation (2.70).

$$k_{x,M}(\omega) = \frac{\omega}{c} \sin\theta_o - M\frac{2\pi}{\Lambda} = \frac{\omega}{c} \sqrt{\frac{\epsilon_{II}\epsilon_I}{\epsilon_{II} + \epsilon_I}} = k_x(\omega) \tag{2.70}$$

When the wavevector for an order, M, at a given θ_o matches the surface plasmon wavevector, scatter from the grating may be excited. The angle θ_o is associated with 0-order scatter, which can propagate in free-space. Three examples for $\lambda_0 = 4\mu m$ are shown in Figure 2.14 (a). In each case, the grating wavevectors for the given angles intersect the surface plasmon wavevector, which lies to the right of the light line as shown in Figure 2.9 (b), at the same frequency. The emissivity results for each periodicity are shown in Figure 2.14 (b), where the peak emissivity values for each grating period lie at different angles. The results are symmetric for positive angles of observation and the negative solution to the square root in Equation (2.70).

The intersection of the grating wavevector with the surface plasmon wavevector describes the broadband angular and spectral behavior observed for a thermally excited grating which supports highly coherent surface plasmons. Changing the grating period for a fixed angle of incidence changes the frequency or wavelength associated with the angle

41
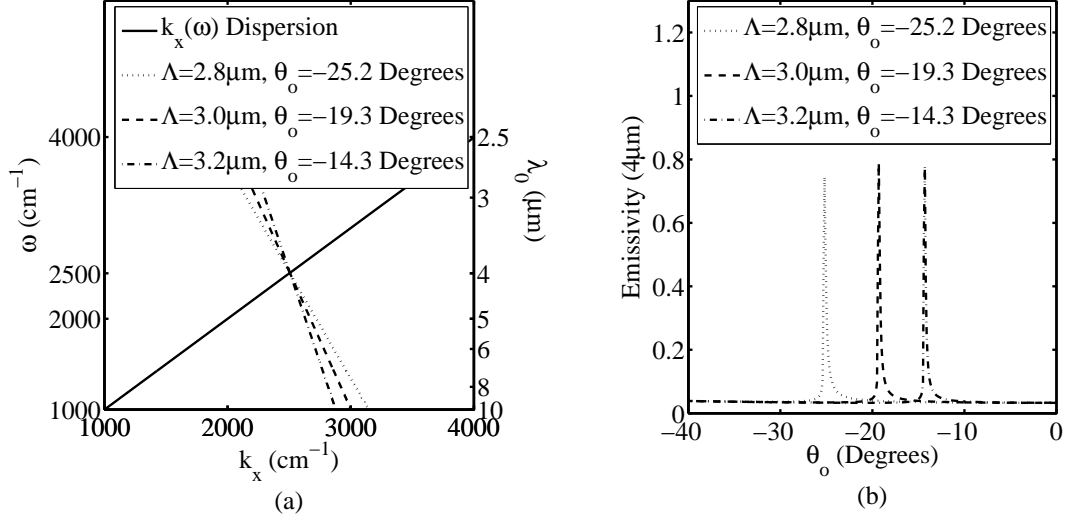
Figure 2.14: (a) The -1-order grating wavevector for three different grating periods, $\Lambda = 3.2$, 3.0 and $2.8\mu m$, intersect the surface plasmon wavevector dispersion relation, $k_x(\omega)$ for a free-space wavelength, λ_0 at three different angles, θ_o. (b) The directional emissivity profiles at a $4\mu m$ free-space wavelength for the same three grating periods as (a) are shown to peak at the same angles.

as shown in Figure 2.15 (a). Likewise, for a fixed grating period, changing the angle under consideration changes the frequency associated with that angle as shown in Figure 2.15 (b).

The complete behavior in wavelength and angle for three different grating periods is shown in the emissivity response surfaces of Figure 2.16 (a)-(c). In each case, the 0 degree angle from Figure 2.15 (a) for each period, $\Lambda = 3, 3.5$ and $4\mu m$, corresponds with the predicted wavelength. Similarly, in Figure 2.16 (c), the wavelength associated with each angle, is the same as that predicted by Figure 2.15 (b) for a $4\mu m$ period grating.

If random roughness is modeled as a distribution of random perturbations, then its periodic content may be expressed by its spatial Fourier transform. The resulting distribution of many grating periods fills the angular and spectral space with free-space propagating components, which share the power associated with the surface plasmons. The result is a lower valued, nearly isotropic increase in the emissivity of the p-polarized state above that shown by the s-polarized state, as shown in Figure 2.12 [9].

42

k$_x(\omega)$ Dispersion
Λ=4.0μm, θ$_o$=0 Degrees
Λ=3.5μm, θ$_o$=0 Degrees
Λ=3.0μm, θ$_o$=0 Degrees

k$_x(\omega)$ Dispersion
Λ=4.0μm, θ$_o$=0 Degrees
Λ=4.0μm, θ$_o$=−15 Degrees
Λ=4.0μm, θ$_o$=−30 Degrees

(a)

(b)
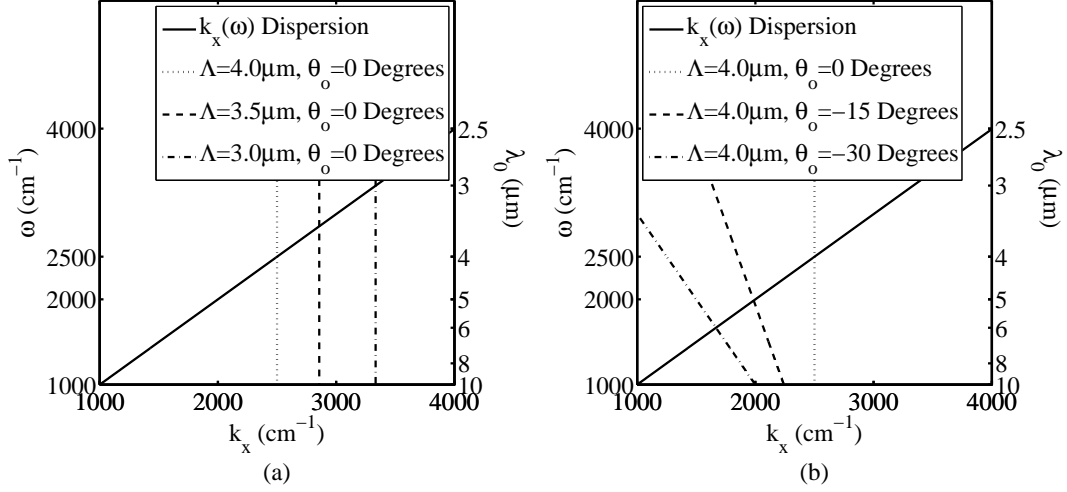
Figure 2.15: (a) The -1 order for gratings of three different periods generate normally directed, $\theta_o = 0$ degrees, responses at different frequencies or wavelengths. The normally directed wavelength always coincides with the grating period, Λ, for a shallow grating. (b) For a fixed grating period the -1-order angles, θ_o, intersect the surface wave dispersion relation at different frequencies or wavelengths.

The grating equation identifies the central angles of the grating orders, but does not specify the angular lobe widths, which are delta functions in angle, or plane waves, only for perfectly coherent excitation. However, the predicted broadening is analogous to the reflected case when a grating is illuminated by a partially longitudinally spatially coherent field. In the thermal excitation case, the angular lobe width is a function of the finite longitudinal spatial coherence length of the surface waves associated with surface plasmons [43].

The cross-spectral density tensor expression, Equation (2.64), shows partial longitudinal spatial coherence over the surface wave propagation length. However, this result is not generally directly applied to predict the angular lobe widths from directionally emitting periodic structures. The most compelling reason for using an alternative methods is that the introduction of a periodic structure effects the surface wave propagation distance. Shallow gratings introduce radiative losses which reduce the surface wave propagation distance

43
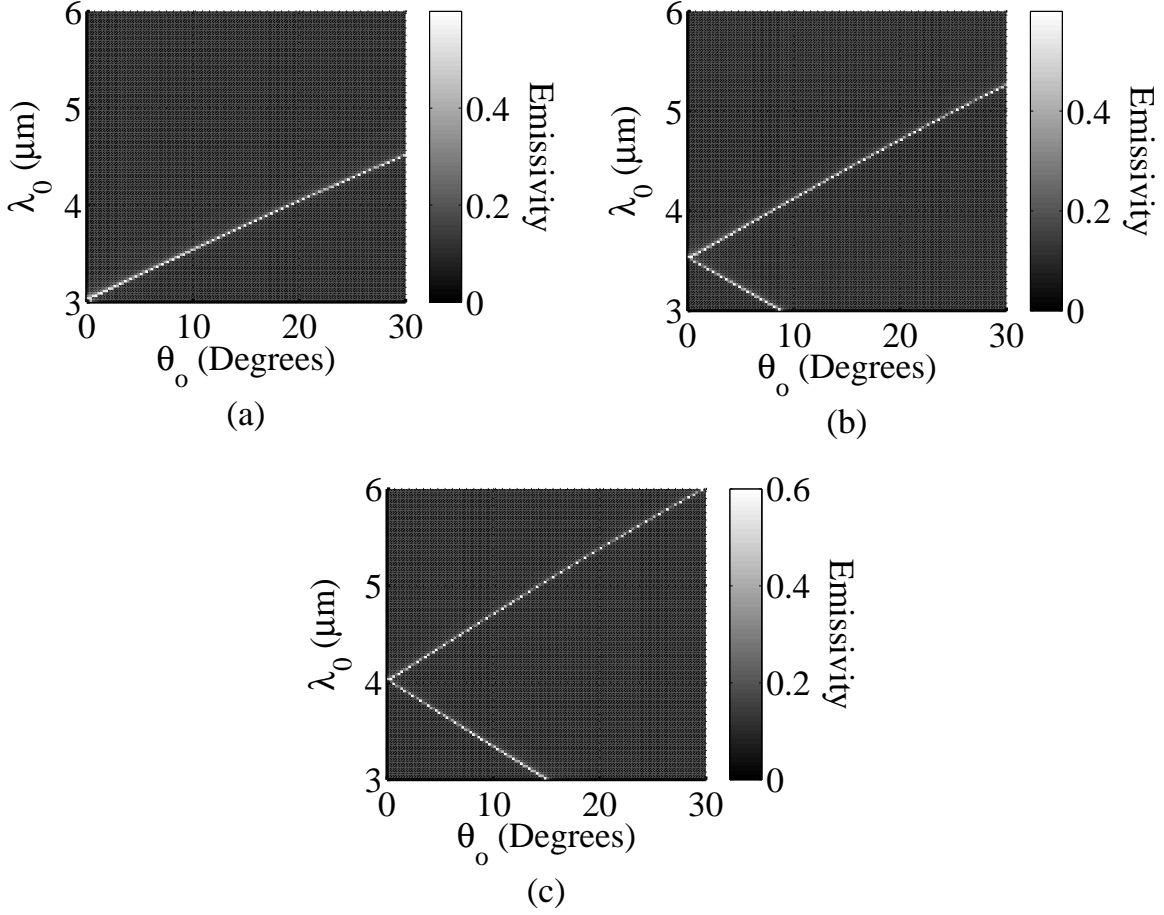
Figure 2.16: (a) The directional and spectral emissivity response surface for a $\Lambda = 3.0\mu m$ shallow grating is shown. (b) The directional and spectral emissivity response surface for a $\Lambda = 3.5\mu m$ shallow grating is shown. (c) The directional and spectral emissivity response surface for a $\Lambda = 4.0\mu m$ shallow grating is shown. The emissivity results are symmetric about 0-degrees. The upper, or longer wavelength, branch of the enhanced emissivity behavior shows the one-to-one wavelength-to-angle mapping predicted by a first-grating-order dispersion relation for a shallow grating with a fixed period. When the lower, or shorter wavelength, branch is visible, it corresponds to second-grating-order coupling.

and the effective coherence length [47]. Alternately, resonant surface structures have been shown to increase the effective coherence length [8, 11].

The current state-of-the-art for predicting the angular lobe widths of periodic structures is to employ a rigorous numerical solution which represents resonant absorption to produce an angular absorption profile. An angular emission profile is then predicted by conservation of energy and Kirchhoff's Law. This practice is supported by experimental measurements, in which the predicted angular emission profile was in excellent agreement with the measured data [8, 11, 46]. This method was employed, using RCWA, to produce Figure 2.13 and Figure 2.14 (b), both of which show definite angular lobe profiles.

Given an angular profile, the local longitudinal spatial coherence length, l_c, of a fabricated or modeled structure may be estimated from the full-width half-maximum of the angular lobe, $\Delta\theta$, for a give free-space wavelength, λ_0 [7, 8, 11].

$$l_c = \frac{\lambda_0}{\Delta\theta} \tag{2.71}$$

Angular lobes with full-width half-maximum values as narrow as 1 degree have been experimentally measured for thermally excited gratings in silicon carbide. This corresponds to a local coherence length of approximately 60 wavelengths at $11.36\mu m$ [7]. For a silicon carbide structure which enhanced the longitudinal spatial coherence length, emission features with full-width half-maximum values less than 0.08 degrees, corresponding to 716 wavelengths at $11.6\mu m$, have been measured [11]. The accurate evaluation of structures which exhibit rapidly angularly varying emission and reflection properties requires special consideration in terms of radiance measurements.

2.4.6   Directional Emission Measurement.

The form of thermal self emission, driven by surface wave interactions with a periodic structure, described above is markedly different than the slowly angularly varying deviations shown in Figure 2.6. A directional main lobe, in the vein of the 4-element array antenna pattern shown in Figure 2.3, is produced. Given the expected form of the emission

features, a more general treatment is given, towards a functional definition of directional emission which is directly observable in measurements.

The basic description of the angular scatter from a surface is the bi-directional reflectance distribution function . The function $BRDF\,(\theta_i, \theta_r, \Delta\phi_r)$ is the ratio of reflected radiance, L_r, to incident irradiance, E_{irr}, at an angle, θ_i, at a particular wavelength. The scattered is evaluated for a reflected elevation angle, θ_r, in a differential azimuthal angle, $\Delta\phi_r$. For clarity, the wavelength dependence is not shown in equation (2.72) [24].

$$BRDF\,(\theta_i, \theta_r, \Delta\phi_r) = \frac{L_r}{E_{irr}} \tag{2.72}$$

So, the flux, Φ_r, collected in a finite solid angle defined by θ_r and ϕ_r, as scattered from a fixed surface area, A_s, can be computed by a straightforward integral.

$$\Phi_r = \int_{\theta_r} \int_{\phi_r} \int_{A_s} BRDF\,(\theta_i, \theta_r, \Delta\phi_r)E_{irr} \cos{(\theta_r)} \sin{(\theta_r)}\, d\theta_r d\phi_r dA_s \tag{2.73}$$

If the surface is not a perfect reflector, then there is also a self-emission component. The flux leaving the surface, Φ_e, is computed by a similar integral, bounded by the blackbody radiance, L_{e-BB}, at the surface temperature [3]. The directional emissivity $\epsilon(\theta_o, \phi_o)$, performs a role similar to that of the BRDF. In this case, flux is assessed at observation angles, θ_o and ϕ_o, rather than the reflected angles.

$$\Phi_e = \int_{\theta_o} \int_{\phi_o} \int_{A_s} \epsilon\,(\theta_o, \phi_o)L_{e-BB} \cos{(\theta_o)} \sin{(\theta_o)}\, d\theta_o d\phi_o dA_s \tag{2.74}$$

Of course, angular emissivity cannot be directly measured. A physical instrument collects a portion of the flux leaving the emitting surface, which is commonly calibrated to a radiance value. The following derivation demonstrates how the radiance of a field-of-view filling surface and blackbody may be used to extract the angular emissivity of a surface.

First, the form of the flux leaving a reference blackbody is defined. The surface is assumed to be Lambertian and is integrated over the full 2π steradians of a hemisphere, and

46

the surface area. The emissivity of a blackbody, ϵ_{BB}, and radiance, L_{e-BB}, do not exhibit any angular variation. So, these terms may be taken outside the angular integrals.

$$\Phi_{e-BB} = \epsilon_{BB} L_{e-BB} \int_0^{2\pi} d\phi_o \int_0^{\pi/2} \cos{(\theta_o)} \sin{(\theta_o)} \, d\theta_o \int_{A_s} dA_s \qquad (2.75)$$

If the differential flux per area is taken, then the exitance of the Lambertian surface, M_{e-BB}, is found in its standard form, when the emissivity value is taken as unity for a blackbody.

$$M_{e-BB} = \frac{d\Phi_e}{dA_s} = L_{e-BB} \int_0^{2\pi} d\phi_o \int_0^{\pi/2} \cos{(\theta_o)} \sin{(\theta_o)} \, d\theta_o = \pi L_{e-BB} \qquad (2.76)$$

The exitance integral may also be defined for a surface exhibiting an angularly varying emissivity. Once again, the exitance is computed by integrating the flux over the entire 2π steradians of the hemisphere above the surface, and the full surface area.

$$M_e = \frac{d\Phi_e}{dA_s} = L_{e-BB} \int_0^{2\pi} d\phi_o \int_0^{\pi/2} \epsilon(\theta_o, \phi_o) \cos{(\theta_o)} \sin{(\theta_o)} \, d\theta_o \qquad (2.77)$$

With the exitance terms defined, the emissivity of the surface may be computed from its given definition in equation (2.78) [3]. The emissivity may also be defined by the ratio of the differential fluxes of equation (2.76) and (2.77).

$$\epsilon \overset{\Delta}{=} \frac{M_e}{M_{e-BB}} = \frac{d\Phi_e}{dA_s} \frac{dA_s}{d\Phi_{e-BB}} \qquad (2.78)$$

The differential flux for a surface exhibiting an angular emissivity is then defined, and taken in an improper integral for convenience. The objective is to recast the integrals in terms of an observing detector, assuming that the area of the surface and reference blackbody are the same, and fill the field-of-view of the detector.

$$\Phi_e = L_{e-BB} \int_{A_s} \int_{\theta_o} \int_{\phi_o} \epsilon(\theta_o, \phi_o) \cos{(\theta_o)} \sin{(\theta_o)} \, d\theta_o d\phi_o dA_s \qquad (2.79)$$

The observed solid angle is substituted for the its geometric description in terms of the differential detector area, dA_d, viewing angle between the surface normal and detector, θ_d,

and distance to the detector, R_d. The observation geometry is assumed to be constant for both the test surface and reference blackbody.

$$\Phi_e = L_{e-BB} \int\limits_{A_s} \int\limits_{\theta_o} \int\limits_{A_d} \epsilon(\theta_o, \phi_o) \cos(\theta_o) d\theta_o dA_s \frac{\cos(\theta_d)}{R_d^2} dA_d \qquad (2.80)$$

A similar change of variables then replaces the dependence on θ_o, dA_s, and R_d with the solid angle field-of-view of the surface observed.

$$\Phi_e = L_{e-BB} \int\limits_{\Omega_{FOV}} \int\limits_{A_d} \epsilon(\theta_o, \phi_o) \cos(\theta_d) d\Omega_{FOV} dA_d \qquad (2.81)$$

The integral substitutions then allow the angular emissivity function to be removed from the remaining integral.

$$\Phi_e = L_{e-BB} \epsilon(\theta_o, \phi_o) \int\limits_{\Omega_{FOV}} \int\limits_{A_d} \cos(\theta_d) d\Omega_{FOV} dA_d \qquad (2.82)$$

Taking the second derivative of both sides of equation (2.82), and dividing by the cosine of the detector angle, leaves an angularly scaled Lambertian radiance, set equal to a differential expression. The differential expression represents an angularly varying radiance, now identified as $L_e(\theta_o, \phi_o)$.

$$\frac{d^2 \Phi_e}{d\Omega_{FOV} dA_d \cos(\theta_d)} = L_{e-BB} \epsilon(\theta_o, \phi_o) = L_e(\theta_o, \phi_o) \qquad (2.83)$$

This expression can be further simplified, showing that the directional emissivity is the ratio of the radiance collected from a surface and a blackbody, when the radiance measurements are collected by the same observation geometry and the surfaces fill the entire field-of-view.

$$\epsilon(\theta_o, \phi_o) = \frac{L_e(\theta_o, \phi_o)}{L_{e-BB}} \qquad (2.84)$$

This relationship is particularly important, since many radiometric instruments output values calibrated to radiance.

2.5 Conclusion

The theoretical underpinnings for predicting and measuring the spectrally and directionally selective emission from a thermally excited structure have been presented. Methods for computing the reflectance from planar and periodically structured interfaces between optical materials and free-space were presented, based on the time harmonic form of Maxwell's equations. These methods highlighted the key role which the complex relative permittivity, or index of refraction, plays in determining the reflectance and transmittance observed in the far-field. The spectral and directional absorptance of an interface was developed for both structure types considered.

Then, classical radiometry was reviewed and directional emissivity derived from the directional absorptance, which implies a degree longitudinal spatial coherence in the far-field. The Van Cittert-Zernike theorem was reviewed, showing that the typical far-field observation for a planar interface, due to delta-correlated current sources, does not predict the near-field behavior. The delta-correlated current source assumption of the Van Cittert-Zernike theorem was then carried into a spectral cross correlation computation for a planar interface supporting surface waves, due to a pole in the TM Fresnel transmission coefficient from the material region to free space. This development employed a dyadic Green's function, in which the Fresnel transmission coefficients are explicitly observable, to demonstrate that the pole is retained in the spectral cross correlation in the near-field. Two surface structures which can couple the coherent near field to the far field are briefly summarized. These structures are more fully developed in the literature review in Chapter 3. Finally, a functional relationship for determining angular emissivity from measurable radiance values was presented.

III. Literature Review

3.1 Introduction

A review of published works relevant to the exploitation of the spatial coherence of surface waves on conductive surfaces for directional emission is presented. First, key accomplishments in exploiting surface plasmons for coherent thermal emission from patterned surfaces are presented chronologically, including advances in the computational methods required to predict their behavior. Directional emitters which were fabricated and measured are emphasized, as well as the physical mechanisms exploited by the surface structure designs. The trend towards more complex structures and fabrication processes is also shown.

3.2 Surface Plasmons

The initial conditions for modifying an opaque surface to produce spectrally and directionally selective thermal emission are a low smooth surface absorptivity and a spatially coherent near-field condition. These conditions are correlated in metals, as well as polar dielectrics, when the surface wave condition is met, which is also expressed as a pole in the Fresnel transmission coefficients [26]. The study of surface plasmons as a physical phenomenon was quite mature when the 1982 and 1988 reviews by Agronovich [10] and Raether [9], respectively, were published. However, it was expressed largely in terms of lattice structure vibrations, and charge densities, rather than field behaviors. Initially, surface plasmons were studied under the assumption of coherent excitation by an external source coupled by several different methods.

The first method used to excite surface plasmons was attenuated total internal reflection. This method involves bringing a high index prism into very near proximity with the metal surface. The angle of incidence of a source wave on the prism is selected such that

it experiences total internal reflection at the prism base. The wave traveling perpendicular to the lower interface of the prism is coupled across the air gap between the prism and the metal surface by its evanescent field. The increased wave vector, whose magnitude is the propagation constant, of the evanescent component allows it to match the surface plasmon wave vector on the metal surface. A surface plasmon initiated in this manner then propagates over its decay length along the metal surface [9]. This method has numerous applications in experimentation and metrology, but it does not represent a viable path to surface emission property modification due to the presence of the prism on the incident field side.

The second most common method used for the external excitation of surface waves is through a grating. In this method, an optically shallow periodic structure is ruled on the surface. Experimentally, optically shallow implies a grating depth on the order of $1/40th$ to $1/20th$ of the wavelength of interest. When the incident field's wavevector parallel to a periodic surface equals the surface plasmon wavevector a reflection null is observed, coinciding with the stimulation of a surface plasmon. This null was identified as the Wood's anomaly, observed in metallic gratings since 1902 [9].

3.3 Near Field Coherence

The modern published investigation of coherence in thermally excited surface waves began in 1988 with the first observation of spectral emission peaks in a heated grating structure. The observed angular distribution of spectral peaks aligned precisely with the location of the Wood's anomalies in reflection. The implications of this result were cautiously presented for the stated reason that a complete theoretical treatment of deep gratings with finite conductivity was not available for comparison to the measured results [48].

The key implication of the observation of emission corresponding to the Wood's anomaly location is that the thermally excited emission of the grating exhibited a degree of

spatial coherence. The oft-cited work by Kreiter in 1999 demonstrated directional thermal emission from a gold grating. A 4.849μm-period grating was etched into a glass substrate, which was wetted with 3nm of chromium before 140nm of gold was evaporated onto the profile. The depth of the grating was not given. This sample was then heated to 700$°C$ in an evacuated chamber, and re-imaged onto a detector through a polarization analyzing optical train, with an entrance pupil subtending 2.7°. Angularly narrow and dependent emission peaks were observed for 710nm and 810nm in the TM polarization, but not the TE polarization, as predicted by the surface wave theory underlying coherent emission. The work experimentally proved that directional, thermally excited emission was possible, but the experimental conditions precluded the observation of extremely narrow angular features [49].

Similar qualitative observations were made of directional thermal emission from a shallow grating in silicon carbide in the 10-11.5 μm regime. This emission was directly attributed to the action of surface plasmons [46]. An emission spectrum which varied by observation angle was observed in both reflection and direct emission measurements. The measurement results clearly demonstrated an inverse relationship, although the feature angular widths varied between the experiments. The measured reflection results were also compared to the reflected diffraction efficiencies computed for a shallow sinusoidal grating based on the Rayleigh Hypothesis, which assumes small perturbations. Since the achieved grating depth was slightly less than 1/10th of a wave, which does not meet the shallow grating requirement, this numerical treatment did not accurately reproduce all of the observed behaviors. A volume integral computational method was able to achieve much better results, within 0.1% error [46].

With a rigorous, if extremely time consuming, model in close agreement with reflection observations and reasonable agreement with angularly resolved self emission observations, the question of spatial coherence could be mathematically addressed. For

temporal coherence, the Weiner-Khinchin theorem states that the time correlation function is the Fourier transform of the power spectral density of the field. This implies that the width of a spectral feature is inversely proportional to the coherence time. A spatial form of this theorem was presented based on derivations and demonstrations by other works, which had not previously been applied to a thermal source. In short, the spatial form implies that peaks in the angular power density imply high spatial coherence. In the shallow grating case, the angular and spectral features observed are the result of a temporally and spatially coherent surface waves scattering off the grating and coherently mixing in the far field [46].

In the works discussed thus far, Kirchhoff's law was assumed to be valid for directional emission. While this was experimentally evident and was well established by thermodynamic arguments when emission was integrated over all angles, no rigorous proof existed for directional emission. Proof of the validity of Kirchhoff's law was formally given in 1998 for any type of surface, specific direction and specific wavelength, based on coherence theory. This proof removed an important concern regarding the accuracy of using time harmonic solutions to Maxwell's equations for reflection to examine the emissive behavior of surfaces [45]. Another extremely useful result of further mathematical endeavors was the demonstration that spatial coherence lengths on a surface supporting surface waves are on the order of the surface plasmon propagation length [26]. These results made it possible to establish the validity of, and bounds over which, computational methods developed to analyze time harmonic solutions to Maxwell's Equations may be used to predict emissive behaviors.

3.4 Directional Emission

In 2002, the first publication in which spectrally and directionally selective thermal emission from a surface due to grating coupling of surface waves was purposefully and accurately designed. Examination of the angular widths at a given wavelength indicated that the spatial coherence length was on the order of the surface wave propagation distance

at the same wavelength [7]. A numerical duplication of the work from the provided grating dimension and published complex indexes of refraction is shown in Figure 3.1. The same group refined their work in 2004, providing several other substantial contributions [47].
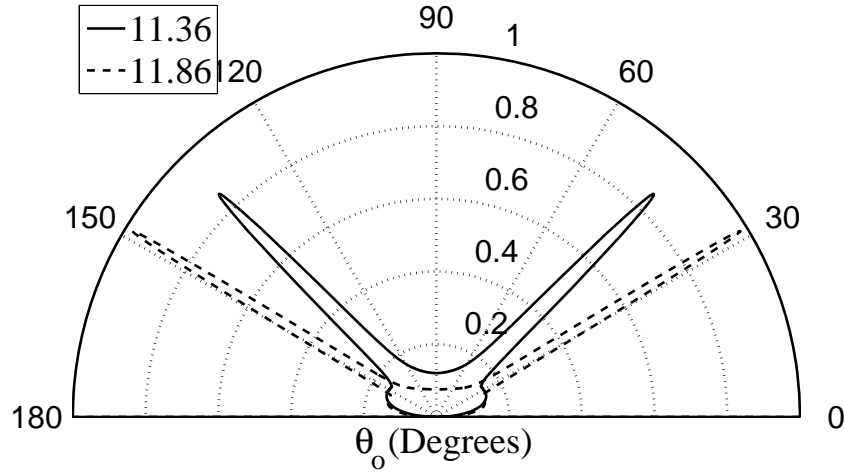
Figure 3.1: Numerically reproduced results of the directional emissivity of a shallow silicon carbide grating surface at $700°K$ for two wavelengths, $11.36\mu m$ and $11.86\mu m$, duplicating a published result [7].

First, an additional emission pattern was developed in which a nearly monochromatic isotropic source was produced by exploiting a region of very shallow slope in the surface plasmon dispersion relation. This result, which appears to have focused the research effort for several years, pointed to the possibility of tunable infrared sources with very long coherence times. The second major contribution of the publication was the use of the rigorous coupled wave analysis method in the design of selective emitters. With the validity of Kirchhoff's law established on a spectral basis, RCWA provided a much needed, efficient method to calculate reflection coefficients for structures deeper than the shallow grating regime, where perturbational methods do not yield accurate results [47].

The final contribution of this work was to present a measurement scheme and extraction technique to evaluate the coherence length of emission from a thermal source.

The results corresponded well with the theoretical predictions and showed that shallow grating structures reduced the spatial coherence length of the surface waves. While not strictly proven, this result is held to be true, since the surface waves lose energy due to radiative as well as resistive losses on a surface with a grating [47].

In low-loss materials such as silicon carbide, which exhibits approximately 36 wavelengths of spatial coherence at 11.6μm, a further loss of coherence was an impediment to the production of narrow band thermal sources. Overcoming this limitation required the transition from surface dispersion modification design methods to a truncated waveguide concept, first implemented in 2007 [8]. In this method, standing waves in a truncated metal-insulator-metal waveguide, Figure 3.2 (a) and (b), are developed in vertical cavities in a surface. These coupled resonant cavities are then coherently coupled by surface waves [11].
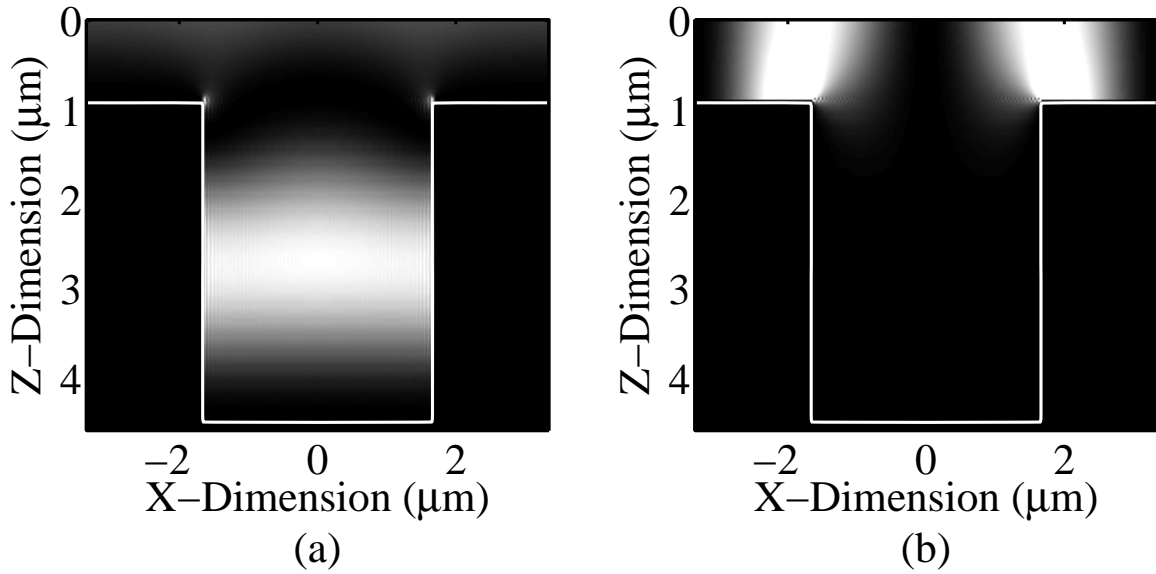
Figure 3.2: The x-directed (a) and z-directed (b) electric field distribution inside an infinite periodic array of truncated metal-insulator-metal waveguides arranged as coupled resonant cavities. A Fabry-Perot-type cavity resonance is visible in the field distribution shown in (a). The high field values, indicative of the surface waves which couple the fields between cavities are visible on the inter-cavity ridges in (b).

The required resonant cavities have depths between 1/4 and 1/2 wavelength and the spectral design shifts from surface dispersion modification to cavity resonance calculation. Due to the non-Perfect Electrical Conductor (PEC) cavity base, the truncation could not be accurately predicted by assuming a 180° phase shift at the cavity base. Instead, the optimal depth, accounting for the reflected phase and cavity propagation constant, was found using RCWA by sequentially varying the depth of the cavity [11]. A numerical duplication of the published results is shown in Figure 3.3. In the original design, the cavity centers were separated by one free-space wavelength at the design wavelength, so that the phase shift between cavities was nulled and surface waves arriving from other cavities in the array interfered constructively with the cavity resonance. It also ensured that the grating was zero order at normal incidence for the design wavelength so that all higher order diffractions drove evanescent surface waves [11].
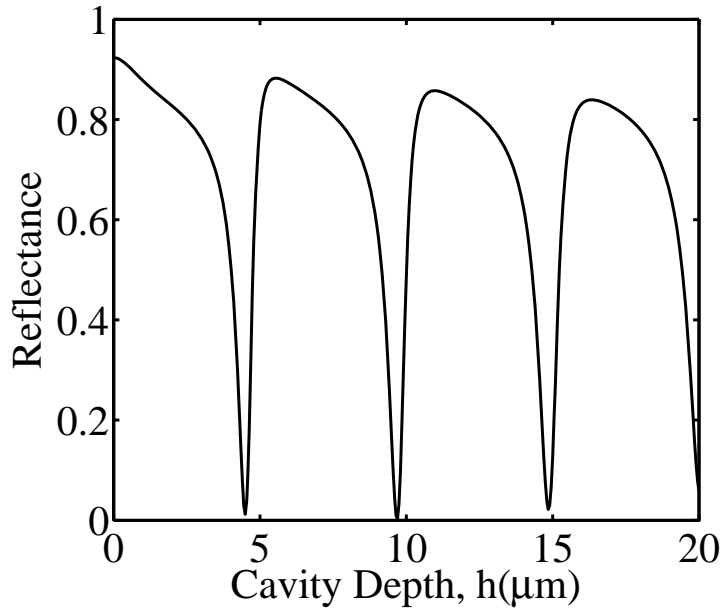
Figure 3.3: Numerical regeneration of the cavity depth optimization method employed by Dahan *et al*. [11]. The Reflectance nulls indicate cavity depths, h, at which the Fabry-Perot-type resonance is maximized for the modeled wavelength and a normally incident field.

56

This design produced a normally directed emission at the design wavelength, which is of much greater utility for an infrared source than the off-axis lobes previously demonstrated. The resonant cavities were shown to increase, rather than decrease, the spatial and temporal coherence of the source by almost an order of magnitude, even in the presence of radiative losses. The computed spectral emissivity, observed at observation angles, $\theta_o = 0°$ and also at $\theta_o = 1°$, are shown in Figure 3.4, and these results were in close agreement with the measured results [11]. A clear peak near the blackbody spectral emissivity peak is shown at normal, but rapidly falls to the baseline emissivity value when the angle of observation is moved out to 1°.
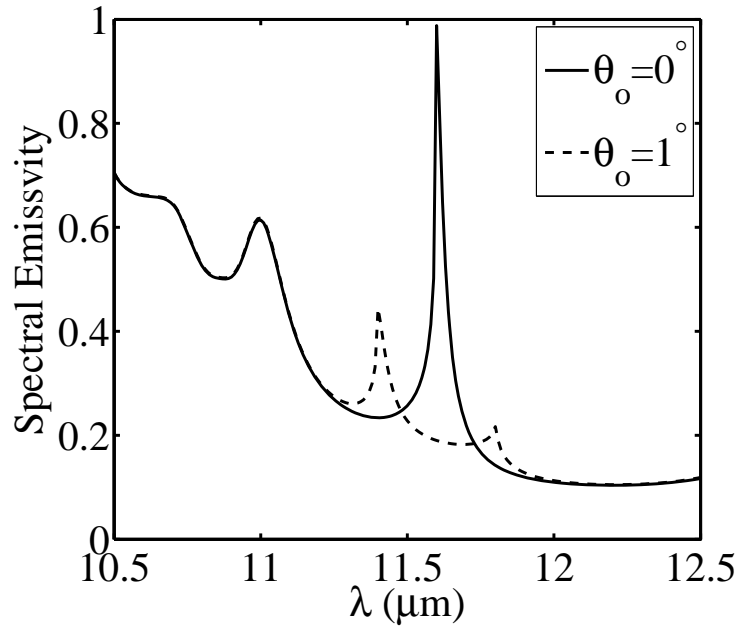
Figure 3.4: Numerically computed spectral emissivity for two angles of observation, from RCWA, duplicating the results of Dahan, *et al.* [11]. The peak at normal occurs only for the design wavelength of 11.6μm. Observing the spectral emissivity even one degree off-normal shows a drastic drop in the 11.6μm response.

3.5   Directional Emission Designs

With a direct chronology of the exploitation of surface wave spatial coherence for directional emission established, the broader investigation of directionally and spectrally selective absorption and emission may be addressed. Additional relevant works involving only periodically patterned surfaces are presented, followed by planar structures, photonic crystals, and literally micro-formed antennas. Then, a series of compromise designs are considered in which fabrication difficulties or scalability were actively considered in the design process.

3.5.1   Patterned Surfaces.

The thermal radiation from two dimensional cavities, fabricated in chromium on silicon, was investigated by Maruyama *et al.* in 2001. Specifically, a very open structure of square apertured cavities with depths down to $13.7 \mu m$ and a fixed period of $5 \mu m$ was fabricated with sidewall thickness of only $1 \mu m$. This design format was predicated upon the concept of cavity quantum electrodynamics, in which the total surface emissivity goes as the incoherent summation of many geometric resonating cavities. This suggests that maximizing the ratio of the cavity contributions to the flat surface contributions enables the surface emissivity to approach the blackbody limit. The broadband emissivity of the structures was measured, showing an increasing emissivity with cavity depth, which grossly corresponded to geometrical cavity resonance modes, for sample temperatures ranging from $739 - 769°K$. It was noted that very little directional dependence was observed, even though chromium supports long range surface waves at the wavelengths of interest [50]. This lack of directivity is attributable to the phase of the surface waves traveling over the inter-cavity ridges, which were purposefully very narrow, not matching the cavity phase at the cavity apertures.

Sai *et al.* published a series of papers from 2001 to 2005 targeting the exploitation of surface patterning to produce selective absorbers and emitters specifically for TPV

applications. In particular, the objective was to exploit spectral selectivity, with the possible addendum of directional selectivity, to excite narrow band-gap photovoltaic cells without inducing undesirable junction heating. Surface patterning was explored to free the design and optimization process from the spectral constraints of rare-earth element emitters [51].

In the initial paper, two-dimensional arrays of inverted pyramids were fabricated in silicon by exploiting the (100) versus (111) plane selective etching of silicon by tetramethylammonium hydroxide at various fill factors and pitches. Platinum was sputtered onto each pyramid to approximately $37nm$ of thickness, in line with the current photovoltaic absorber practices, although the structural periods of $2\mu m$ was much smaller than the conventional values. The emission properties of heated structures were measured, then compared to step-approximation RCWA calculations of the spectral absorptance. Ten step-levels were used, along with published optical constant data, providing reasonable agreement with measured data for a polarization angle of $45°$ and normal incidence to simulate an un-analyzed polarization measurement. The peak emissivity value was observed at the structure period wavelength, although no attempt to measure strict angular dependence was made [52].

The next key step was to extend the TPV selective emitter into a more thermally stable material. Fast atom beam etching was employed to etch tungsten with two different sub-micron sized cavity profiles for examination. Once again, RCWA was used to predict the angular emissivity, by way of absorptance. The difference between published optical properties and the actual properties of particular metal surfaces at high temperatures accounts for a substantial portion of the observed modeled-versus-measured-results deviations. It is important to note that surface reflectance due to the exitance of a surface wave condition falls rapidly for tungsten beginning at $2\mu m$, until the plasma frequency is reached in the visible wavelengths. This limits the overall impact of any

periodic coupling, and only a weak angular dependence was observed, which was desirable in this case [53].

The etched tungsten rectangular grating concept was further examined at higher temperatures and for crystalline and noncrystalline tungsten. In both cases, the rectangular cavities were spaced on a $1\mu m$ period with $200nm$ thick sidewalls and a depth-to-width ratio of 1:1. Emissivity measurements were made at temperatures up to $1400°K$, after which damage to the structure was observed. At $1180°K$, the structure did not suffer damage or deformation, indicating the peak operating temperature for the structured surface. In all cases, the primary source of error between the measured and modeled emissivity values appears to have been the use of tabulated, rather than specifically measured, complex permittivity values in the RCWA model [51].

With the non-resonant absorption and emission behavior of tungsten well established, Sai *et al.* turned their attention to profile and form optimization for the TPV selective emitter problem. Apparently in response to the published inaccuracies of the step-approximation in RCWA, but without citation [38], the finite difference time domain method was applied in lieu of RCWA. The published comparison of RCWA to FDTD for a rectangular cavity test case, for which both models are mathematically rigorous to the limit of their sampling and expansion-order approximations, shows the tell-tale spectral peak shifting of numerical dispersion in the FDTD data. No comment is made on this point in the paper, though the accuracy of the FDTD method for the cylindrical cavities modeled may well be better than RCWA. The paper concludes that for tungsten cavities, tuned for near-infrared emissivity for TPV applications, the emissivity gains of more complex cavities are marginal over rectangular cavities. For this reason, the simpler-to-fabricate rectangular cavities provide a qualitatively better solution to the selective emitter problem [54].

Finally, a more rigorous FDTD study was presented, employing a multi-Lorentz dispersion model for the complex permittivity values of tungsten and similar geometries

to the previous studies. The results and conclusions remained similar to the largely experimental work previously presented, but better isolated the surface-plasmon-versus-geometric-cavity-resonance contributions [55]. Due to the application of interest, for which isotropic emission was desired, no attempt was made to purposefully couple the emission mechanisms as Dahan *et al.* eventually did in silicon carbide [8].

The coupled resonant cavity concept was approached in tungsten, in 2004 in a two-dimensional rectangular cavity experiment conducted by Kusunoki *et al.* Tungsten was selected for this high temperature application due to its high melting point and low thermal coefficient of expansion. In this case, the inter-cavity walls were kept thicker, $2\mu m$ for a $5\mu m$ period structure, with a 1.23:1 width-to-depth ratio. Spectral narrowing was observed as was an increased density of states, but since the inter-cavity ridge and cavity depths were not coordinated for resonance, the emissivity peak remained relatively broadband and isotropic [56].

Additional numerical studies were published to further optimize the dimensions of tungsten gratings for thermal photovoltaics. High aspect ratio structures, with depths greater than the cavity opening, were studied to further equalize the TE and TM polarized contributions for spectrally selective emission [57]. A more robust optimization, employing a genetic algorithm and design parameters bounded by surface plasmon, cavity resonance, and Wood's anomaly conditions, was published in 2012. The optimal values are quite close to Sai's earlier publications, concluding that a period of $0.650\mu m$, a depth of $0.6\mu m$ and a fill factor of 0.28 which implies a $468nm$ cavity opening produces a spectral directional emissivity over 0.90 within a $20°$ angular cone over the range of $0.6-2\mu m$ while minimizing the emissivity from $2-4\mu m$ [58].

3.5.2 Planar Structures.

The focused study of surface plasmons and the spatial and temporal coherence of thermally excited systems inevitably led to the consideration of stacks of thin films in terms

61

of coherence. It was theoretically shown in 2004 that even a single-layer thin film of the appropriate complex permittivity could support leaky wave modes in free space. A thermal antenna behavior effect was predicted to be observable, if the film thickness was on the order of the coherence length of thermal excitations in the thin film [59].

Further advances in multilayered coherent thermal emission have largely been made when the stack is considered in terms of a one-dimensional photonic crystal, rather than as an absorbing coating. In the 2005 design proposed by Lee *et al.*, thermally excited surface waves at a silicon carbide to photonic crystal stack interface were exploited for directional thermal emission in both TM and TE polarizations [60]. A finite photonic crystal version of this design was fabricated and measured in 2006, along with a near-infrared asymmetric Fabry-Perot resonance cavity structure. The second structure is composed of a partially reflective gold coating on a silicon dioxide dielectric spacer, deposited over a fully reflecting gold substrate or coating, which harkens to the Salisbury screen [61]. While this concept produces directional emission in both the TE and TM polarizations, it does not occur at the same angle and wavelength pairings for each polarization, due to the difference in the reflection phases at the interfaces. The very shallow skin depths of metals in the mid- to far-infrared proved to be the limiting factor for this design [62].

An extended study of the one-dimensional photonic crystal design was published in 2007. A detailed examination of the angular and spectral emissivity was produced showing an emission peak which was spectrally flat over several degrees. The emissivity then exhibited an angularly and spectrally varying walk off, extending to near grazing [63]. This design was optimized for $11.5\mu m$ operation, showcasing its advantage over the asymmetric Fabry-Perot design in the far infrared. However, it is a relatively complex design, requiring 61 deposition layers.

A similar, more detailed modeling and experimental treatment was given to the asymmetric Fabry-Perot resonator by the same authors in 2009. The key weakness of the

concept remains that the skin depth of the reflecting layers and losses in the dielectric layer limit the application of the design to near- to mid-infrared spectral ranges [64]. An attempt was made to reduce the layered media concept to a mere two layers, but this required an unusual substrate for far-infrared emission, sodium chloride, with limited practical application [65]. Improved temperature stability was achieved for the asymmetric Fabry-Perot resonator structure by adding a thin protective silicon dioxide topcoat, a platinum barrier layer, and a titanium adhesion layer between the silicon substrate and opaque gold layer [66].

A refined design concept, intended to extend the spatial coherence of the thermal excitation, was proposed in which a grating coupler was ruled onto the surface of a slightly lossy dielectric waveguide. It was found that a precise balance had to be struck between coupling the directional emission out and perturbing the waveguide so much that it failed to enhance the spatial coherence length [67]. A similar design, in which the waveguide was excited by surface waves supported on a metallic substrate with radiation coupled to free space by a grating on the upper waveguide surface, was fabricated in 2007. This design was optimized for near isotropic emission, and its behavior can be considered more in line with a frequency selective surface [68].

3.5.3 *Photonic Crystals.*

A photonic crystal is simply defined as a periodic arrangement of low loss media, which allows or prohibits wave propagation in certain directions. The refractions and reflections from the material interfaces produce many of the same effects for photons which electrons experience due to periodic atomic potentials in crystals. The definition is applied to one-dimensionally periodic stacks, two-dimensionally periodic slabs, and three-dimensionally periodic complex structures. Of course, the response of these structures always obeys Maxwell's equations, so it is not strictly necessary to differentiate them from other periodic structures [69]. Chan *et al.* show quite distinctly that the photonic

crystal construct is a valid framework for posing the coherent thermal emission problem [70]. So, in terms of directionally and spectrally selective emission, the complexity of the proposed structures is taken as the distinguishing feature of photonic crystal solutions. In parallel with the simpler one-dimensionally periodic structures examined thus far, higher dimensionality photonic crystal concepts were also being explored.

The seminal 3-D tungsten photonic crystal structure moved into the infrared spectrum between 1998 [71] and 2002 [72]. Coherent thermal emission was predicted and observed from these structures in 2003 [14, 73]. By 2004, the direct and rigorous calculation of thermal emission for dispersive and lossy photonic crystals was established, dispelling some earlier claims that greater than black-body emission could be achieved at thermal equilibrium [74]. The same computational method was extended to three dimensional photonic crystals in 2006, using stochastic electrodynamics in a finite difference time domain algorithm to directly calculate the emissivity [74]. Publications studying the photonic crystal aspects of even one-dimensional surface gratings continued past 2008, to complete the description of surface plasmons in terms of photonic bandgaps [75].

The complexity of three-dimensionally periodic photonic crystals drove the numerical and experimental examination of simpler geometries. By extending the periodicity from one dimension to two dimensions, Laroche *et al.* were able to show leaky waves on an air-to-photonic-crystal interface, which could not be achieved with one-dimensional photonic crystals. This design was developed for the near-infrared, although the system may be tuned in wavelength and directionality by varying the lattice parameters [76].

A study of two-dimensionally periodic structures in metals was considered, in terms of photonic crystals for thermal emission. Dips, or cavities, in line with the two-dimensional surface structures were examined, with results in line with those previously predicted. The extension of this design by including a dielectric fill of the cavity structure, or a dielectric surface layer which was also penetrated by the cavity structure, showed more

distinct behaviors. In particular, adding a dielectric top-coat changed the phase propagation of surface waves along the metal-dielectric interface. This allowed spectrally narrow emission, similar to the coupled resonant cavity concept, to be exhibited with substantially less than one wavelength spacings between cavities [77]. The cavity design concept was implemented in tungsten to specifically study the effect of cavity radius and depth on emission peak position and value. While the design method was different than the RCWA method used by Sai *et al.*, the measured results are appropriately similar [12].

Multi-dimensionality systems have also been proposed. In these designs, a one-dimensionally periodic photonic crystal forms the substrate for a two-dimensionally periodic photonic crystal, which serves as the interface to free-space. The emission from this type of structure is the coupled combination of the surface modes of the top layer and resonant transmission from the underlying structure [78, 79].

3.5.4 *Microfabricated Antennas.*

Advances in microfabrication technology also enabled the fabrication of more traditional antenna types at infrared dimensions. This concept has been pursued both for antenna coupling detector arrays, and direct emission, although detector applications predominated initially.

Two-dimensional arrays of antenna elements were fabricated on common infrared focal plane array pitches, $25 - 30 \mu ms$, by 2002. Initially, simple arrays of dipoles were fabricated and coupled to microbolometer elements to take advantage of the response time of small microbolometer elements, without sacrificing flux collecting area on the detector surface [80]. This quickly led to more advanced designs, such as bow tie elements. From this point, the complexity of the antenna arrays was limited only by the fabrication tolerances and pitch size. In 2003, log periodic designs were implemented [81], and research was being directed at insulating materials and the associated technology required to achieve optimal performance with this type of detector arrangement [18]. Spiral

elements enhanced by Fresnel zone plates were fabricated in 2005 [82]. Orthogonal dipole elements were then coupled in a Wheatstone bridge arrangement to produce a polarization independent antenna response [83]. Beam shaping was demonstrated with multiple dipole elements in 2008, when the elements were coupled with coplanar strip interconnects [84].

This type of scaled-down antenna elements was also employed in thermal emission. Both dipole, for linearly polarized responses, and tripole, for circular polarization, elements were fabricated. A spacing element, much thinner than the normally directed decay length of infrared surface waves on an aluminum substrate, allowed the delocalized surface plasmon modes to coherently excite the antenna elements [85]. The directional behavior of the antenna array was enhanced by coupling normally directed coherent thermal emission from a patterned substrate to the antenna elements. In this arrangement, the antenna elements, whether they were dipoles, bend dipoles, or spirals, acted as a frequency selective surface for the substrate emissions [86].

3.5.5 *Compromise Designs.*

With the general trend towards ever more complicated structures established, a more pragmatic set of designs is considered. In each of the cases presented, some consideration was made at striking a compromise between the design objectives or control and ease of fabrication.

In regards to fabrication simplicity, few techniques show the promise for production demonstrated by simply acid etching features in bulk metals. Monolithic metal structures also have the added benefit of not introducing a thermal discontinuity. A coupled resonance cavity design was fabricated in a polished steel substrate by Mason *et al.* in 2010. Rectangular resonating cavities could not be formed by the isotropic chemical etch process employed, which produced bowled profiles, and the overall fabrication quality was low due to grain structure in the alloy steel. However, selective emission was still observed. The somewhat limited results suggest that highly conductive materials have surface wave

properties which are relatively forgiving, in contrast to the published expectations for a resonant structure [17].

A resonant cavity design, with features deep enough to generate TM and TE polarization resonances, was fabricated by a micro-mold technique. This fabrication process successfully demonstrated gold deposition with very sharp relief features and high aspect ratios, which are not achievable by direct sputtering. Additional bulk deposition techniques, such as electroplating, were proposed to provide structural strength to the molded surfaces [13]. An even simpler method of addressing the polarization dependence on emission was to produce a checker board pattern of microstructures, oriented to emit in crossed polarizations. While this limits the peak emissivity value to 0.5 in total, angular and spectral control was achieved with very simple individual structures, which eased fabrication [87].

Simple physical designs have also been shown to produce desirable behaviors, similar to those of much more complex structures. Complex gratings composed of the sum of two simple gratings were proposed to enhance the emissivity of tungsten thermal photovoltaic emitters. This could be implemented with a single photolithography step and a single etch step which is shallower than the near 1:1 aspect ratios required for rectangular and cylindrical cavities to achieve similar results. This can substantially speed and ease the fabrication process [88].

A biharmonic structure was also investigated in terms of bandgap generation in silicon carbide. The structure is composed of the superposition of two shallow gratings of the same periodicity but different cavity location phases and fill factors. The result is a structure demonstrating two shallow cavity widths and two different cavity spacings [89].

3.6 Conclusion

Despite the remarkable success of the physics of the cited works, these microstructured surface designs have seen very limited experimental transition. In some cases, this is

67

due to performance limitations, but generally the problem lies in the fabrication processes. Low-throughput steps consistently hinder the fielding of any but the simplest surface treatments, such as roughening, for mid- to far-infrared applications. If microstructured surfaces are to be fielded for low-temperature directional emitters, the designs must be optimized to facilitate high-throughput fabrication processes.

This literature review also highlights a series of practical lessons learned, generally regarding modeling and measurement comparison. Two primary sources of modeled-versus-measured emissivity error were identified. The first was the use of canonical, rather than measured, complex index of refraction values in the design and verification models. The second was the need to predict, or capture, systematic deviations in the structures' profile. These deviations must be reconciled in the model for accurate comparison. The necessary modeling to address these issues is presented in Chapter 4. Numerous examples are given in which reflectance models and measurements are used to evaluate directional absorptivity. The implication of finite longitudinal spatial coherence is not considered in the models and serves as a source of error in the measurements. While it was demonstrated that measurement error was dominated by other sources, the lack of rigorous methods to predict the results of finite longitudinal spatial coherence was identified. So, a method of extending RCWA for this type of reduced coherence modeling is presented in Chapter 5.

IV. Metalized Surface Modeling

4.1   Introduction

The proposed fabrication process requires that a metal, aluminium in this case, be deposited onto a plastic substrate. Aluminium is particularly amenable to DC magnetron sputtering, one of a family of physical vapor deposition methods employed to produce thin metal films. It is also commonly used in compact disc manufacture [25]. In the DC magnetron sputtering arrangement, a biased target of the metal to be deposited is bombarded by an argon plasma at a pressure of approximately $100mTorr$. A powerful magnet behind the target confines electron movement near the target's surface to improve the ionization efficiency. Metal atoms are ejected from the target by the argon ion bombardment and condense on the deposition substrate, forming an amorphous metal film [90]. This amorphous film deposition process introduces two sources of deviation from the ideal conditions, which must be addressed in modeling.

First, the optical properties of the amorphous metal film differ from those of the crystalline form. Since the accuracy of electromagnetic models depends upon the accuracy of the complex index of refraction, or complex relative permittivity, values employed, these properties must be measured for the as-deposited film. The modeling steps required to extract complex index of refraction values from measured data, using a particular commercial ellipsometer, are presented. Second, the proposed fabrication technique requires that metal be deposited onto a profiled substrate. The resulting final surface profile deviates from that of the underlying substrate according to a simple and well-developed model. This model is presented and incorporated into the design process in Chapter 6.

4.2 Complex Index of Refraction Extraction

Published values for crystalline aluminium and aluminium oxide are readily available [29]. However, the optical constants in thin films can vary considerably due to differences in microstructure imparted by processing conditions [91, 92]. Specifically, the room temperature growth of aluminum yields a columnar microstructure which can give rise to decreases in packing density as well as birefringence [91]. Since thin-film deposition is an additive process, varying experimental conditions can lead to the introduction of defects such as voids, substitutional and interstitial impurities [93], surface roughness, and variations in crystallinity. All of these impurities and defects lead to changes in the spectral behavior of the complex refractive index or permittivity [91, 92].

An unpatterned reference sample of aluminium, deposited on a flat plastic substrate, was produced for initial material property measurements. The sample was sputtered with 200nm of aluminium, and exposure to atmospheric oxygen was expected to produce a passivation layer of aluminium oxide approximately 10nm thick [94]. A series of measurements was then conducted on a J. Woollam Infrared Variable Angle Spectroscopic Ellipsometer (IR-VASE)® system to extract the complex index of refraction values of each layer. The IR-VASE® is a rotating compensator ellipsometer, which includes a robust optical property fitting software package [95].

The optical path and extraction process for the IR-VASE® is straightforward. First, the broadband infrared emission from a hot silicon carbide glowbar source is collimated, polarization-filtered, and passed through a rotating compensator element. The collimated, polarized, field illuminates a sample under test at a series of incidence angles, and the specular scatter passes through a rotating analyzer element. The polarization filtered scatter is then digitized at a detector module. The rotating elements enable the collection of the peak polarization differences, and the ratio of the measured polarized responses in p-polarization (TM) and s-polarization (TE) are taken on an angular and spectral basis to

produce total, Ψ, and phase, Δ, values. These values are related to the complex Fresnel coefficients, $r_{TE(s)}$ and $r_{TM(p)}$[95].

$$\tan(\Psi) \cdot e^{j\Delta} = \frac{r_{TE(s)}}{r_{TM(p)}} \qquad (4.1)$$

Collecting data at multiple angles of incidence provides the necessary variation in optical path length to extract the complex indexes of multiple layers. A model, including initial optical constants and thicknesses, is developed for each layer based on the Fresnel reflection and transmission equations for polarized light passing through, and scattering from, planar interfaces. Complex index models may be based on functional forms for optical constants, or initial table values, as well as general oscillator models such as the Drude, Gaussian, and Lorentzian models. The Levenberg-Marquardt non-linear regression algorithm is then used to fit the modeled solution to the measured data, solving the inverse problem [95]. The measured and modeled Ψ and Δ values for four incidence angles are shown in Figure 4.1 (a) and (b), respectively, for an aluminium sample with a passivation layer of its native oxide.

A fitting model was developed by allowing parameter variation of the general oscillator models initialized for crystalline aluminium and aluminium oxide. This ensured that the general form of the material properties was maintained, while allowing for deviations, particularly due to the amorphous film deposition. The most common figure of merit for ellipsometry data fitting, is a Mean Squared Error (MSE), computed by equation (4.2). In this equation, the experimental values, Ψ^{Exp} and Δ^{Exp}, are subtracted from the modeled values, Ψ^{Mod} and Δ^{Mod}, and normalized against the experimental standard deviations, $\sigma_{\Psi,i}^{Exp}$ and $\sigma_{\Delta,i}^{Exp}$, for a data set in which the total number of points, N, and number of measurements angles, M, are considered. The converged MSE between the two layer model and measured data was found to be $0.1514°$, indicating excellent agreement between the modeled and measured values for an oxide-over-metal-substrate measurement, and
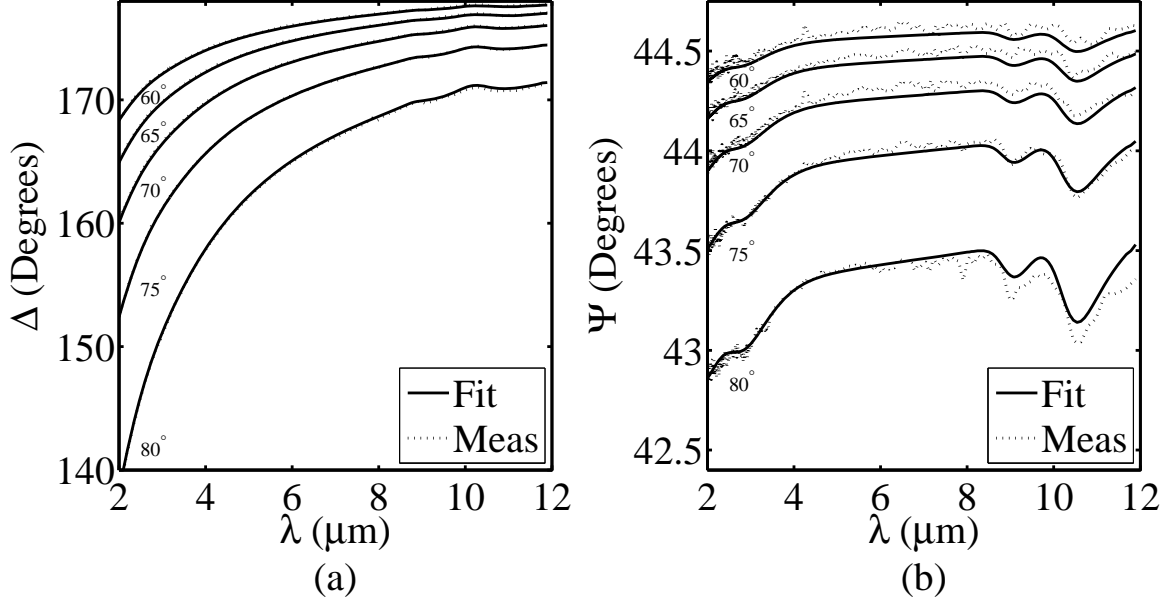
71

Figure 4.1: Modeled (solid line) over measured (dashed line) data fits for (a) Ψ and (b) Δ values at four angles of incidence, for a passivation layer of aluminium oxide over an optically thick aluminium substrate.

well below the experimentally determined threshold of $0.5°$ minimum MSE for acceptable convergence for this type of deposition recommended during instrument training.

$$MSE = \sqrt{\frac{1}{2N-M} \sum_{i=1}^{N} \left[\left(\frac{\Psi_i^{Mod} - \Psi_i^{Exp}}{\sigma_{\Psi,i}^{Exp}} \right)^2 + \left(\frac{\Delta_i^{Mod} - \Delta_i^{Exp}}{\sigma_{\Delta,i}^{Exp}} \right)^2 \right]} \tag{4.2}$$

The fitted oscillator model yields the complex index of refraction values for each layer, unlike a raw Ψ and Δ extraction, which represents a total effective value. The extracted values are shown in Figure 4.2 (a) for aluminium and (b) for aluminium oxide, and along with tabulated crystalline structure data from Palik [29]. The aluminium model follows the crystalline trend, exhibiting somewhat lower conductivity than the crystalline form, as expected for an amorphous deposition with voids and fractures. The aluminium oxide conversely shows more general losses than its crystalline form, the behavior of which is dominated by a lattice resonance in the far-infrared[29]. The measured complex index of

refraction values, rather than the tabulated values, were employed in the structure design process.
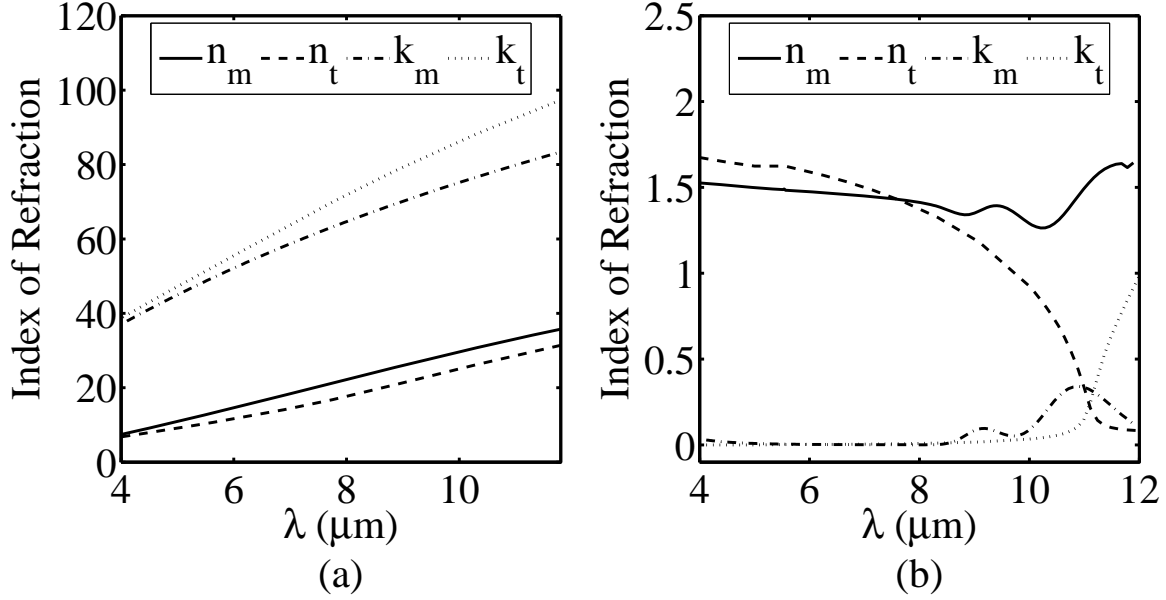

Figure 4.2: The complex index of refraction values for (a) aluminium and (b) aluminium oxide. The measured, n_m, and tabulated, n_t values of the real components of the complex indexes of refraction are shown for each sample. The measured, k_m, and tabulated, k_t, values for the imaginary components are similarly depicted. The deviation between the measured and tabulated data in (a), may be generally ascribed to the lower conductivity of an amorphous deposition of aluminium, when compared to its crystalline form. Similarly, the complex index of refraction of the crystalline form of aluminium oxide in (b) is dominated by a well-defined lattice resonance in the far-infrared, while the amorphous passivation layer shows a more complex, non-resonant behavior.

4.3   Sputtered Metal Deposition Modeling

When metal is deposited onto a patterned substrate, the surface profile of the pattern changes as the metal thickness increases. Since the thermal and electrical limits of the proposed substrate require low temperature and bias voltage deposition, to avoid damaging the substrate, classical models of sputter deposition are well suited to the application. The Blech model for DC planar magnetron sputtering is particularly applicable because it was

developed specifically to predict the profile resulting from the deposition of metallic films, such aluminium, onto the stepped features of integrated circuits [96]. These are precisely the type of simple vertical features which are studied in this work, so the Blech model was incorporated into the design process.

The Blech model is a relatively simple line-of-sight model, which assumes that no re-emission occurs during the sputtering process. It is further simplified by employing the cosine law for growth, which implies incremental film growth in the direction of the depositing vapor stream, rather than the more rigorous tangent law, which implies incremental film growth normal to the surface at the deposition point. It is also assumed that the substrate rotates about a central axis so that the entirety of a step feature may be covered. The vapor stream of metal is assumed to originate from a point source and the vapor stream flux is a function of the angle, θ, between the point of deposition and the source. The vapor stream flux is further represented by independent horizontal, $J_x(\theta)$, and vertical, $J_z(\theta)$, component functions for two dimensional profiles. To generate an incremental layer growth, the profile is discretized into test points. Next, the minimum and maximum unmasked viewing angle from each growth point on the current surface profile is determined. Then, the vapor stream flux functions are integrated over the angle range to produce x- and z-directed growth vectors. Once a growth vector is developed for each point on the current surface profile, a new profile is computed by adding the growth vectors to the coordinates of each test point [96]. A coarse extracted model from the published vapor stream flux data produced profiles matching the published results.

A detailed calibration of the deposition systems was not possible, so a canonical form of the of the vapor stream flux functions was developed to act as a worst case deposition scenario. A sinusoidal form was taken for the x-directed vapor stream flux function as shown in Figure 4.3 (a), while a Gaussian profile was taken for the z-directed flux function in Figure 4.3 (b). Centering the $J_x(\theta)$ flux values at 45 degrees, rather than the more typical

physical values of 30-35 degrees, ensures that cavity closure occurs at shallower deposition depths in the model than is expected during physical deposition. The gaussian distribution of the $J_z(\theta)$ flux distribution is a good approximation to measured data for most systems [96]. Because the sputtering systems were reported to show less than 10% variation in sputter depth over the sample sizes to be fabricated, additional functions for off-axis points were not developed.
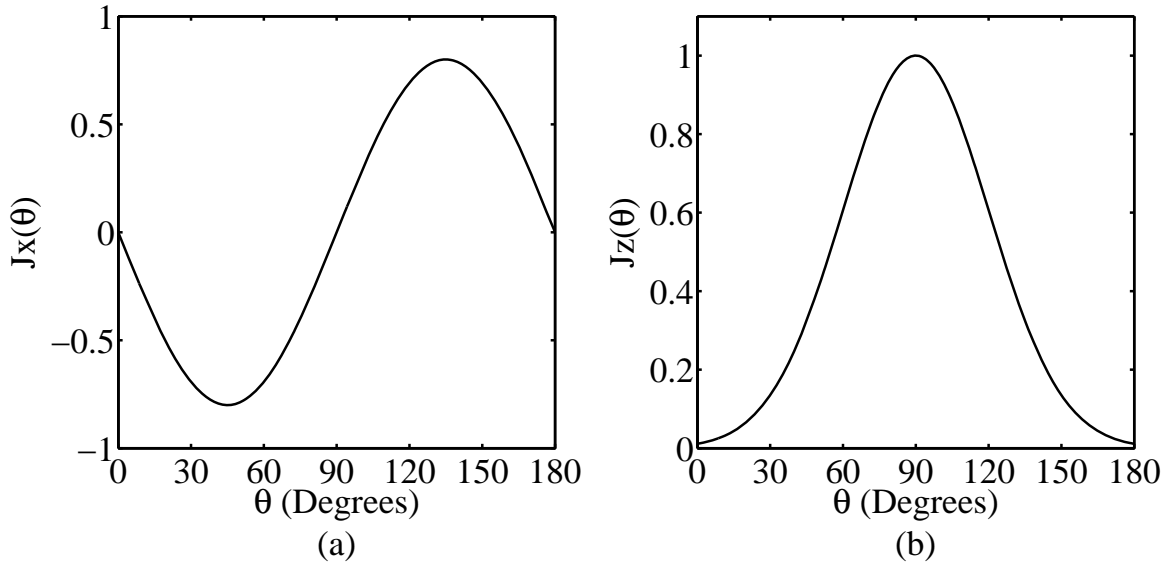

Figure 4.3: Canonical vapor flux model functions for the (a) x-directed flux, $J_x(\theta)$, and (b) z-directed flux, $J_z(\theta)$. Centering the $J_x(\theta)$ flux values at 45 degrees, rather than the more typical physical values of 30-35 degrees, ensures that cavity closure occurs at shallower deposition depths in the model than is expected during physical deposition. The gaussian distribution of the $J_z(\theta)$ flux distribution is a good approximation to measured data for most systems [96].

The incremental reshaping of a rectangular cavity with increasing metal deposition thickness is shown in Figure 4.4. The canonical form of the $J_x(\theta)$ function shifts the peak deposition angle out to 45 degrees over the more typical 30 degrees, accelerating cavity closure in line with the worst case scenario predictions. It is particularly noteworthy that

the upper surfaces of the profile grow at a substantially higher rate than the masked lower surfaces, so the cavity becomes deeper and is reshaped as metal is deposited.
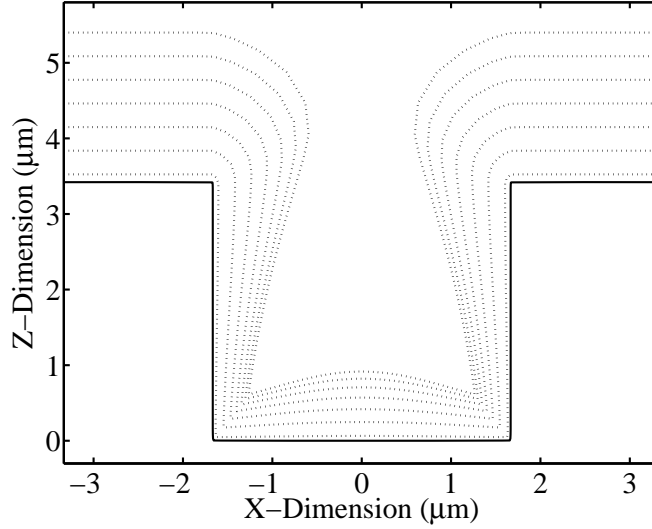

Figure 4.4: Blech deposition model results for DC magnetron sputtering of a rectangular cavity. The dotted lines indicate deposition thickness intervals of approximation 200nm, and the classic cavity closure behavior is observed with increasing metal deposition thickness.

4.4   Conclusion

The as-deposited, complex index of refraction values were measured for aluminium and aluminium oxide. A well-developed model for predicting deposition over a stepped profile was also presented, and the reshaping effects illustrated for a rectangular cavity. The measured complex index of refraction values are used in all subsequent modeling steps, and the effects of cavity reshaping on a given structure's performance are examined in Chapter 6. The consideration of these deviations is necessary to accurately represent the structure in an RCWA model. Another assumption of the RCWA method, which must be addressed to match experimental measurement conditions, is considered in Chapter 5.

V. Longitudinal Spatial Coherence Modeling

5.1 Introduction

All of the differential methods for predicting scatter from a grating, including RCWA, express the physical form of the structure as a periodic distribution of complex permittivity values. This allows plane-wave expansion for excitation and scatter, and assigns diffraction efficiency values to diffracted order angles with infinitesimal angular span. As such, the diffraction efficiency values and order angles produced by RCWA are the ideal limit of the scatter distribution [97]. In the measurement of actual grating lobe distributions, the deviation from the plane-wave ideal is considered to be part of the instrument function introduced by the finite and imperfect instrument. In practice, the angular span of an instrument's collecting aperture is made large relative to the grating lobe angular span, so that all of the power in a measured order is captured by the detector [24].

Given that the objective of the scatter measurements in this work is to examine thermally excited, directional self-emission, the assumptions of RCWA merit additional consideration. First, the validity of plane-wave illumination, implying infinite longitudinal spatial coherence, in predicting selective emission is discussed. Then, a method is developed to reduce the longitudinal spatial coherence of the incident field, to accurately predict scattered lobe widths in the presence of angularly varying absorptive losses.

5.2 Plane Wave Excitation Validity

It has been established that predicting the total angular spectral reflectance of a periodic surface is sufficient to predict the angular emittance, without regards to the computational means used [45]. The angular emittance derived from RCWA computations has also been experimentally shown to be in excellent agreement with measurements [11], even though the incident field is perfectly coherent. Topically, this perfectly coherent

77

illumination assumption appears to contradict the finite spatial coherence length extracted from the modeled data. However, an examination of the computational process shows why the assumption is necessary.

The coherent thermal emittance of well-fabricated non-transmissive structures is computed by RCWA through a straightforward process [11]. First, the total reflected power is computed for each of a series of finely spaced angles of incidence, at a single wavelength, by summing the calculated reflected diffraction efficiencies [67]. The resulting profile reflects the efficiency with which the incident field is coupled into a loss mechanism. Since the field does not penetrate the surface of the materials of interest efficiently, the primary losses occur when the incident field is coupled into surface waves and then absorbed into the material. This absorption is the physical link, within the model, between the far field and surface waves. The angular reflectance profile is then converted to an angular emittance profile by applying Kirchhoff's Law [52]. The angular emittance profile always extends and varies over some finite angular width, and this width may be taken to indicate the number of resonant structures which may emit coherently [45].

The accuracy of this result, as the limit of spatial coherence length, can be arrived at by considering array antenna theory. In terms of antenna theory, the surface wave propagation properties of the material, structure profile, and structure period produce a fixed inter-element amplitude and phase evolution. In this regard, the structure is an infinite array of receiving elements, which generates a fixed angular receiving pattern. This pattern is probed by the incident field through a range of angles. If the antenna is then employed in transmission with element excitation at the limit of infinite coherence, the transmission pattern is the same as the reception pattern [21]. If the spatial coherence of the excitation signal breaks down randomly, or localizes, the directivity of the beam pattern can only be reduced. Hence, it represents the limit of coherent excitation performance.

From a modeling-centric point of view, the plane-wave assumption is also necessary. For emission prediction in RCWA, the plane-wave assumption is required to produce accurate absorption results. Physically, the plane-wave assumption represents the limiting case of both infinite longitudinal spatial coherence and zero angular divergence. If the incident field in each calculation is expanded over a finite angular extent, then the predicted absorption efficiency becomes a function of the incident field amplitude and phase profile, as well as the surface wave propagation properties of the material and structure. It is no longer the ideal result for a single infinitesimal incidence angle, rather the composite of many, and the coherent interference of the incident field must be considered at the interface.

5.3   Reduced Spatial Coherence Modeling

While an inappropriate addition to the model for directional emission prediction, reducing the incident field spatial coherence is necessary under some conditions. An applicable situation immediately arises when it is necessary to represent a periodic structure within a larger framework for scatter modeling. Common modeling methods employ ray tracing and BRDFs, or data tables, to predict the scattered distribution of an incident field from a differential area of a surface.

As typically employed, RCWA produces ideal diffraction efficiency weights, assigned to diffracted angles of infinitesimal angular width. To produce bi-directional reflectance data from modeled grating orders, it is necessary to assign some angular width to the computed grating lobes. Fundamentally, this is because the scatter of a periodic structure is sensitive to the number of periodic elements which contributed coherently to form the scattered lobes. The lobe width is a function of both the length over which the structure's features are periodically consistent enough to produce scattered fields with a fixed phase relationship, and the longitudinal spatial coherence length of the incident field [22].

A straightforward method of assigning lobe widths to grating data is to simply convolve the order weights of the computed diffraction efficiencies with an angular

Gaussian spreading function, indicative of the assumed total longitudinal spatial coherence length, and normalize the results to conserve energy [23]. When the loss of spatial coherence in the structure is primarily due the limitations of physical grating fabrication, results in good agreement with measurements may be achieved by this method. However, when the spreading is due primarily the spatial coherence of the incident field, this method may fail to produce good results. In particular, it fails to produce accurate results when angularly dependent incident losses are a dominant feature. Since this condition defines the behavior of plasmonic surface structures, partial spatial coherence must be introduced into the computational method in a more robust manner.

To this end, a method for applying RCWA to finite longitudinal spatial coherence modeling is proposed and examined. The method is based on the extension of RCWA for modeling Pulse-Width Modulated (PWM) gratings and a partially coherent illumination modeling method common in the study of imaging systems [22]. The result of this method is scattering data which may be incorporated into various modeling constructs, either directly or after functional fitting. It will be shown that the need to model an extended surface, and the incumbent computational burden, is the primary limitation of the method.

5.4 Supercell Expansion

The first requirement to introduce a reduced local longitudinal spatial coherence into the scattering results of the RCWA method is to extend the physical dimensions of the defined unit cell. This extension is necessary to develop an incident wavefront which exhibits localized longitudinal spatial coherence. The context for extending the unit cell in RCWA is already established through efforts to model pulse width modulated gratings [98] and is similar in nature to the supercell extension method employed in photonic crystal defect modeling [69]. The supercell expansion is presented for in-plane diffraction from a grating periodic in one dimension. It may be similarly developed for conical diffraction and

periodicity in two dimensions, but with increasing computational cost. Then, the numerical error implications of the expansion are addressed.

To model a PWM grating, a supercell with period, Λ_{sp}, composed of an integer, P, subcells each with period, Λ_{sb}, is defined. An example is shown in Figure 5.1 of a 16-subcell binary grating in which the width of a dielectric pillar in each subcell increases linearly for each subcell within the supercell (top) or remains constant (bottom).
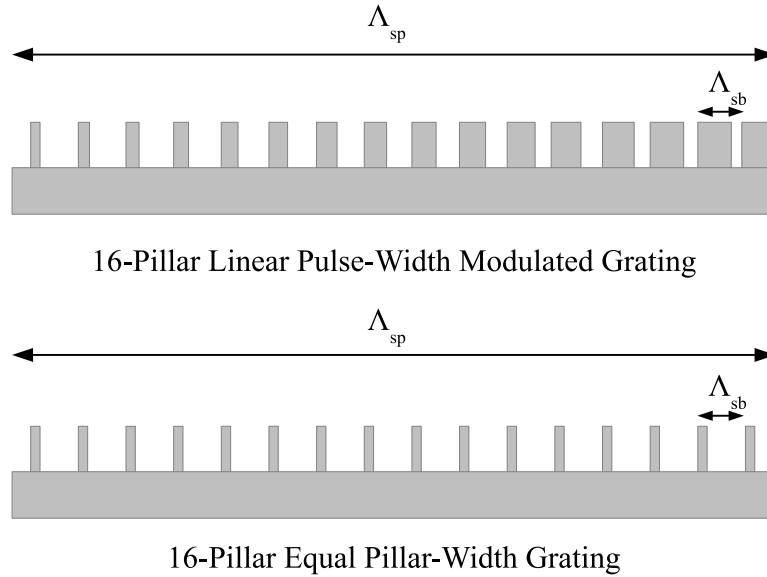

16-Pillar Linear Pulse-Width Modulated Grating

16-Pillar Equal Pillar-Width Grating

Figure 5.1: Example of a linear pulse-width modulated grating (top) and a degenerate equal pillar-width grating (bottom). In both cases, the supercell period, Λ_{sp}, is comprised of 16 subcells with period, Λ_{sb}.

When these two structures are modeled by the RCWA method, the impact of the variation of the pillar width is clearly visible in the Fourier domain. Figure 5.2 (a) shows the absolute value of the Discrete Fourier Series (DFS) coefficients by Fourier expansion order, N, for a highly converged solution, while Figure 5.2 (b) shows the convergence of the transmitted zero-order diffraction efficiency for the TM or p-polarized case as a function of N. Regions of low modulation spanning blocks of 16 N-values become visible as N increases in Figure 5.2 (b). These regions correspond to the smaller valued DFS

coefficients in Figure 5.2 (a), and identify with spatial frequencies which are periodic in the supercell, but not each subcell, that express the non-uniform pillar widths. The converged DFS coefficients and the convergence of a degenerate form of the same PWM grating, in which the pillar widths are constant, are shown in Figure 5.2 (c) and (d). In this case, the regions of low modulation are constant, and the zero-valued DFS coefficients identify with spatial frequencies which are not periodic in each subcell and are not part of the unique solution.
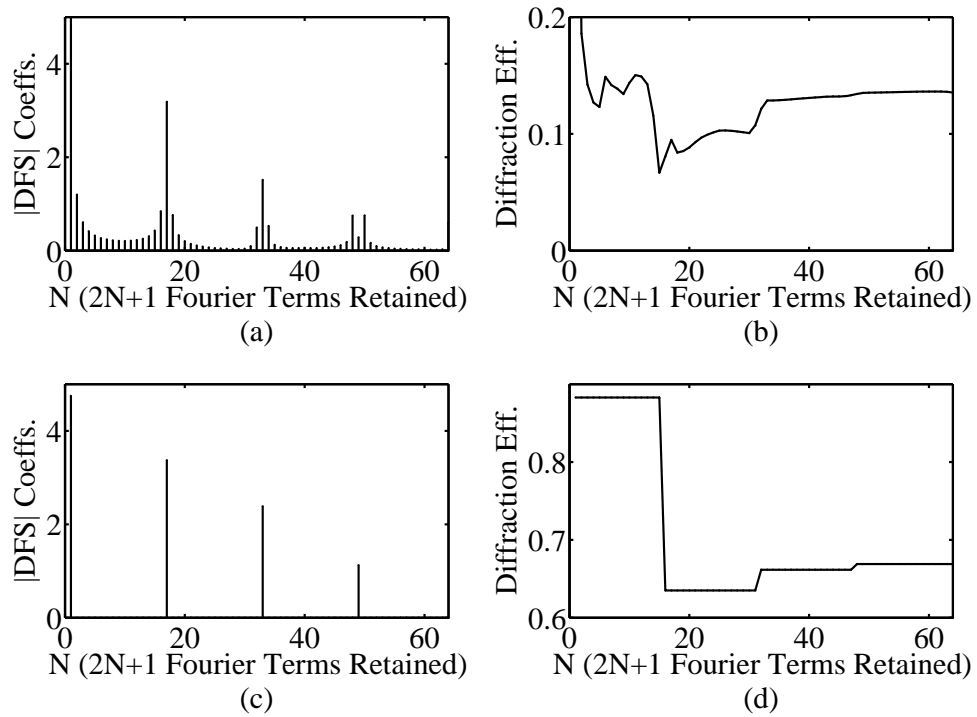
Figure 5.2: Comparison of two cases of a 16-pillar Pulse-Width Modulated (PWM) dielectric grating's Discrete Fourier Series (DFS) coefficient weights and zero-order transmitted diffraction efficiencies. (a) Linearly modulated pillar-width grating DFS coefficients. (b) Linearly modulated pillar-width grating zero-order transmitted diffraction efficiencies. (c) Degenerate, equal pillar-width grating DFS coefficients. (d) Degenerate, equal pillar-width grating zero-order transmitted diffraction efficiencies.

In the degenerate case, the convergence of the extended solution may be directly examined from the evaluation of a single subcell of period, Λ_{sb}. Figure 5.3 shows

convergence in $P \cdot N$ Fourier expansion terms for integer even multiples, P, of the base period, Λ_{sb}, and P-subcells per supercell of period, Λ_{sp}. Only those Fourier expansion terms corresponding to spatial frequencies which are periodic in each subcell advance the convergence of the solution.
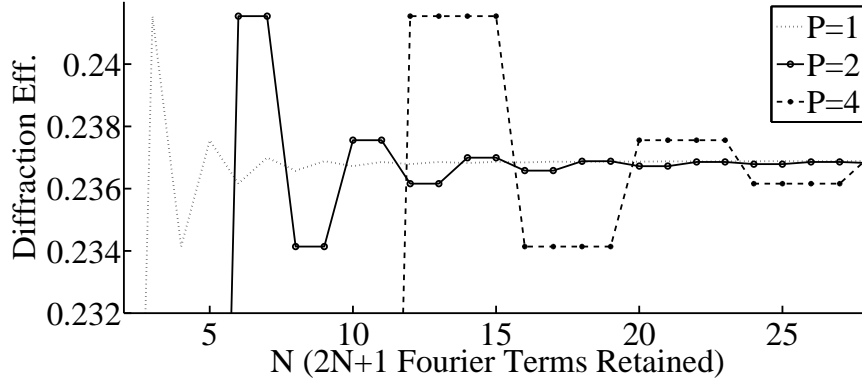

Figure 5.3: First-order transmitted diffraction efficiency convergence example for a dielectric grating with P subcells per supercell. A base subcell composed of a 50/50 binary dielectric/free-space grating of period, Λ_{sb}, is extended into a supercell of period Λ_{sp}. When P=1, only one grating cycle is represented, and $\Lambda_{sb} = \Lambda_{sp}$. When P is greater than one, multiple dielectric/free space cycles with subcell period, Λ_{sb}, are represented within a supercell of period, $\Lambda_{sp} = P \cdot \Lambda_{sb}$.

A natural consequence of this degenerate extension to a supercell is an increase in the angular density of diffraction orders and a corresponding increase in the number of Fourier expansion terms required to converge a solution. The increased diffraction order density offers a physically intuitive insight into the $P \cdot N$ convergence. The grating equation for the supercell period, Λ_{sp}, in which θ_i is the angle of incidence, n is the diffracted order index, and λ_0 is the free-space wavelength of the incident field yields the diffraction order angle, $\theta_{d,n}$. Only a subset of the angles of the orders when $n = P \cdot N$ correspond exactly to the angles of the orders when $n = 1 \cdot N$.

$$\theta_{d,n} = \sin^{-1}\left(n\frac{\lambda_0}{\Lambda_{sp}} - \sin\left(\theta_i\right)\right) \tag{5.1}$$

The remaining sets of diffraction angles correspond to sets of constant values in Figure 5.3, or zeroed DFS component values in Figure 5.2 (c), and are assigned no power by the RCWA calculation of the diffraction efficiencies. The non-zero-valued diffraction efficiencies, as a function of diffracted angle, for an ideal degenerate supercell are precisely the same as those for a single unit cell.

5.5   Numerical Error

Since numerical implementations are never ideal, two issues of numerical error, which could be relevant to the extension to a subcell and supercell arrangement, are addressed. First, the consequences to the numerical implementation of the algorithm of extending the number of necessary Fourier terms is considered, primarily to check the implementation of the algorithm. Second, the error introduced by the staircase approximation to a smooth surface is examined [38].

A numerical noise baseline was developed by computing diffraction efficiencies for different numerical interpretations of physically identical dielectric and metallic gratings over a range of retained Fourier expansion terms (N). Physically, but not numerically, equivalent realizations of the structure were generated by shifting the center of the grating pillar over a range of locations. This results in changes to the complex weights of the DFS coefficients which describe the complex permittivity profile of the modulated region. In the computed test cases, the resulting error between grating realizations ranged from the 12th to the 9th decimal place as N increased to 3000.

First, the deviation between a single subcell grating and a supercell grating composed of P subcells was evaluated. The deviation tracked with the numerical noise floor when a single subcell converged at N Fourier expansion terms was compared with supercell results composed of P subcells converged at $P \cdot N$ Fourier terms for a range of N and P

combinations. This result numerically demonstrates the accuracy of comparing N to $P \cdot N$ convergence results, and anecdotally demonstrates the numerical stability of the Enhanced Transmission Matrix Approach [33].

Second, numerical contamination in the supercell extension due to the stair-step approximation to a smooth surface was evaluated. This error source is known to limit the applicability of the RCWA method to approximating smooth non-lamellar surfaces, although it does not preclude its use in many cases down to measurable levels of error [38]. To highlight any numerical contamination introduced by extending the staircase approximation, a 198-layer linearly sloped silver sawtooth grating, periodic in only one dimension with $\Lambda_{sb} = \lambda_0 = 1\mu m$, was taken as a test case. The grating was illuminated at an incident angle, $\theta_i = 30°$, and modeled in the p-polarized or TM grating orientation to maximize the observability of the staircase error.

When the number of Fourier expansion terms retained was held relatively low and the number of subcells in the supercell increased, the deviation between equivalent convergence levels of a single subcell computation remained at the numerical noise floor for the number of $N \cdot P$ Fourier expansion terms retained. Similarly, when the supercell was composed of only two subcells but the number of Fourier expansion terms retained was allowed to become large, the error remained on the order of the numerical noise floor for $P \cdot N$ Fourier expansion terms. While extending the sawtooth to P subcells in the supercell does increase the number of physically represented corners by P, these corners are not expanded in unique DFS coefficients. So long as the extension is spatially and numerically degenerate, increasing P causes no appreciable additional numerical contamination.

From these results, it may be safely concluded that modifying the employment of the RCWA algorithm by extending the directly defined incident region from a single subcell to a collection of repeated subcells in a supercell remains numerically valid. This extension provides both the spatial extent necessary to consider an incident field with finite spatial

coherence and the angular expansion in diffracted orders necessary to represent the scatter. The convergence of the extended solution is also known since the convergence of a single unit cell is a precise predictor of the convergence of the super-cell arrangement.

5.6   Reduced Longitudinal Spatial Coherence Field

With the grating interface defined over multiple sub-periods, an incident field distribution which exhibits localized longitudinal spatial coherence may be integrated into the RCWA algorithm. A method common to atmospheric turbulence modeling in which multiple deterministic fields with random, but Gaussian-correlated, phase is employed [22]. In this method, multiple instances of the incident field are propagated through the system and their irradiance results averaged to produce a partial coherence effect. A method of generating an incident field distribution, by this method, is presented in which the grating is periodic in the x-dimension.

The process begins with a Gaussian random distribution of phase values, g(x), over the supercell length with spatial variance, σ_g^2, and spatial sampling, dx.

$$g(x) = \frac{1}{\sigma_g \sqrt{2\pi}} \exp\left(-\frac{1}{2}\left(\frac{x}{\sigma_g}\right)^2\right) dx \tag{5.2}$$

These values are delta-correlated. So, to induce a spatial correlation, a deterministic Gaussian response function, f(x), is developed with a spatial variance, σ_f^2,

$$f(x) = \frac{1}{\pi\sigma_f^2} \exp\left(\frac{-x^2}{\sigma_f^2}\right) dx^2 \tag{5.3}$$

and convolved with the random phase values, $g(x)$. The spatial autocorrelation function, $G(x')$, of this convolution at an observation point, x', has the form of

$$G(x') = \exp\left\{-\frac{\sigma_g^2}{\pi\sigma_f^2}\left[1 - \exp\left(-\frac{x'^2}{\sigma_f^2}\right)\right]\right\} \tag{5.4}$$

Furthermore, this autocorrelation function is approximately Gaussian when

$$\sigma_g^2 / 2\pi\sigma_f^2 \gg 1 \tag{5.5}$$

Under this condition, the longitudinal spatial coherence length, L_{lsc}, is related to the random phase and response function variances by

$$L_{lsc}^2 = \frac{4\pi\sigma_f^4}{\sigma_g^2} \tag{5.6}$$

It has been shown [99] that the variances required to produce a nearly arbitrary longitudinal spatial coherence length may be determined by the simple relationships shown.

$$\sigma_f = 2.5L_{lsc} \tag{5.7}$$

$$\sigma_g = \sqrt{4\pi\sigma_f^4/L_{lsc}^2} \tag{5.8}$$

Once the longitudinal spatial coherence length, L_{lsc}, of the desired incident field is selected, the required variance terms, σ_f^2 and σ_g^2, are found by equations (5.7) and (5.8), and g(x) and f(x) computed per equations (5.2) and (5.3). The results are convolved to produce a spatially correlated phase, $\Phi(x)$.

$$\Phi(x) = g(x) \otimes f(x) \tag{5.9}$$

The unit amplitude incident field at the grating interface then goes as equation (5.10), where F_i represents the incident electric, $E_{i,x}$, or magnetic, $H_{i,y}$, field terms.

$$F_i \propto \exp(j\Phi(x)) \tag{5.10}$$

It should be noted that, since the supercell is periodically defined, the incident fields, $H_{i,y}$ and $E_{i,x}$, derived from Equation (5.10) are periodic, and must be defined over a length in the x-dimension sufficient to effectively isolate the spatially coherent regions of the field.

5.7 Reduced Coherence RCWA Excitation

With the desired periodic incident field known, the RCWA method intrinsically provides a means of exciting the system if the field may be represented by a summation of plane-waves. Following the development and notation convention of Moharam and

Gaylord [32] for the two-dimensional in-plane TM or p-polarized case, the incident field inputs of the author's equation (41) are complex, scaled delta functions, δ_{n0}, of order, n, corresponding to a single incident plane wave, and n_I is the complex index of refraction of the incident-side medium. This expression also correspond to the RHS incident field terms, of the same form, in equation (2.35). In both cases, only a single non-zero input value is defined in each block, corresponding to the zero-order incidence angle, θ_i.

$$\begin{bmatrix} \delta_{n0} \\ j\delta_{n0} \cos\theta_i / n_I \end{bmatrix} \tag{5.11}$$

The incident and reflected fields are described by their Fourier expansion in the incident region at the boundary between the incident and first modulated regions. Any arbitrary periodic field distribution, over the defined supercell region, may be constructed from the DFS coefficients of the desired spatial field distribution, where the delta functions of Equation (5.11) are replaced the appropriate DFS coefficient weights for the desired incident magnetic field, $H_{n,y}$, and electric field, $E_{n,x}$. Since the desired fields are generated by a discrete numerical method, the Discrete Fourier Transform (DFT), $\mathcal{F}$ in N points is taken to produce the necessary coefficients for equation (5.12) from the correlated field distribution determined in equation (5.10). The transformed terms serve only to represent field components incident from multiple angles, $\theta_{d,n}$, which may also have a non-uniform relative phase.

$$\begin{bmatrix} \mathcal{F}\left\{H_{i,y}\right\} \\ j\mathcal{F}\left\{E_{i,x}\right\} \cos\left(-\theta_{d,n}\right) / n_I \end{bmatrix} \tag{5.12}$$

The solution can then be computed, but since the incident field power is distributed within the orders, the diffraction efficiency computation must be scaled to account for the tangential field projections. This is accomplished by

$$A_{proj} = \sum_n \left\{ \mathcal{F}\left\{H_{i,y}\right\} \mathcal{F}\left\{H_{i,y}\right\}^* \right\}_n \cos(-\theta_{d,n}) \tag{5.13}$$

where the *nth* component of the conjugate squared input field weight is scaled by the $n - th$ incident angle projection due to $\theta_{d,n}$ and the tangential field projections are summed. This scaling is integrated into the diffraction efficiency calculation replacing the $\cos(\theta_i)$ term of Moharam and Gaylord's equation (45) [32]. The computed diffraction efficiencies for a given central incident angle are then averaged over many random phase instances to produce a mean, reduced longitudinal spatial coherence diffraction pattern.

5.8   Modeling Results

A series of test runs was conducted on high-order, lossless dielectric gratings to test the general functionality of the method. Energy conservation was maintained by the projection scaling, and the finite longitudinal spatial coherence lengths were accurately translated into diffraction lobe widths. The results were in excellent agreement with antenna theory, and clearly indicated the utility of simply convolving the computed diffraction efficiencies from a single sub-cell with an appropriate angular spreading function in the high-order, lossless case.

To demonstrate the utility of the proposed method, the scattering from a simple plasmonic structure is presented. The grating region is composed of a silicon-dioxide-coupled-resonance-cavity structure with $\Lambda_{sb} = 8.9\mu m$, ridge fill factor, $f = 0.50$, and ridge height, $h = 2.7\mu ms$, shown in Figure 5.4. This cavity depth optimizes $\lambda = 8.9\mu m$ absorption at normal incidence, and has been shown, numerically and experimentally, to produce coherent thermal emission at the same wavelength [8]. The complex permittivity of silicon carbide at $8.9\mu m$ was modeled as $\epsilon = -3.285 + j1.371$, so both bulk and plasmonic losses are present in the structure [8].

To aid in optimizing the solution convergence level, angular resolution and computation time, a convergence response surface was computed for a single unit cell of the coupled resonance cavity structure. The convergence is mapped as a function of incidence angle, θ_i,
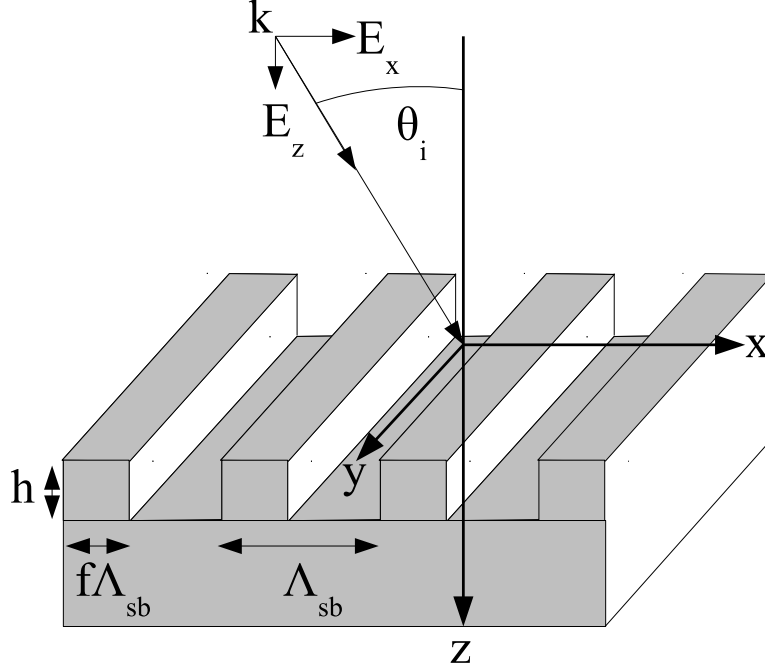
Figure 5.4: Diagram of a binary grating CRC structure of silicon carbide, with complex permittivity, $\epsilon = -3.285 + j1.371$, and free space. The incident field, E, is shown p-polarized (TM) in-plane at an incident angle, θ_i. The grating parameters are ridge height, $h = 2.7\mu m$, subcell period, $\Lambda_{sb} = 8.9\mu m$, and ridge fill factor, $f = 0.50$.

and number of retained Fourier expansion terms, N, in Figure 5.5. It is notable that, even though the value of the diffraction efficiency is falling near normal, the variability remains higher than at larger angles of incidence. This is because more Fourier expansion terms are required to represent the non-plane-wave propagation within the cavity when surface plasmon polariton (SPP) modes are excited.

The number of subcells which must be represented for accurate results is a function of both the desired angular resolution and the proposed longitudinal spatial coherence length. In this case, a longitudinal spatial coherence length of $L_{lsc} = 10\lambda$, or ten wavelengths of the incident field, was selected. An expansion of at least 10 times this value is necessary to sufficiently decouple the periodic solution. To provide some margin and numerical convenience, a P value of 128 was selected. The angular resolution is also set by the

90
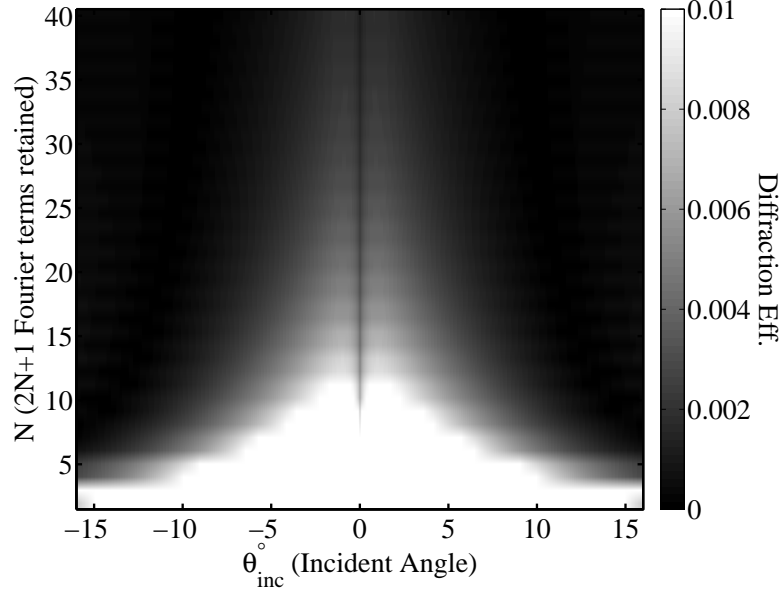
Figure 5.5: Convergence response surface of a SiO_2 CRC. The change in 0-order reflected diffraction efficiency between increasing numbers N of Fourier terms retained is mapped as a function of N and incidence angle (θ_i). In this case, the relative error falls below 1% with as few as 14 terms, even near the resonance at 0 degrees.

supercell period length, as defined by the grating equation (5.1). The expansion factor of 128 gives an angular sample spacing of less than 0.5°, which is sufficient for the proposed purpose.

Finally, 256 iterations of the random phase were computed and the individually computed diffraction efficiencies averaged for four angles of incidence. The results are shown in Figure 5.6 in terms of normalized reflectance distribution on the Left-Hand-Side (LHS) axis. The angular Energy Conservation (EC) profile is represented on the RHS axis for reference in terms of normalized reflectance.

The angular EC profile exhibits broad variation, and precludes simply expanding the scattering lobes through convolution because the incident field angular components are not uniformly weighted. This produces some reshaping of the first-order diffraction lobes. Likewise, the reflected scatter shows distinctive reshaping due to the sharp plasmonic absorption feature.
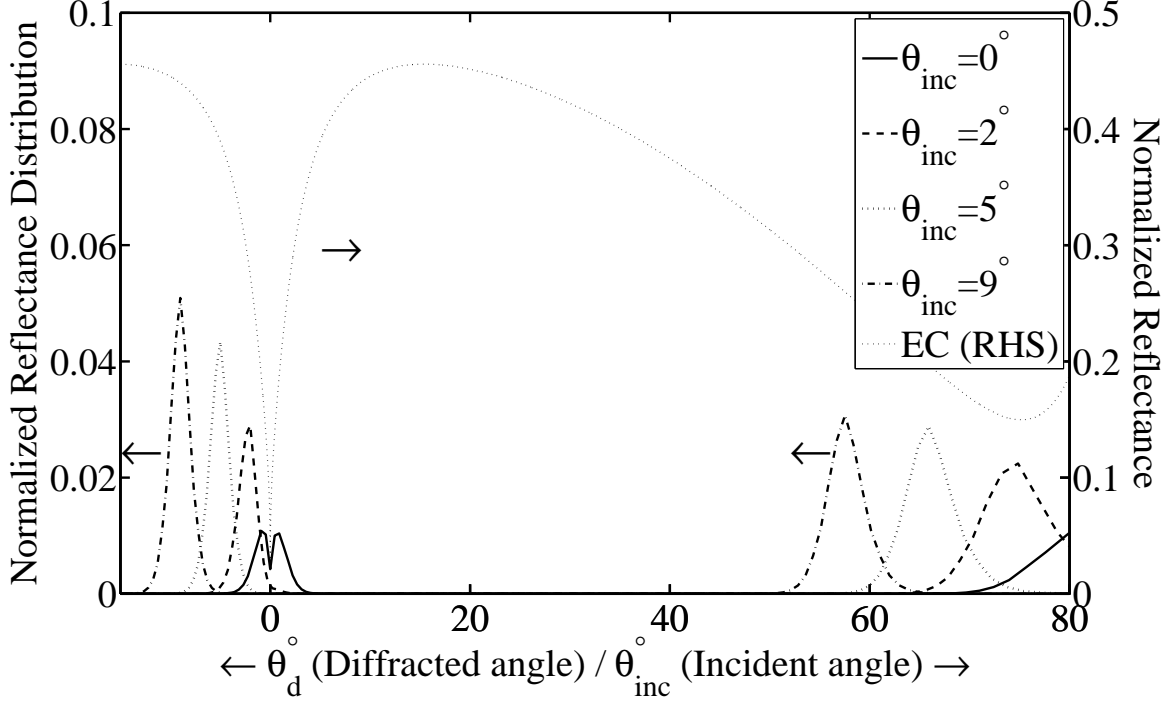
Figure 5.6: Normalized scatter results for $L_{lsc} = 10\lambda_0$, SiO_2, coupled resonance cavity at four angles of incidence (LHS axis) overlaid with the angular Energy Conservation (EC, RHS axis). The EC plot provides a reference for the angularly dependent incident losses due to bulk and surface wave absorption. Significant scattered lobe shaping, due to losses incurrent in the incident field, is shown in both the zero and first-order lobes.

5.9   Conclusion

The validity of employing the plane-wave expansion and energy conservation in RCWA to predict the limit of coherent thermal emission performance, from a periodically patterned surface, was readily established. A novel method was also developed for extending RCWA to predict the reflected scatter from a periodically patterned surface when then incident field exhibits only partial longitudinal spatial coherence. This is necessary for producing modeled data for comparison with real reflectance based scatterometry instruments under some conditions.

The numerical rigor of the extended computational method was established, as well as an efficient means of determining the suitability of the method to particular

applications. The method is distinctly suitable for modeling the scatter from periodically patterned surfaces which exhibit strong directionally dependent absorption, and may be used to generate bi-directional reflectance distribution data for such surfaces. The primary limitation of this method is its computational burden.

VI. Design Analysis and Development

6.1 Introduction

With the concept of coupled resonance cavities established in silicon carbide [11] and tungsten [55, 88], there was substantial reason to explore alternative materials. The most notable example, highlighted in the Literature Review of Chapter 3, involved wet etching steel to produce coupled resonance cavities. The motivation for this work was efficient mass fabrication of the structures, but the results suggest that highly conductive metals offer some exploitable trade space when designed for the mid- to far-infrared [17].

To justify further designs, the pertinent properties and behavior of aluminium are compared and contrasted with silicon carbide in the development of an ideal coupled resonance cavity structure designed for the far-infrared. With a trade space established, a coupled resonance cavity structure in the mid-infrared is designed and corrected to account for the requirements of the fabrication process. As it has been shown in the published works section, the coupled resonance cavity structure produces an extremely narrow angular response. So, a second design is developed which exploits the surface properties of aluminium to produce a directional emitter and absorber which exhibits a broader angular response.

6.2 Material Properties Comparison

The fundamental electromagnetic behavior of material is captured in its complex permittivity at optical and infrared wavelengths, and the values may vary substantially with wavelength. The complex permittivity defines both the spectral range over which a surface will support surface waves and the surface wave propagation distance. These properties are computed and compared for silicon carbide and aluminium, highlighting the design trade space advantages generally offered by metals. The data for comparison is drawn from two

94

different sources. The complex permittivity values for aluminium and its native oxide are based on measurements of the as-deposited materials as presented in Chapter 4, Section 4.2. The complex permittivity values for silicon carbide are derived from published sources [8]. Figure 6.1 (a) and (b) show side-by-side comparisons of the real and imaginary components of the complex relative permittivity of aluminium and silicon carbide over a broad range of the infrared regime ignoring the oxide layer of aluminium.
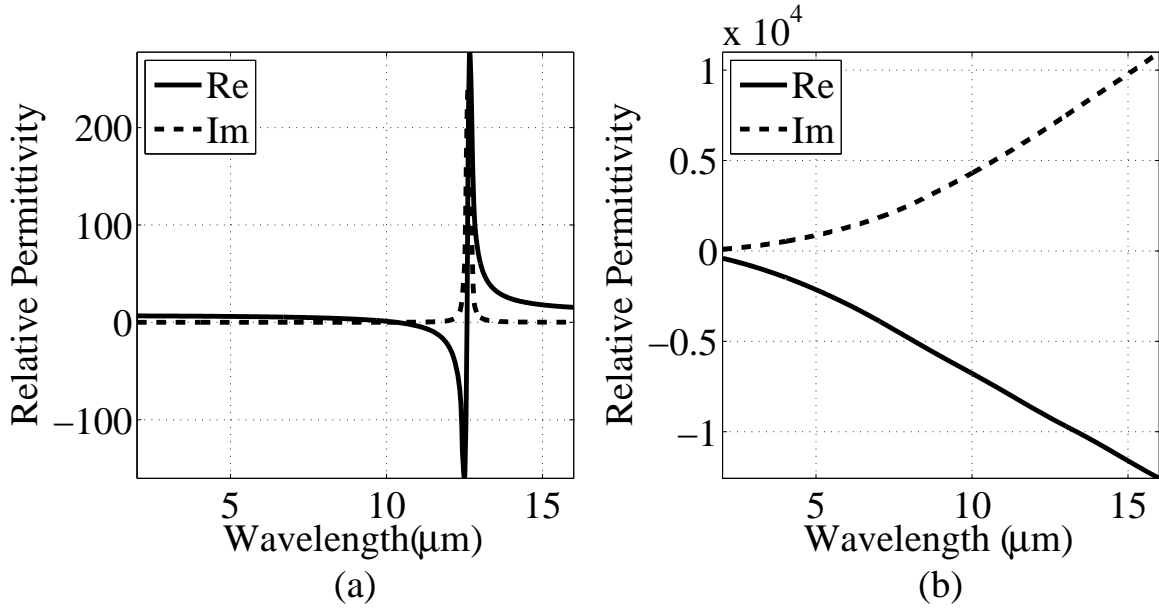

Figure 6.1: Silicon carbide (a) and aluminium (b) complex permittivities.

The physical results of the different complex permittivity forms shown in Figure 6.1 (a) and (b) can be observed in the angular and spectral reflectance of flat smooth surfaces of monolithic materials. The angular and spectral reflectance of silicon carbide shown in Figure 6.2 is evaluated from the TM form of Fresnel's equation (2.14). At an interface to free space, the surface waves of interest only occur when the real part of a material's complex relative permittivity is less than negative one [9]. The high reflectance region from $10.5 - 12.5 \mu m$ corresponds to a spectral region where the material supports surface waves.
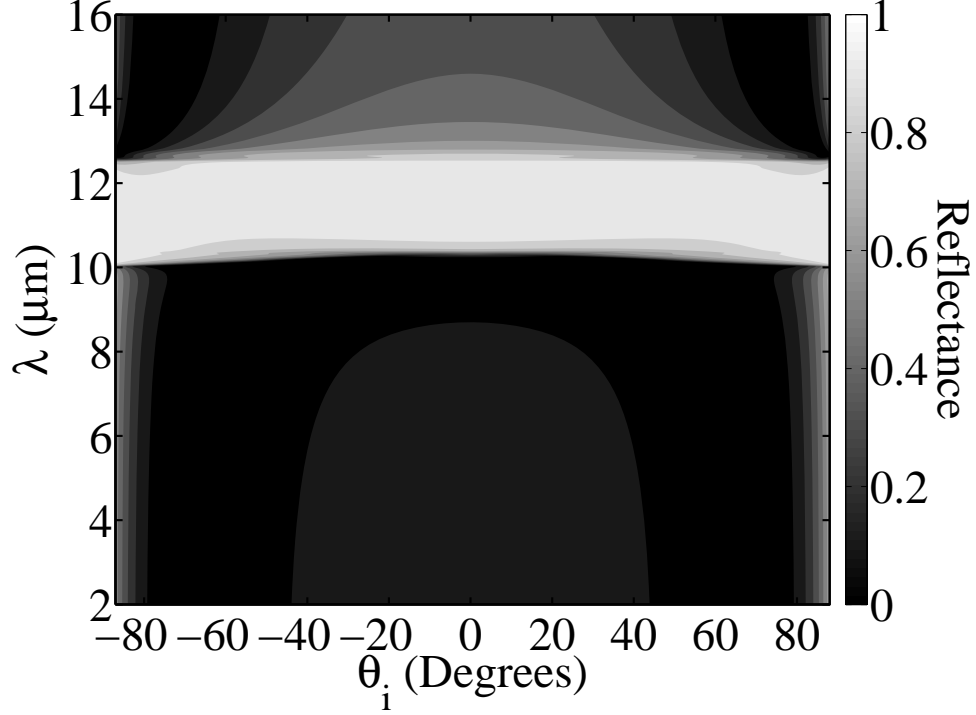
Figure 6.2: Silicon carbide directional and spectral reflectance derived from Fresnel's equation. Silicon carbide only supports surface waves over the high-reflectance region between 10.3μm and 12.2μm.

Similarly, the TM angular and spectral reflectance of an aluminium surface is shown in Figure 6.3. As with all metals, aluminium demonstrates a high degree of reflectance for wavelengths longer than its plasma wavelength, which lies in the below the visible wavelengths [9], and a slight null in reflectance before grazing.

Clearly aluminium, and most metals in fact, offers substantially more spectral bandwidth for modification than lossy dielectrics, so long as the frequencies of interest are sufficiently below the plasma frequency. Considering only the respective regimes in which both materials support surface waves, the complex permittivities may be used to compute the three $1/e$ propagation lengths of interest, along the surface and into each medium [9].

The first length of interest is the surface propagation distance, δ_{prop}, where real, ϵ_m', and imaginary, ϵ_m'', components of the complex material's permittivity are required. The
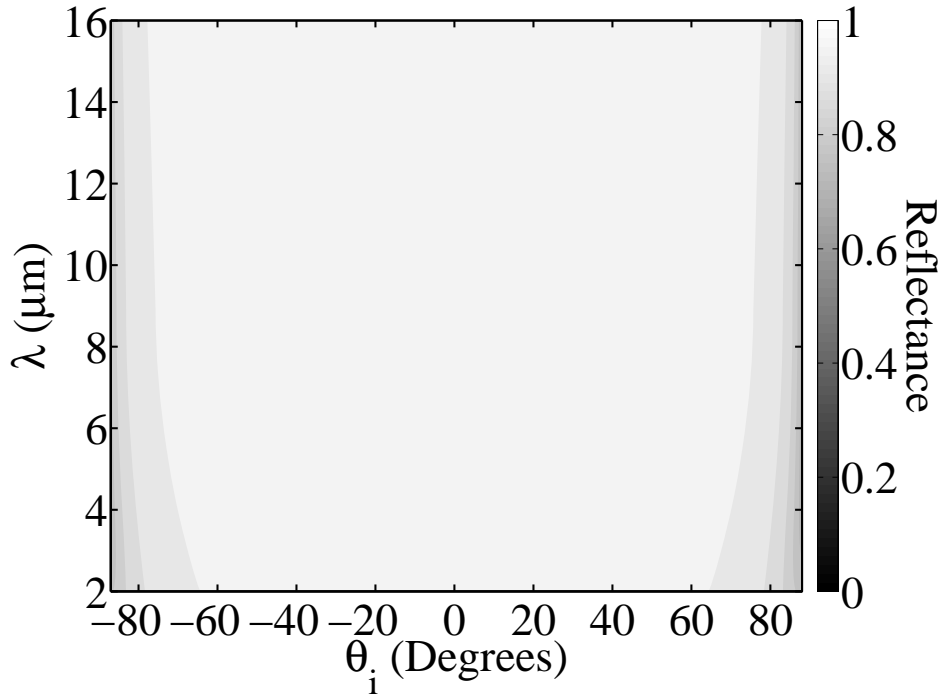
Figure 6.3: Aluminium directional and spectral reflectance derived from Fresnel's equation. Aluminium supports surfaces waves over the entire spectral range shown.

adjoining medium is assumed to be free-space, with only a real complex permittivity component, ϵ_0.

$$\delta_{prop} = \lambda_0 \frac{\epsilon_m^{''2}}{2\pi\epsilon_m^{''}} \left(\frac{\epsilon_m' + \epsilon_0}{\epsilon_m' \epsilon_0} \right)^{3/2} \tag{6.1}$$

The penetration of the field into the complex dielectric, δ_m, or skin depth, is approximated by

$$\delta_m = \frac{2\pi}{\lambda_0} \left| \frac{\epsilon_m' + \epsilon_0}{\epsilon_m'^2} \right|^{\frac{1}{2}} \tag{6.2}$$

Finally, the decay length of the field into free-space, δ_0, is similarly approximated [9].

$$\delta_0 = \frac{2\pi}{\lambda_0} \left| \frac{\epsilon_m' + \epsilon_0}{\epsilon_0^2} \right|^{\frac{1}{2}} \tag{6.3}$$

A perfect aluminium surface can support surface waves which propagate orders of magnitude farther than silicon carbide over the same spectral band. Similarly, the field

resides primarily outside the medium in aluminium, so the free-space decay distance is much larger than for silicon carbide. The differences are shown in Figure 6.4 (a) and (b). The immediate implication of the surface wave propagation distance is that the coherently coupled surface area need not be resonantly enhanced to generate very narrow angular features in aluminium in the mid- to far-infrared. A second implication is best considered in the context of the coupled resonance cavity structure.

(a)   (b)
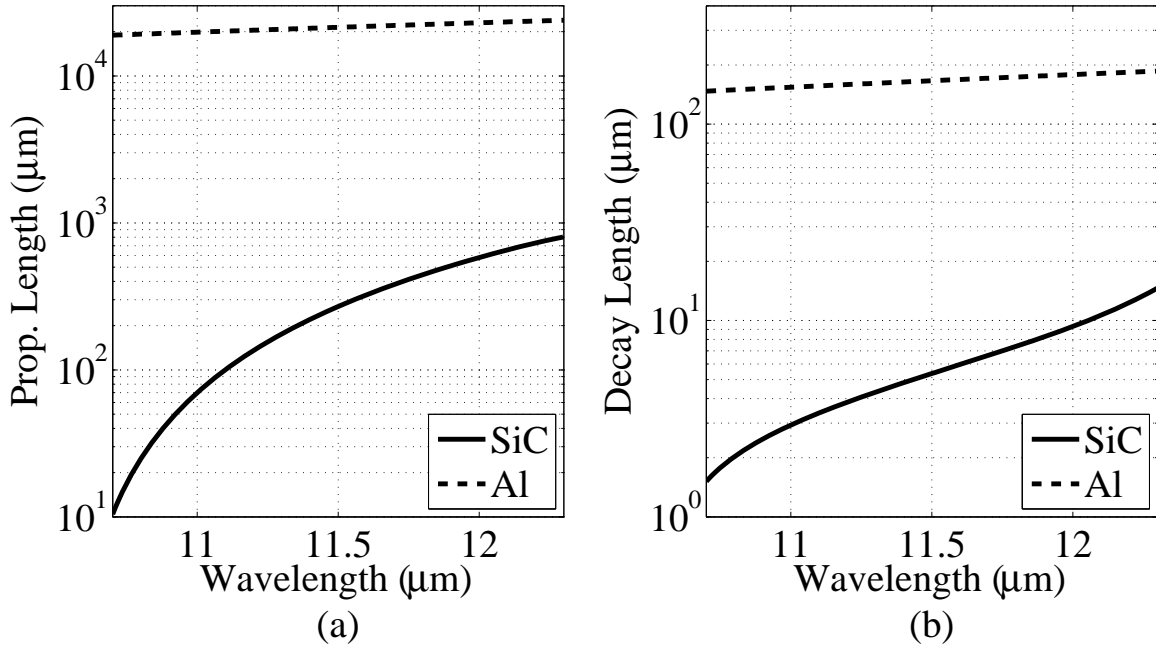
Figure 6.4: Surface wave decay distances of silicon carbide and aluminium (a) along the interface and (b) into free space, over the spectral region in which silicon carbide supports surface waves.

6.3 Ideal Coupled Resonance Cavities

Ideal CRCs are arrays of truncated complex dielectric waveguides, designed such that a Fabry-Perot-type field cancelation occurs at the guide apertures. This sets up a resonating field inside each cavity. The cavity spacing and widths are set such that surface waves

propagating along the inter-cavity ridges arrive at neighboring cavities with the appropriate phase to maintain cavity resonance [8]. The physical geometry is shown in Figure 6.5.
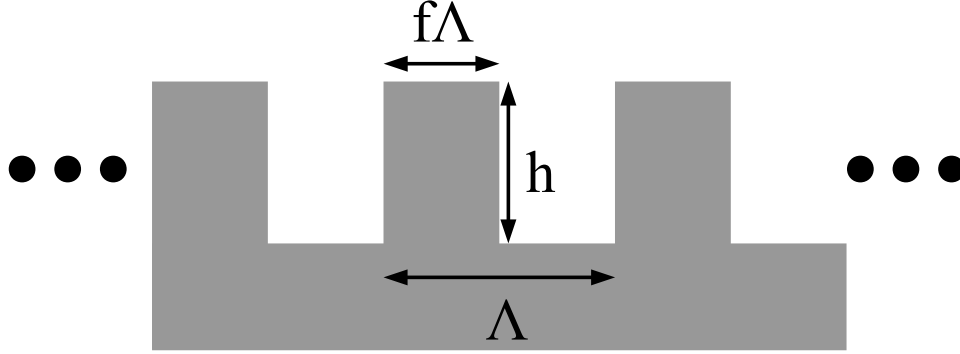
Figure 6.5: Coupled resonance cavity geometry. A fill factor, f, scales the structure's period, Λ, to define a cavity width. A constant cavity depth, h, further defines the ridges and grooves of the binary structure.

For the structure to resonate properly, the fields must couple both between cavities and across the cavity gaps [8]. Whereas it bears computation to determine whether or not a silicon carbide cavity can achieve coupling between cavity walls for a given geometry, aluminium provides substantial margin for any mid- to far-infrared wavelength. For proper cavity resonance, it is also necessary that the cavities not couple through the complex material. The skin depth, δ_m, may be computed from equation (6.2), and is a matter of nanometers for aluminium throughout the mid- to far-infrared. For silicon carbide, the skin depths are much deeper, and coupling can fail even for far-infrared wavelengths [8].

It has been noted, that coupled resonance cavity structures are very sensitive to the cavity dimensions for proper resonance [11]. This manifests itself in terms of the required cavity dimension to achieve resonance, and the tolerance in these critical dimensions. In Figure 6.6 (a), a response surface for a silicon carbide cavity is shown with the normally directed emissivity at $11.6\mu m$ as a function of both the gap width and cavity depth. Similarly, Figure 6.6 (b) shows the same response for an aluminium cavity. The most

forgiving behavior would be a symmetric circle of extremely high emissivity around the optimized values. This is not the case for either structure. From a fabrication standpoint however, the greater symmetry around the $f = 0.5$ point, at $5.8\mu m$, of the aluminium CRC allows for more process variation than the silicon carbide CRC. It should also be noted that silicon carbide requires a slightly lower than $f = 0.5$ fill factor to achieve optimal resonance [11]. The symmetry of the aluminium cavity response around the $f = 0.5$ fill factor is more amenable to microfabrication consistency.
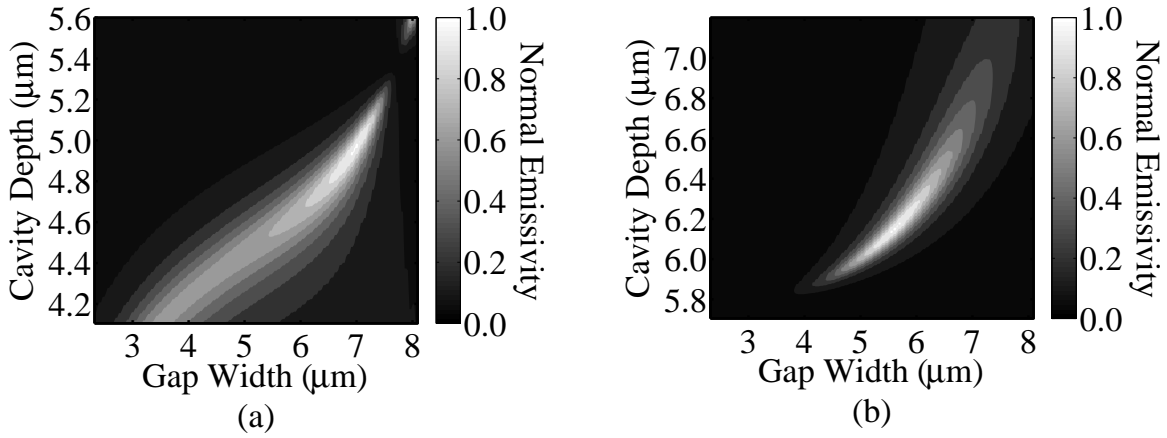
Figure 6.6: Response surface of two ideal cavities in (a) silicon carbide and (b) aluminium at $\lambda = 11.6\mu m$ and normal incidence. The unit cell period is $11.6\mu m$ so $5.8\mu m$ corresponds to cavity fill factory, f=0.50

This analysis suggest that the aluminium structure is also less sensitive to dimensional deviations, but another analytical method will show this more clearly. The resonant cavity configuration may be analyzed by considering each cavity as truncated Metal-Insulator-Metal (MIM) waveguide. So, the spectral propagation behavior of aluminium and silicon carbide MIM waveguides is computed, in terms of an effective complex index of refraction, following the development of Kong [100]. It should be noted that MIM waveguides do not exhibit the proper geometric modes of a PEC waveguide. When the guide walls are brought sufficiently close together that the decaying electric fields of surface waves on

opposite walls interact, as required for coherent coupling, a continuum of finite propagation distances is formed on a spectral basis [9].

The critical behavior of propagating waves at the guided wavelengths may be determined from the propagation constant in the axis of travel, which may be found by solving a transcendental equation simplified from the following set of equations. The free-space propagation constant, $k_0 = 2\pi/\lambda_0$, is defined in terms of the wavelength, λ_0, of interest. The complex relative permittivity is expressed in five regions. The minimal pair of metal surfaces is defined by their complex permittivity, ϵ_{rm}, and the central region by free-space, ϵ_{r0}. An upper cladding surface is defined with complex permittivity, ϵ_{rc}, and a lower substrate region with complex permittivity, ϵ_{rs}. A simplifying value, ρ_x, may then be used to form the transcendental equation for k_x, where the symmetry of the guided wave is defined as even by $m = 1$ or odd by $m = 2$.

$$\rho_x = \frac{\epsilon_{r0} \sqrt{k_0^2 (\epsilon_{r0} - \epsilon_{rm}) - k_x^2}}{\epsilon_{rm} k_x} \tag{6.4}$$

$$k_x = \frac{\lambda \left(2\tan^{-1}(\rho_x) + (m-1)\pi\right)}{2\pi} \tag{6.5}$$

The resulting k_x value is used to determine an effective complex permittivity.

$$\epsilon_{erf} = \epsilon_{r0} - \left(\frac{k_x}{k_0}\right) \tag{6.6}$$

The cladding and substrate regions, which may be free space, are similarly defined to find the y-directed propagation constant, k_y. Here, ρ_{cy} is a simplifying expression for the cladding and ρ_{sy} is a simplifying expression for the substrate.

$$\rho_{cy} = \frac{\sqrt{k_0^2 \left(\epsilon_{erf} - \epsilon_{rc}\right) - k_y^2}}{k_y} \tag{6.7}$$

$$\rho_{sy} = \frac{\sqrt{k_0^2 \left(\epsilon_{erf} - \epsilon_{rs}\right) - k_y^2}}{k_y} \tag{6.8}$$

In the resulting transcendental equation for k_y, an infinite number of modes, n, may be defined, although the lowest order mode is typically of interest for coupled resonance cavity design.

$$k_y = \frac{\left(\tan^{-1}\left(\rho_{cy}\right) + \tan^{-1}\left(\rho_{sy}\right) + (n-1)\pi\right)}{h} \tag{6.9}$$

The overall propagation constant, β, may then be defined

$$\beta = \sqrt{k_0^2 \epsilon_{erf} - k_x^2 - k_y^2} \tag{6.10}$$

and two metrics developed from it. The effective index of refraction, N_{eff}, provides insight into the effects of the propagation constants,

$$N_{eff} = \text{Re}\left[\frac{\beta}{k_0}\right] \tag{6.11}$$

while the wave propagation distance, identifies the $1/e$ point for the traveling wave.

$$L_{spp} = \frac{1}{2\text{Im}\left[\beta\right]} \tag{6.12}$$

A comparison of the effective indexes of refraction for one-dimensional, free-space cladding and substrate, MIM guides composed of silicon carbide and aluminium is shown in Figure 6.7. The aluminium shows a smaller variation in propagation constant, as manifested through the effective index of refraction. Thus, the effects of cavity profile deviations, such as taper, will be smaller for an aluminium structure than a silicon carbide structure at the same wavelength.

6.4   Novel Coupled Resonance Cavity Design

A novel implementation of the coupled resonant cavity construct, constrained by the fabrication process and exploiting the advantages highlighted previously, is developed. Two degrees of abstraction are considered in the development. First, the effect of an idealized oxide layer on the design is considered. Modeling considerations such as convergence
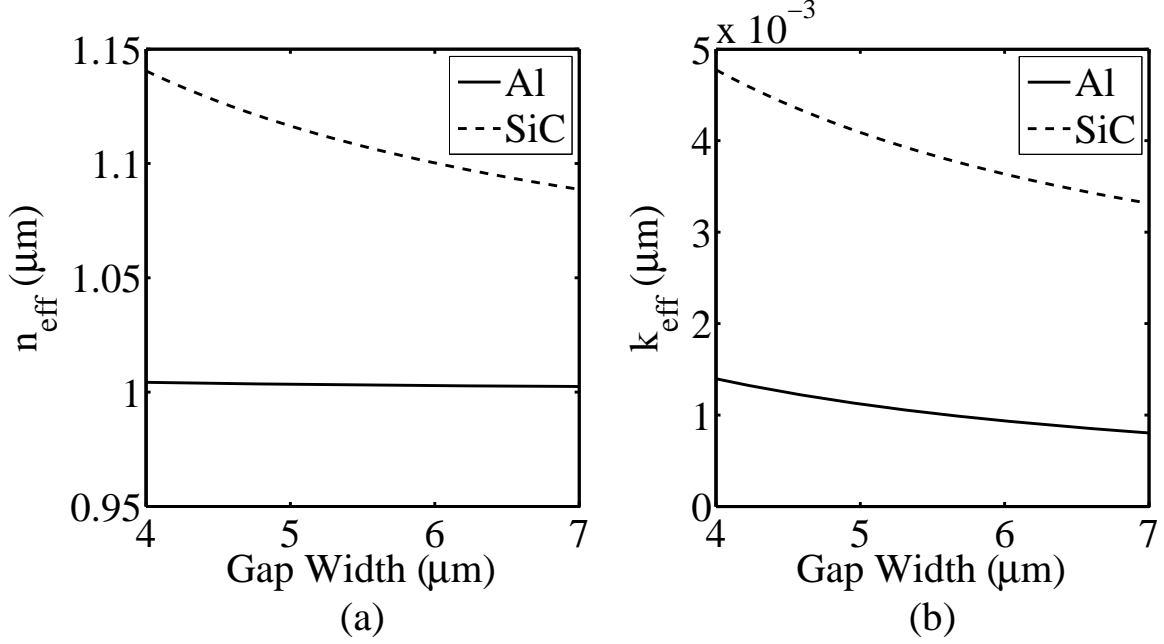
Figure 6.7: The real component (a) and the imaginary component (b) of the effective index of refraction for an infinite plasmonically coupled waveguide is shown for aluminium and silicon carbide at $\lambda = 11.6\mu m$, as a function of the waveguide gap width. The effective index values of Aluminium shows less sensitivity gap width variation than silicon carbide.

and depth optimization are shown. Then, the impact of increasing the deposited metal thickness, per the Blech model, is considered.

First, a design wavelength must be selected for the low temperature coupled resonance cavity structure. The wavelength, λ_{peak}, at which a blackbody radiance reaches its maximum for a given temperature is readily found by Wein's Law. In the form shown in equation (6.13), the wavelength is computed in μm, for an emitter temperature, T, in K. At $80°C$, the maximum safe operating temperature of the proposed substrate, equation (6.13) gives a peak wavelength of $8.2\mu m$.

$$\lambda_{peak} = \frac{2.989 * 10^3}{T} \tag{6.13}$$

However, since the thermal emission of the sample is measured with minimal background cooling, and includes a room-temperature reflected component, the peak radiance wavelength is not the ideal design wavelength. The spectral radiance curves for a

blackbody at $23°C$ and $80°C$ are shown in Figure 6.8 (a), and the difference between the two spectral radiance curves is shown in Figure 6.8 (b). Examining Figure 6.8 (b) shows that the greatest signal-to-background margin is found at wavelengths shorter than $8\mu m$. With this constraint, and consideration given for the availability of suitable photomasks and the available lithography equipment's performance, the design wavelength for the CRC was selected to be 150 *cycles/mm* or a period of $6.666\mu m$.
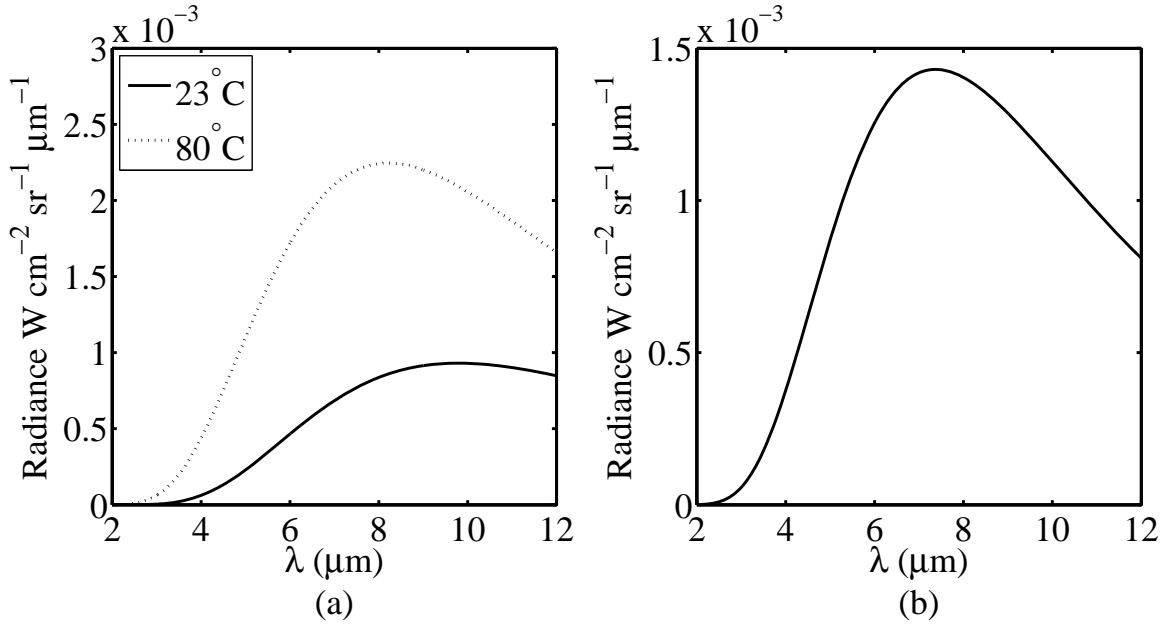
Figure 6.8: (a) The spectral radiance of a blackbody at $23°C$ and $80°C$ are shown. (b) The difference between the spectral radiance values over a wavelength region of interest are shown. The maximum difference occurs below $8\mu m$.

Using the RCWA algorithm developed from [33], a convergence case was run for the limiting condition. In this case of a binary grating, it is known that the number of Fourier terms required for convergence increases with depth, so an $f = 0.5$ fill factor binary grating with a period, $\Lambda = 6.666\mu m$, and a depth of 2Λ was modeled to test convergence. In the test case in Figure 6.9 (a), the zero-order reflected diffraction efficiency value at an angle of incidence, $\theta_i = 30$ degrees, against the number of Fourier expansion terms, N, retained

is shown. A refined search is shown in Figure 6.9 (b), and final design data was computed with N=200 for fourth-decimal-place stability.
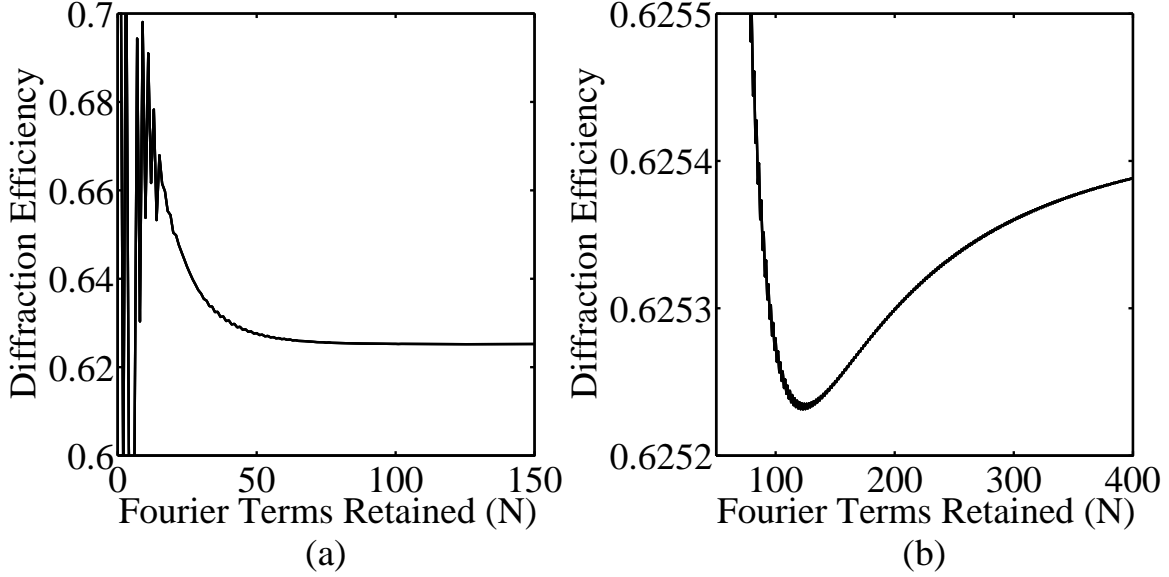
Figure 6.9: Convergence test case basic (a) and zoomed view (b), for a $\lambda_0 = \Lambda = 6.666\mu m$, $h = 2\Lambda$, 50/50 fill factor grating at an incidence angle, $\theta_i = 30$ degrees, for a varying number of retained Fourier terms, N. Fourth decimal place stability is achieved within 400 Fourier terms.

The cavity depth was then optimized for an $f = 0.5$ fill factor aluminium cavity, with a 10nm native oxide coating. Figure 6.10 (a) shows a broad sweep of cavity depth values versus total reflectance at normal while (b) shows a refined view. The optimal depth, h, is found to be 3.540μm by this method.

Due to the nature of metal surfaces when excited in the TM orientation and finite spatial coherence length of the CRC structure, the total reflectance as a function of incident angle, θ_i, must be considered as shown in Figure 6.11 (a) at the designed wavelength. The near-grazing reflectance minima are clearly visible, and the total reflectance has dropped below 0.90 by 45 degrees. To better demonstrate the expected emission behavior, the total reflectance is converted to normalized emittance by Kirchhoff's Law and the Law
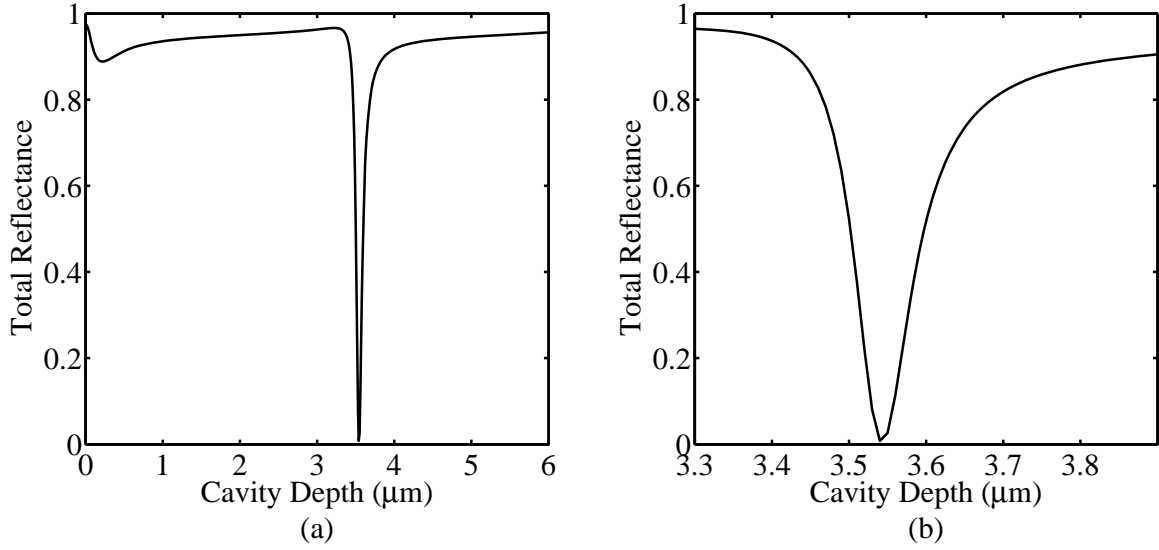
Figure 6.10: (a) Computed total reflectance for a coupled resonance cavity structure by cavity depth, and (b) a zoomed view of the first reflectance null.

of Conservation of Energy. A narrower angle of incidence range is shown in Figure 6.11 (b).
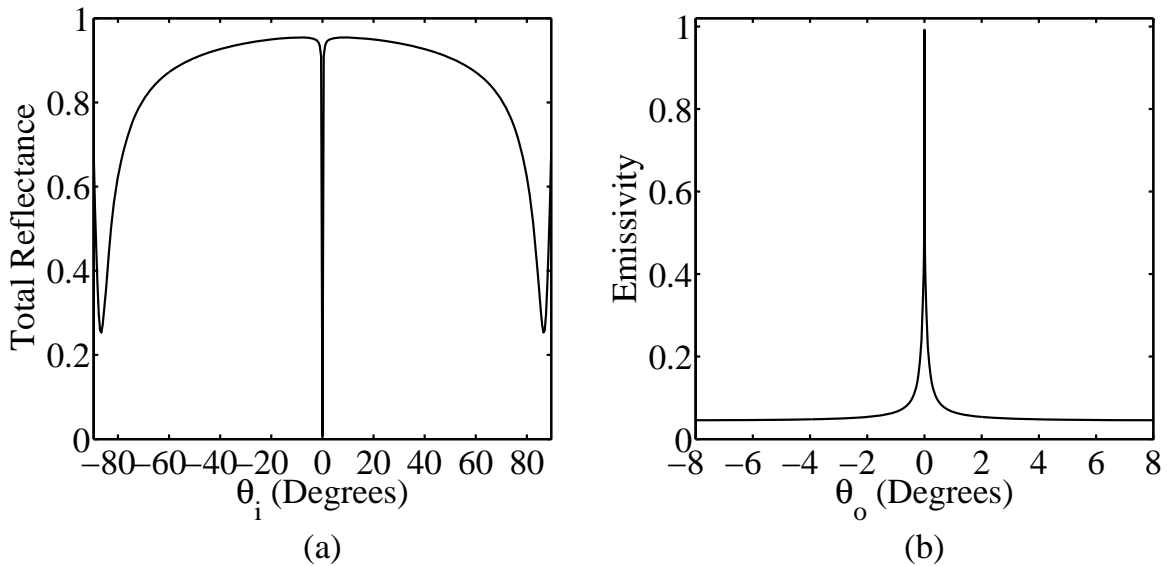
Figure 6.11: (a) The directional total reflectance for an oxide-coated coupled-resonant-cavity-structure is shown. (b) A zoomed view of the near normal reflectance null is shown, converted to directional emissivity.

The angular and spectral behavior of the CRC structure, with a native oxide layer, is shown over relatively narrow wavelength and angle-of-incidence ranges in Figure 6.12. This shows the angularly narrow features near normal, and represents the ideal behavior for a perfectly rectangular structure. If the sputtered metal layer is thicker than a skin depth over the entire surface and sufficiently thin that it does not significantly alter the cavity profile, this provides an excellent performance model.
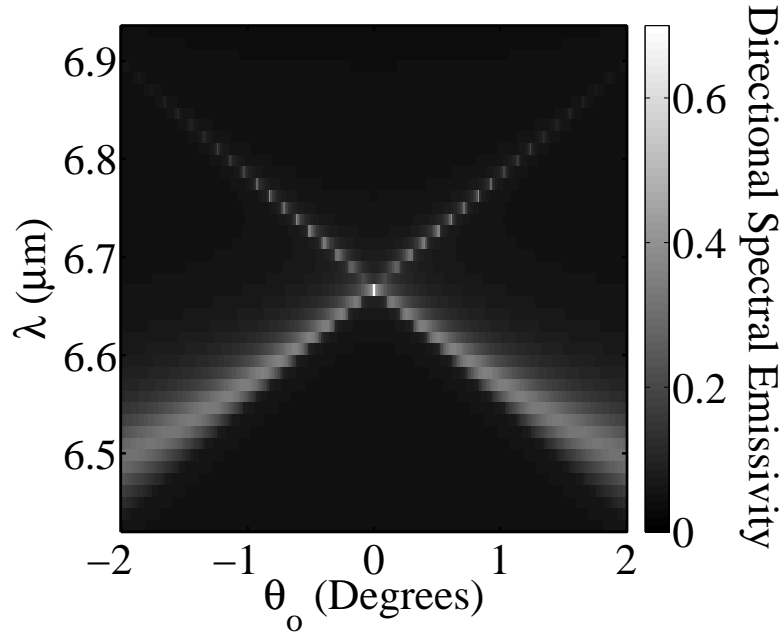
Figure 6.12: The directional and spectral emissivity of a coupled-resonant-cavity-structure is shown. At the design wavelength of 6.666μm, a highly directionally and spectrally selective emissivity peak, which approaches unity, is observed. The emissivities' of the longer wavelength branches rapidly attenuate, while the emissivities' of the shorter wavelength branches fall off and broaden, but do not attenuate completely. The image is scaled to a peak emissivity of 0.7 for contrast.

If however, the metal thickness is increased sufficiently to significantly effect the film durability and thermal conductivity, the profile of the cavity begins to change shape. Although a case was made for the relative resiliency of highly conductive cavities to profile deviations, eventually the cavity will take on a milk-bottle profile, inhibiting resonance.

It is observed however, that a trade space remains. A close consideration of the Blech model reveals that a cavity's metal deposition rate on the upper and lower surfaces are unequal. The metal thickness increases faster on the upper, unmasked, surface than the lower partially masked surface. This suggests that a cavity resonance may be achieved for an under-depth cavity, onto which additional metal is applied. An example is shown for a $f = 0.5$ fill factor CRC at $\Lambda = \lambda_0 = 6.666\mu m$ and a cavity base depth of $3.4\mu m$ in Figure 6.13, where (a) is the deposited metal thickness and (b) is the total reflectance at normal as a function of the deposited metal thickness.
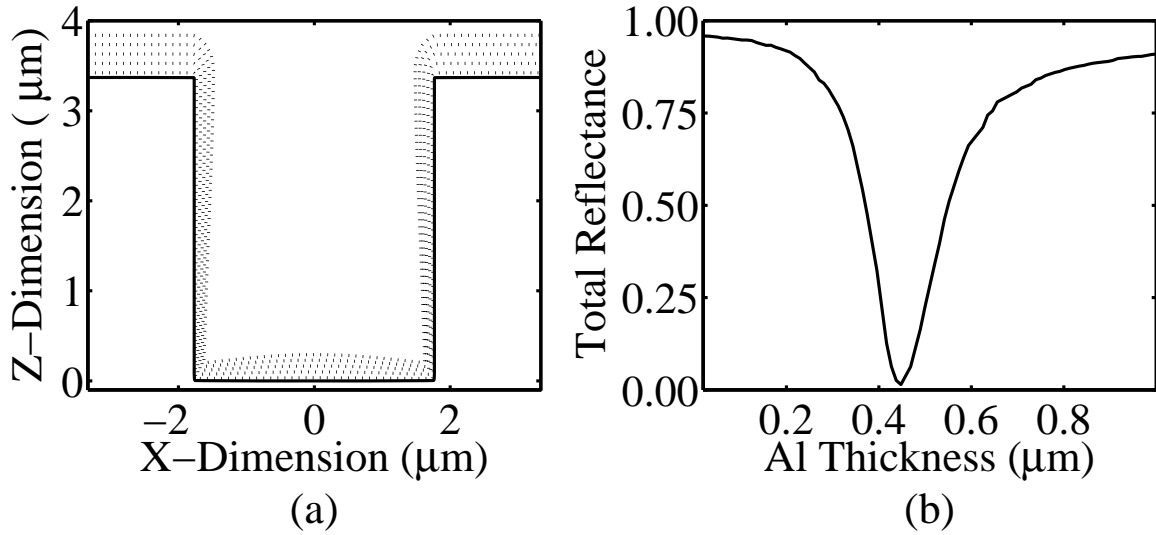
Figure 6.13: (a) The filling effect of Blech-modeled metal deposition on a rectangular cavity, and (b) the impact on the total reflectance as a function of sputtered metal depth on the total reflectance at normal incidence.

To assess whether the rounding of the cavity opening corners should be expected to cause dephasing between cavities, an angular sweep of the same profile at the design wavelength was computed. The angular emittance at the design wavelength is shown in Figure 6.14.
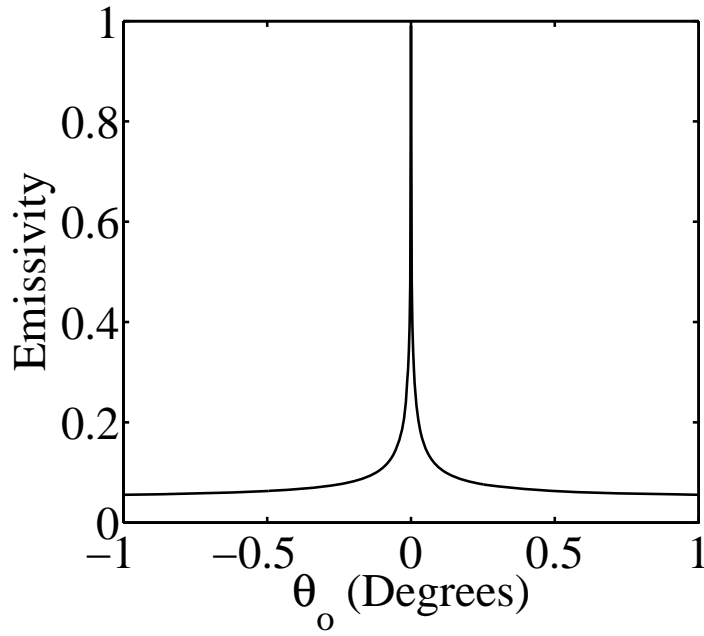
Figure 6.14: The directional emissivity of Blech-model-profiled cavity, at the predicted optimal metal deposition thickness and design wavelength, exhibits a narrow angular response and near unity peak emissivity value. Near unity emissivity is achieved despite the cavity profile deformation introduced by the extended deposited metal thickness.

The cavity profile, at its optimal metal deposition depth, is shown in Figure 6.15 (a). The off-normal angular and spectral emissivity, as a function of angle and wavelength for this profile, is shown in Figure 6.15 (b). Based on the presented modeling, a CRC structure with substantial deposited metal depth may be designed within the constraints of a fabrication process which is already well established for mass production [25].
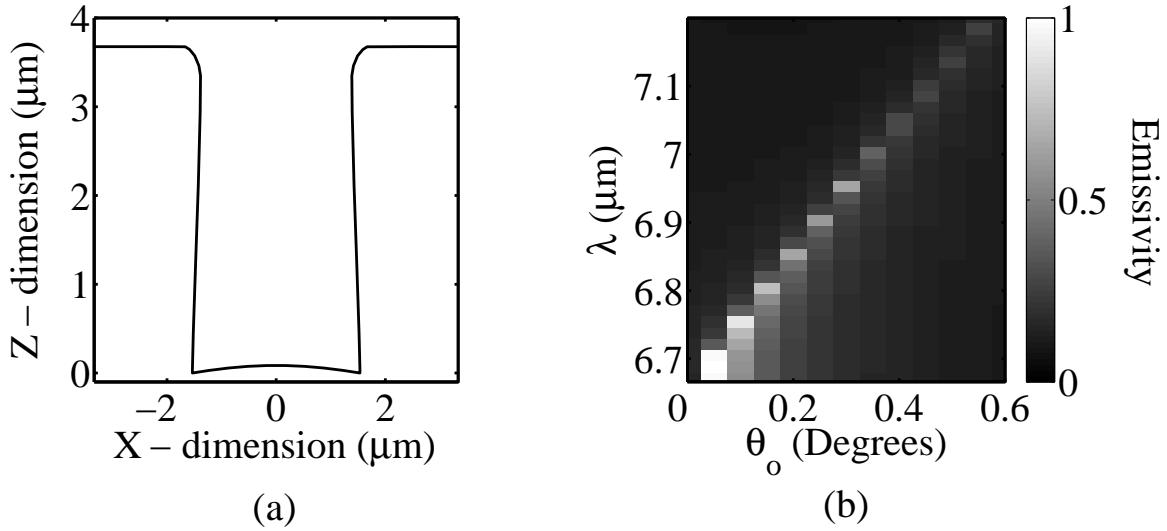
Figure 6.15: (a) An ideal sputtered profile and (b) the normalized directional and spectral emissivity, predicted by RCWA for this profile. The directional and spectral selectivity at, and near, the design wavelength is slightly decreased from a rectangular cavity case.

6.5 Dual-Cavity-Width Design

Predicated on the model of the first design, a prior-art concept executed in a novel fashion with substantial fabrication constraints, a second fully novel design is proposed. The very narrow angular responses, which are desirable in some cases, can be too narrow for other applications. When slightly directional absorptance or emittance is desired, planar multilayered structures are the traditional geometry. In particular, antireflection coatings and Salisbury screens are well developed [61]. However, designs in this wavelength regime generally suffer from a limited choice of materials and process. Low-loss far-infrared

materials are virtually non-existent, and due to the low photon energies and skin depths, the required layer thickness may be extremely thin. This not only complicates planar multilayered designs, it makes it impossible for some material combinations. This suggests that surface patterning may still have a role to play in this design regime. Towards the objective of generating a directional, but relatively wide angular response, from a patterned surface, an alternative patterning form based on array antenna concepts is proposed.

The first difficulty with binary periodic structure designs is that if directional emission is desired, then the emission angle must follow the zero-to-first-order grating transition line, which bounds the light-to-dark regions of Figure 6.16. The line runs from $4\mu m$ at 0 degrees to $8\mu m$ at 90 degrees for the $4\mu m$ period structure shown. This remains true for under- and over-depth CRC structures and shallow gratings.
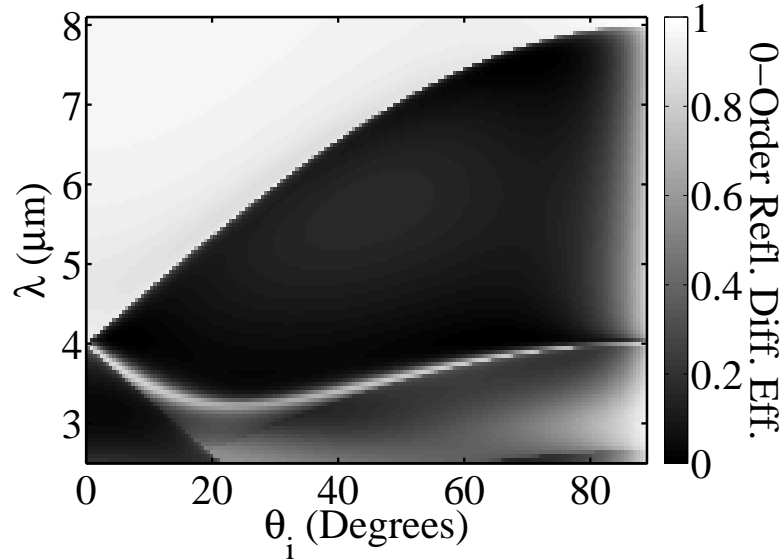
Figure 6.16: The 0-order, or specular reflected diffraction efficiency for a $4\mu m$ shallow grating is shown as a function of incidence angle, θ_i, and wavelength, λ. The sharp light-to-dark transition highlights the order-transition-line, on which the Wood's anomaly may be observed for a shallow grating.

It is desirable to fill the 0-order region above the transition line, but this cannot be done with a uniform unit cell. A second scattering mechanism is required. Borrowing from

antenna theory, the simplest way to achieve this is to introduce some sort of deviation in the periodic profile, such that two distinct emitter phases are present. When these combine in the far field, the directed lobe width can be controlled even for large numbers of coherent emitters.

Alternating either the depths or the widths of near rectangular cavities of the same period will produce two distinct phases at the cavity apertures. While the technology to fabricate a two-depth structure exists, the fabrication costs and time were beyond the scope of this research. So, a width-variation scheme was selected. A schematic of a unit cell is shown in Figure 6.17.
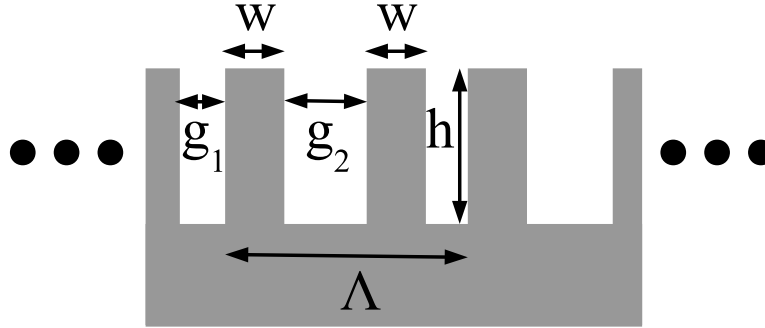
Figure 6.17: Dual-cavity-width design geometry. All of the features in a unit cell of period, Λ, share a common depth, h, and inter-cavity ridge width, w. Two unique cavity gap-widths, g_1 and g_2, are repeated in each unit cell.

Based on a degenerate pair of cavity widths, g_1 and g_2, and a constant cavity ridge width, w, the minimum feature size which could be reliably designed was $2\mu m$. This requires that the minimal overall period, Λ, be greater than $8\mu m$. The photomask critical dimensions tolerance was, at worst, $200nm$ of deviation, per edge. So, to ensure a reliable difference between cavities which could not be subsumed by fabrication errors, the minimum cavity width ratio was 1.2. For simplicity and to allow for fabrication errors, a secondary cavity width ratio of 1.5 was selected as the design point so that the required cavity depth and wavelength of interest were retained as independent variables for analysis.

As previously established in the Chapter 5, the longer unit-cell periods affect convergence, as well as the depth. Since metal deposition coverage is only reliable down to 1:1 aspect ratios, the maximum depth considered was $2\mu m$. This was taken as the convergence test case at $10.4\mu m$ after some coarse empirical runs to search out an appropriate convergence checkpoint. The convergence of the total reflectance is shown in Figure 6.18 (a) as a function of the number of Fourier terms retained, N, and a zoomed version is shown in Figure 6.18 (b).
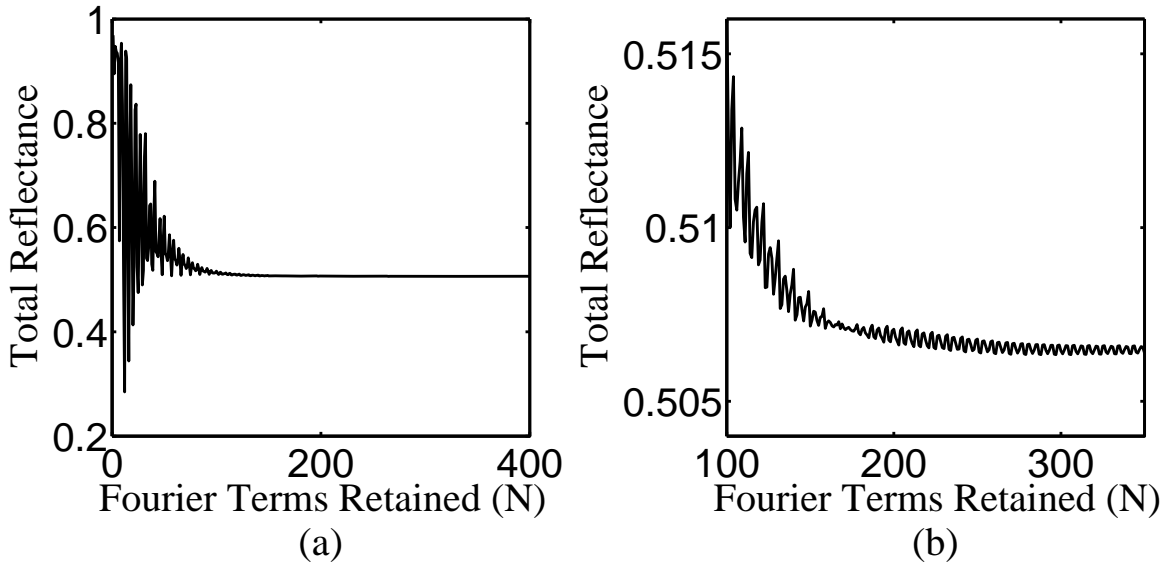
Figure 6.18: (a) A complete convergence test case for a dual-cavity-width structure is shown for a $\lambda_0 = 10.4\mu m$, $\Lambda = 9\mu m$, and $h = 2\Lambda$ structure at normal incidence for varying numbers of retained Fourier terms, N. (b) A refined view of the results is also shown.

There are two methods of generating a phase difference between cavities for consideration; the differences in the cavity widths may be altered for a fixed depth, or the depth may be altered for a fixed set of cavity widths. First, the sensitivity of the dual-cavity-width design is shown with a fixed primary cavity and ridge width of $2\mu m$, fixed cavity depth of $1\mu m$, and a varying secondary cavity width, in Figure 6.19. This test causes the unit cell period to vary between configurations. Second, a fixed set of cavity widths

is selected, in this case, a $2\mu m$ ridge, $2\mu m$ cavity, $2\mu m$ ridge, and $3\mu m$ cavity. The cavity depth is then varied in Figure 6.20.
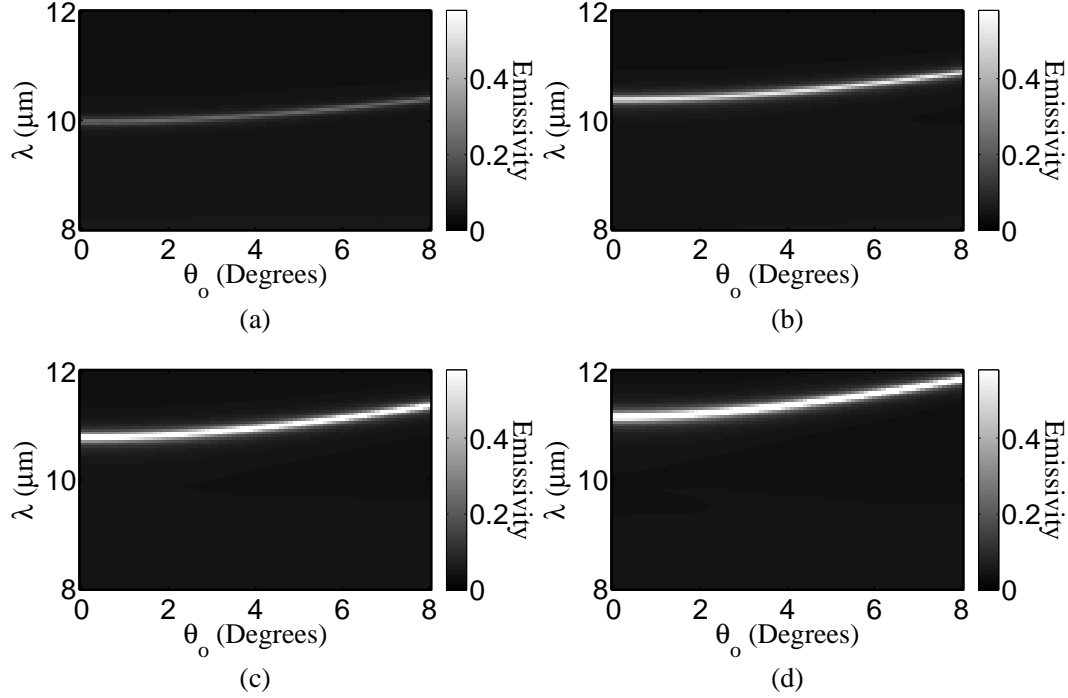

Figure 6.19: Directional and spectral emissivity variation due to cavity width variations. The primary cavity width and ridge width are fixed at $2\mu m$ and the depth is fixed at $1\mu m$ for all iterations. The secondary cavity widths displayed are (a) $2.5\mu m$, (b) $3.0\mu m$ (c), $3.5\mu m$, and (d) $4.0\mu m$. The emissivity feature moves to longer wavelengths with increasing secondary cavity width.

In all cases considered, the emission line separates from the grating order transition. The angular and spectral position of the peak response is clearly a function of both depth and cavity width. This provides a substantial trade space to meet fabrication requirements which may limit minimum feature sizes or cavity depths. A converged final angular and spectral emittance profile for the design parameters is shown in Figure 6.21.
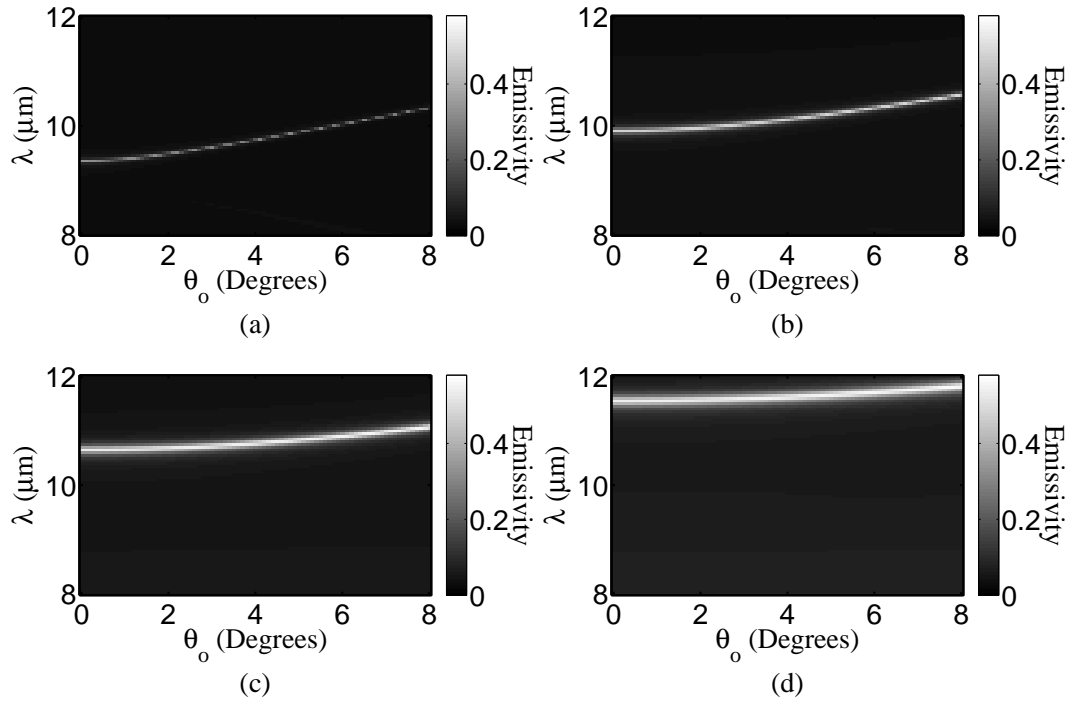
Figure 6.20: Directional and spectral emissivity variation due to cavity depth variations. The cavity depth is varied over (a) 0.5μm, (b) 0.8μm, (c) 1.1μm, and (d) 1.4μm for a structure with ridge widths of 2μm, a primary gap width of 2μm, and a secondary gap width of 3μm. The emissivity feature moves to longer wavelengths with increasing cavity depth.
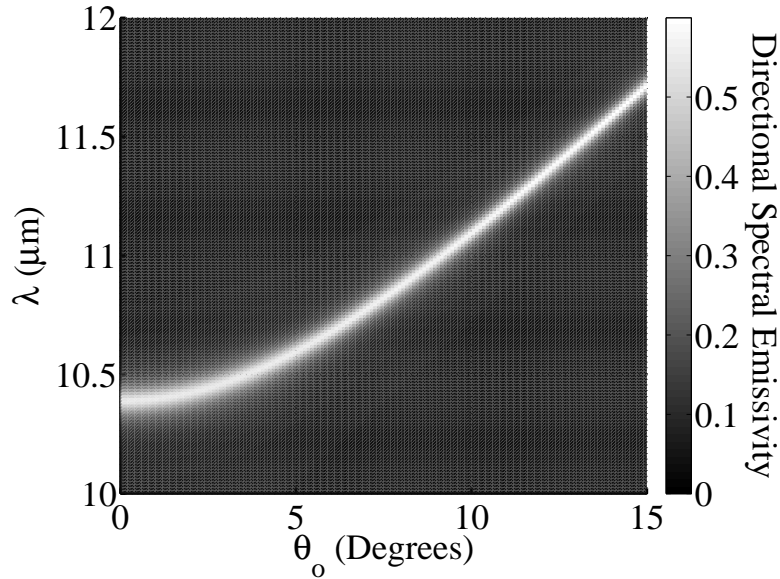

Figure 6.21: Dual-cavity-width concept idealized directional and spectral emissivity profile for a 9μm total period binary profile composed of a 2μm ridge, 2μm cavity, 2μm ridge, and 3μm cavity, with a feature depth of 1μm.

6.6   Conclusion

The surface wave propagation properties of metals in the mid- to far-infrared were shown to be superior to lossy dielectrics, in terms of the supported design trade-space. For aluminium in particular, surface waves are supported over the entire wavelength regime of interest. Similarly, it can be concluded from the free-space decay length of the field normal to a surface that the cross-cavity coupling requirement for coherent thermal emission can be met for virtually any set of cavity dimensions. For a CRC structure, working in metals is predicted to offer enhanced dimensional tolerances. It definitely offers an advantageous dimensional bias, allowing the cavity gap to be narrowed below half the structure's period, while retaining near unity directional emissivity at normal.

Based on the extended trade space, a pair of designs was developed for fabrication and investigation. First, a CRC structure was designed at a wavelength optimized for low temperature applications. The impact of sputter deposition on the design's performance was also predicted. Second, a dual-cavity-width design was proposed to generate directional emission over a broader angular distribution then for the CRCs. This design exploits the long surface wave propagation lengths predicted for the wavelengths of interest to generate directional emission without resonant enhancement.

VII.   Fabrication Methodology and Results

7.1   Introduction

The focus of this work is the exploitation of electromagnetic properties of metals in the infrared to produce directionally and spectrally selective thermal emission to fit a constrained, high throughput, fabrication process. The fabrication process required tuning and refinement at each step, but no scholarly contribution to the science of microfabrication was intended or achieved.   Therefore, an overview of the process and critical step parameters is presented, followed by an examination of the results for each structure fabricated.

7.2   Fabrication process flow

The proposed fabrication method is based on the mass production process of compact discs. The full process, including stamp production, is shown in Figure 7.1 (1)-(6). In general, a silicon stamp is fabricated in steps (1)-(3) by common lithographic and etching processes. A plastic substrate is then hot embossed in step (4) to produce a patterned plastic sample in step (5). Finally, metal is deposited on the sample to produce the final patterned surface shown in step (6). The details of each fabrication step are expounded upon in the following subsections. Fabrication processing was conducted in both Air Force Institute of Technology (AFIT) and Air Force Research Laboratory (AFRL) facilities. Cleanrooms at AFIT and the AFRL, Sensors Directorate, Aerospace Components and Sub-systems Technology Division (AFRL/RYD) were employed and some metal deposition work was conducted in the AFRL, Materials and Manufacturing Directorate (AFRL/RX) deposition laboratory.
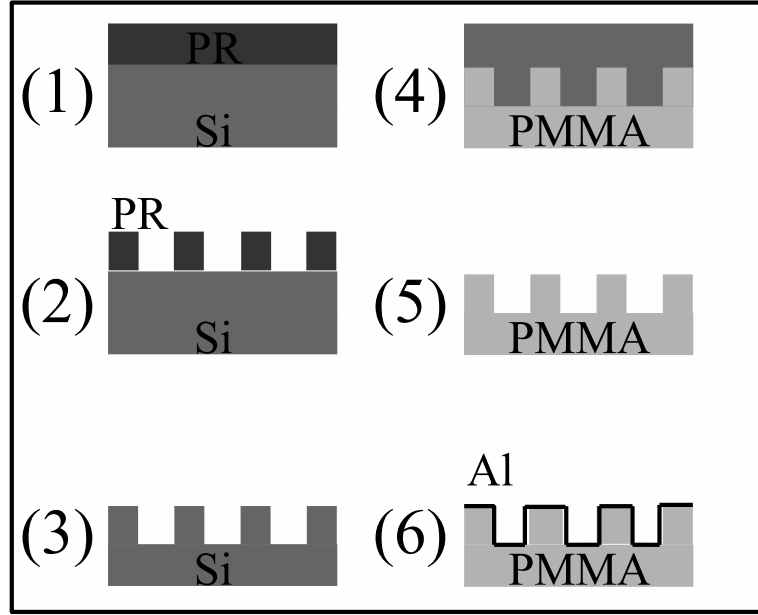
Figure 7.1: Six discrete fabrication process steps are shown. (1) Photoresist is spun onto a silicon substrate. (2) The photoresist is exposed through a photomask and the resist developed. (3) The photoresist masked wafer is then etched, and the residual resist removed. (4) The patterned wafer is used as a stamp to hot emboss a PMMA substrate. (5) The substrate and stamp are separated to reveal a patterned PMMA substrate, which is then plasma ashed to remove residual roughness and prepare the surface for metal deposition. (6) Aluminium is DC magnetron sputtered onto the patterned PMMA substrate.

7.2.1 Photoresist Processing.

The following sample preparation and lithography process was followed for samples produced in the AFIT cleanroom. Some CRC structures were also fabricated in the AFRL/RYD cleanroom, following a similar process specific to the equipment available. To initially clean the cleaved $25mm \times 25mm$ silicon substrates, the samples were spun at $500rpm$ under acetone for 30 seconds to throw off any silicon shards from cleaving. Then, the samples were ultrasonic-cleaned for 10 minutes in acetone and returned to the spinner for a defilming cleaning. A buffered oxide etch was not used, and the passivation oxide layer was not found to play a significant role in the structure development.

The samples were spun at $500rpm$ and cleaned with acetone, methanol, and isopropyl alcohol for 60 seconds each, then nitrogen dried. The cleaned samples were then dehydration baked on a $115°C$ hotplate for 5 minutes to completely remove any remaining solvents. The samples were then cooled on an aluminium heat sink block for 5 minutes to return them to ambient temperature for further processing.

The shallow gratings and dual-cavity-width structure were fabricated using Shipley 1805 photoresist, while the CRC structures were fabricated with Shipley 1818. In both cases, the photoresist was applied and spun at 4000 rpm for 30 seconds, in line with the manufacturer's recommendations. The samples were allowed to stand on the spinner for 2 minutes to release the initial solvents, then the edge bead and any resist which lapped over the sample edges was manually removed. The squared corners of the samples tended to exacerbate the edge bead problem. Once the photoresist was applied, the sample was soft baked on a $115°C$ hotplate for 60 seconds, then cooled on an aluminium heat sink block for 5 minutes to return to ambient temperature for further processing.

The photoresist was exposed through a photomask on a Karl Suss Microtek MJB-3 mask aligner. A reference sample edge was aligned with the mask features to aid measurement alignments, and the resist was exposed in contact mode. A series of exposure experiments was conducted for each photomask. The 150 $cycles/mm$ mask and dual-cavity-width mask performed best in line with the logged exposure tables in the AFIT cleanroom. These samples were exposed for 4 seconds when Shipley 1805 was used and 8 seconds when Shipley 1818 was used. The 250 $cycles/mm$ mask was observed to have slightly under-deposited chrome and the exposure had to be reduced to 2 seconds to achieve patterning results.

The exposed photoresist was developed in a solution of 5:1 deionized water to Microposit 351 developer for 30 seconds with gentle agitation. The development was reduced to 20 seconds for the 250 $cycle/mm$ mask. The sample was then spun at $500rpm$

and flushed with deionized water for 60 seconds to stop the development process. After nitrogen drying the sample and evaluating the initial development, the sample was post-exposure baked for 120 seconds at $110°C$. The samples were then descummed in a plasma asher at $200W$ in $500 sccm$ O_2 at $2.5 - 3 Torr$ for 120 seconds.

7.2.2 Etching.

Two different etching processes were used to the patterned silicon samples. The first process, a Reactive Ion Etching (RIE) process was used only for the shallow grating features, produced from the 250 $cycles/mm$ mask. A second Deep Reactive Ion Etching (DRIE) process was used for both the coupled resonant cavity and dual-cavity-width samples.

To produce shallow features, CF_4 (tetraflouromethane)-based reactive ion etch was conducted in a Trion Phantom III RIE system. The duration of the etch was based on an established 40 $nm/minute$ etch rate for this process. Because the features of the etched pattern produce a high resist edge exposure ratio, a solvent-based removal process was effective. The residual photoresist was removed by ultrasonic cleaning in acetone. Two 5-minute cycles, with acetone replacement, were found to remove the resist fully and avoid redeposition.

CF_4-based etches cannot produce sufficiently vertical sidewalls, down to the required CRC etch depths. So, a DRIE etch, utilizing a tuned Bosch process, was required. In the three-step Bosch process employed, a short isotropic SF_6 (sulfur hexaflouride) etch is followed by an inert passivation layer deposition of C_4F_8 (octoflouralbutane), then a milder etch which preferentially removes the passivation layer from the base of the unmasked region. The alternating produces the characteristic DRIE "mousebites." It was necessary to refine the etch process for the feature size of interest, $2 - 3\mu m$, and this calibration was conducted by AFRL/RYD personnel.

The refined etch process used was conducted at $25mTorr$ and $30sccm$ of Argon at $1500W$ Inductively Coupled Plasma (ICP) power. The primary etch step was conducted at $650V$ of Radio Frequency (RF) bias for 1.25 seconds at $100sccm$ of SF_6. The passivation deposition occurred at $10V$ RF bias and $150sccm$ of C_4F_8 flow. The secondary etch was conducted for 0.7 seconds at $10V$ RF bias and $100sccm$ of SF_6. The total etch depth was $200nm$ per full cycle, with testing running down to $44\mu m$. Figure 7.2 shows a calibration test image, in which the central period was focused ion-beam milled out to evaluate the depth.
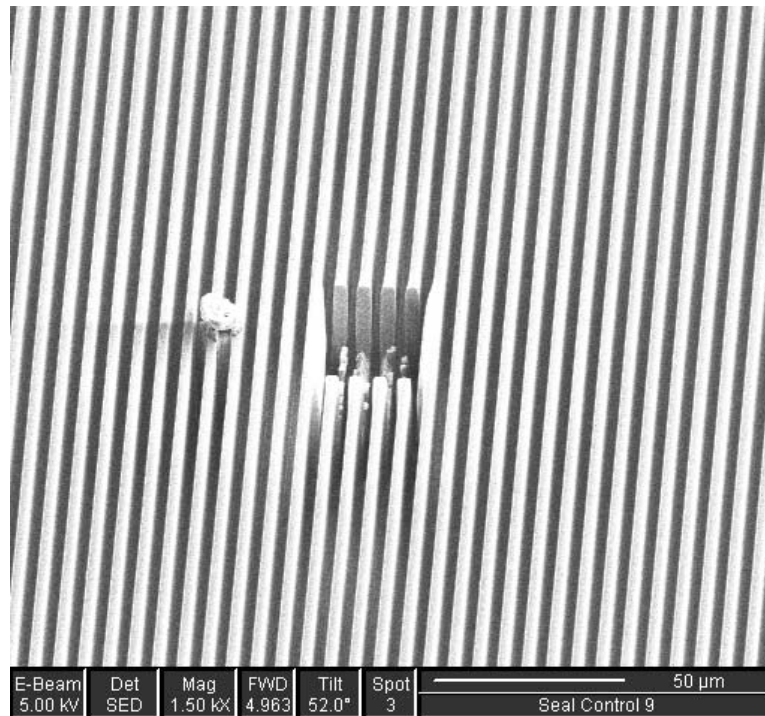
Figure 7.2: The 150 $cycle/mm$ mask was used to pattern photoresist, which was then etched to a depth of approximately $40\mu m$. A small test area was then focused ion beam milled out to allow the etched profile to be examined.

7.2.3   Imprinting.

The imprinting, or hot-embossing, process is the key high-throughput step of the process. Up until this point, the fabrication process has been directed at producing a

stamp, which can be used to produce many copies in a thermal-polymer. The imprinting process requires substrate preparation, imprinting, stamp separation, and final processing. In compact disc manufacturing, the substrate is typically a polycarbonate such as Lexan. Commercially, the imprinting is often carried out via an injection-compression molding technique, or high-pressure injection molding. This process generally works best with high melt-temperatures, rapid injection into the mold, low mold pressure and short mold times. Specialized, lower-viscosity polycarbonates are often used in the commercial process [25]. However, due to equipment limitations, the lower working temperatures of PMMA were preferable in the hot-embossing equipment available.

Substrates were prepared from a commercially produced 2.5mm thick cast acrylic PMMA sheet. Substrates were score cut, then specifically trimmed to match the dimensions of each fabricated stamp and the edges deburred. The substrates were then spin-cleaned to remove particulates accumulated in the cutting process, then ultrasonic-cleaned in de-ionized water for 10 minutes and nitrogen dried to remove any residual oils or adhesives. Prior to imprinting and between steps, the stamp was also cleaned with acetone and nitrogen dried to remove any residual PMMA in the grooves.

With a substrate and stamp prepared, the process illustrated in Figure 7.1 (4) was executed. The substrate and stamp were aligned and loaded between the two silicone membranes of a Nanonex NX-2600 nanoimprinting tool. The membranes were evacuated to remove air pockets, then contact was asserted between the stamp and substrate at 827Kpa for 120 seconds, while the substrate temperature was brought up to 100$°C$, just below the PMMA glass temperature of 105$°C$. After the set points for the pre-imprint were reached, the temperature and pressure were increased to 150$°C$ and 1379Kpa and maintained for 120 seconds to imprint the substrate. The substrate and stamp were allowed to cool to 25$°C$ together, under pressure, before the chamber pressure was released. Then, the imprinted substrates and stamp were removed from the chamber, and manually released.

Imprinting into a monolithic substrate with a system intended for nano-imprint lithography of thin films of plastics on silicon substrates posed a series of problems. The first imprinting problem was caused by the thick substrates, which caused a larger-than-normal membrane gap at the sample edges. This increased the gas volume trapped by the membranes and required additional pump down time to ensure complete evacuation. Whether the failure was due to insufficient pump-down duration or simply mechanical, as it occasionally was, the result was readily observable as large areas of failure to imprint. Samples which failed were readily identified, because they showed no spectral scattering effects at visible wavelengths. Some failed samples exhibited a clearly visible demarkation between the imprinted and unimprinted regions caused by gas bubbles trapped between the stamp and substrate.

The second effect limited the imprint temperature, which must be high enough to produce a sufficient volume of viscous PMMA to flow into the mold. Overheating caused outgassing within the substrate and visible bubbling, as well as a breakdown in the substrate rigidity at $160°C$. Because the substrates were slightly larger than the stamp size to avoid putting pressure on unsupported portions of the stamp, some of the viscous material would flow around the stamp edges under pressure. This complicated stamp release, but was mechanically removable. The final constraint limiting the stamping process arose from the thermal gradient established within the thick substrate. During cooling, the substrate would bow away from the stamp. Maintaining pressure during cooling kept contact until the PMMA was below the glass temperature. Releasing the pressure before full cooling occurred caused the stamp to separate while the PMMA was still viscous. This pulled microstrands of plastic into the imprinted grooves as shown in Figure 7.3.

7.2.4   Metalized Plastic Method.

Aluminum was deposited on the patterned PMMA substrates, as illustrated in Figure 7.1 (6) by DC magnetron sputtering at AFRL/RX. Prior to deposition, individual
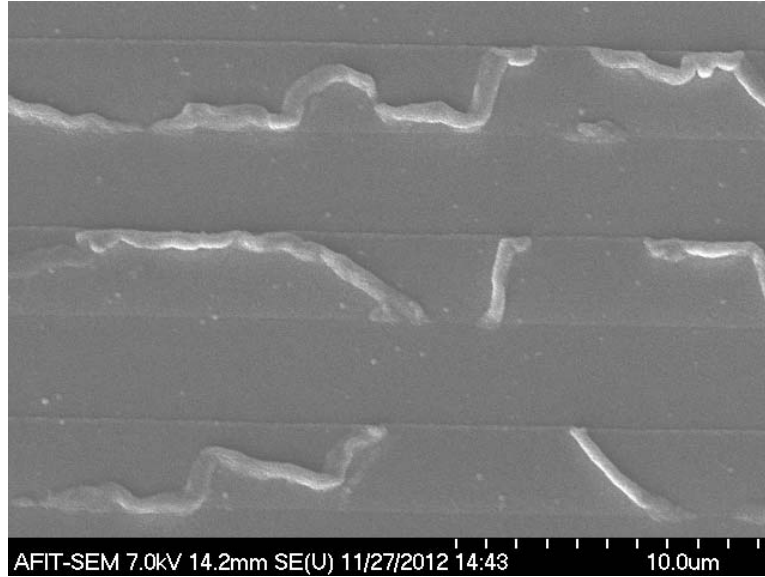
Figure 7.3: Metalized PMMA strings, pulled out of the cavity sidewalls during stamp separation, are visible in the grooves of an early CRC sample. The stringing was due to insufficient cooling time, and corrected in later samples.

substrates were loaded into a high vacuum chamber which was subsequently evacuated to a base pressure below $1.0e^{-6}$ $Torr$ ($1.33e^{-4}Pa$). The chamber was backfilled with 10 $mTorr$($1.33Pa$) of ultra-high purity argon gas (99.9995%) to facilitate the sputtering process. Argon-aluminum plasma was generated using an Advanced Energy MDX-500 magnetron power supply at 100W in conjunction with an unbalanced 2-inch MeiVac MAK magnetron sputtering source. The source material consisted of a 2-inch diameter aluminum target (99.99% purity, K.J. Lesker). The distance between the surface of the aluminum sputtering target and the PMMA substrate was set at 9cm. Substrates were placed, individually, upon a sample stage rotating at 8.5rpm. Sample rotation was utilized in order to minimize the inherent anisotropy associated with the sputtering process. Polyimide tape was used to create a mask on the as-deposited aluminum. Monitoring of deposition time, as well as measurement of the thickness steps via stylus profilometry (KLA-Tencor), yielded a sputter rate of 44 nm/min.

7.3 Shallow Grating Fabrication

A pair of shallow gratings was fabricated, towards two different objectives. The first was a calibration grating, fabricated at an appropriate pitch to transfer between all of the instruments. In this case, aluminium was directly applied to the grating etched in silicon. For the second shallow grating, the fabrication flow was completed to produce a metalized plastic example, to evaluate the overall process quality.

In both cases, the reduced exposure duration lithography process was followed, using the 250 $cycles/mm$ photomask shown in Figure 7.4. This pitch corresponds to a $4\mu m$ grating period and $2\mu m$ features. A shallow grating of this period and $f = 0.5$ fill factor generated a grating order transition line, varying with angle from $4\mu m$ to $8\mu m$ with an absorption response above $6\mu m$ absorption line lying at angles above 30 degrees. A distinctive angularly and spectrally varying absorption line was predicted for depths from $100 - 300nm$.
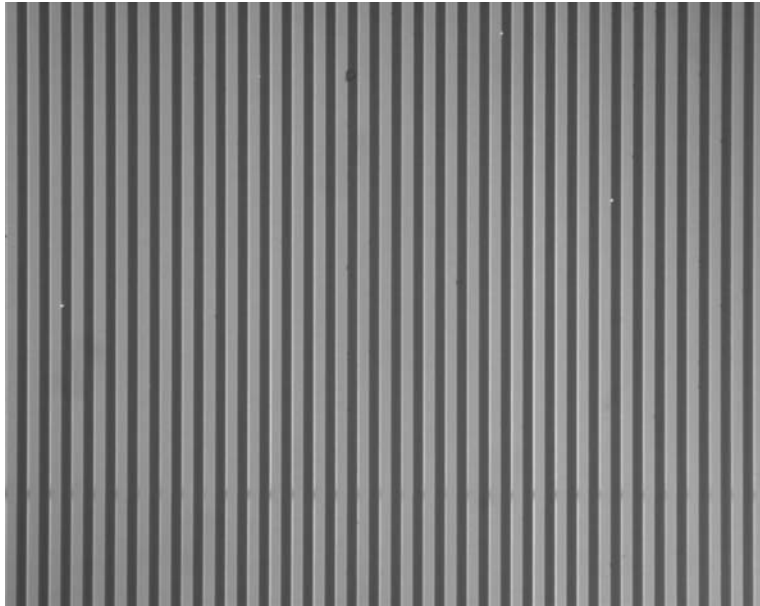
Figure 7.4: A visible micrograph of the 250 $cycles/mm$ or $4\mu m$ period photomask used to produce shallow gratings is shown.

The samples were etched for 6 minutes using the CF_4 RIE processing to producing an etch depth of 250nm, as measured across a masked sample edge. Hence, the depth is approximately 1/8th of the feature width, and sidewall anisotropy can be effectively ignored in modeling. Aluminium was then directly deposited on one sample, shown in the visible microscope image in Figure 7.5. A Scanning Electron Microscope (SEM) image of the final metalized plastic shallow grating is shown in Figure 7.6.
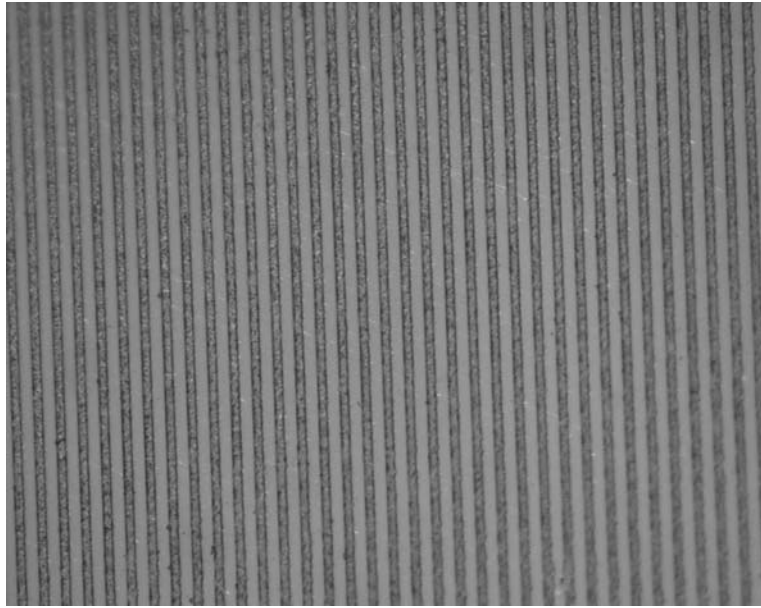

Figure 7.5: A visible micrograph of the aluminium-on-silicon shallow test grating is shown. The roughening of the bottom of the trench, from the etch process, was not completely smoothed by the aluminium deposition. This roughness provides the contrast in the white light image.

7.4   Coupled Resonance Cavity Fabrication

The additional depth of the coupled resonant cavity structure, compared to the shallow gratings, compounded the fabrication challenges. Figure 7.7 shows a micrograph of the photomask used to produce the coupled resonance cavity structures. The features are wider than those of the shallow grating, at 3.333μm wide, but the target depth of 3.54μm
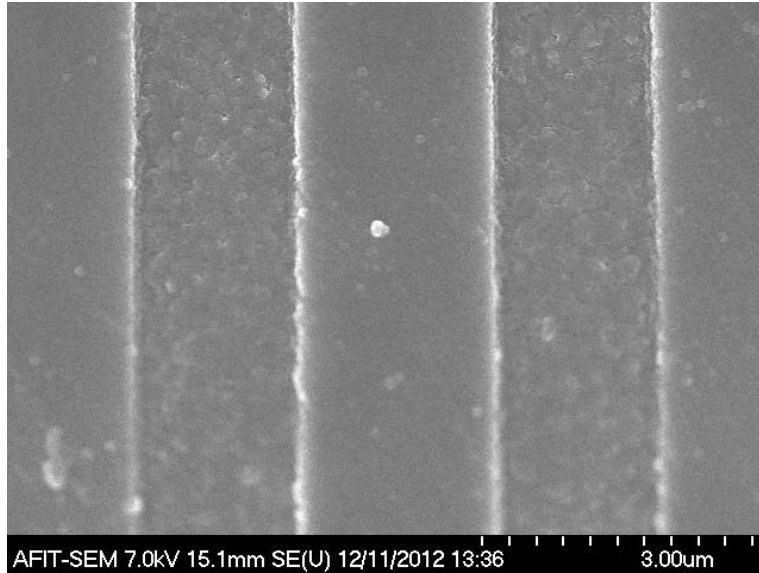
Figure 7.6: An SEM image of the aluminium-on-PMMA shallow grating is shown. The roughening, and resulting structure in the deposited aluminium, is larger than that shown in the micrograph in Figure 7.5 of the aluminium-on-silicon shallow grating.

required the use of Shipley 1818 photoresist, deposited at $1.8\mu m$ thickness when produced in the AFIT cleanroom, or Shipley 1813 at $1.3\mu m$ thickness when produced on AFRL/RYD equipment, to provide sufficient photoresist to mask the silicon.

A top-down view of the fabricated stamp is shown in Figure 7.8. The periodicity and critical dimensions were clearly well transferred. The depth achieved by the etch process was measured by cleaving the sample across the grating lines and vertically mounting it in the AFIT cleanroom SEM. An etch depth of $3.5\mu m$ is shown in Figure 7.9. This is a compromise depth, ensuring that the fabricated stamp is under-depth, based on examining the individual etch cycle development, shown in Figure 7.10. At $200nm$ per cycle, one more cycle would have produced an over-depth stamp, ensuring that the designed normal emission would not be observed for a shallow metal deposition.
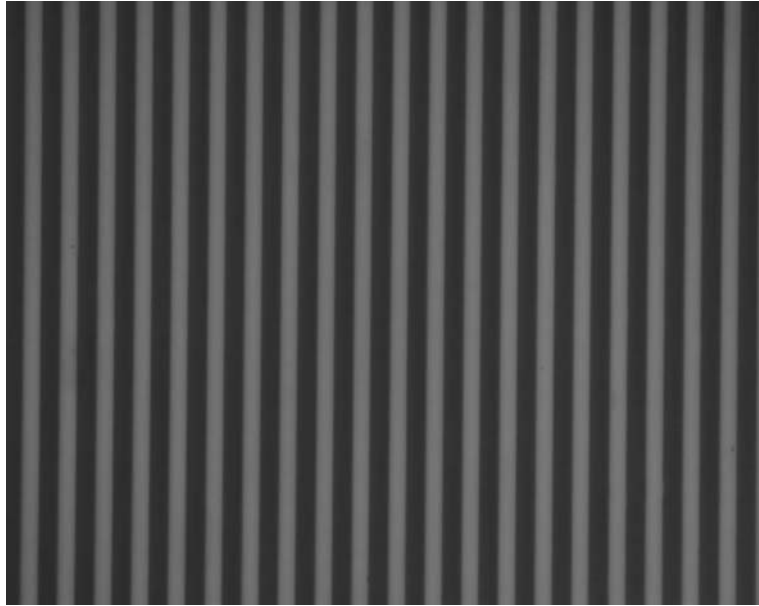
Figure 7.7: Micrograph of the 150 *cycle/mm* photomask. The periodicity and feature-width consistency was excellent, but the mask exhibited a fairly high defect rate. This appeared to be due to poor cleanliness in its intermediate process steps.
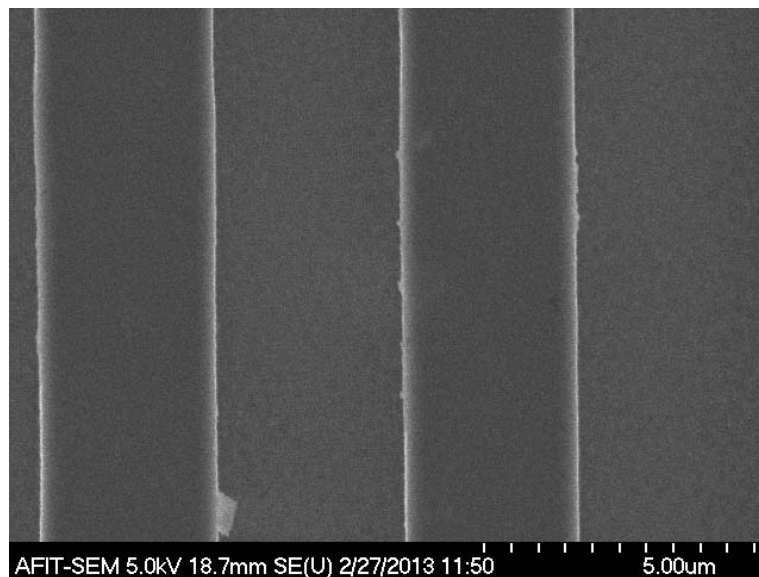

Figure 7.8: An SEM image of the silicon CRC stamp is shown, viewed from top-down. The stamp was produced from 150 *cycle/mm* photomask in Figure 7.7.
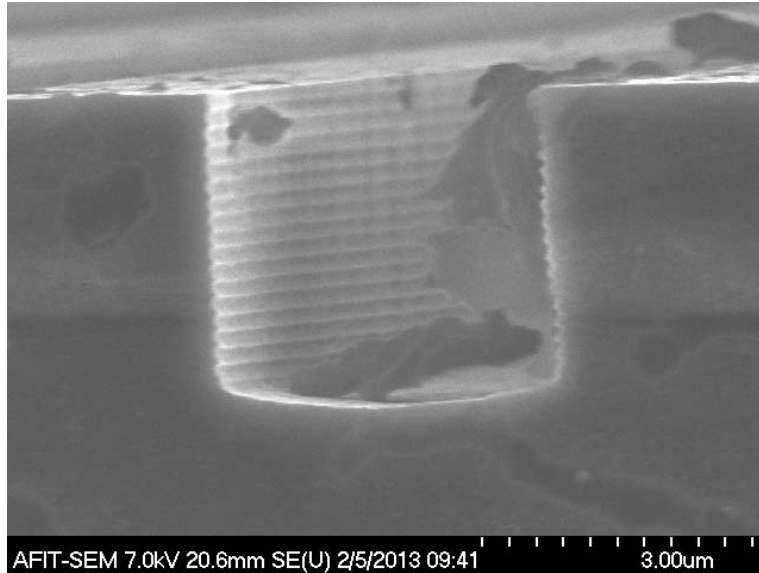
Figure 7.9: SEM image of the silicon CRC stamp. This sample was cleaved, and viewed edge-on for depth and profile evaluation.
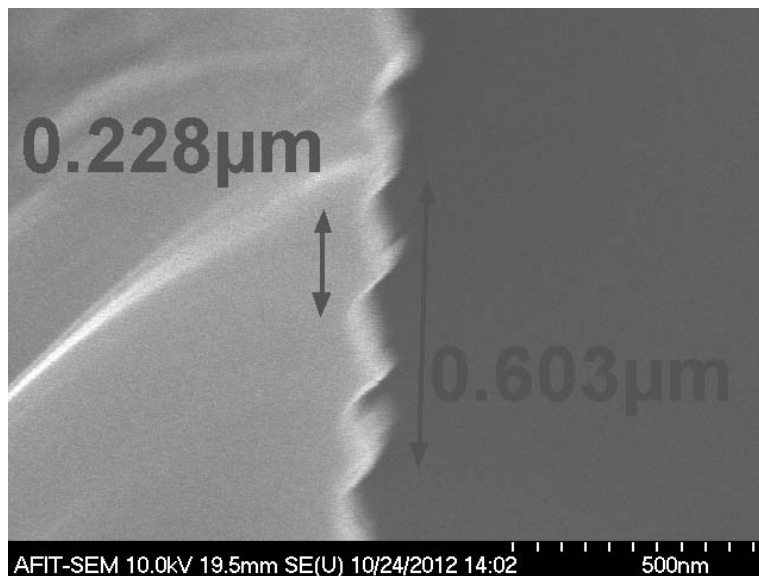
Figure 7.10: An SEM image of a silicon CRC stamp, highlighting the mousebite dimensions, is shown from edge-on.

The CRC imprinting suffered from the previously identified failure modes, and substantial mold release difficulties. The initial mold release was readily observed to sheer

off the tips of the mousebites during separation, which made release difficult. Subsequent imprints from the same stamp released more easily. The substantial mold penetration into the substrate also seemed to increase the pressure on the stamp due to substrate bowing and limited stamp life. Nonetheless, a sufficient number of imprints was produced for metal deposition, an example of which is shown in Figure 7.11. An initial set of deposition values ranging from $200 - 400nm$ thickness was produced, then a refined set from $350 - 500nm$ was fabricated based on initial measurement results.
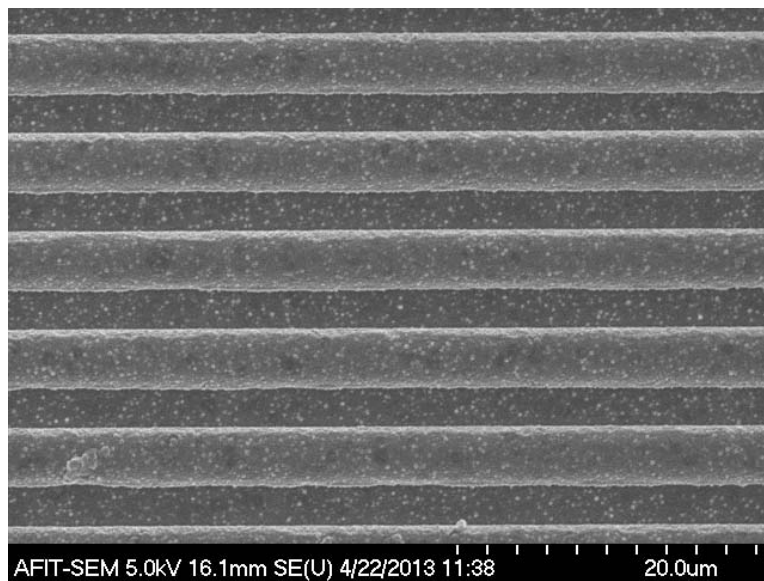
Figure 7.11: An SEM image of a CRC structure in PMMA, sputtered with $500nm$ of aluminium, is shown from top-down.

7.5 Dual-Cavity-Width Fabrication

The final structure to be fabricated was the dual-cavity-width design. In this case, it was possible to directly implement lessons learned from the CRC fabrication process. The photomask shows greater critical dimension variations than the shallow grating and CRC structure masks, although its overall quality was higher, exhibiting fewer defects. The variations evident in Figure 7.12 are within the photomask company's stated specifications.
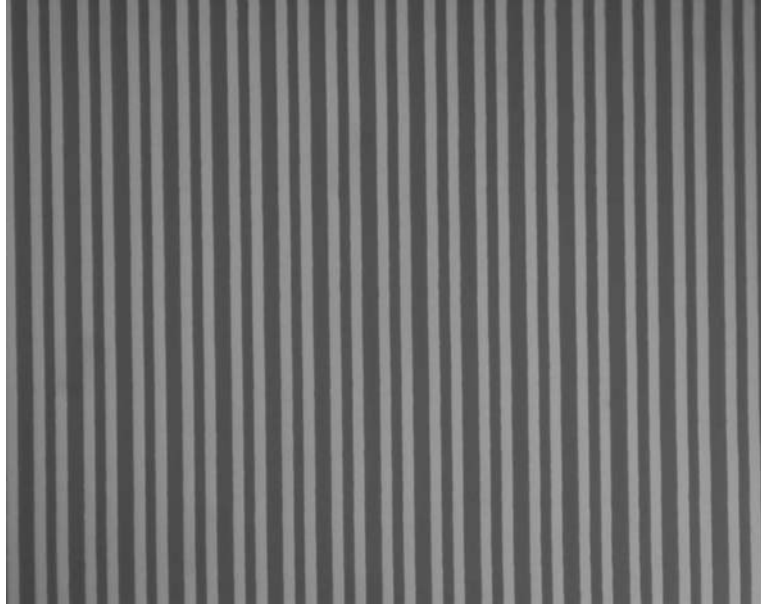
Figure 7.12: A Micrograph of the dual-cavity-width photomask is shown. The critical dimension variation is noticeably larger than the interferometrically produced constant dimension masks, but the mask is of over-all higher quality.

Although the target depth of $1\mu m$ is within CF_4 RIE chemistry limits, the DRIE process was used for its better anisotropy and speed. The shallower target depth allowed the thinner Shipley 1805 photoresist to be employed, producing the best pattern transfer possible with the MJB-3 mask aligner. A top-down view of the resulting stamp is shown in Figure 7.13, annotated with dimensions. Figure 7.14 shows the stamp depth to be $686nm$, while Figures 7.15 and 7.16 show the critical feature widths and unit cell period of a cleaved sample.

Imprinting was more consistent than the CRC imprinting, owing primarily to the lesser required imprint depth, and only a single series of structure was fabricated. Finally, Figure 7.17 shows the result of sputtering $100nm$ of aluminium onto the dual-cavity-width stamped PMMA substrates.
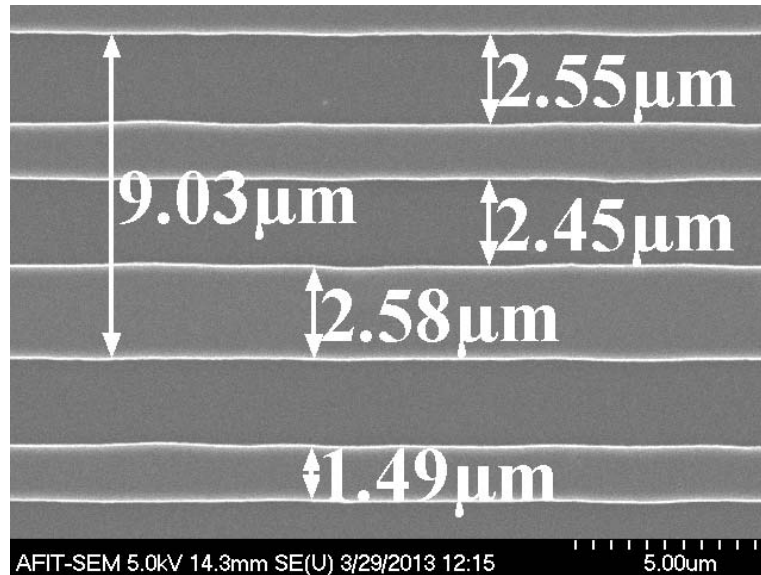
Figure 7.13: An annotated SEM image of the dual-cavity-width silicon stamp is shown from top-down.
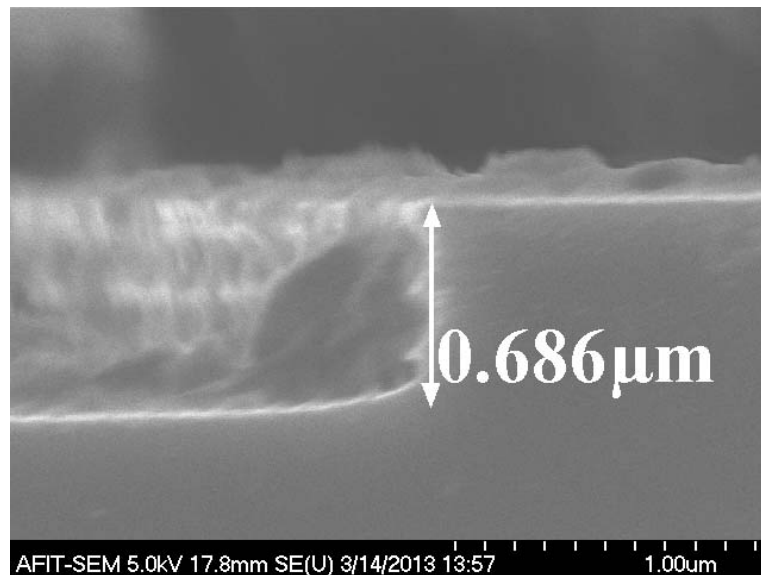

Figure 7.14: An annotated SEM image of a cleaved dual-cavity-width silicon stamp is shown from edge-on.
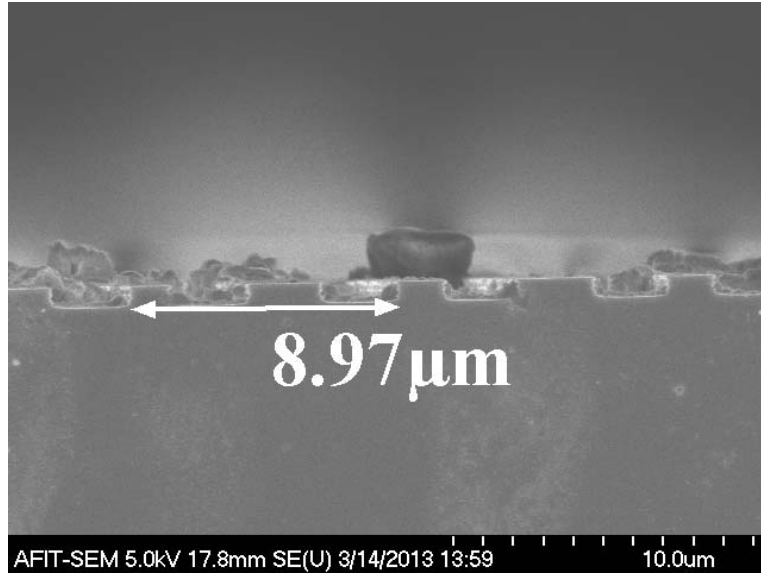
Figure 7.15: An annotated SEM image of a cleaved dual-cavity-width silicon stamp is shown from edge-on. This image shows the measured feature periodicity of 8.97μm.
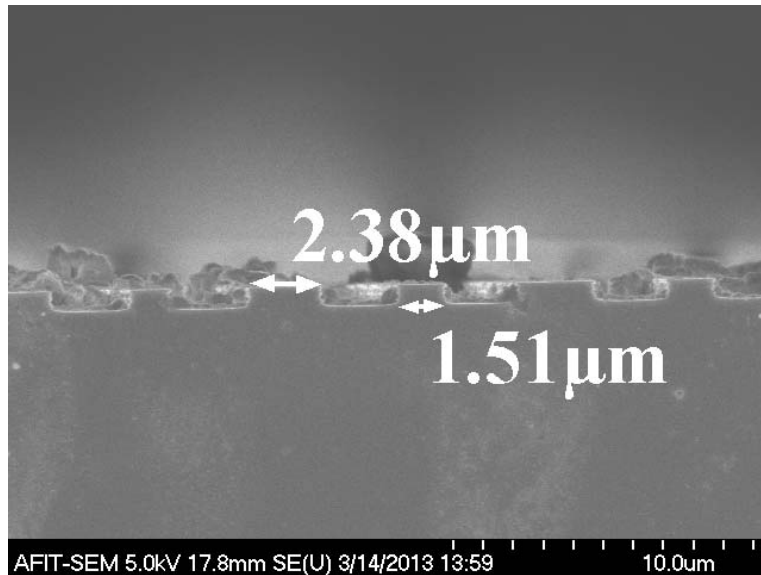

Figure 7.16: An annotated SEM image of a cleaved dual-cavity-width silicon stamp is shown from edge-on. This image shows the as-build feature widths of 2.38μm and 1.51μm. The second ridge was of similar width.
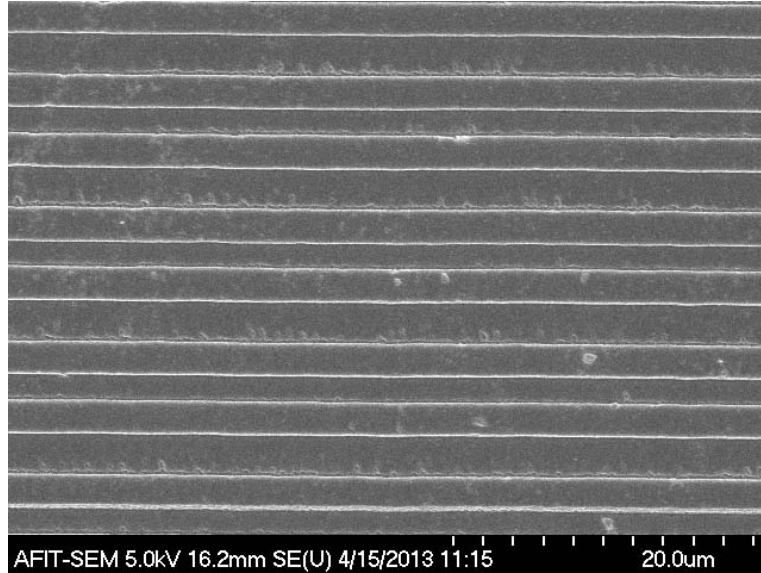
Figure 7.17: An SEM image of a dual-cavity-width structure, imprinted in PMMA and sputtered with aluminium, is shown from top-down. Edge roughness from the imprinting process is clearly visible, even after metal deposition.

7.6 Conclusion

The fabrication process workflow followed very standard guidelines and methods for microfabrication. Nonetheless, extensive test and calibration work was required to produce acceptable microfabricated surfaces. A set of aluminized shallow grating test articles was fabricated directly in silicon and by imprinted PMMA. These test articles were produced for instrument calibration and to evaluate the process performance. Then, a set of CRC samples was fabricated in PMMA and aluminium was deposited, at differing thicknesses, onto these samples. Finally, a set of dual-cavity-width design samples was fabricated in PMMA and aluminium was deposited at a single thickness.

VIII. Measurements and Analysis

8.1 Introduction

Evaluating the emission and reflection behavior of the designed structures introduces a set of sometimes conflicting requirements on the measurement instruments. Because the structures are designed to produce angularly and spectrally narrow and varying behaviors over a substantial wavelength range, measurement instruments must also be responsive over a broad spectral range. Accurately evaluating angularly narrow responses also requires that the measurement instruments' apertures subtend small solid angles to provide sufficiently fine angular resolution. This reduces the flux-collecting area of the instrument and imposes signal-to-noise challenges. The low operating temperature requirement imposed by the designs and fabrication techniques exacerbates the signal-to-noise ratio problem, and practically mandates that both emission and reflection measurements be used to accurately evaluate the designed structures' performance.

To collect broadband responses, all of the instruments used in this work employ Fourier Transform Infrared (FTIR) Spectrometers in the detection section of their optical trains. So, the basic operation and limitations of these devices is reviewed. The relatively large apertures required to make measurements from broadband sources, in particular at low temperatures, introduce non-negligible instrument effects into the measurements. The angular instrument function component is of particular importance when measurements are taken over a range of angles, and the concept is addressed in light of typical scatterometry applications and the measurement goals of this work. An instrument characterization methodology is presented for each of the three instruments employed and the angular instrument functions developed for application to the designed structures. Finally, the performance of each design is evaluated and modeled data is compared to the measured values.

8.2   Fourier Transform Infrared Spectrometer

All of the radiometric instruments used in this work employ a FTIR spectrometer as the final stage in the optical train. The key advantage of FTIR spectrometer-based systems is the ability to make measurements which are both spectrally broadband and have high spectral resolution. A brief synopsis of the FTIR operating principles is presented to develop the instrument function, which limits the spectral resolution of FTIR-based system, and to preface the discussion of the three radiometric normalization schemes employed by the FTIR-based instruments.

In all FTIR spectrometers, an incident field is directed from the test sample into an interferometer. Although designs vary, the operating principles are readily understood in terms of the classic Michelson interferometer. In this arrangement, an incident field is divided by a beam splitter into two of the four arms of the system. The split components of the incident field travel to a fixed mirror and a moving mirror, respectively. The field components are then reflected back through the beam splitter to recombine on a detector, where a voltage level is recorded for a given moving mirror position. Then, the moving mirror position is incremented, changing the optical path length in the moving mirror arm of the device by twice the increment distance, and another voltage measurement is recorded. This process is repeated at finite distance increments over the full available span of moving mirror positions [101].

A voltage profile, or interferogram, is formed by collecting the voltage values from sequential measurements. For a monochromatic incident field, the recorded voltage on the detector varies sinusoidally with the optical path difference. For a broadband incident field, the recorded voltage value at any optical path difference is the sum of the weighted and shifted sinusoidal contribution of each wavelength. When the optical path difference between the interferometer arms is zero, all of the wavelengths experience constructive

interference and the peak voltage measurement is recorded for the sinc-function like interferogram of a broadband signal [101].

Because a measured interferogram is a function of optical path distance in *cm*, and is known to be comprised of the sum of a set of sinusoidal signals, the spectral content of the incident field may be extracted by evaluating its spatial Fourier transform. Assuming that the incident field intensity is constant over the measurement scan, the spatial Fourier transform produces spectral weights as a function of wavenumber in cm^{-1} [101]. At this point, the spectral weights are voltage-referenced signals which still require radiometric calibration [102]. The method of calibration depends upon the application and instrument configuration, and will be addressed in each instrument section individually.

In any realizable system, the moving mirror path distance, detector integration time, and digitization levels must be finite. So, a discretely sample, spatially limited signal is Fourier transformed. This requires apodization to control aliasing and introduces low pass filtering into the spectral component weighting. All of these factors limit how finely the instrument may resolve a monochromatic signal and define the instrument function [102]. However, all of the FTIR-based instruments used in this work could be operated at sufficiently fine spectral resolution, by extending the number of measurement which were averaged, that their instrument functions were not the dominant instrument effect.

8.3 Angular Instrument Function

In all scatterometry systems, the receiving optical train observes the reflection or emission from a sample over a series of angles. The angle of incidence is defined by the angle between the receiving optical axis and the sample surface normal. The response of the system to a plane-wave input at a given angle of incidence is the angular instrument function. An ideal instrument would report only a delta function response for an incident plane wave. However, for any real system, the measured response to a plane wave extends over some finite angular width [24].

Because the measurement systems employed in this work do not produce images as detector outputs the terminology of non-imaging optical concentrators is used to develop the angular instrument function. However, image forming systems are a subset of optical concentrators, and the stops and pupils of imaging systems are equivalent to the more general apertures of optical concentrators [103]. So, the angular instrument function is developed for general apertures, but comparisons are made to image forming systems for clarity.

For an optical concentrator, the maximum angle, relative to the optical axis, at which an incident plane wave enters the optical system and reaches the detector defines the angular aperture, θ_{AA}, of the system [103]. For imaging systems, the angular aperture is identified as the field-of-view angle, θ_{FOV}. The field-of-view angle is determined by the field stop in an imaging system, and at its largest, is determined by the angle between the detector edge at (D) and the optical axis at the entrance pupil at (O) as shown in Figure 8.1 (a) [28]. If the imaging condition is relaxed, as it may be for radiometric systems, the detector need not be located at the focal point. Additionally, the detector dimensions may stray outside the paraxial region without consequence. So, in the non-imaging case shown in Figure 8.1 (b), the angular aperture is determined by the edge ray method [103]. In both cases, it is desirable that the sample subtend the entire angular aperture in the measurement configuration, to simplify the reflectance or radiometetric computations.

For an imaging system, the entrance pupil determines the maximum marginal ray angle, θ_s, and the thus the amount of light which contributes to the formation of an image of an object at (S) on the detector (D). In Figure 8.2 (a), the elements (A) or (O) could be constricted to define the entrance pupil, or the image (C) of element (B) could remain the entrance pupil as shown [28]. In the non-imaging case shown in Figure 8.2 (b), some image or element still limits the amount of light which is concentrated on the detector, but it is identified as the entrance aperture, rather than the entrance pupil. In this case,
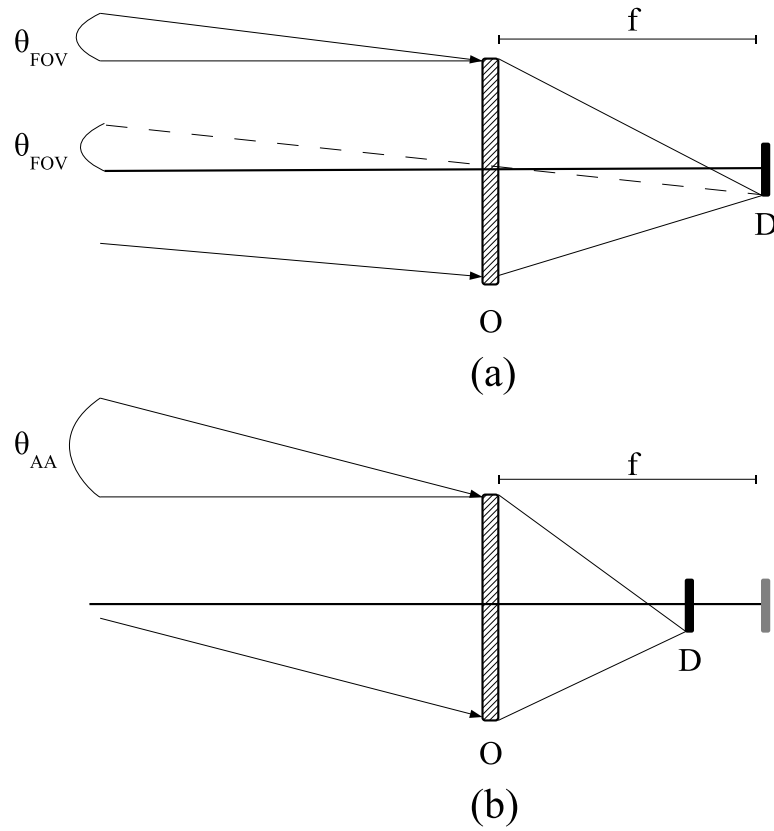
Figure 8.1: (a) The field of view angle, θ_{FOV}, of an imaging system is determined by the angle between the edge of the detector at (D) and the optical axis at the entrance pupil at (O), when the detector edge serves as the field stop. (b) The angular aperture, θ_{AA} of a non-imaging system is determined by the edge ray method. The entrance aperture of the system lies at O and the detector lies at D, which need not be at the focal point, f.

edge rays from a source point at (S), must fall somewhere on the detector at (D), and it is still necessary to project the images (C) of element (B) to determine if it limits the light collecting capabilities of the system. However, the role of the detector at (D) and its dimensions can no longer be ignored. In the case of an imaging system, the entrance pupil is the entrance aperture [103].
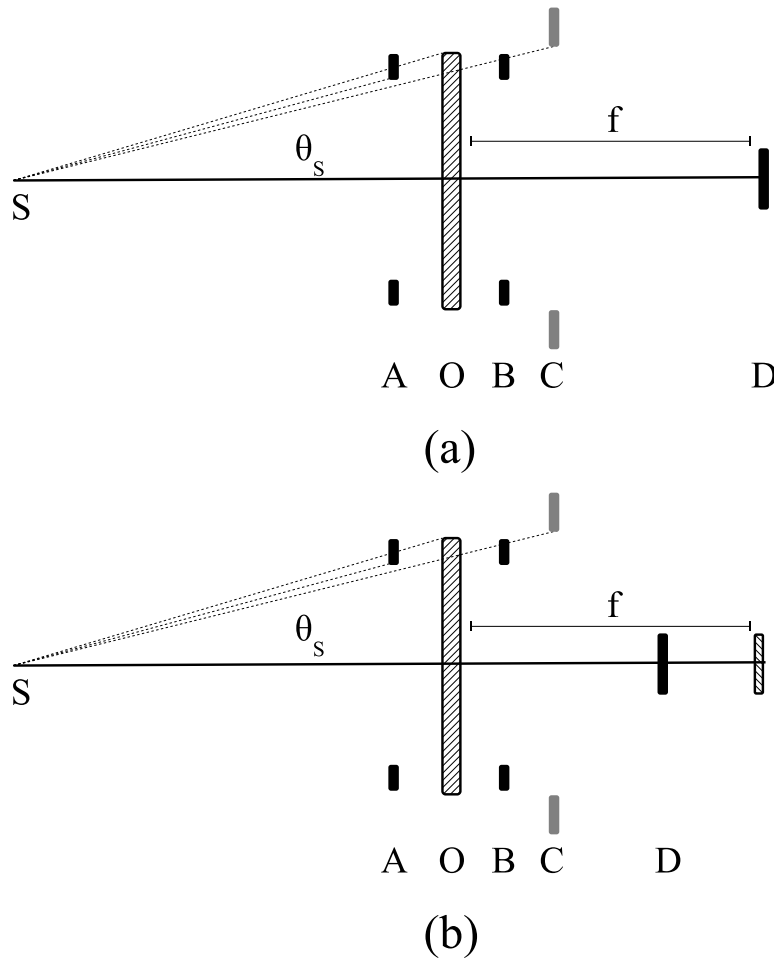

Figure 8.2: (a) In an imaging system, the entrance pupil is the image of the element which limits the maximum off-axis angle of a marginal ray. (b) In a non-imaging system, the entrance aperture is also the image of the element which limits the maximum off-axis angle of a source ray, but the location of the detector must be considered for further vignetting. The entrance aperture of an imaging system is the entrance pupil, and in both cases, this element subtends some angle, θ_S, when observed from a source at point (S). This angle determines the angular resolution of the system, in a given geometric configuration from the source.

In both cases, the optical system subtends some angular span, θ_S, as viewed from the source (S) and any plane-wave leaving the surface at an angle inside this angular span will reach the detector. This angular span determines the cone of rays which will be integrated to generate a single scatter value for an angle of incidence, and defines the angular resolution of the system. Unlike in imaging systems, a larger entrance aperture is not desirable in scatterometry systems, so long as the system signal-to-noise requirements are met. In laser-sourced scatterometry instruments, entrance apertures are generally quite small, and angular resolution values ranging from 0.01 to 0.1 degrees are readily achieved [24]. Broadband infrared scatterometry instruments typically employ larger entrance apertures, to meet the system signal-to-noise requirements, and demonstrate angular resolution values of 1 to 5 degrees. So, at best, FTIR-based systems perform at the upper limit of the angular resolution of narrow-band laser sourced instruments [24].

If a measured signal varies slowly with angle, as with observations of roughened surface, the impact of the angular instrument function may not be apparent. However, when the signal is angularly narrow, such as a grating lobe, its effects are very distinct and significant for large angular resolution systems [24]. The angular instrument function averages out angularly narrow features, and spreads the effect of the feature across an angular span. Therefore, it was necessary to determine the angular instrument function for each instrument configuration, which meets the signal-to-noise level requirements for effective design evaluation.

8.4 IR-VASE®

The J. Woolam IR-VASE® is not, by design, a scatterometry instrument. However, it can be used to collect specular reflectance and transmittance data over a finite angle range. As configured, the rotation stage and Receiver (RX) arm are scanned such that a specular view, where the incident and reflected angles are the same, $\theta_i = \theta_r$, is maintained over

a selected range of incident angles from the Transmitter (TX) arm. Figure 8.3 shows a simplified diagram.
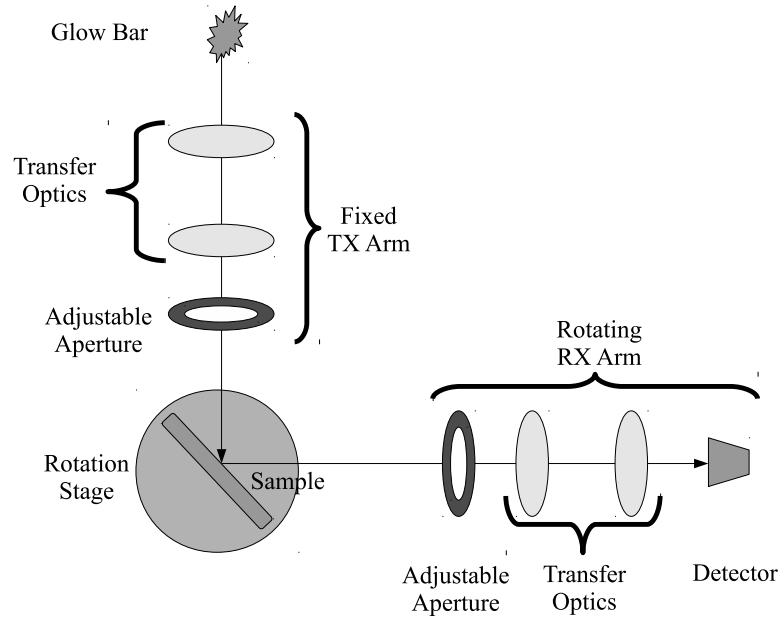

Figure 8.3: Simplified J. Woolam IR-VASE® Schematic.

Radiometric calibration is achieved by normalizing the measured spectral weight voltages to a baseline measurement, after background subtraction. The background level is taken by observing the back of the black anodized aluminium sample stage, which is assumed to be at the room temperature. In the absence of strong localized thermal sources in the room, this measurement results in a very near approximation to a blackbody at room temperature. A source reference measurement is then taken with the sample and stage removed from the field of view of the detector, which directly images the glow bar. The resulting normalized value defines only the near specular reflectance value from the sample [104].

The accuracy of this referencing method is highly dependent upon the system signal-to-noise ratio, determined by the adjustable aperture diameters and number of scans

averaged, and does not provide any insight into the angular instrument function of the system. To make accurate and efficient measurements, a system configuration which balances the time required for measurements against the acceptable noise level must be determined. Once these parameters are set, the angular instrument function of the system, as configured, may be determined.

The IR-VASE® offers only limited control of the illuminating source, from which a reference signal level measurement may be taken. Power to the glow bar is strictly controlled, and was set to 18.3V for 1.09A to produce 20W of current draw. Otherwise, the raw signal level is controlled by the unmetered adjustable diaphragm apertures on each system arm. For consistency, the apertures were set by gently closing the diaphragm around preset vernier calipers. A set of reflectance measurements was in the source reference measurement configuration, described above, at aperture values of 4mm, 6mm, 8mm, and 10mm, which subtend 1.9 degrees, 2.8 degrees, 3.8 degrees, and 4.7 degrees respectively, at the receiver. The results are shown in Figure 8.4 (a)-(d) and are used to determine the minimum aperture diameter which generated an acceptable signal-to-noise ratio.

The data set shows the average of 100 scans, giving mean reflectance values of 1.0001, 1.0019, 0.9998, and 0.9997 for 4mm, 6mm, 8mm, and 10mm aperture diameters, respectively, over the range of 2-12μm. The reflectance MSE values were $2.2899e^{-4}$, $4.8029e^{-5}$, $5.7187e^{-6}$, and $1.6854e^{-6}$, respectively. So, for increasing aperture size, the MSE decreases monotonically as expected. Based on the aperture error results, an aperture diameter of 8mm (3.8 degrees) was selected, which produces sufficient noise performance. The number of FTIR scans taken in the final average was varied to include 16, 25, 36, 49, 64, 81, and 100 scans for the fixed aperture diameter. Four values are shown in Figure 8.5.

The resulting mean square error values showed order of magnitude consistency over the full range. The reflectance MSE for the averaging of 25 samples was $5.2249e^{-6}$, falling above, but consistent with, the $1.0172e^{-6}$ value found for averaging 100 samples.
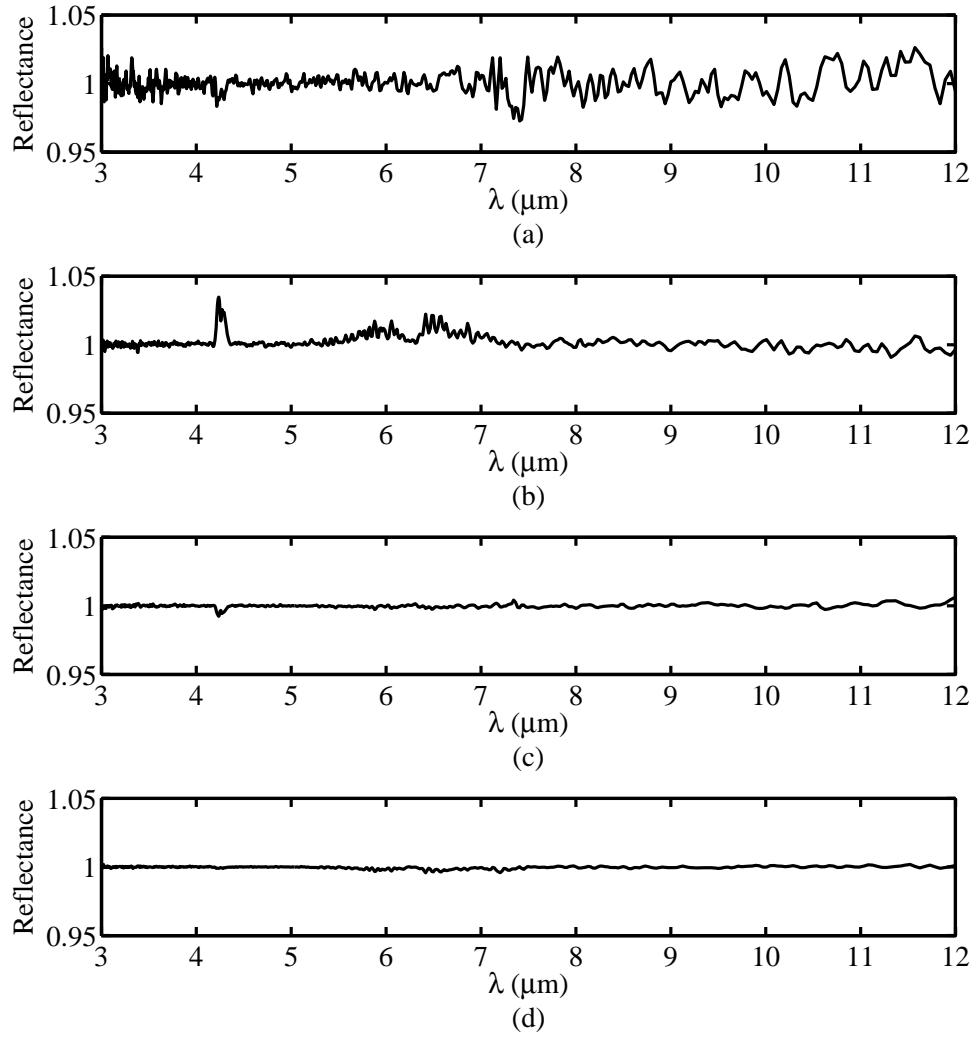
Figure 8.4: A series of normalized reflectance measurements are shown for the IR-VASE® in the source reference measurement configuration at (a) 4*mm*, (b) 6*mm*, (c) 8*mm*, and (d) 10*mm* aperture diameters. The noise performance of the system improves sharply between the 6*mm* and 8*mm* aperture diameters.
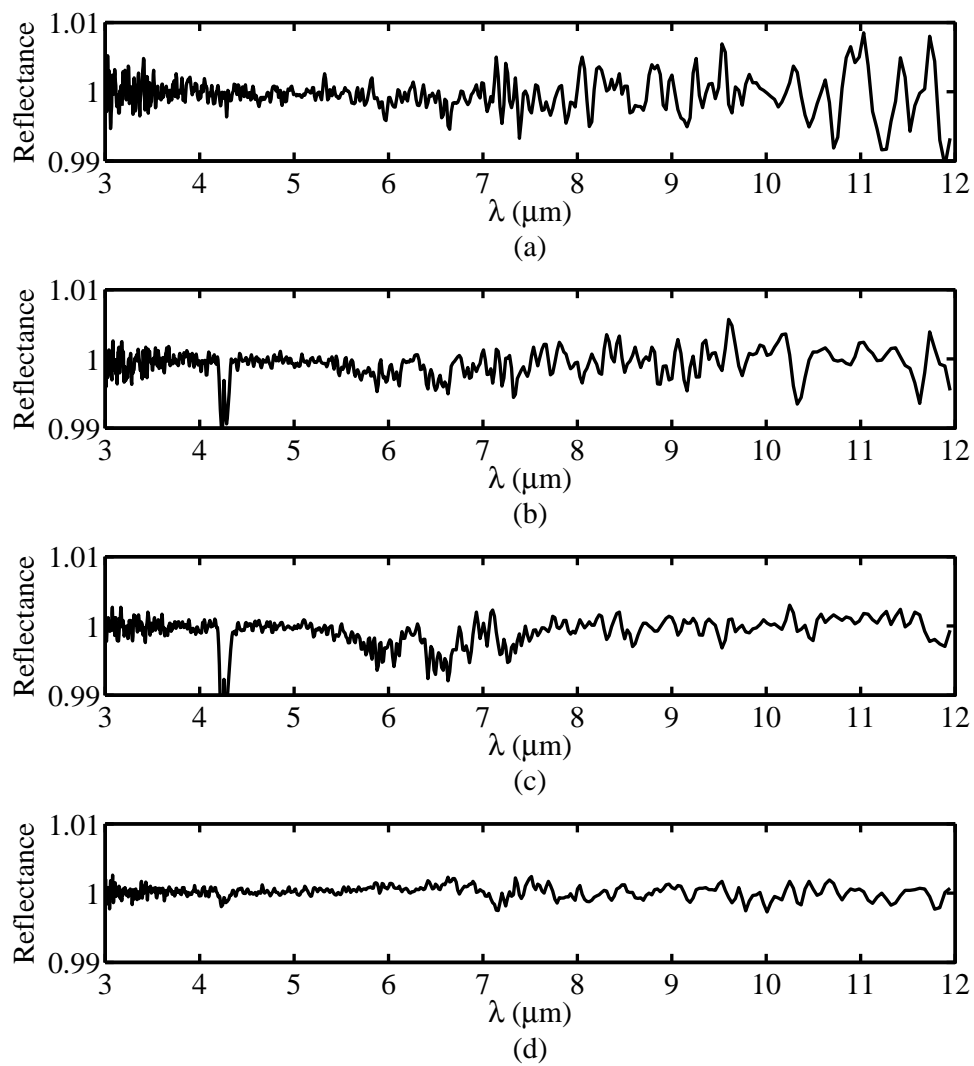
Figure 8.5: Averaging noise for (a) N=16, (b) N=25, (c) N=64, and (d) N=100 FTIR scans per measurement.

The time per measurement when averaging 25 FTIR scans was sufficiently short that the value was adjusted up to 36 scans for approximately 40 seconds per angle measurement times. Setting the aperture to 8*mm* and taking 36 or 100 scans offered a reasonable compromise between measurement time, angular resolution and experimental flexibility. By maintaining a constant aperture and varying only the number of scans, two different configuration baselines could be kept for a single alignment. This allowed slightly coarser and finer data to be calibrated against the saved baselines without reconfiguring the system.
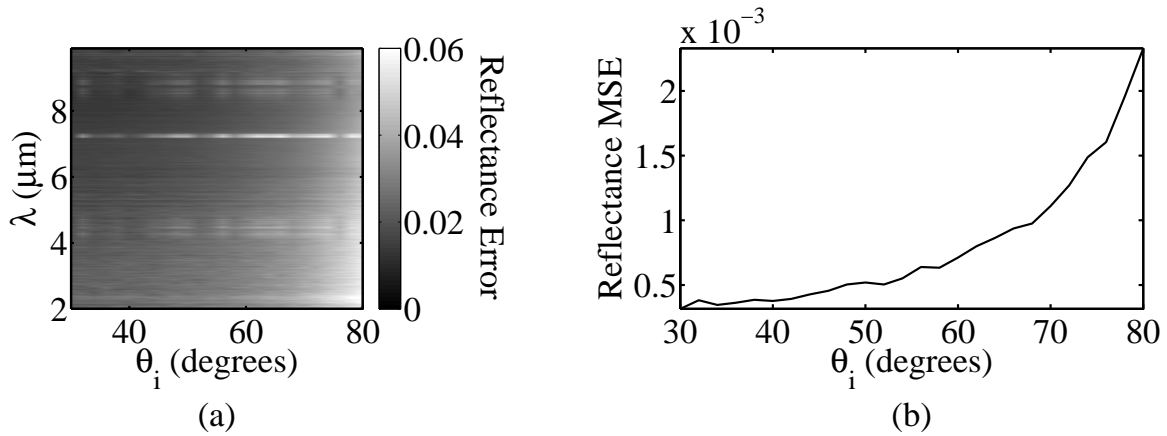

Figure 8.6: (a) The error between the specular reflectance of a gold mirror, computed from published complex index of refraction data and measured on the IR-VASE®, is shown as a function of wavelength, λ, and angle of incidence, θ_i. (b) The MSE of the specular reflectance shows a clear trend with increasing angle of incidence.

To evaluate the system's radiometric performance in the same geometric configuration in which sample measurements are taken, a reference gold mirror was mounted and aligned on the sample stage. A specular reflectance reference scan, Figure 8.6 (a), was taken to verify the reflectance behavior of the gold mirror. The results showed excellent modeled to measured value agreement, as shown in Figure 8.6 (b). Since a gold mirror's reflectance changes slowly with angle, the aperture effect is virtually unobservable.

Geometrically, the 8*mm* aperture 12.07*cm* from the sample axis of rotation subtends 3.7920 degrees, assuming that the forward iris is in fact acting as the aperture stop of the

optical train. To evaluate the angular instrument function, the angle of incidence was held

constant at 45 degrees while the receiver arm was swept across the specular angle. A

surface plot of reflection angle, θ_r, by wavelength λ in Figure 8.7 shows no measurable
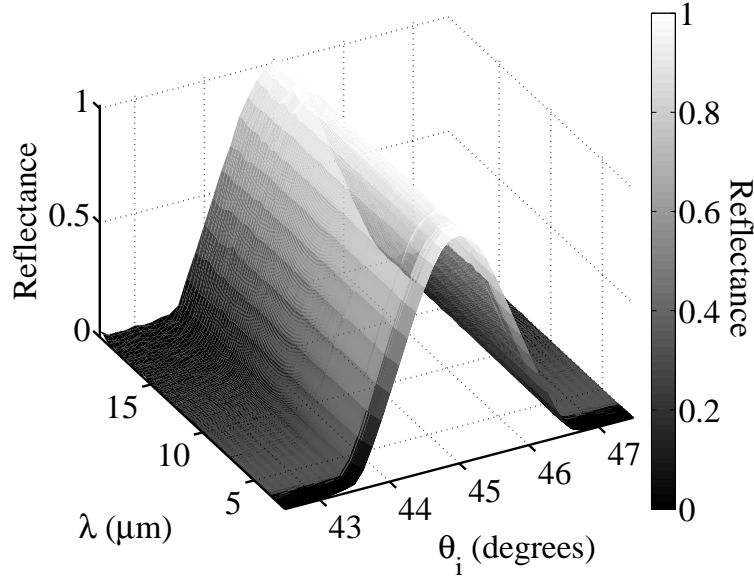
angular width dependence on wavelength, simplifying further analysis.

Figure 8.7: Perspective view in wavelength, (λ), and reflection angle, (θ_r), of a gold mirror for a fixed angle of reflection $\theta_r = 45$ degrees.

In cross section, the wavelength independence is again apparent, as shown in Figure

8.8 (a). This measurement was repeated at $\theta_i = 35$ degrees, $\theta_i = 45$ degrees, and $\theta_i = 75$

degrees in Figure 8.8 (b). The angular width of the profile remains constant, with only

small amplitude variations with wavelength and incident angle attributable to the angular

and spectral dependence of the gold mirror reflectance.

The cross sections at given wavelengths and incident angles were then fit with an

idealized angular instrument function. In this case, the ideal angular instrument function

goes as the normalized convolution of the area of two circles, assuming a uniform incident
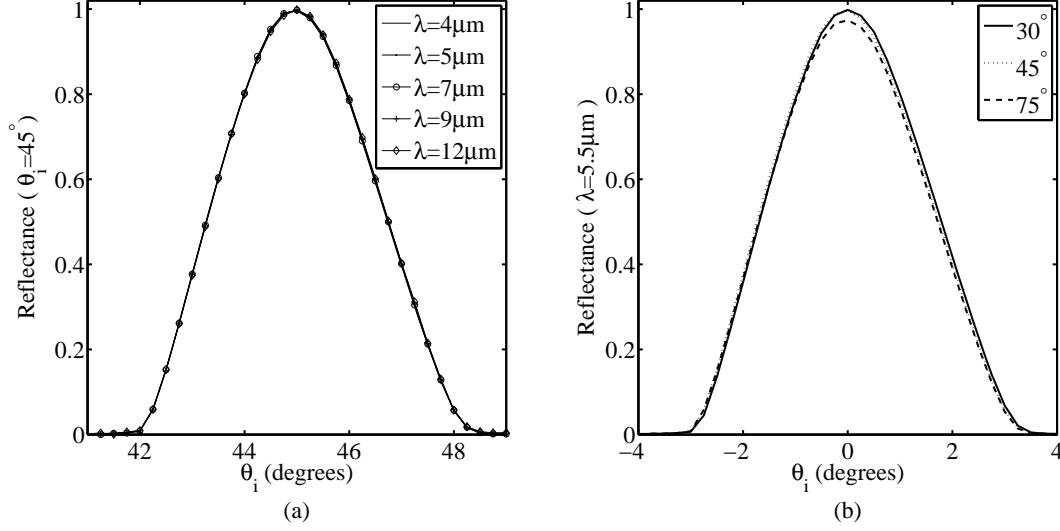
147

Figure 8.8: (a) Specular reflectance angular cross section of a gold mirror by wavelength for 4μm, 5μm, 7μm, 9μm, and 12μm. (b) Specular reflectance angular cross section at $\lambda = 5.5\mu m$ for 35, 45, and 75 degrees.

field. The results of this fitting for θ_i = 30 degrees, Figure 8.9 (a), and θ_i = 75, degrees Figure 8.9 (b), both demonstrate a slightly narrower profile base than the predicted ideal fits at 3.792 degrees in angular diameter. This may be due to deviations in the actual shape of the irises, but the angular error is still quite small compared to the angular span. The MSE values between the measured reflectance distributions and fitted distributions are 9.528e^{-4} and 8.1853e^{-4}, respectively.

While determining the angular instrument function is instructive for understanding the limits of the system, the more useful information it provides is a means of predicting the measured signal values from modeled data. The aluminium-on-silicon shallow grating, which exhibits directionally and spectrally selective emission and absorption, was measured on the IR-VASE® in its scatterometry mode. The specular reflectance in TM polarization is shown in Figure 8.10 as a function of wavelength, λ, and angle-of-incidence, θ_i. When a single wavelength is examined, it is apparent that the specular reflectance nulls,
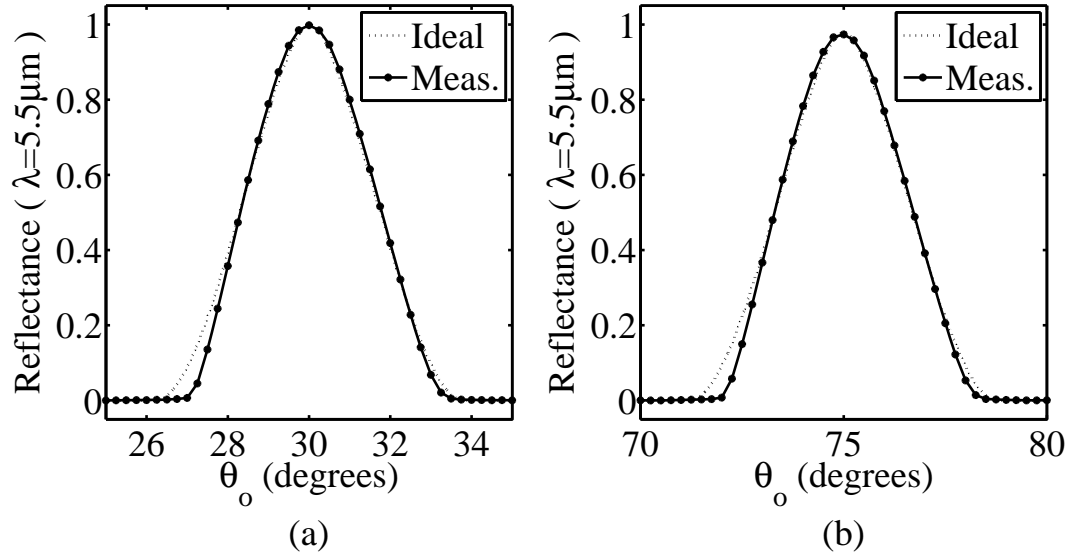
Figure 8.9: The convolution of two circular functions, properly scaled, shows good experimental agreement with the measured data at (a) 30 degrees incidence angle and (b) 75 degrees incidence angle.

such as the feature running from $6\mu m$ at 30 degrees to $6.8\mu m$ at 45 degrees, extend over an angular width slightly wider than 3.8 degrees.

The angular TM specular reflectance and absorptance values for the aluminium-on-silicon shallow test grating were finely computed via RCWA, over a broad range of angles at $6.786\mu m$. Figure 8.11 shows the specular reflection as a function of incident angle, as well as the total reflectance, which is related to the absorptance by conservation of energy for an opaque sample. These results were computed at 0.1-degree increments, assuming an infinitesimal aperture by the plane-wave expansion. This data can be convolved with an appropriate angular instrument function, developed for the given angular resolution, to predict measured values.

The specular reflectance measurement method employed by the IR-VASE® in scatterometry mode requires that the effects of aperture convolution be treated differently than the common scatterometry case. In more typical scatterometry, for bi-directional
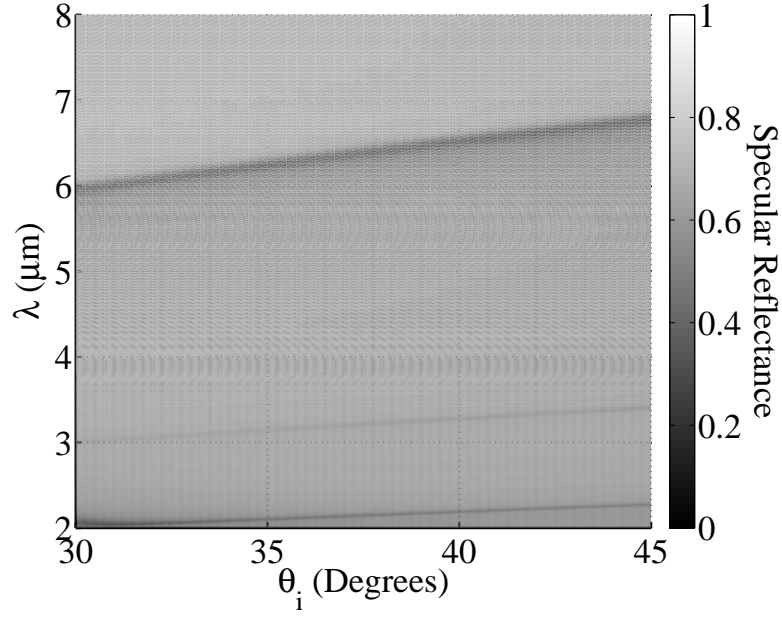
149

Figure 8.10: The TM polarized specular reflectance from a $4\mu m$ period aluminium-on-silicon shallow grating is shown, as measured by the IR-VASE®.
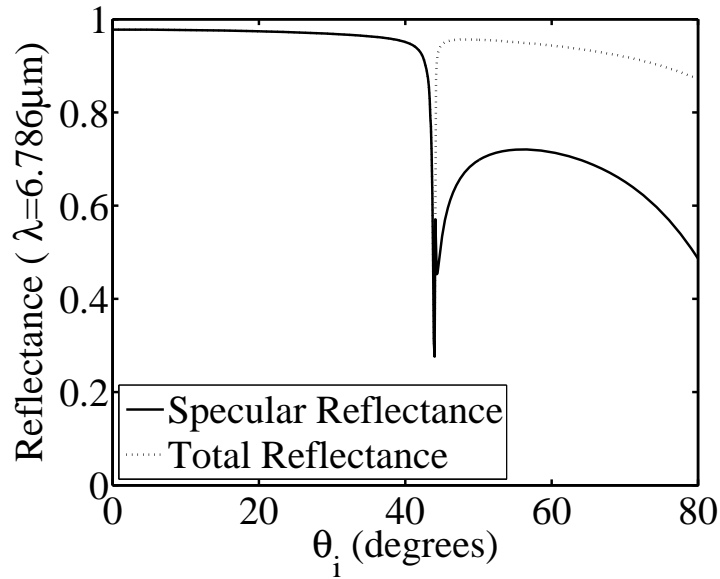

Figure 8.11: Aluminium-on-silicon shallow test grating angular specular reflectance at $6.786\mu m$ and total reflectance, related to the angular absorptance by conservation of energy, as computed by RCWA.

reflectance distribution data collection, the angle of incidence is held constant and the detector is swept across some angular arc. Then, a new angle of incidence is selected and another set of measurements is taken. In the matched specular case, the angle of incidence and measurement angle move together, to maintain specular viewing of the sample. The objective is to transform the modeled specular reflectance results for the grating, computed separately by RCWA for each angle of incidence, into a form which predicts the signal measured by the IR-VASE®. This requires that the effects of the sample rotation be accounted for along with the angular instrument function. The weighting of the RCWA data goes as the convolution of the area of a pair of circular apertures, with a final angular width equal to that of the angular instrument function. Excellent results are shown in Figure 8.12 for the specular reflectance measurements. The specular reflectance MSE over the entire angular range considered was $1.9027e^{-4}$. The IR-VASE®provides the finest resolution reflective measurements of the reference sample available for this work.

8.5   SOC-100

The Surface Optics Corporation, Model 100 Hemispheric Directional Reflectometer system collects normalized reflectance measurements for hemispherically illuminated samples at fixed observation angles. In the Hemispheric Directional Reflectance (HDR) configuration, a blackbody source is situated at one focal point of hemi-ellipsoidal mirror. The measurement sample is situated at the other focal point, such that it is illuminated over the full 2π steradians of the hemisphere. The total reflected or transmitted field is collected by an Off-Axis Parabolic (OAP) mirror on the RX arm, which directs it through a series of transfer and collimating optics to an FTIR-based detection system, as shown in Figure 8.13. Spectral reflection or transmission values are normalized against a specular gold mirror or an unimpeded direct transmission measurement.
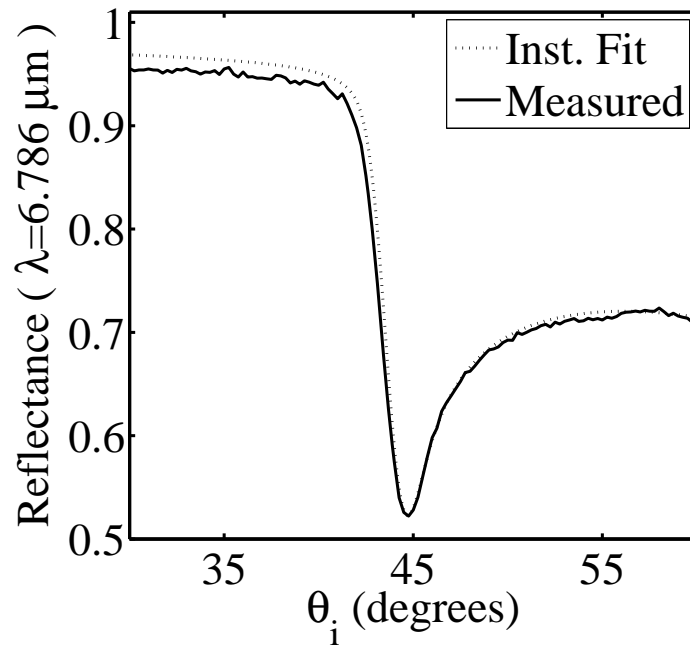
Figure 8.12: Aluminium-on-silicon shallow test grating angular spectral reflectance computation via RCWA, convolved with the angular instrument function, shown with measured data. Excellent agreement is observed between the modeled and measured reflectance values.
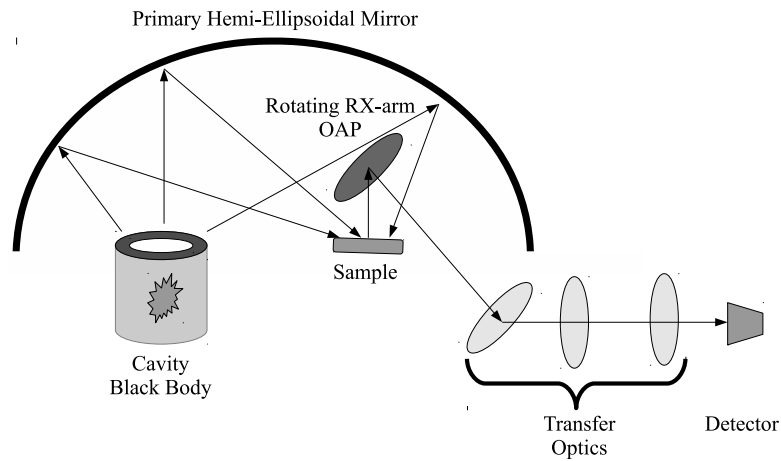

Figure 8.13: Simplified schematic for the SOC-100 Hemispheric Directional Reflectometer configuration.

To develop a noise baseline, a series of measurements was taken in the Hemispherical Directional Transmittance (HDT) mode with no sample in the holder. In this configuration, the FTIR is directly viewing the blackbody and is functionally self-referencing. The deviation of the normalized transmittance is shown as a function of the number of measurements averaged in Figure 8.14. Although the reflectance MSE goes down from $8.6782e^{-6}$, $4.6185e^{-6}$ to $3.9600e^{-6}$ predictably with increasing number of sample averages, the extensive measurement time requirement suggests that the lower value is acceptable, in particular since the achieved reduction in MSE is just over a factor of 2, at this signal level.

The worst-case angular instrument function was computed from geometric measurements, where the OAP mirror is $2.54cm$ in diameter and $18.27cm$ from the sample surface at normal. This implies a maximum entrance pupil angular diameter of 7.9 degrees. Since the instrument's operation is controlled by commercial software, and the transfer and collimating optical train includes a large number of unspecified optics, the angular instrument function was evaluated from measurements of the aluminium-on-silicon $4\mu m$-period shallow test grating, previously examined on the IR-VASE®. The angle of incidence, θ_i, was swept from 10-40 degrees by 0.2 degree increments and the results are shown in Figure 8.15.

An unexpected feature is shown in the measured directionally and spectrally dependent reflectance nulls. The reflectance null which runs from $2\mu m$ at 12 degrees to $5\mu m$ at 40 degrees was not predicted by RCWA analysis, and is not present in the IR-VASE® measurements shown in Figure 8.10. It will also not be apparent as an emission feature of the aluminium-on-silicon shallow grating in Figure 8.22 (b). It appears to be associated only with periodically patterned surfaces, as it is not present in unpatterned diffuse or specular test samples. However, the unpredicted feature is readily avoided for angular instrument function fitting.
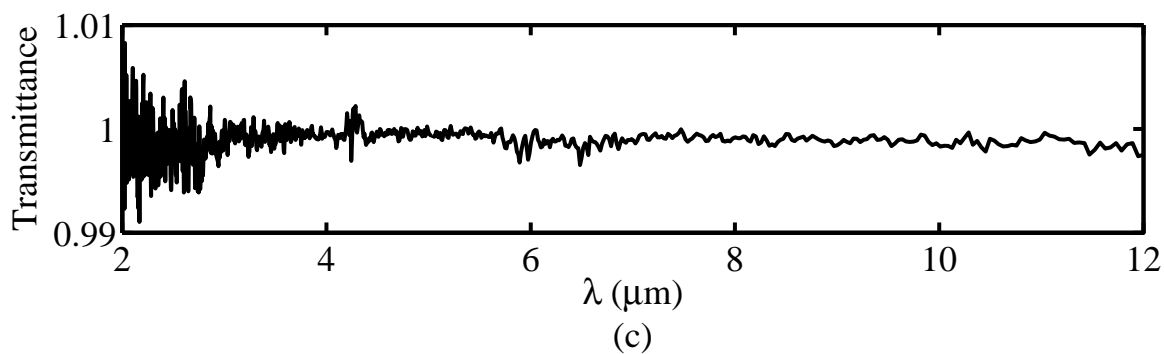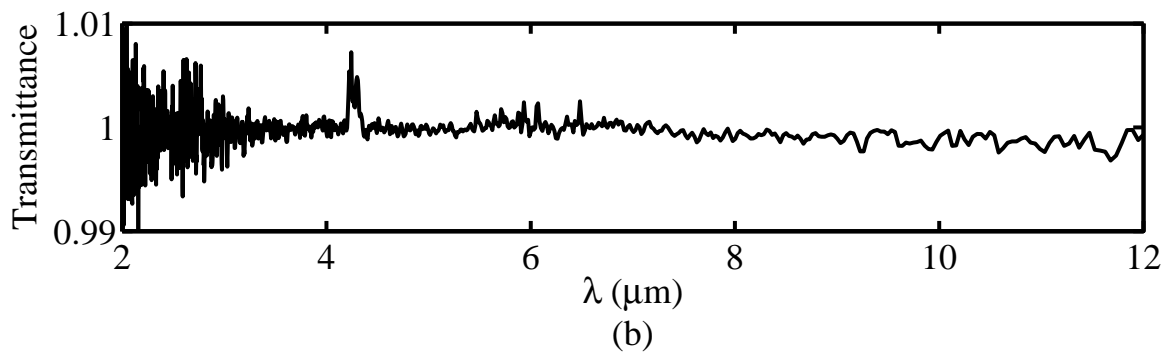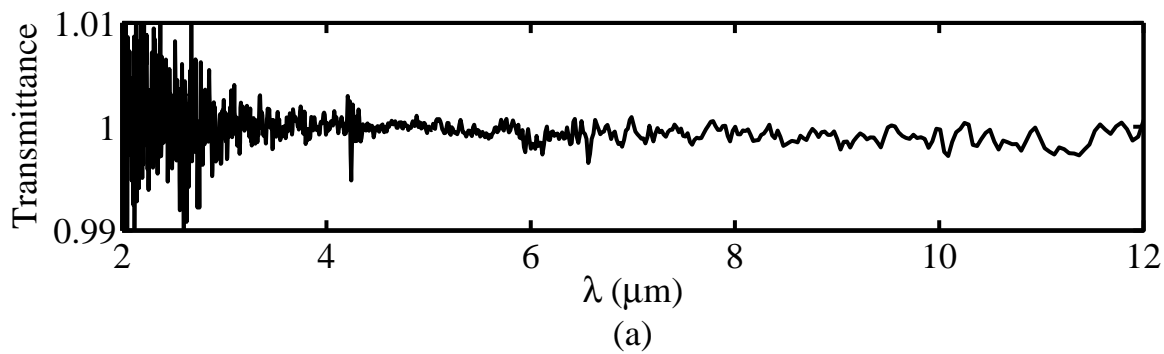
Figure 8.14: SOC-100 blackbody transmission measurement with (a) 16, (b) 25, and (c) 36 measurements averaged to produce the spectrogram. The measurements were taken without N_2 purging, and the CO_2 feature, near $4.3\mu m$, is clearly visible.
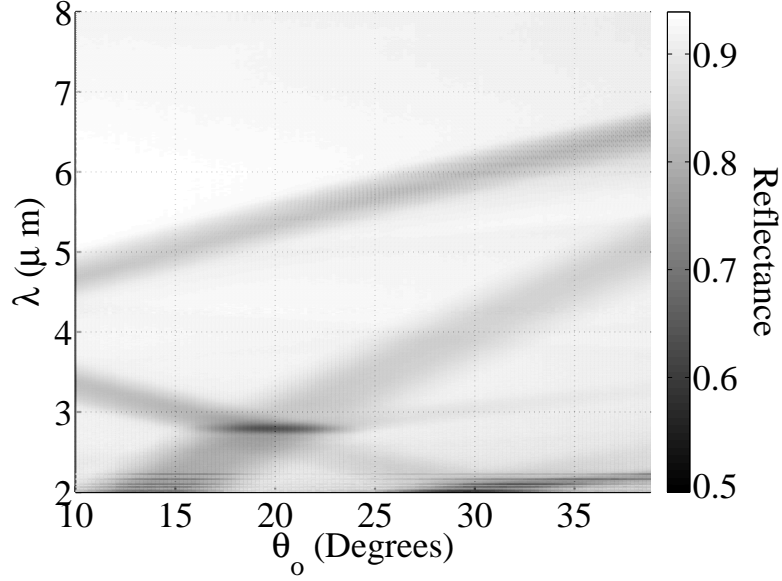
Figure 8.15: SOC-100 measurements of the $4\mu m$ aluminium-on-silicon grating angular spectral reflectance.

To evaluate the angular instrument function, measured shallow grating data was fit at $5.6\mu m$, as with the IR-VASE®. In this case, the 0-order or specular reflection model cannot be used. By definition from HDR, the only losses to the measured reflectance of a non-transmissive sample should be due to absorption. Therefore, the appropriate RCWA modeling result for comparison is the total reflectance for each angle-of-incidence, which represents only absorptive losses.

An angular instrument function was fit to the measured data at $5.6\mu m$, as shown in Figure 8.16. The best-fit angular instrument function aperture diameter is 7.3 degrees, as compared to the 7.9 degrees which was predicted geometrically if the receiver arm off-axis parabolic mirror defined the entrance aperture. This simply implies that one of the other transfer optics of Figure 8.13 is in fact the entrance aperture.

A substantial deviation between the measured and modeled data is apparent from 26 to 40 degrees. This is precisely the angular region where the power in higher-order diffracted components are missing from the specular reflectance of this grating, as shown
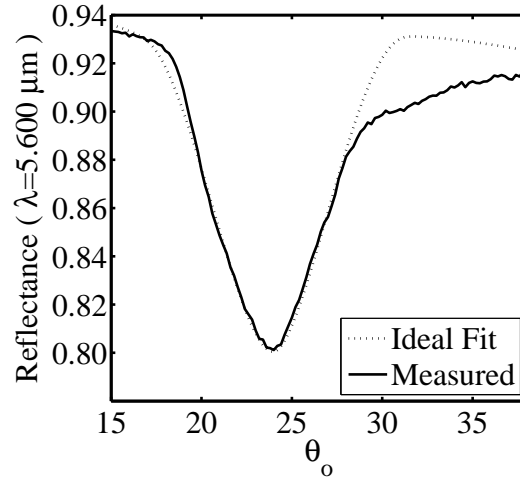
Figure 8.16: Angular instrument function fit for the SOC-100. The difference in the reflectance measured from 26-40 degrees may be attributable to the unexpected formation of weak grating lobes.

in Figure 8.11. Although this data is presented at a different wavelength, $6.786\mu m$ rather than $5.6\mu m$, the behavior is general, because this absorption features occurs at the spectral order transition angle. A substantially more complete model of the sample illumination may be required to determine the source of the deviation.

8.6 Emissometer

To directly verify the designed structures' performance, an emissometer system was constructed. The system was set up using discrete optical bench components and a BOMEM MR-154 FTIR Spectrometer, with a short focal length telescope front end. The sample was mounted for an elevation angle sweep, with tip-tilt and rotation control to orient the sample normal to the FTIR telescope at 0 degrees indicated angle. A wire grid polarizer at the telescope aperture was oriented in the sample TM orientation. The sample was heated by forced convection with the heat source oriented to minimize specular and high-order reflection while maintaining as uniform of a surface temperature as possible, as shown in Figure 8.17.
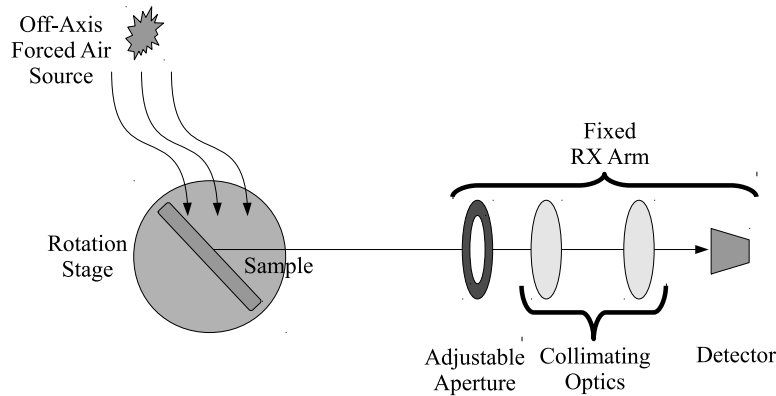
Figure 8.17: Schematic of the constructed emissometer.

A series of trials was conducted to determine the maximum distance the telescope aperture could be placed from the sample, minimizing the entrance aperture's angular size, while meeting the signal-to-noise requirements for an acceptable measurement time per angle. The minimum distance was also required to allow the optical system to focus on the sample, and for the system field stops to be set such that the sample filled the entire field of view. Based on the results of these tests, the telescope aperture was placed $120cm$ from the sample holder front surface, with the internal field stops set to the $1.6mm$ diameter setting. This distance and aperture combination allowed a 30-degree-tilted $25mm$ sample to fill the entire field of view of the system, in focus.

To provide a radiometric calibration reference for the spectral weights, a series of measurements of an Electro Optics Industries Inc., CES200-02 large area blackbody source was taken for each data set. So long as the target and blackbody both fill the field of view of the system, the spectral weights in voltage can be assigned spectral radiance values relative to a blackbody without further modification, hence the field-of-view filling requirement. For each calibration, the blackbody is measured at a range of temperatures, and voltage values are related to spectral radiance by a multi-point linear or quadratic fit. An example of the system's ability to produce radiance values from blackbody measurements is shown in

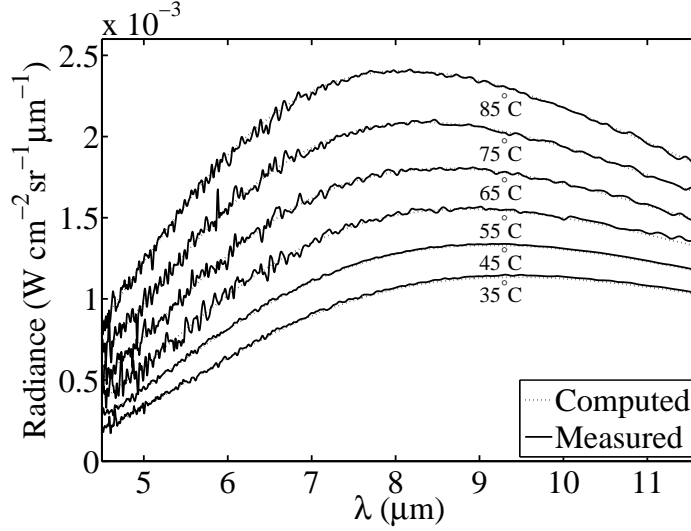Figure 8.18. Substantial detector noise is evident below $7\mu m$ even when 625 measurements are averaged.

Figure 8.18: Calibrated spectral radiance measurements of a known blackbody source. In general, the lower the required span of signal levels, the more stable the results are, particularly below $7\mu m$.

The reference blackbody surface exhibits unity emissivity by definition, and the FTIR's radiometric calibration process removes an small deviations from this ideal. So, subject to noise, the blackbody measurements shown in Figure 8.18 do not exhibit any reflected background component. This will not be the case for a non-blackbody measured sample.

In the more typical measurement case, the sample exhibits a spectral emissivity, $\epsilon_S(\lambda, T_s)$, and a reflectance, $\rho_s(\lambda, T_s)$, at the sample temperature, T_S. The emissivity term scales a blackbody spectral radiance at the sample temperature, $L_{BB}(\lambda, T_s)$, and at the reflectivity term scales a blackbody spectral radiance, $L_{BB}(\lambda, T_{bkg})$, at the background temperature, T_{bkg}. The measured flux, Φ_{meas}, also depends upon the instrument field-of-view, Ω_{FOV}, and the area of the detecting aperture, A_{EA}. The measured flux value is then scaled to a radiance value in the FTIR's radiometric calibration process. Since both the

blackbody and samples fill the entire field-of-view of the instrument as configured, the reported spectral radiance values may be used without regard to the instrument parameters.

$$\Phi_{meas} = \Omega_{FOV} A_{EA} \left[\epsilon_S \left(\lambda, T_S \right) L_{BB} \left(\lambda, T_S \right) + \rho_S \left(\lambda, T_S \right) L_{BB} \left(\lambda, T_{bkg} \right) \right] \qquad (8.1)$$

When low temperature self-emission measurements are made, the difference between the blackbody spectral radiance at T_S and T_{bkg} is relatively low, as previously illustrated in Figure 6.8. In this case, the reflected component introduced into measured data is not negligible. To demonstrate the reflected component contribution and verify a means of predicting it in simulation, a white-painted-aluminium sample was used in the following series of measurement and modeling steps.

The reflectance of a painted aluminium test sample was measured in the SOC-100 over a range of angles at room temperature and at an elevated temperature. The selected sample had been through repeated thermal cycles in previous measurements, which improved the temperature stability of the measured spectral reflectance. The SOC-100 heater stage controller is not stable at low values, and the temperature value varied between $75°C$ and $90°C$ in a systematic fashion. The mean temperature was then $82.5°C$. The reflectance showed nominal directional and temperature sensitivity, and the average value was taken as a reference shown in Figure 8.19. This reflectance measurement was used to determine the emissivity by the application of Kirchoff's Law and the conservation of energy. The response is notably flat in the range of $7 - 11\mu m$, so this region was selected for further evaluation. In this process, the measured spectral reflectance and derived spectral emissivity are used in place of modeled data. In the evaluation of periodically patterned samples, modeled data will be used to predict the measured directional and spectral radiance.

The sample was then moved to the emissometer, situated at a 15 degree angle of incidence, and an initial background level measurement was taken. The result of
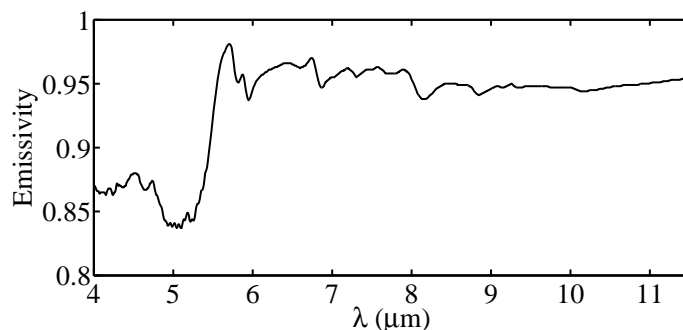
Figure 8.19: The emissivity of a painted aluminium sample was predicted from HDR measurements taken on the SOC-100. Measurements were taken at 10 degrees, 15 degrees and 20 degrees angles of incidence, to establish that there was no substantial angular dependence, and that the aperture function played a minimal role. Only the 15 degree result is shown.

this measurement, when calibrated to radiance, is shown in Figure 8.20 (a). This result is the combination of a room temperature reflected background component and a room temperature sample self-emission component. The average measured room temperature was $27°C$, and the measured spectral radiance approximates a blackbody at this temperature, as expected. Based on this background temperature, the reflected spectral radiance contribution for modeling was computed by scaling the spectral reflectance measurement, Figure 8.19, by the spectral radiance of a blackbody at the background temperature. This predicted spectral radiance contribution is shown in Figure 8.20 (b).

The white-painted-aluminium sample was then heated on the emissometer sample holder to a mean temperature of $85.2°C$. A nine surface-point variance of $2.9°C$, was measured with thermocouples, peaking at $90.4°C$. This deviation exceeds the thermocouple measurement uncertainty, so temperature measurements must be made across the surface of every test sample to accurately establish a mean surface temperature. A spectral radiance measurement was then taken for the sample. This measurement includes a self-emission and reflected background component. Due to the directional independence of the samples
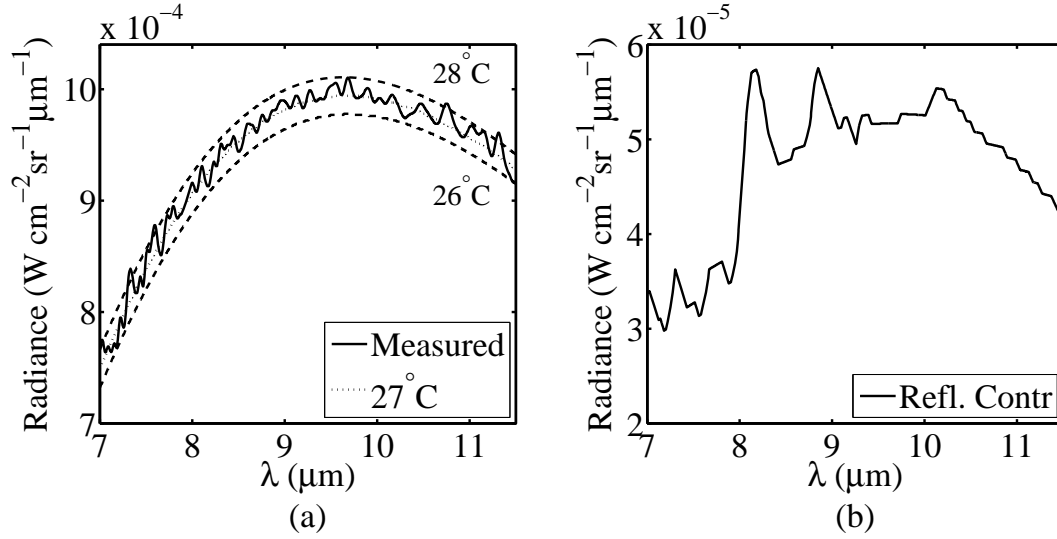
160

Figure 8.20: To account for the reflected component from the room in later measurements, a spectral radiance measurement was taken before heating the sample. (a) The measured spectral radiance value is compared to the room temperature, and bounded. (b) The measured sample reflectance was applied to a blackbody spectral radiance curve at the mean room temperature to predict the reflected component which must be added to the spectral radiance computed for the sample at an elevated temperature to match the measured results.

reflectance and emissivity, the impact of the emissometer's angular instrument function is negligible.

Next, a modeled spectral radiance, L_{mod}, comprised of the sum of a reflected component at the background temperature, and a self-emission component at the mean sample temperature was computed. The reflected component was computed by weighting a blackbody spectral radiance curve at $27°C$, $L_{BB}(\lambda, T_{bkg})$, by the measured spectral reflectance of the sample, $\rho_S(\lambda, T_S)$. The self-emission component was computed by weighting a blackbody spectral radiance curve at $85°C$, $L_{BB}(\lambda, T_S)$, by the sample emissivity, $\epsilon_S(\lambda, T_S)$.

$$L_{mod} = \epsilon_S(\lambda, T_S) L_{BB}(\lambda, T_S) + \rho_S(\lambda, T_S) L_{BB}\left(\lambda, T_{bkg}\right) \qquad (8.2)$$

The results of the measured and modeled spectral radiance values are shown in Figure 8.21 and show excellent agreement. This straightforward process for incorporating the reflected background contribution, which will be present in any measurement, into a radiance model for a test sample is required for all subsequent modeling.
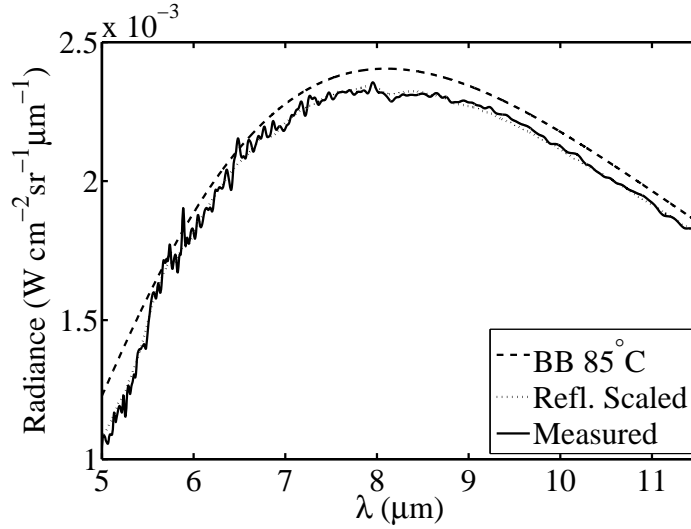

Figure 8.21: Comparison of the measured radiance of a heated white painted aluminium sample and a modeled value, including background reflection components and self emission. A bounding curve at $85°C$ is shown for reference.

The aluminium-on-silicon test grating was then measured over a range of angles, both to demonstrate that the plasmonic effect was observable, and to establish the angular instrument function of the emissometer. In Figure 8.22 (a) and (b), the measured spectral radiance values were normalized to the spectral radiance of a blackbody at the sample surface temperature to produce an apparent emissivity, ϵ_{App}, which includes the reflected background component for ease of comparison with modeled and reflectance-based measured data from other systems.

$$\epsilon_{App} = \frac{\epsilon_S\left(\lambda, T_S\right) L_{BB}\left(\lambda, T_S\right) + \rho_S\left(\lambda, T_{bkg}\right) L_{BB}\left(\lambda, T_{bkg}\right)}{L_{BB}\left(\lambda, T_S\right)} \tag{8.3}$$
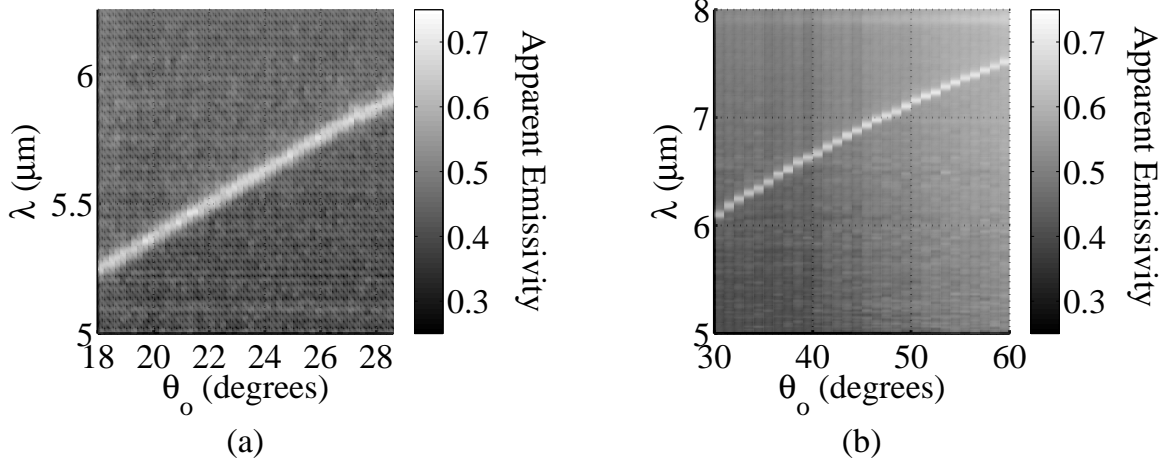
162

Figure 8.22: (a) The measured apparent emissivity of an aluminum-on-silicon $4\mu m$-period shallow test grating at $82°C$ is shown with 0.2-degree angular sampling from 18 to 30 degrees. (b) A coarser measurement of the same grating at $85°C$ is shown with 1.0-degree angular sampling from 30 to 60 degrees. The measured radiance of the heated samples, which includes a reflected background component, is normalized to the mean surface temperature of the sample.

To fit the aperture function to an angular sweep at $5.6\mu m$, the total reflectance, calculated by RCWA methods and shown in Figure 8.11 was converted to a directional emissivity profile by conservation of energy and the application of Kirchhoff's Law. In this case, only the instrument function of the emissometer system needed to be convolved with the RCWA data, since the computed emissivity values define the angular profile. The measured and modeled apparent emissivity data fit at $5.6\mu m$ is shown in Figure 8.23.

An $82°C$ mean surface temperature and $27.2°C$ reflected background temperature were employed for the modeled data. In the measurement configuration, the $2.54cm$ lead optic, tilted at 21 degrees, and $120cm$ from the sample yields a 1.13-degree entrance aperture, while the measured data fitted at 1.17 degrees with a MSE of $4.75e^{-4}$ degrees. Given the other sources of error in the experiment a 0.04-degree error in the instrument function angular diameter is not significant.
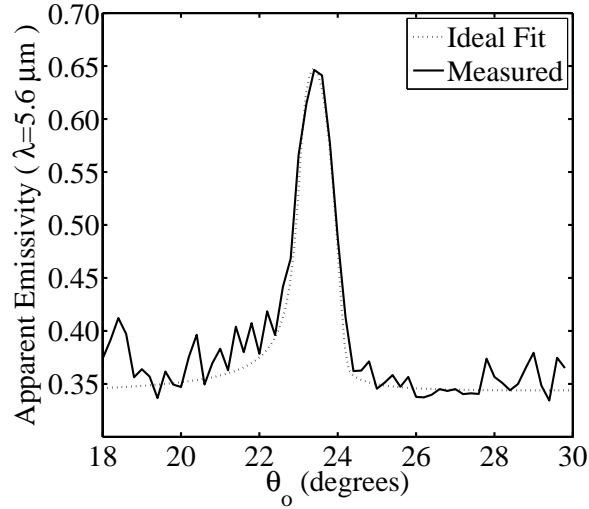
163

Figure 8.23: The ideal instrument function fit, with an angular aperture subtending 1.17 degrees, is shown in terms of apparent emissivity. The measured, mean surface temperature employed in the modeled data and to normalize the measured data was $82°C$. The background temperature was $27.2°C$.

8.7 Shallow Grating in PMMA

A shallow grating was imprinted and sputtered to provide a test article with established performance, allowing the process quality to be evaluated. Ideally, the measured reflectance and emissivity profiles from the aluminium-on-silicon and aluminium-on-PMMA gratings would be the same. To determine the difference, and hence the error, an initial matched specular sweep was conducted of an 100nm aluminium-on-PMMA imprinted grating with a 4μm period and $f = 0.5$ fill factor on the IR-VASE®. The specular reflectance of the aluminium-on-silicon shallow test grating, Figure 8.24 (a), is compared to the aluminium-on-PMMA shallow grating, Figure 8.24 (b).

The reflectance values are clearly lower for the aluminium-on-PMMA sample in broad angular and spectral regions which prompted further examination. To examine the source of this deviation, a fixed transmission angle was set, 45 degrees, and an angular sweep taken in the same manner as that was used to establish the angular instrument function bounds. In this case, the aluminium-on-silicon grating, Figure 8.25 (a), shows the same angular
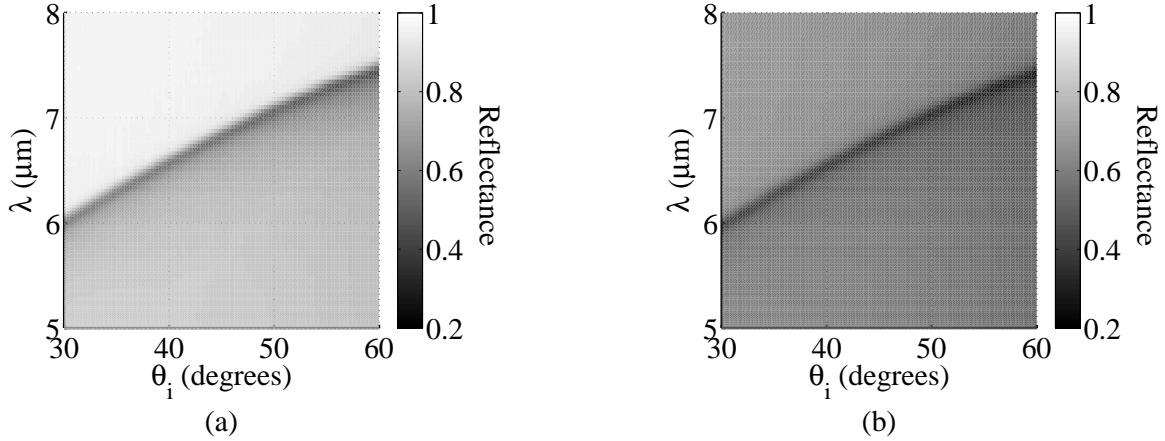
164

Figure 8.24: The matched specular reflectance is shown for (a) an aluminium-on-silicon grating and (b) an aluminium-on-PMMA grating. The overall reflectance of the aluminium-on-PMMA grating is clearly lower over this range.

bounds as the Gold Mirror (GM), with the peak height adjusted by the relative specular reflectance of the grating. The aluminium-on-PMMA shallow grating, Figure 8.25 (b), shows substantial broadening.
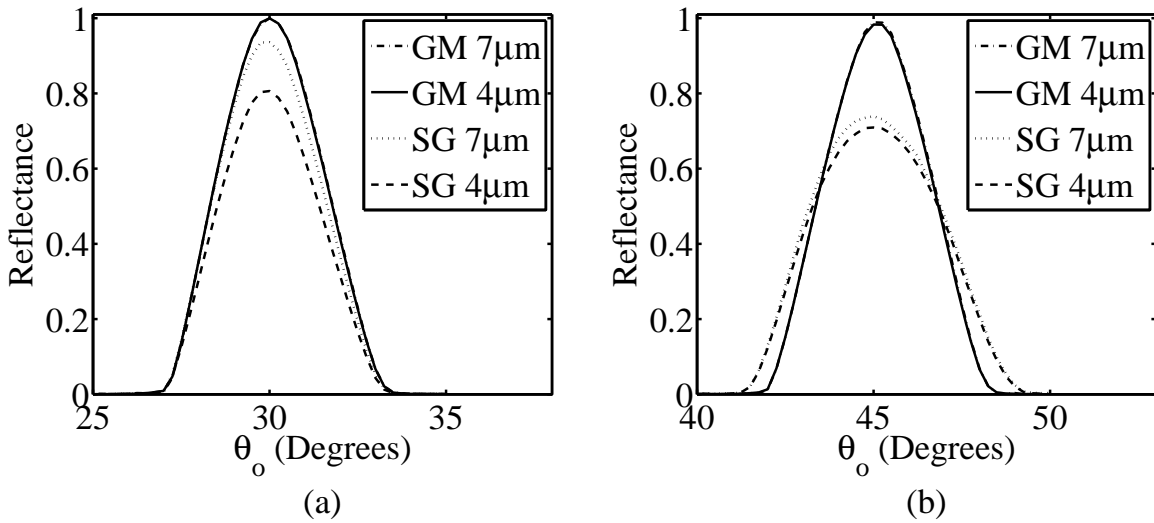

Figure 8.25: (a) The angular profile of the reflected lobe of a gold mirror and an aluminium-on-silicon shallow grating is shown for two wavelengths. The profiles share the same angular bounds. The angular profile of the reflected lobe of an aluminium-on-silicon and an aluminium-on-PMMA shallow grating are shown in (b). The aluminium-on-PMMA profiles shows substantial broadening.

165

The ratios of the total reflectance between the aluminium-on-silicon and aluminium-on-PMMA shallow gratings are compared in the spectrally flat region above $8\mu m$ in Figure 8.26. In (a), the fixed transmission angle measurements show a mean ratio of 0.74, while the matched specular values show a reflectance value of 0.88. However, when the ratio is globally computed in the spectral and angular space in (b), it is evident that where the absorption dominates, the sharp spectral feature was retained and no constant ratio is observed. This precludes a simple linear loss modification to the RCWA computed data. It does however, suggest that the measured curvature of the samples, averaging a $3.2m$ curvature radius, plays a key role.
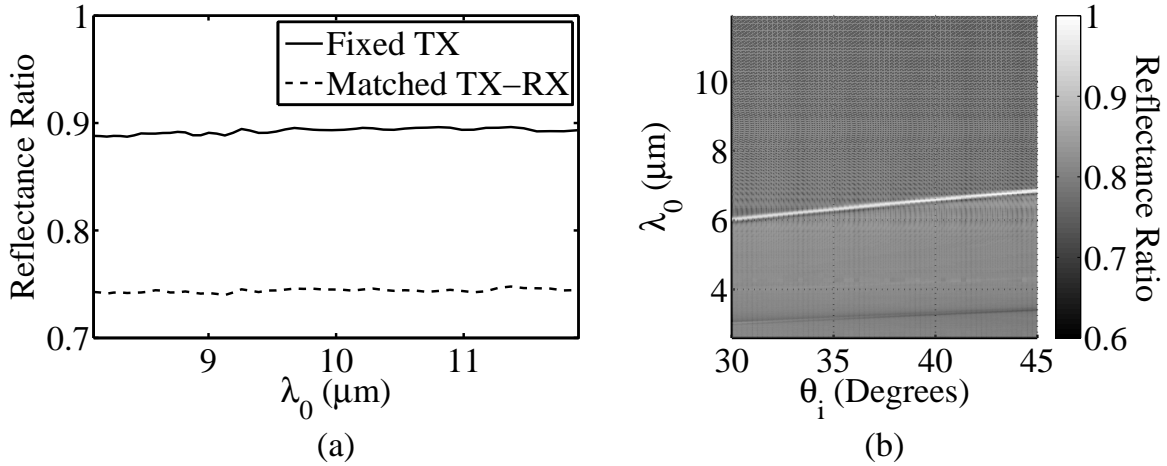
Figure 8.26: (a) The aluminium-on-silicon to aluminium-on-PMMA shallow grating spectral reflectance ratios for both a fixed angle-of-incidence sweep and a matched specular angular sweep. (b) The ratio of the specular reflectances, measured on the IR-VASE®is non-uniform near the absorption feature running from $6\mu m$ at 30 degrees angle-of-incidence to $7\mu m$ at 45 degrees angle-of-incidence.

While surface curvature is clearly evident in Figure 8.26, some surface roughness losses must also be present. To better isolate the contributions, the sample was also measured on the SOC-100. In this case, the larger collecting aperture diameter and hemispherical illumination mitigates the impact of the surface curvature. Figure 8.27

166

shows a very high reflectance, averaging 0.96 in (a) the TE case above the absorption feature region, while (b) the TM case shows somewhat reduced values averaging 0.88. The reduction in the TM case constitutes an average 0.10 reduction in reflectance. So long as the effect of the scattering and roughness is random, it acts primarily to reduce the selectivity of the emission peak.
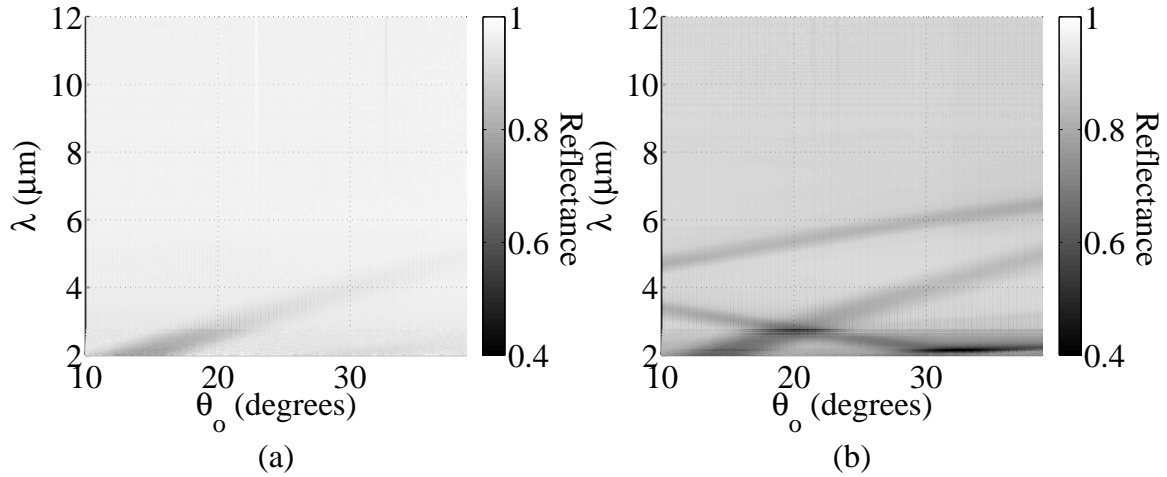

Figure 8.27: (a) TE and (b) TM polarized HDR measurements of a $4\mu m$ period aluminium-on-PMMA shallow grating. The measured reflectance values are approximately 10% lower than those measured for the aluminium-on-silicon shallow grating.

Both surface curvature and increased diffuse scatter cause angularly narrow emission peaks to be broadened slightly, but the form of the emission feature remains constant. This is precisely what is observed in Figure 8.28 (a), where the measured directional spectral radiance values are normalized to the mean surface temperature of the sample to produce an apparent emissivity. Peak broadening is observed in the angle-dependent radiance measurement shown in Figure 8.28 (b), which includes a $26°C$ background contribution in the modeled data. The summed reflection and emission components were convolved with the previously determined angular instrument function to produce the expected radiance values. A reasonable fit is observed, with the peak broadened and lowered.
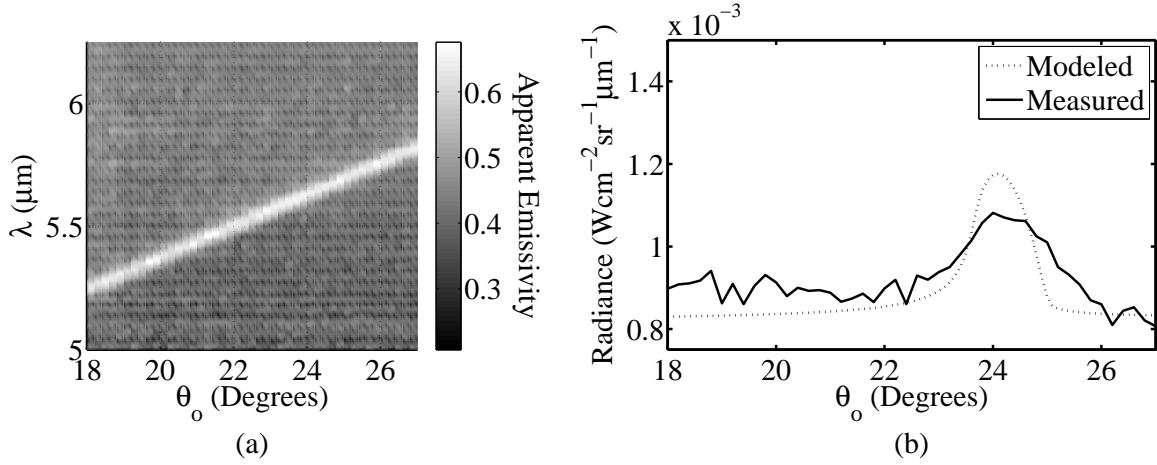
Figure 8.28: (a) Apparent emissivity, including a background reflected component, normalized to the mean surface temperature of the sample. (b) Angular aperture function background and self-emission radiance at $5.6\mu m$ convolved solution for modeled and measured data.

8.8 Coupled Resonant Cavities

The coupled resonant cavity design is the most difficult of the designs developed to measure. This is primarily due to the lack of notable features away from normal, where all of the reflectance measuring instruments operate, which are precisely indicative of the normally directed response. Besides implementing and evaluating a coupled resonant cavity design, the additional objective of examining the emissivity behavior of the device as additional metal thickness was deposited was addressed. For clarity, the device performance will be addressed at the metal thickness at which peak performance was observed, then the metal thickness variation is examined.

First, the IR-VASE® was used to establish the presence of surface curvature, and predict the reflectance in a region expected to exhibit low feature content. The effect of surface curvature is clearly evidenced in Figure 8.29 (a). The broadening is similar to that observed for the shallow grating, but substantially more power is missing in the tails of the angular measurement than in the shallow grating case.

168

To examine any increase in the diffuse scatter or general absorption, the CRC structure reflectance was measured in a region with low angular-spectral variation on the SOC-100. The sample was moved to the emissometer and swept through a series of angles, both to confirm that there was no overt angular background dependence, and to establish the effective temperature of the background. The effective temperature is observed to be $28°C$, subject to minor variations and noise. When heated, the mean surface temperature was found to be $82°C$ which is slightly high for the PMMA substrate. However, the sample survived the initial measurements. Figure 8.29 (b) shows excellent measured to modeled agreement for these temperatures for the approximately 0.91 reflectance value measured for this spectral range on the SOC-100.
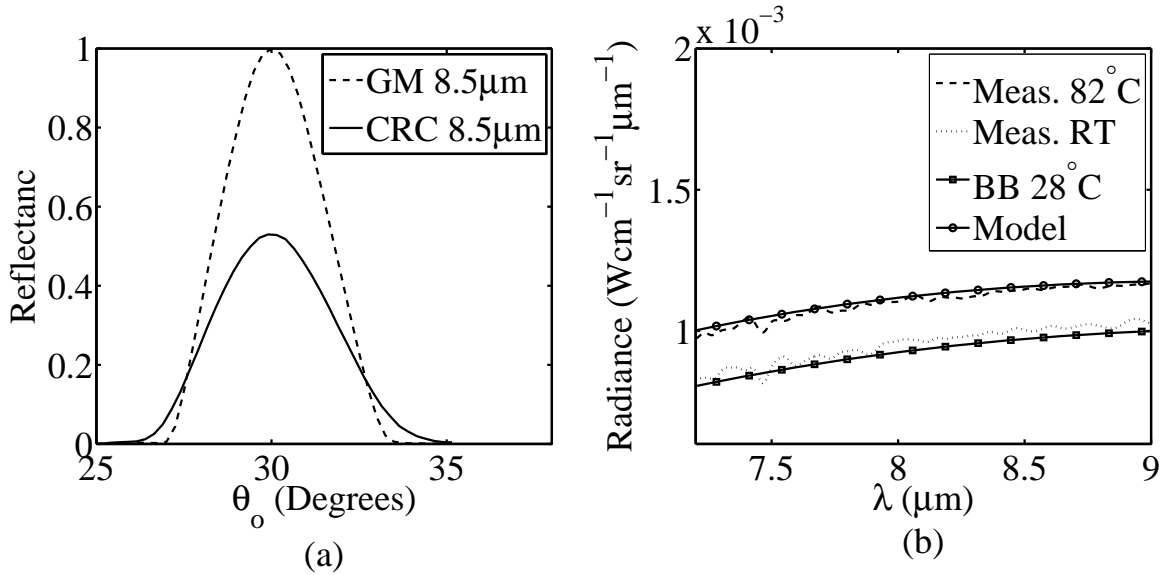
Figure 8.29: (a) The specular reflectance profile of a CRC is shown, as measured on the IR-VASE®, for a fixed angle of incidence at $8.5\mu m$. The effects of surface curvature are clearly visible. (b) Reflectance values were measured for the CRC sample on the SOC-100 and used to computed the modeled radiance values at $8.5\mu m$ including a background component. These values are compared with the radiance measured by the emissometer for the sample at room temperature, $28°C$, and at an elevated temperature, $82°$.

With the background and self-emission temperatures established, a directional emission measurement sweep was taken. The results of the direct measurement, in apparent emissivity, are shown in Figure 8.30 (a). In angular and spectral space, with the effects of the emissometer aperture function, it is clear that the CRC exhibits the normal peak. It also exhibits an emission branch at longer wavelengths, which varies with angle, and a lower branch, below the design wavelength, as predicted by RCWA. The low signal-to-noise ratio makes additional analysis difficult. However, in Figure 8.30 (b), it is observed that the peak and location are reasonably well fit, with additional broadening similar to that observed in the aluminium-on-PMMA shallow grating case.
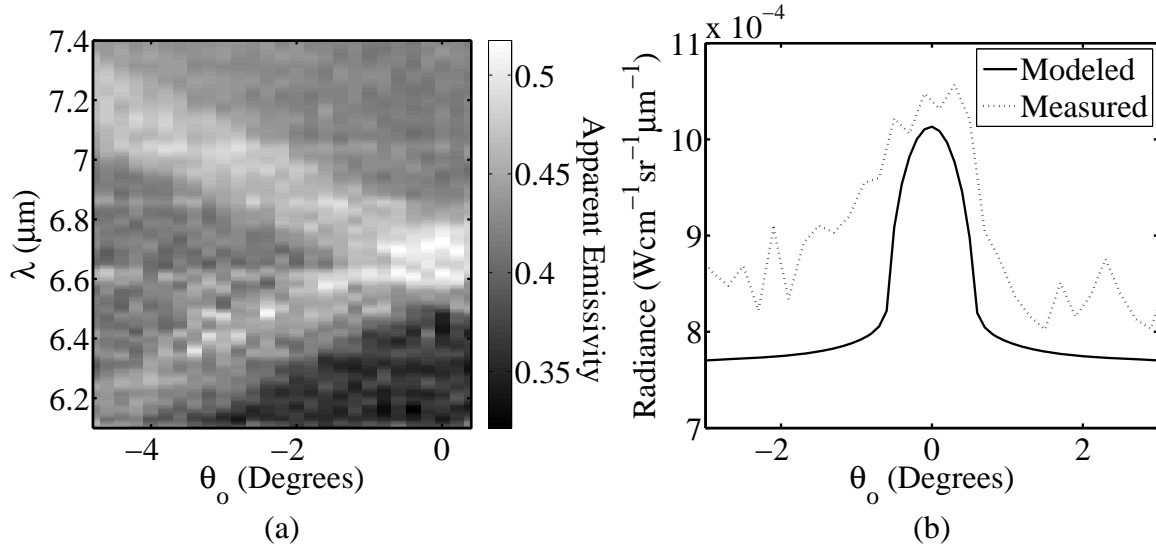
Figure 8.30: (a) The directional and spectral apparent emissivity of a CRC sample, with a sputter aluminium depth of 400nm is shown. (b) The measured background and sample surface temperatures were used to generate modeled data, employing the angular instrument function, for comparison with the measured results. While the peak and base levels of the modeled convolution at 6.666μm demonstrate functional agreement with the noisy measured data, there is notable broadening in the measured data.

Based on the previous measurements, the impact of varying the deposited metal thickness on the imprinted substrate may be addressed. Considering the noise and angular resolution, the behavior is treated spectrally at normal for this known behavior case. The

metal thickness was varied by 50*nm* intervals from 50*nm* to 500*nm*, and the measured apparent emissivity values were computed for each sample, based on the measured surface temperatures. The results are shown in Figure 8.31.

Although all of the angular instrument function effects are present, it is clear that resonant behavior at 6.666*μm* is absent at aluminium deposition thicknesses less than 250*nm*, appears and peaks between 300*nm* and 450*nm*, then falls off by the 500*nm* thickness point. The cavity structure demonstrated the predicted behavior, as the differential metal filling rates between the upper and lower surfaces increased the depth of the cavities to the resonant depth, then overshot. The angular precision of the measurement scheme precludes a more detailed evaluation of the resonant behavior in PMMA substrates, which do not tolerate higher temperatures. The observed surface curvature also reduces the reliability of any cavity quality metric.

8.9   Dual Cavity Width Design

The dual cavity width design was expected to show at a minimum, an increased diffuse scatter due to dimensional deviations. This expectation is born out in the reflectance measurements shown in Figure 8.32 (a) for the IR-VASE®, which can be directly compared to the values taken on the SOC-100, 8.32 Figure 8.32 (b) at the same angles. The larger angular aperture function of the SOC-100 nearly masks the directional absorptance response at 10*μm*. The specular and directional reflectance away from the designed absorption features show substantially lower values than the model in both cases. Figure 8.32 (b) shows close agreement between the specular and HDR values, which indicates that the surface absorption is significant.

To further isolate whether the reflection deviations are due to surface roughening, dimensional deviations or curvature, cross polarized results are compared in Figure 8.33. The TE results show the expected high reflectance values in (a), indicating that the overall
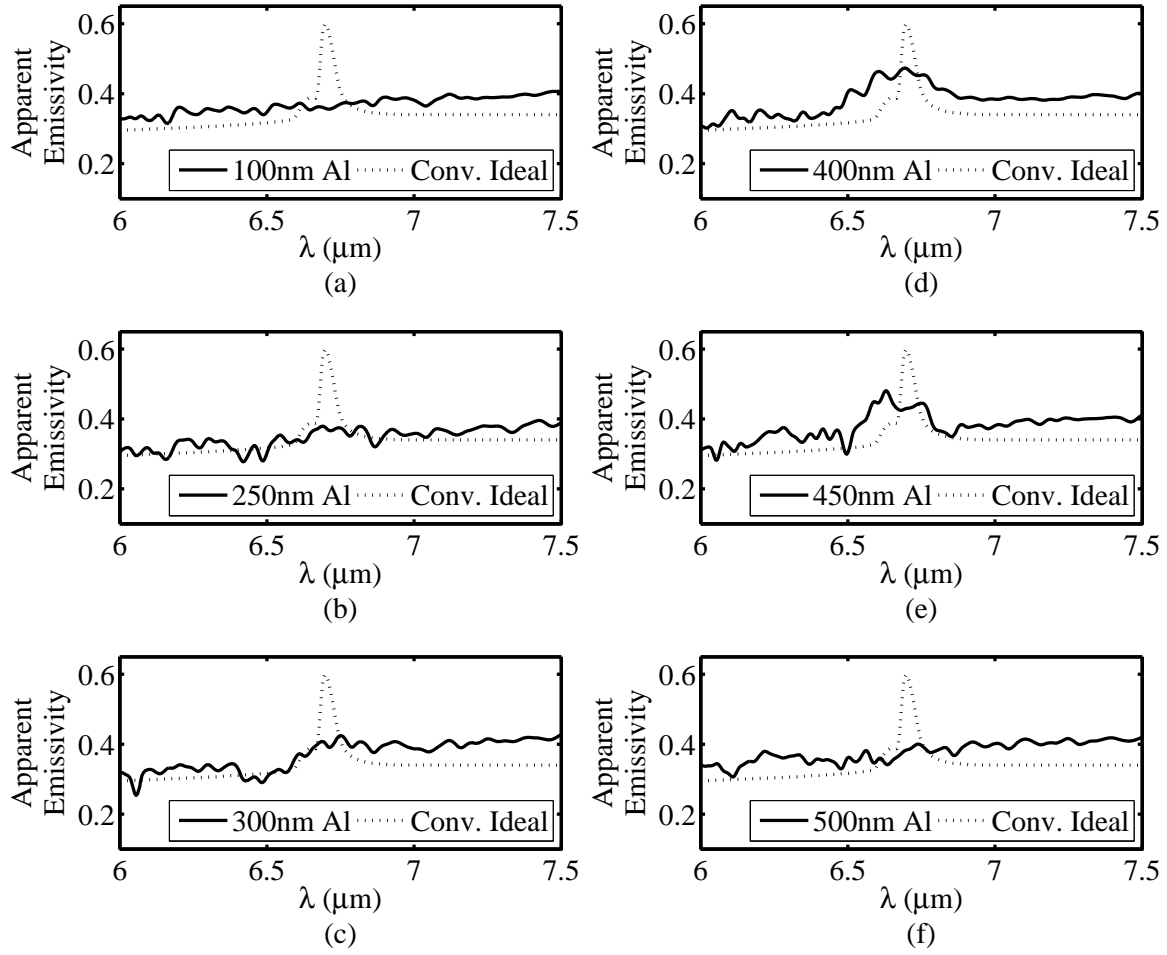
171

Figure 8.31: Subfigures (a)-(f) show the evolution of the normally directed apparent spectral emissivity of the aluminium-on-PMMA CRC structures with increasing metal deposition thickness. The ideal apparent spectral emissivity was computed for a CRC structure at the resonant cavity depth, including reflected background contributions and angular instrument function effects, for the design wavelength of 6.666μm, at a surface temperature of 80°C and background temperature of 26°C. This objective behavior is shown on each subplot for reference. The spectral response is flat, as predicted, for aluminium deposition thickness of 250nm or less (a)-(b). A spectral peak, centered around 6.666μm then appears as the aluminium deposition thickness increases the cavity depth to the resonant condition, beginning at 300nm and peaking by 450nm of metal thickness (c)-(e). The peak then rapidly falls off, once the resonant cavity depth is surpassed and is absent once the metal deposition thickness increases to 500nm (f).
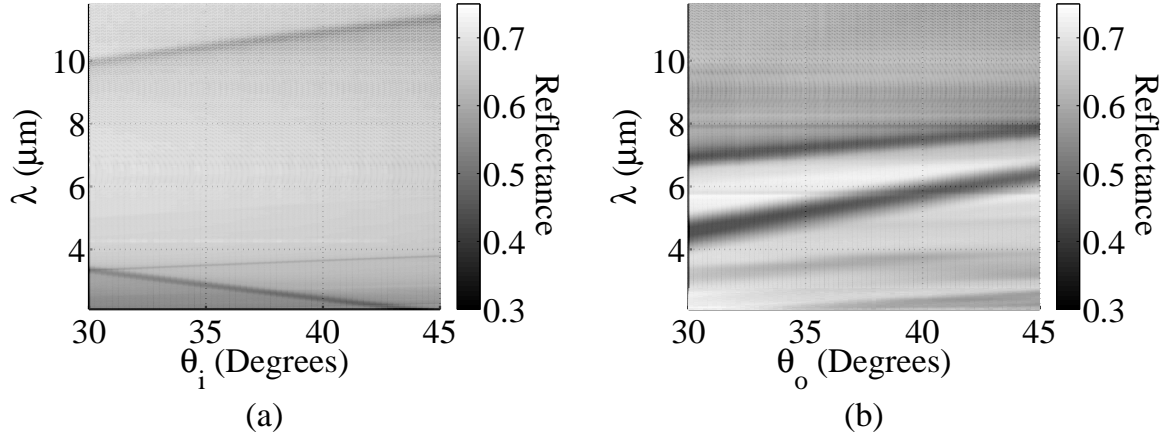
Figure 8.32: The TM polarized specular reflectance of the dual cavity width sample, (a) as measured on the IR-VASE®is compared with (b) the hemispherical directional reflectance from the SOC-100 as part of evaluating the quality of the fabrication, rather than its designed response.

quality of the surface was good. The TM results in (b), which are a close approximation to the absorption behavior persist in showing substantial absorption in spectrally flat regions.
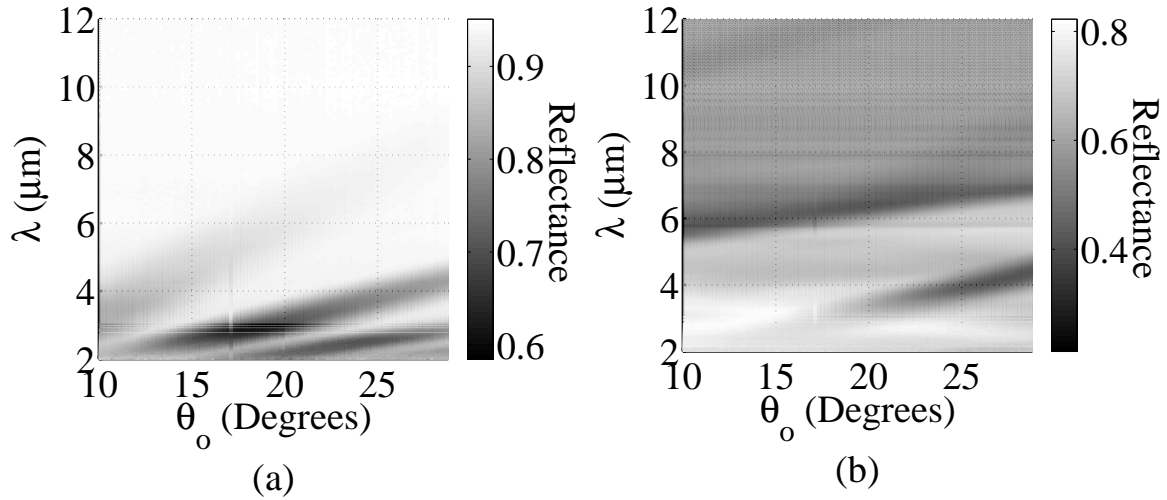
Figure 8.33: TE and TM polarized HDR measurements. (a) Clearly, the TE polarization shows very much the values expected for a flat aluminium surface above the geometric regime at $9\mu m$. (b) The TM polarization shows substantially more apparent absorption in the design region than predicted.

Surface curvature was expected and is exhibited relative to a gold mirror as shown in Figure 8.34 (a). In Figure 8.34 (b), emissometer data taken at room temperature and normal is used to establish the background contribution. As with previous samples, the background value was used to compute a reflected component, based on an SOC-100 measurement, and added to the self-emission component at the heated sample temperature to compute the expected radiance observed in a region showing little angular and spectral variation. Excellent agreement is shown for the average temperature values using the TM reflectance value of 0.5024 found by HDR measurements. This indicates that the effects of the roughening observed in the fabrication process are minimal.
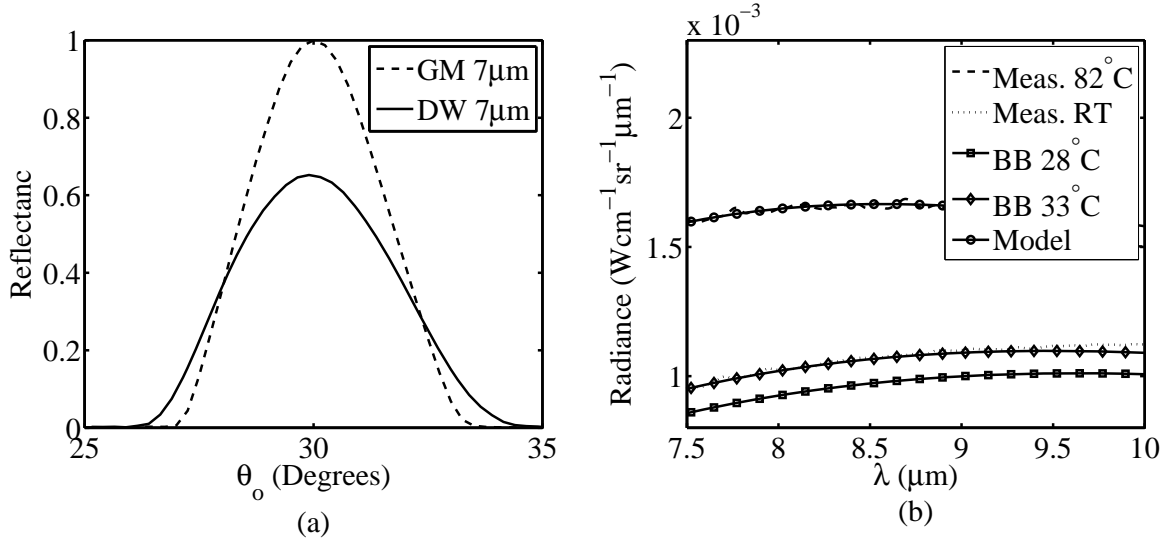

Figure 8.34: (a) The specular reflectance profile of the dual-cavity-width structure, as measured on the IR-VASE®, shows response broadening due to surface curvature similar to all of the previous aluminium-on-PMMA samples. (b) Modeled and measured radiance values for the dual-cavity-width structure show excellent agreement, away from the designed absorption features. So, the effects of the roughening observed in the fabrication process are minimal.

A full angular sweep of measurements was taken and normalized to produce an apparent emissivity. Based on the spectral feature locations, the samples did not take the full impression depth in this case, as was observed with the coupled resonant cavity

design. So, the absorption feature is centered at $9.5\mu m$ in Figure 8.35 (a), rather than the expected $10\mu m$ for a full $1\mu m$ depth. However, it is clearly lifted away from the $9\mu m$ period order transition line, and broadened in accordance with the predicted profile, shown with angular instrument function effects in Figure 8.35 (b). Since the surface roughness effects on the emissivity were observed to be minimal, it is likely that the larger critical dimension deviations of the dual-cavity-width photomask, coupled with the surface curvature, is responsible for the higher-than-predicted apparent emissivity around the designed feature.

(a)   (b)
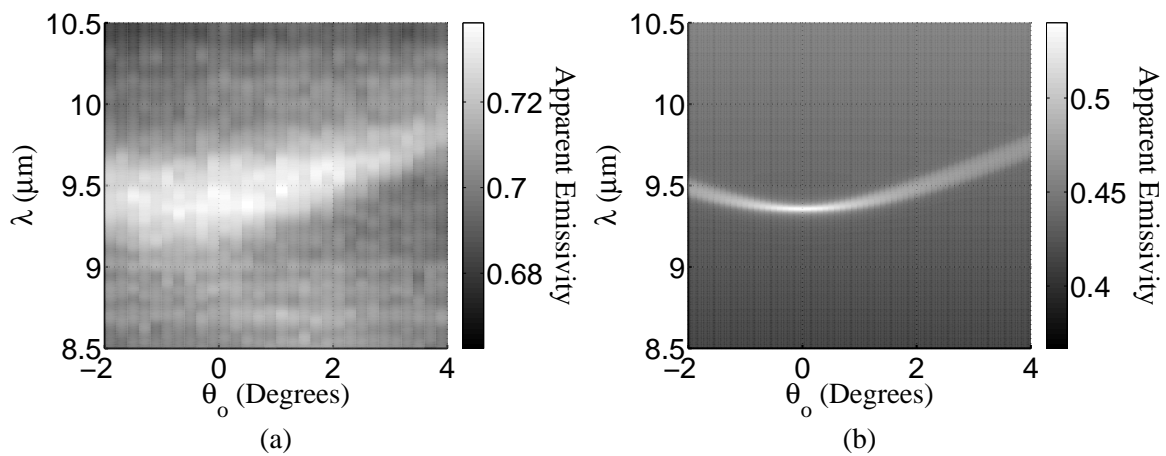
Figure 8.35: The apparent emissivity of the dual cavity width design, normalized to the sample mean surface temperature (a) is compared to a computed apparent emissivity value, which includes background scatter and angular aperture effects (b).

8.10 Conclusion

The basic operation of FTIR instruments was reviewed, and the scatterometry concept of the angular instrument function was developed. For each instrument, a measurement configuration was developed which optimized the angular instrument function with respect to system noise and measurement time. Geometrically developed angular instrument functions showed good agreement with measured responses taken for a common test article. Then, the performance of fully processed shallow grating, CRC, and dual cavity width

samples was evaluated. The fabricated surfaces showed random error and a definite bias due to surface curvature.

The measurements verified the thermal self-emission behavior of a CRC structure fabricated in an aluminium-sputtered PMMA substrate to complete a novel implementation of this design concept. It has been shown that the expected engineering challenges can be effectively addressed and that the primary unexpected error source, excessive surface curvature, is a result of the particular fabrication equipment employed. This degree of curvature is not typical in the compact disc manufacturing process and is not a barrier to effective high-throughput fabrication[25]. The viability of increasing the metal deposition thickness on a patterned substrate to meet additional mechanical, thermal, or electrical property requirements for a CRC structure has also been verified. The simulated self-emission performance of a novel dual-cavity-width design was also experimentally verified.

IX. Conclusion

9.1 Summary

The primary shortcoming of current directional thermal emitter designs is the fabrication process. Difficult, time-consuming and expensive processes such as etching silicon carbide or multiple etch and removal processes must be employed to fabricate each example of the emitter, as detailed in Chapter I. This substantially limits fabrication throughput, making the mass production of most directional thermal emitter designs unrealistic. The primary objective of this work was to demonstrate the fabrication of directional thermal emitters by a high-throughput fabrication process.

A theoretical overview for directional thermal emission was developed beginning with the theoretical foundation of spectrally and directionally selective reflection and absorption in Chapter II. The Rigorous Coupled Wave Analysis (RCWA) method of computing the scattered field for a periodic surface was presented for computing both directional reflection and absorption. Classical thermal emission was reviewed, which leads to the nearly isotropic far-field emission pattern of a thermally excited surface. The partial coherence of the near-field, above surfaces which support surface plasmons, was presented in terms of the cross-spectral density tensor. This allowed a partial coherence distance to be established for the near-field, which has been shown to go as the surface wave propagation distance. The basis for coupling the partially coherent near-field to the far field was then presented for smooth, randomly roughened and periodic surfaces, highlighting the relationship between shallow grating parameters and the directional and spectral distribution of its thermal emission.

Key points in the study of surface plasmons, which are the source of the near-field spatial coherence exploited for directional emission, were presented in Chapter III. It was then shown how these surface plasmons studies led to the evolution of directional thermal

177

emitters, through physical structures of ever-increasing physical complexity. Published directional emitter designs now include multi-layer coatings, multi-dimensional gratings, photonic crystals and micro-fabricated antennas, as presented in Chapter III.

A scalable fabrication process for low-temperature directional thermal emitters, described in detail in Chapter VII, introduced specific modeling, design, and measurement requirements. Two modeling requirements, which enable accurate design work, were addressed in Chapter IV. First, the complex index of refraction of as-deposited DC magnetron sputtered aluminium and its passivation oxide layer were measured, rather than determined from published data. Second, a well established method for predicting the physical profile of DC magnetron sputtered metals over step-profiled surfaces was implemented and coupled with an RCWA model. In Chapter V, a third modeling requirement was addressed. The RCWA method was extended to compute reflected scatter from directional absorbers under finite longitudinal spatial coherence conditions, as might be encountered in the proposed applications.

A design trade space, based on the surface wave propagation properties of highly conductive metals at mid- to far-infrared wavelengths, was established in Chapter VI. It was then exploited to design a Coupled Resonant Cavity (CRC) directional emitter which accommodated an exceptionally thick deposited metal layer. A novel dual-cavity-width design, particularly suited to the fabrication constraints, was then developed to produce an angularly broadened emission profile from a periodically patterned surface. The fabrication method itself is predicated upon well-known techniques. However, as with all microfabrication processes, significant experimentation and calibration was required to produce the desired results. The complete fabrication process and examples for the designed structures were presented in Chapter VII.

The expected reflection and emission behavior of the fabricated structures required that the angular resolution versus signal-to-noise ratio be optimized for each instrument

178

employed. Angular instrument functions were developed to map a common set of ideal modeled results into measurement predictions for each instrument, allowing cross-instrument measured result comparisons. The measured results from the final structures unambiguously demonstrated the predicted behavior, subject to fabrication-induced deviations. The instrument characterization and design measurements were presented in Chapter VIII.

9.2 Contributions

The contributions of this work are divided into four key areas, but the complete expression of each contribution does not necessarily coincide with a single chapter.

9.2.1 *Finite Longitudinal Spatial Coherence Modeling.*

The RCWA method for predicting the scatter from periodic surfaces was extended to include the excitation of a surface by an incident field with finite longitudinal spatial coherence. This extension overcomes a failure of the previous method, i.e. convolution of computed order weights with a broadening function and normalization, of assigning angular lobe widths to the scatter from periodic structures. The previous method does not accurately represent the impact of rapidly varying directional absorption on the scattered angular lobe profiles. The method developed here accurately represents both the angular lobe profile broadening due to the finite longitudinal spatial coherence of the incident field and the directional absorption inherent in these structures on the angular lobe profile. The improvement introduced by this method will allow for the incorporation of fabricated directional thermal emitters into ray-tracing-based optical design methods which require surface Bi-directional Reflectance Distribution Functions (BRDF). The development is described in Chapter V and the work was submitted for publication as "Partially coherent bidirectional reflectance distribution data computation for modeling periodic plasmonic structures at infrared wavelengths" to Infrared Physics and Technology on 24 January 2013, and is currently in revision based on reviewer comments.

9.2.2 *Novel Fabrication of Coupled Resonant Cavity Structures.*

The novel application of a high-throughput fabrication process to the production of CRC directional emitters was established. The process enables an order-of-magnitude increase in fabrication throughput over current methods, for compatible directional thermal emitter designs. The novel incorporation of a fabrication model into the directional thermal emitter design process allowed the prediction of the evolving response of the structure to increasing metal deposition thicknesses. Increasing the metal deposition thickness improves the mechanical and thermal properties critical to the durability of an exposed thin-film coated surface, but reshapes stepped-profiles. This reshaping rapidly degrades the emission performance of CRC designs optimized for rectangular stepped-profiles. It was shown, for the first time, that a mid-infrared CRC structure can be specifically designed to support metal deposition thicknesses sufficient to reshape the cavity profile at a minimal cost to the emission performance.

The CRC structure design process was presented in Chapter VI. The structure was fabricated by the process described in Chapter VII, and the thermal self-emission performance predictions were verified in Chapter VIII. This work is prepared for submission for publication as, "Selective Thermal Emission from a Patterned Metalized Plastic" to Optics Express.

9.2.3 *Dual-Cavity-Width Structure Design.*

A new directional thermal emitter design was developed with the objective of generating flat-multilayer-like emission performance from a periodic surface microstructure. This new dual-cavity-width design overcomes the limited availability of materials with the necessary permittivities at infrared wavelengths for the fabrication of selectively emitting flat-multilayer structures. The design was constrained to suit the high-throughput fabrication process developed in this work. The dual-cavity-width grating structure design process was presented in Chapter VI. The structure was fabricated by the process described in Chapter

VII, and its performance was evaluated in Chapter VIII. This work is also being prepared for submission to Optics Express, emphasizing the design of thin-film-stack-like emission performance from a periodically patterned surface.

9.2.4 *Novel Infrared Instrumentation Modeling.*

Finally, a process of instrument characterization was developed to correlate the results of specular reflectance, hemispherical directional reflectance, and low-temperature emissivity measurements, including reflected components, of directional thermal emitters with a common set of modeled data. The novelty of this contribution lies in the use of a common modeled data set across the different measurement instruments. The comparison of measured data from multiple instruments to a common modeled data set improves the assessment of fabrication quality for directional thermal emitters, which are otherwise difficult to assess as-fabricated. In this work, it enabled the differentiation between the impacts of unintended induced surface curvature from surface profile deviations on the designed structures' performance. Methods for transforming the common set of modeled data into forms directly comparable to the data measured by each instrument were presented in Chapter VIII Section. The methodologies and examples are being prepared for submission for publication in the Review of Scientific Instruments.

9.3 Future Work

The fabrication process established in this work showed several areas in which fabrication-specific research could be conducted. First, the Deep Reactive Ion Etching (DRIE) Bosch process produces sidewalls which are not actually smooth. The development of a final etch process which reduces the sidewall features of photoresist masked DRIE profiles would be particularly useful in future directional thermal emission research. It is particularly pertinent since far-infrared features generally require features of depths for which non-Bosch process etch chemistries are generally inadequate.

In another fabrication specific research area, simply completing a full Blech model calibration on any given magnetron sputtering system for a particular set of metal deposition parameters is a substantial experiment. If this were completed, then a more refined deposition model could be employed, and validated, to better predict deposition profile deviations on surface micro-structures.

In terms of measurement research, signal-to-noise requirements generally require that any *in situ* infrared properties measurement be made with the sample illuminated by an external source. However, the measured results presented here indicate that instruments such as the SOC-100 hemispherical directional reflectometer and possibly portable instruments which work on similar principles, require a more complete model to predict the measured scatter from periodic surfaces designed as directional thermal emitters. The development of such a model is a substantial contribution to measurement science which remains to be made.

Bibliography

[1] J. C. Jafolla and W. R. Reynolds, "Bidirectional Reflectance Measurements for High-Resolution Signature Modeling," pp. 184–197, 2004.

[2] J. W. Goodman, *Statistical Optics*. New York: Wiley, 2000.

[3] E. L. Dereniak and G. D. Boreman, *Infrared Detectors and Systems*. New York: John Wiley and Sons, Inc., 1996.

[4] W. L. Wolfe and G. J. Zissis, *The Infrared Handbook*. 1978.

[5] M. F. Modest, *Radiative Heat Transfer*. New York: McGraw-Hill, 1993.

[6] C. Fu and Z. Zhang, "Thermal Radiative Properties of Metamaterials and Other Nanostructured Materials: A Review," *Frontiers of Energy and Power Engineering in China*, vol. 3, no. 1, pp. 11–26, 2009.

[7] J. J. Greffet, R. Carminati, K. Joulain, J. P. Mulet, S. Mainguy, and Y. Chen, "Coherent Emission of Light by Thermal Sources," *Nature*, vol. 416, no. 6876, pp. 61–64, 2002.

[8] N. Dahan, A. Niv, G. Biener, Y. Gorodetski, V. Kleiner, and E. Hasman, "Enhanced Coherency of Thermal Emission: Beyond the Limitation Imposed by Delocalized Surface Waves," *Phys.Rev.B*, vol. 76, no. 4, p. 045427, 2007.

[9] H. Raether, *Surface Plasmons on Smooth and Rough Surfaces and on Gratings*. New York: Springer-Verlag, 1988.

[10] J. E. Sipe, "New Green-Function Formalism for Surface Optics," *J.Opt.Soc.Am.B*, vol. 4, no. 4, pp. 481–489, 1987.

[11] N. Dahan, A. Niv, G. Biener, Y. Gorodetski, V. Kleiner, and E. Hasman, "Extraordinary Coherent Thermal Emission from SiC Due to Coupled Resonant Cavities," *Journal of Heat Transfer*, vol. 130, no. 11, p. 112401, 2008.

[12] I. Celanovic, N. Jovanovic, and J. Kassakian, "Two-dimensional Tungsten Photonic Crystals as Selective Thermal Emitters," *Applied Physics Letters*, vol. 92, no. 19, p. 193101, 2008.

[13] K. Ikeda, H. T. Miyazaki, T. Kasaya, K. Yamamoto, Y. Inoue, K. Fujimura, T. Kanakugi, M. Okada, K. Hatade, and S. Kitagawa, "Controlled Thermal Emission of Polarized Infrared Waves from Arrayed Plasmon Nanocavities," *Applied Physics Letters*, vol. 92, no. 2, p. 021117, 2008.

[14] S. Y. Lin, J. Moreno, and J. G. Fleming, "Three-Dimensional Photonic-Crystal Emitter for Thermal Photovoltaic Power Generation," *Applied Physics Letters*, vol. 83, no. 2, pp. 380–382, 2003.

[15] N. C. Lindquist, P. Nagpal, K. M. McPeak, D. J. Norris, and S.-H. Oh, "Engineering Metallic Nanostructures for Plasmonics and Nanophotonics," *Reports on Progress in Physics*, vol. 75, no. 3, p. 036501, 2012.

[16] C. M. Watts, X. Liu, and W. J. Padilla, "Metamaterial electromagnetic wave absorbers," *Advanced Materials*, vol. 24, no. 23, pp. OP98–OP120, 2012.

[17] J. A. Mason, D. C. Adams, Z. Johnson, S. Smith, A. W. Davis, and D. Wasserman, "Selective Thermal Emission from Patterned Steel," *Opt.Express*, vol. 18, no. 24, pp. 25192–25198, 2010.

[18] F. J. Gonzlez, M. Abdel-Rahman, and G. D. Boreman, "Antenna-Coupled VOx Thin-film Microbolometer Array," *Microwave and Optical Technology Letters*, vol. 38, no. 3, pp. 235–237, 2003.

[19] J. Y. Park, K. Kim, and S. Moon, "Fabrication Method of 3D Feed Horn Shape MEMS Antenna Array using MRPBI System and Application for Microbolometer," vol. 4592, pp. 377–387, SPIE, 2001.

[20] J. Alda, C. Fumeaux, M. A. Gritz, D. Spencer, and G. D. Boreman, "Responsivity of Infrared Antenna-coupled Microbolometers for Air-side and Substrate-side Illumination," *Infrared Physics and Technology*, vol. 41, no. 1, pp. 1–9, 2000.

[21] C. A. Balanis, *Antenna Theory : Analysis and Design*. New York: Harper and Row, 1982.

[22] X. Xiao and D. Voelz, "Wave Optics Simulation Approach for Partial Spatially Coherent Beams," *Opt.Express*, vol. 14, no. 16, pp. 6986–6992, 2006.

[23] T. A. Germer, "SCATMECH: Polarized Light Scattering C++ Class Library," 2008.

[24] J. C. Stover, *Optical Scattering : Measurement and Analysis*. New York: McGraw-Hill, 1990.

[25] K. C. Pohlmann, *The Compact Disc Handbook*. Madison: A-R Editions, 1992.

[26] R. Carminati and J. J. Greffet, "Near-Field Effects in Spatial Coherence of Thermal Sources," *Phys.Rev.Lett.*, vol. 82, no. 8, pp. 1660–1663, 1999.

[27] C. A. Balanis, *Advanced Engineering Electromagnetics*. New York: Wiley, 1989.

[28] E. Hecht and A. Zajac, *Optics*. Reading: Addison-Wesley Pub. Co., 1974.

[29] E. D. Palik and G. Ghosh, *Handbook of Optical Constants of Solids*. San Diego: Academic Press, 1998.

[30] M. G. Moharam and T. K. Gaylord, "Rigorous Coupled-Wave Analysis of Planar-Grating Diffraction," *J.Opt.Soc.Am.*, vol. 71, no. 7, pp. 811–818, 1981.

[31] M. G. Moharam and T. K. Gaylord, "Rigorous Coupled-Wave Analysis of Metallic Surface-Relief Gratings," *J.Opt.Soc.Am.A*, vol. 3, no. 11, pp. 1780–1787, 1986.

[32] M. G. Moharam, E. B. Grann, D. A. Pommet, and T. K. Gaylord, "Formulation for Stable and Efficient Implementation of the Rigorous Coupled-Wave Analysis of Binary Gratings," *J.Opt.Soc.Am.A*, vol. 12, no. 5, pp. 1068–1076, 1995.

[33] M. G. Moharam, D. A. Pommet, E. B. Grann, and T. K. Gaylord, "Stable Implementation of the Rigorous Coupled-Wave Analysis for Surface-Relief Gratings: Enhanced Transmittance Matrix Approach," *J.Opt.Soc.Am.A*, vol. 12, no. 5, pp. 1077–1086, 1995.

[34] L. Li and C. W. Haggans, "Convergence of the Coupled-Wave Method for Metallic Lamellar Diffraction Gratings," *J.Opt.Soc.Am.A*, vol. 10, no. 6, pp. 1184–1189, 1993.

[35] L. Li, "Use of Fourier Series in the Analysis of Discontinuous Periodic Structures," *J.Opt.Soc.Am.A*, vol. 13, no. 9, pp. 1870–1876, 1996.

[36] L. Li, "New Formulation of the Fourier Modal Method for Crossed Surface-Relief Gratings," *J.Opt.Soc.Am.A*, vol. 14, no. 10, pp. 2758–2767, 1997.

[37] M. G. Moharam and T. K. Gaylord, "Diffraction Analysis of Dielectric Surface-Relief Gratings," *J.Opt.Soc.Am.*, vol. 72, no. 10, pp. 1385–1392, 1982.

[38] E. Popov, M. Nevière, B. Gralak, and G. Tayeb, "Staircase Approximation Validity for Arbitrary-Shaped Gratings," *J.Opt.Soc.Am.A*, vol. 19, no. 1, pp. 33–42, 2002.

[39] G. Sun and C. W. Trueman, "Numerical Dispersion and Numerical Loss in Explicit Finite-Difference Time-Domain Methods in Lossy Media," *Antennas and Propagation, IEEE Transactions on*, vol. 53, no. 11, p. 3684, 2005.

[40] Y. A. Cengel, *Introduction to Thermodynamics and Heat Transfer*. New York: McGraw-Hill, 1997.

[41] Z. M. Zhang, "Nano/Microscale Heat Transfer," 2007.

[42] C. Henkel, K. Joulain, R. Carminati, and J. Greffet, "Spatial Coherence of Thermal Near Fields," *Optics Communications*, vol. 186, no. 1-3, pp. 57–67, 2000.

[43] K. Joulain, J. Mulet, F. Marquier, R. Carminati, and J. Greffet, "Surface Electromagnetic Waves Thermally Excited: Radiative Heat Transfer, Coherence Properties and Casimir Forces Revisited in the Near Field," *Surface Science Reports*, vol. 57, no. 3-4, p. 59, 2005.

[44] W. E. Born, Max., *Principles of Optics : Electromagnetic Theory of Propagation, Interference and Diffraction of Light*. Cambridge: Cambridge University Press, 2006.

[45] J. J. Greffet and M. N. Vesperinas, "Field Theory for Generalized Bidirectional Reflectivity: Derivation of Helmholtz's Reciprocity Principle and Kirchhoff's Law," *J.Opt.Soc.Am.A*, vol. 15, no. 10, pp. 2735–2744, 1998.

[46] J. L. Gall, M. Olivier, and J. J. Greffet, "Experimental and Theoretical Study of Reflection and Coherent Thermal Emissionby a SiC Grating Supporting a Surface-Phonon Polariton," *Phys.Rev.B*, vol. 55, no. 15, pp. 10105–10114, 1997.

[47] F. Marquier, K. Joulain, J. P. Mulet, R. Carminati, J. J. Greffet, and Y. Chen, "Coherent Cpontaneous Emission of Light by Thermal Sources," *Phys.Rev.B*, vol. 69, no. 15, p. 155412, 2004.

[48] P. J. Hesketh, J. N. Zemel, and B. Gebhart, "Polarized Spectral Emittance from Periodic Micromachined Surfaces. I. Doped Silicon: The Normal Direction," *Phys.Rev.B*, vol. 37, no. 18, pp. 10795–10802, 1988.

[49] M. Kreiter, J. Oster, R. Sambles, S. Herminghaus, S. Mittler-Neher, and W. Knoll, "Thermally Induced Emission of Light from a Metallic Diffraction Grating, Mediated by Surface Plasmons," *Optics Communications*, vol. 168, pp. 117–122, 1999.

[50] S. Maruyama, T. Kashiwa, H. Yugami, and M. Esashi, "Thermal Radiation from Two-Dimensionally Confined Modes in Microcavities," vol. 79, no. 9, pp. 1393–1395, 2001.

[51] H. Sai, Y. Kanamori, and H. Yugami, "High-Temperature Resistive Surface Grating for Spectral Control of Thermal Radiation," *Applied Physics Letters*, vol. 82, no. 11, pp. 1685–1687, 2003.

[52] H. Sai, H. Yugami, Y. Akiyama, Y. Kanamori, and K. Hane, "Spectral Control of Thermal Emission by Periodic Microstructured Surfaces in the Near-Infrared Region," *J.Opt.Soc.Am.A*, vol. 18, no. 7, pp. 1471–1476, 2001.

[53] H. Sai and Y. Kanamori, "Spectrally Selective Thermal Radiators and Absorbers with Periodic Microstructured Surface for High-Temperature Applications," *Microscale Thermophysical Engineering*, vol. 7, pp. 101–115, 2003.

[54] H. Sai, Y. Kanamori, K. Hane, H. Yugami, and M. Yamaguchi, "Numerical Study on Tungsten Selective Radiators with Various Micro/Nano Structures," in *Photovoltaic Specialists Conference, 2005. Conference Record of the Thirty-first IEEE*, pp. 762–765, 2005.

[55] H. Sai, Y. Kanamori, K. Hane, and H. Yugami, "Numerical Study on Spectral Properties of Tungsten One-Dimensional Surface-Relief Gratings for Spectrally Selective Devices," *J.Opt.Soc.Am.A*, vol. 22, no. 9, pp. 1805–1813, 2005.

[56] F. Kusunoki, T. Kohama, T. Hiroshima, S. Fukumoto, J. Takahara, and T. Kobayashi, "Narrow-Band Thermal Radiation with Low Directivity by Resonant Modes Inside Tungsten Microcavities," *Japanese Journal of Applied Physics*, vol. 43, no. 8A, pp. 5253–5258, 2004.

[57] J. T. K. Wan, "Tunable Thermal Emission at Infrared Frequencies Via Tungsten Gratings," *Optics Communications*, vol. 282, no. 8, pp. 1671–1675, 2009.

[58] N. Nguyen-Huu, Y. Chen, and Y. Lo, "Development of a Polarization-Insensitive Thermophotovoltaic Emitter with a Binary Grating," *Opt.Express*, vol. 20, no. 6, pp. 5882–5890, 2012.

[59] P. Ben-Abdallah, "Thermal Antenna Behavior for Thin-film Structures," *J.Opt.Soc.Am.A*, vol. 21, no. 7, pp. 1368–1371, 2004.

[60] B. J. Lee, C. J. Fu, and Z. M. Zhang, "Coherent Thermal Emission from One-Dimensional Photonic Crystals," *Applied Physics Letters*, vol. 87, no. 7, p. 071904, 2005.

[61] B. A. Munk, *Frequency Selective Surfaces: Theory and Design*. New York: John Wiley and Sons, 2000.

[62] B. J. Lee and Z. M. Zhang, "Design and Fabrication of Planar Multilayer Structures with Coherent Thermal Emission Characteristics," *Journal of Applied Physics*, vol. 100, no. 6, p. 063529, 2006.

[63] B. J. Lee and Z. M. Zhang, "Coherent Thermal Emission from Modified Periodic Multilayer Structures," *Journal of Heat Transfer*, vol. 129, no. 1, pp. 17–26, 2007.

[64] L. P. Wang, B. J. Lee, X. J. Wang, and Z. M. Zhang, "Spatial and Temporal Coherence of Thermal Radiation in Asymmetric Fabry¢Perot Resonance Cavities," *International Journal of Heat and Mass Transfer*, vol. 52, no. 13-14, pp. 3024–3031, 2009.

[65] J. Drevillon, K. Joulain, P. Ben-Abdallah, and E. Nefzaoui, "Far Field Coherent Thermal Emission from a Bilayer Structure," *Journal of Applied Physics*, vol. 109, no. 3, p. 034315, 2011.

[66] B. J. Lee and Z. M. Zhang, "Indirect Measurements of Coherent Thermal Emission from a Truncated Photonic Crystal Structure," *Journal of Thermophysics and Heat Transfer*, 2009.

[67] K. Joulain and A. Loizeau, "Coherent Thermal Emission by Microstructured Waveguides," *Journal of Quantitative Spectroscopy and Radiative Transfer*, vol. 104, no. 2, p. 208, 2007.

[68] C. Wang, Y. Chang, M. Tsai, Y. Ye, C. Chen, Y. Jiang, Y. Chang, S. Lee, and D. P. Tsai, "Reflection and Emission Properties of an Infrared Emitter," *Opt.Express*, vol. 15, no. 22, pp. 14673–14678, 2007.

[69] J. D. Joannopoulos, *Photonic Crystals : Molding the Flow of Light*. Princeton: Princeton University Press, 2008.

[70] D. Chan, M. Soljacic, and J. Joannopoulos, "Thermal Emission and Design in One-dimensional Periodic Metallic Photonic Crystal Slabs," *Phys.Rev.E*, vol. 74, no. 1, p. 016609, 2006.

[71] S. Y. Lin, J. G. Fleming, D. L. Hetherington, B. K. Smith, R. Biswas, K. M. Ho, M. M. Sigalas, W. Zubrzycki, S. R. Kurtz, and J. Bur, "A Three-Dimensional Photonic Crystal Operating at Infrared Wavelengths," *Nature*, vol. 394, no. 6690, pp. 251–253, 1998.

[72] J. G. Fleming, "All-metallic Three-dimensional Photonic Crystals with a Large Infrared Bandgap," *Nature (London)*, vol. 417, pp. 52–55, -05 2002.

[73] S. Y. Lin, J. G. Fleming, and I. El-Kady, "Three-Dimensional Photonic-Crystal Emission Through Thermal Excitation," *Opt.Lett.*, vol. 28, no. 20, pp. 1909–1911, 2003.

[74] D. Chan, M. Soljacic, and J. Joannopoulos, "Direct Calculation of Thermal Emission for Three-dimensionally Periodic Photonic Crystal Slabs," *Phys.Rev.E*, vol. 74, no. 3, p. 036615, 2006.

[75] G. Biener, N. Dahan, A. Niv, V. Kleiner, and E. Hasman, "Highly Coherent Thermal Emission Obtained by Plasmonic Bandgap Structures," *Applied Physics Letters*, vol. 92, no. 8, p. 081913, 2008.

[76] M. Laroche, R. Carminati, and J. J. Greffet, "Coherent Thermal Antenna Using a Photonic Crystal Slab," *Phys.Rev.Lett.*, vol. 96, no. 12, p. 123903, 2006.

[77] D. L. C. Chan, M. Soljacic, and J. D. Joannopoulos, "Thermal Emission and Design in 2D-Periodic Metallic Photonic Crystal Slabs," *Opt.Express*, vol. 14, no. 19, pp. 8785–8796, 2006.

[78] H. Fu, Y. Jiang, M. Tsai, S. Lee, and Y. Chen, "A Thermal Emitter with Selective Wavelength: Based on the Coupling Between Photonic Crystals and Surface Plasmon Polaritons," *Journal of Applied Physics*, vol. 105, no. 3, p. 033505, 2009.

[79] A. Battula and S. C. Chen, "Monochromatic Polarized Coherent Emitter Enhanced by Surface Plasmons and a Cavity Resonance," *Phys.Rev.B*, vol. 74, no. 24, p. 245407, 2006.

[80] F. J. Gonzlez, M. A. Gritz, C. Fumeaux, and G. D. Boreman, "Two Dimensional Array of Antenna-Coupled Microbolometers," *International Journal of Infrared and Millimeter Waves*, vol. 23, no. 5, pp. 785–797, 2002.

[81] F. J. Gonzlez, C. S. Ashley, P. G. Clem, and G. D. Boreman, "Antenna-Coupled Microbolometer Arrays with Aerogel Thermal Isolation," *Infrared Physics and Technology*, vol. 45, pp. 47–51, 1 2004.

[82] F. J. Gonzalez, B. Ilic, J. Alda, and G. D. Boreman, "Antenna-Coupled Infrared Detectors for Imaging Applications," *Selected Topics in Quantum Electronics, IEEE Journal of*, vol. 11, no. 1, pp. 117–120, 2005.

[83] P. Krenz, J. Alda, and G. Boreman, "Orthogonal Infrared Dipole Antenna," *Infrared Physics and Technology*, vol. 51, no. 4, p. 340, 2008.

[84] C. T. Middlebrook, P. M. Krenz, B. A. Lail, and G. D. Boreman, "Infrared Phased-Array Antenna," *Microwave and Optical Technology Letters*, vol. 50, no. 3, pp. 719–723, 2008.

[85] J. Ginn, D. Shelton, P. Krenz, B. Lail, and G. Boreman, "Polarized Infrared Emission Using Frequency Selective Surfaces," *Opt.Express*, vol. 18, no. 5, pp. 4557–4563, 2010.

[86] S. L. Wadsworth, P. G. Clem, E. D. Branson, and G. D. Boreman, "Broadband Circularly-Polarized Infrared Emission from Multilayer Metamaterials," *Opt.Mater.Express*, vol. 1, no. 3, pp. 466–479, 2011.

[87] H. T. Miyazaki, K. Ikeda, T. Kasaya, K. Yamamoto, Y. Inoue, K. Fujimura, T. Kanakugi, M. Okada, K. Hatade, and S. Kitagawa, "Thermal Emission of Two-Color Polarized Infrared Waves from Integrated Plasmon Cavities," *Applied Physics Letters*, vol. 92, no. 14, p. 141114, 2008.

[88] Y. B. Chen and Z. M. Zhang, "Design of Tungsten Complex Gratings for Thermophotovoltaic Radiators," *Optics Communications*, vol. 269, no. 2, pp. 411–417, 2007.

[89] I. Balin, N. Dahan, V. Kleiner, and E. Hasman, "Bandgap Structure of Thermally Excited Surface Phonon Polaritons," *Applied Physics Letters*, vol. 96, no. 7, p. 071911, 2010.

[90] S. Franssila, *Introduction to Microfabrication*. New Jersey: J. Wiley, 2004.

189

[91] H. A. Macleod, "Structure Related Optical Properties of Thin Films," *Journal of Vacuum Science and Technology A: Vacuum, Surfaces, and Films*, vol. 4, no. 3, pp. 418–422, 1986.

[92] D. E. Aspnes, "Optical Properties of Thin Films," *Thin Solid Films*, vol. 89, no. 3, pp. 249–262, 1982.

[93] A. C. Nyce and L. P. Skolnick, "Optical Constants of Bulk and Thin-Film Aluminum at 6328 å," *J.Opt.Soc.Am.*, vol. 65, no. 7, pp. 792–796, 1975.

[94] C. A. Melendres, S. V. Gils, and H. Terryn, "Toward a Quantitative Description of the Anodic Oxide Films on Aluminum," *Electrochemistry Communications*, vol. 3, no. 12, pp. 737–741, 2001.

[95] J. A. Woollam, B. D. Johs, C. M. Herzinger, J. N. Hilfiker, R. A. Synowicki, and C. L. Bungay, "Overview of Variable-Angle Spectroscopic Ellipsometry (VASE): I. Basic Theory and Typical Applications," in *Society of Photo-Optical Instrumentation Engineers (SPIE) Conference Series* (A.-J. G. A., ed.), p. 3, Jul 1999.

[96] I. A. Blech and H. A. V. Plas, "Step Coverage Simulation and Measurement in a DC Planar Magnetron Sputtering System," *Journal of Applied Physics*, vol. 54, no. 6, pp. 3489–3496, 1983.

[97] M. Neviere and E. Popov, *Light Propagation in Periodic Media : Differential Theory and Design*. New York: Marcel Dekker, 2003.

[98] S. Peng and G. M. Morris, "Efficient Implementation of Rigorous Coupled-Wave Analysis for Surface-Relief Gratings," *J.Opt.Soc.Am.A*, vol. 12, no. 5, pp. 1087–1096, 1995.

[99] D. G. Voelz, *Computational Fourier Optics : A MATLAB Tutorial*. Bellingham: SPIE Press, 2011.

[100] F. Kong, K. Li, B. I. Wu, B. I. Huang, H. Chen, and J. A. Kong, "Propagation Properties of the SPP Modes in Nanoscale Narrow Metallic Gap, Channel, and Hole Geometries," *Progress In Electromagnetics Research*, vol. 76, pp. 449–466, 2007.

[101] B. C. Smith, *Fundamentals of Fourier Transform Infrared Spectroscopy*. Boca Raton: CRC Press, 1996.

[102] "MR Series FT-Spectroradiometers Design Overview and Theory," tech. rep., Bomem Inc., 1995.

[103] J. Chaves, *Introduction to Nonimaging Optics*. Boca Raton: CRC Press, 2008.

[104] *IR-VASE Users Guide*. J.A. Woollam Co., Inc., 2010.

REPORT DOCUMENTATION PAGE

Form Approved
OMB No. 0704–0188

1. REPORT DATE *(DD–MM–YYYY)*	2. REPORT TYPE	3. DATES COVERED *(From — To)*
13–09–2013	Doctoral Dissertation	Sep 2010–Sep 2013

4. TITLE AND SUBTITLE

Directional Thermal Emission and Absorption from Surface Microstructures in Metalized Plastics

5a. CONTRACT NUMBER

5b. GRANT NUMBER

5c. PROGRAM ELEMENT NUMBER

6. AUTHOR(S)

Seal, Michael D., Major, USAF

5d. PROJECT NUMBER

5e. TASK NUMBER

5f. WORK UNIT NUMBER

7. PERFORMING ORGANIZATION NAME(S) AND ADDRESS(ES)

Air Force Institute of Technology
Graduate School of Engineering and Management (AFIT/EN)
2950 Hobson Way
WPAFB, OH 45433-7765

8. PERFORMING ORGANIZATION REPORT NUMBER

AFIT-ENP-DS-13-S-03

9. SPONSORING / MONITORING AGENCY NAME(S) AND ADDRESS(ES)

Intentionally left blank

10. SPONSOR/MONITOR'S ACRONYM(S)

11. SPONSOR/MONITOR'S REPORT NUMBER(S)

12. DISTRIBUTION / AVAILABILITY STATEMENT

DISTRIBUTION STATEMENT A:
APPROVED FOR PUBLIC RELEASE; DISTRIBUTION UNLIMITED

13. SUPPLEMENTARY NOTES

This work is declared a work of the U.S. Government and is not subject to copyright protection in the United States.

14. ABSTRACT

Thermal emission, exhibiting antenna-like directivity, has been generated by a wide variety of both simple and complex micro-structures. The basic demonstrations of directional emission, and specific device performance evaluations, have been conducted at elevated temperatures, typically several hundred degrees Celsius. The most common applications for these high-temperature designs are thermal photo-voltaic and spectroscopic sources. A wide range of lower temperature applications, such as spacecraft thermal management and mid- to far-infrared optical train stray light management, are precluded by the cost and complexity of the fabrication processes employed.

In this work, a novel fabrication and physical surface optimization of a seminal directionally emitting structure is conducted in metalized plastic. The fabrication method is derived from the high-throughput compact disc manufacturing process and exploits the advantageous surface electromagnetic properties of aluminium, at the expense of forgoing high-temperature operation. Then, a novel directionally emitting structure, exhibiting a broader angular response, is design and fabricated by the same methods. The performance of both structures is evaluated through reflectance and self-emission measurements, and compared to rigorous modeling results. The necessity of conducting low-temperature emission and reflectance measurements, on instruments designed for radiometry rather than scatterometry, requires consideration of the longitudinal spatial coherence of field incidence on the surface. To this end, a well-developed modeling method was extended to include finite longitudinal spatial coherence excitation.

15. SUBJECT TERMS

Directional Thermal Emission, Coherent Thermal Emission, Infrared Micro-structures, Metalized Plastic, Binary Grating

16. SECURITY CLASSIFICATION OF:			17. LIMITATION OF ABSTRACT	18. NUMBER OF PAGES	19a. NAME OF RESPONSIBLE PERSON
a. REPORT	b. ABSTRACT	c. THIS PAGE			Dr. Michael A. Marciniak (ENP)
U	U	U	UU	208	19b. TELEPHONE NUMBER *(include area code)* (937)255-3636x4529 michael.marciniak@afit.edu

Standard Form 298 (Rev. 8–98)
Prescribed by ANSI Std. Z39.18